COMPUTER-BASED ANALYSIS OF HISTONE DEACETYLASE 10 AND ITS INHIBITOR COMPLEXES

DISSERTATION

zur Erlangen des akademischen Grades

Doctor rerum naturalium (Dr. rer. nat.)

der Naturwissenschaftlichen Fakultät I

Biowissenschafften der Martin Luther Universität

Halle-Wittenberg

von **Talha Zahid Yesiloglu**

im Februar 2025

Gutachter:

1) Prof. Dr. Wofgang Sippl, Halle, MLU

2) Prof. Dr. Mike Schutkowski, Halle, MLU

3) Prof. Dr. Erden Banoglu, Ankara, Gazi Universty

Datum der Disputation: 25.08.2025

Summary

Pan HDAC inhibitors are approved for cancer treatment, however, their lack of selectivity and poor pharmacokinetic profiles limit their effectiveness. This study focuses on developing selective inhibitors and degraders for HDAC10, a class IIb enzyme with unique polyamine deacetylase activity, to explore new therapeutic strategies.

Advanced computational methods - including molecular docking, molecular dynamics (MD) simulations, binding free energy (BFE) calculations, and co-solvent MD simulations - were employed to design selective inhibitors. Comparative structural analyses have already identified key HDAC10-specific residues, such as Glu274, Trp205, and Asp94, which are essential for polyamine binding and selectivity. These findings guided the development of optimized molecular scaffolds, including piperidine-acryl, piperidine-propyl, and benzyl-linked hydroxamates.

MD simulations validated the stability of HDAC10-inhibitor complexes, confirming critical interactions with catalytic zinc ions and key residues. N^8-acetylspermidine showed superior binding affinity compared to N^1-acetylspermidine, highlighting the importance of precise ligand conformation.

Co-solvent MD simulations identified key regions in HDAC6 and HDAC8 and reinforced Glu274, Trp205, and Ala94 as critical target residues for HDAC10-specific inhibition.

The study also explored PROTAC technology by investigating HDAC10-specific degraders. Molecular docking and MD simulations of ternary complexes involving VHL-based PROTACs revealed the binding states of these complexes and demonstrated the potential for strong interactions, such as hydrogen bonds and zinc coordination bonds, to form between the respective warheads and related proteins. The stability of these interactions was confirmed through MD simulations. Furthermore, docking studies based on the PROTAC6_7 model successfully distinguished between active and inactive degraders.

In conclusion, this research presents a robust framework for developing selective HDAC10 inhibitors and degraders. The gained insights advance our understanding of HDAC10's binding dynamics and offer a foundation for designing next-generation therapeutics that integrate selective inhibition and targeted degradation strategies for HDAC-related diseases.

Kurzfassung

Pan-HDAC-Inhibitoren sind zwar für die Krebsbehandlung zugelassen, doch ihre mangelnde Selektivität und ungünstigen pharmakokinetischen Profile schränken ihre therapeutische Wirksamkeit erheblich ein. Diese Studie zielt darauf ab, selektive Inhibitoren und Degrader für HDAC10, ein Klasse-IIb-Enzym mit einzigartiger Polyamin-Deacetylase-Aktivität, zu entwickeln, um neue therapeutische Ansätze zu erkunden.

Fortschrittliche computergestützte Methoden – darunter molekulares Docking, Molekulardynamik-(MD)-Simulationen, Berechnungen der Bindungsfreien Energie (BFE) und Co-Solvens-MD-Simulationen – wurden eingesetzt, um selektive Inhibitoren zu designen. Vergleichende strukturelle Analysen identifizierten zentrale HDAC10-spezifische Reste wie Glu274, Trp205 und Asp94, die für die Polyamin-Bindung und Selektivität essenziell sind. Diese Erkenntnisse dienten der Entwicklung optimierter molekularer Gerüste wie Piperidin-Acryl-, Piperidin-Propyl- und Benzyl-verknüpfte Hydroxamate.

MD-Simulationen bestätigten die Stabilität der HDAC10-Inhibitor-Komplexe und zeigten kritische Interaktionen mit katalytischen Zinkionen und Schlüsselresten. Bemerkenswerterweise zeigte N8-Acetylspermidin eine überlegene Bindungsaffinität im Vergleich zu N1-Acetylspermidin, was die Bedeutung präziser Ligandkonformationen bei der Inhibitordesign unterstreicht.

Co-Solvens-MD-Simulationen identifizierten zudem wichtige Bereiche in HDAC6 und HDAC8 und bekräftigten Glu274, Trp205 und Ala94 als entscheidende Zielreste für die spezifische Hemmung von HDAC10.

Die Studie untersuchte außerdem die PROTAC-Technologie durch die Erforschung von HDAC10-spezifischen Degradern. Molekulares Docking und MD-Simulationen von ternären Komplexen mit VHL-basierten PROTACs lieferten Einblicke in die Bindungszustände dieser Komplexe und zeigten das Potenzial für starke Interaktionen, wie Wasserstoffbrücken und Zink-Koordinationsbindungen, zwischen den jeweiligen Warheads und assoziierten Proteinen. Die Stabilität dieser Interaktionen wurde durch MD-Simulationen bestätigt. Darüber hinaus konnten Docking-Studien auf Basis des PROTAC6_7-Modells erfolgreich zwischen aktiven und inaktiven Degradern unterscheiden. Zusammenfassend bietet diese Forschung einen umfassenden Rahmen für die Entwicklung selektiver HDAC10-Inhibitoren und -Degrader. Die gewonnenen Erkenntnisse erweitern das Verständnis der Bindungsdynamik von HDAC10 und

schaffen eine Grundlage für die Entwicklung von Next-Generation-Therapeutika, die selektive Inhibition und gezielte Degradationsstrategien für HDAC-assoziierte Erkrankungen integrieren.

Schlüsselwörter: Epigenetik, HDAC10, Selektive Inhibition, PROTAC, Molekulares Docking, MD-Simulationen, Polyamin-Deacetylase, Neuroblastom, *dr*HDAC10.

Acknowledgements

I also want to express my gratitude to my family and friends in Türkiye and the friends I found in Germany; **Sadullah, Ekrem, Fatma Zehra** and **Ayşe** who have always supported me. A special thanks goes to my spouse, **Rumeysa Nur**. Thank you for standing by me throughout this journey and for being such an important part of my life.

Dedication

This work is dedicated to my parents and family, whose boundless love and unwavering support have been the guiding light on every step of this journey. To those who have lifted me with their quiet strength and believed in me when I faltered, I offer this as a testament to their enduring faith and encouragement.

Contents

List of figures

List of tables

List of Abbreviations

μM - Micromolar

nM - Nanomolar

2D - Two Dimensional

3D - Three Dimensional

AM1-BCC - Austin Model1 with Bond Correction Charge

BFE - Binding Free Energy

CADD - Computer-Aided Drug Design

CD - Catalytic Domains

CoREST - Corepressor of REST

DMSO - Dimethylsulfoxide

FEP - Free Energy Perturbation

GAFF - General Amber Force Field

HAT - Histone Acetyltransferase

HDAC - Histone Deacetylase

HDACi - HDAC Inhibitor

IC_{50} - Half-Maximal Inhibitory Concentration

MD - Molecular Dynamics

MMGBSA - Molecular Mechanics - Generalized Born Surface Area

MMPBSA - Molecular Mechanics - Poisson Boltzmann Surface Area

NAD - Nicotinamide Adenine Dinucleotide

NCoR - Nuclear Receptor Corepressor

NuRD - Nucleosome Remodeling and Deacetylase Complex

PDB - Protein Data Bank

pIC_{50} - Negative Logarithm of IC50

POI - Protein of Interest

PROTAC - PROteolysis-TArgeting Chimera

PTM - Post-Translational Modification

QSAR - Quantitative Structure-Activity Relationship

RMSD - Root-Mean-Square Deviation

RMSE - Root-Mean-Square Error

SAR - Structure-Activity Relationship

SBDD - Structure-Based Drug Design

SMRT - Silencing Mediator for Retinoid and Thyroid Receptors

SP - Standard Precision

TI - Thermodynamic Integration

VHL - von Hippel-Lindau E3 Ubiquitin Ligase

WHO - World Health Organization

ZBG - Zinc Binding Group

ZMAL - Z(Ac)Lys - AMC

Zn - Zinc Atom

1. INTRODUCTION

The epigenome is a phenomenon that occurs at the molecular level and is the result of various covalent modifications of histone proteins, DNA and non-histone proteins, and RNA interference occurring in a tremendous harmony and balance [1, 2].

Covalent modifications of histone proteins play an important role in the regulation of chromatin dynamics and contribute to the regulation of biological processes involving chromatin, such as repair, replication, genome stability and transcription [3]. Chromatin is a complex of macromolecules which is structured by DNA, RNA and histone proteins [4]. The elementary building blocks that make up the chromatin are repetitive nucleosomes. These nucleosomes are formed a by positively charged central octamer structure consisting four pairs of core histones (H2A, H2B, H3 and H4) surrounded by negatively charged DNA [5, 6]. Core histone proteins contain several alkaline lysine residues in histone tails that interact with the negatively charged surrounding DNA. These interactions maintain the chromatin structure in the form of inactive, compact heterochromatin. Modification of these alkaline lysine residues by post-translational modifications (PTMs) such as SUMOylation, hydroxylation, ubiquitination, phosphorylation, methylation, sulfation and acetylation leads to the conversion of the chromatin structure [5, 7]. Among these, acetylation is a reversible PTM maintained by rival histone/lysine acetyltransferase enzymes (HATs/KATs) and histone deacetylases (HDACs) [8, 9] (See Figure 1).

HATs neutralize the positive charge of lysine by catalyzing the acetylation of the side chain of lysine residues in histone tails. As a result of this neutralization, the ionic bond between positively charged lysine and negatively charged DNA is eliminated, which relaxes the chromatin structure into the active euchromatin form and makes the genetic code in the DNA readable by transcription factors [7].

On the other hand, HDACs catalyze the removal of the acetyl group from the lysine residue and the reacquisition of a positive charge on the lysine, which will tighten the chromatin structure and result in the silencing of the genetic code [10].
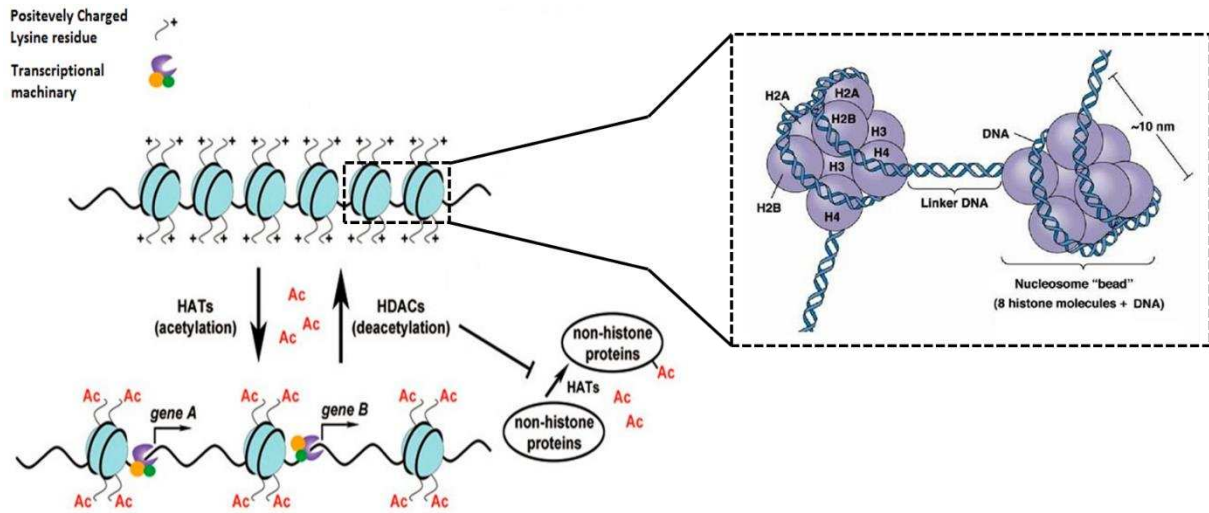
Figure 1: Histone acetylation equilibrium: the role of HATs and HDACs in histone modification and gene expression (adapted from [11, 12]).

High expression of some HDACs has already been reported in cancer and other diseases such as tissue fibrosis, inflammatory and/or autoimmune disease, and even in some metabolic disorders [13]. Targeting deacetylases may offer an efficient therapeutic approach for these aforementioned diseases.

1.1. HDACs

As mentioned earlier, histone deacetylases (HDACs) are enzymes that remove acetyl groups on lysine residues from histone and non-histone proteins. The classification of HDACs is done based on criteria such as subcellular localization, expression pattern, function, structure and homology to yeast HDACs. 18 HDAC subtypes have been discovered so far in humans and are grouped into two families namely, the classical histone deacetylase family, commonly referred to as HDACs, which is further classified into zinc dependent classes I, II and IV, and the Sir2 regulatory family (SIRT) which make up the NAD⁺ dependent class III. Class III HDACs, consisting of isoenzymes known as SIRT1-7, are homologous to the yeast Sir2 protein family, unlike other HDAC classes, and do not show sequence homology with other HDAC classes [14] (See Figure 2, Figure 3).

Class I HDACs (HDAC1, HDAC2, HDAC3 and HDAC8) have sequence similarity to the yeast Rpd3 protein and are nuclear proteins that share a compact structure and are expressed in most tissues and cells. Meanwhile class II HDACs are similar to the yeast Hda1 protein, and are found in both the cytoplasm and nucleus. They are further sub-grouped based on their domain composition and sequence similarity into class IIa (HDAC4, HDAC5, HDAC7 and HDAC9) and class IIb (HDAC6 and HDAC10) [15, 16]. The most recently discovered subtype,

HDAC11, is the only representative of class IV and shows similarities with class I and II HDACs [17]. In contrast to class III HDACs, class I, II and IV HDACs and orthologues yeast Rpd3 and yeast HDA1 share some degree of homology in catalytic domains [18].
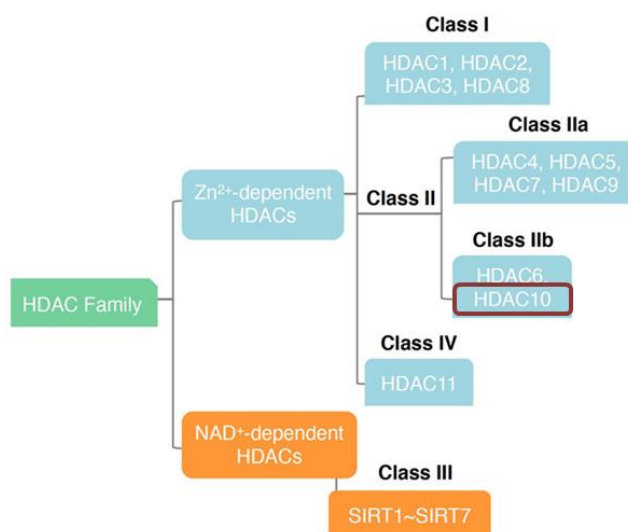
Figure 2: Classification of HDACs.

It has been reported that Archaea and Eubacteria have enzymes related to classical HDACs [19]. This points to the possibility of a common precursor enzyme lacking histone deacetylase activity, which could explain the fact that not all known HDACs utilize histones as substrates and why they have other non-histone substrates such as tumor suppressor protein p53, transcription factor NF-kappaB, chaperone protein Hsp90 and SMC3 belonging to cohesin complex [20-25].

Among HDACs, class I members are omnipresent but preferentially localized in the nucleus. They mainly have histone deacetylase activity and contain on average around 400 amino acids [15]; for exact isoform-specific numbers please see the Figure 3. Moreover, cytoplasmic and tissue-specific activities have also been demonstrated for HDAC1, HDAC3 and HDAC8 isoforms [26-28]. Class I HDACs are found in multiprotein complexes and the composition of these complexes determines the activity and substrate specificity of HDACs in this class. HDAC1 and HDAC2 form the catalytic core of multiple co-repressor complexes such as Sin3, CoREST, MiDAC and NuRD, while HDAC3 is being complexed with SMRT and N-CoR structures [29, 30]. HDAC8, a unique class I deacetylase, does not require any co-repressor structure [31]. For HDAC8, in addition to its lysine deacetylase function, it has been demonstrated to be active in the cleavage of longer chain acyllysines which include octanyllysine and myristoyllysine [32].

The class IIa HDAC enzymes HDAC4, 5, 7 and 9 are located between the cytoplasm and the nucleus and express in a cell type-specific manner while containing 912-1122 amino acids [15]. HDAC4, 5, 7 and 9 isoforms are found in developed brain, heart and muscle cells, while increased concentrations of HDAC7 have been detected in lung tissue [33]. Class IIa HDACs contain a conserved deacetylase domain at the C-terminus plus a unique adapter domain at the N-terminus. This unique adapter structure forms the binding pocket of MEF2, a DNA-binding transcription factor, while the subsequent serine-rich 3~4 phosphorylation sites act as regulatory signals for the assembly of 14-3-3 proteins. The 14-3-3 proteins have the ability to migrate to the cytoplasm or nucleus as a response to several regulatory signals [34]. Phosphorylation if the serum-rich sites induces 14-3-3 proteins binding with class IIa HDACs, resulting in the shuttling of class IIa HDACs from nucleus to cytoplasm. This so-called shuttling is characteristic of class IIa isoforms and serves, among other mechanisms, to regulate activity [35]. Furthermore, like class I HDAC3, class IIa HDACs also interact with SMRT and N-CoR; these interactions of class IIa HDACs are mediated through HDAC domains [33, 36].

Class IIb HDACs, namely HDA6 and HDAC10 possess two domains each, making them unique among the HDAC isoforms. HDAC6, including around 1215 amino acids, contains two active domains (CD1 and CD2), while HDAC10, including around 669 amino acids, contains only one active domain and one inactive enigmatic leucine-rich domain [15, 33]. The activities and substrate specificities of CD1 and CD2 in HDAC6 isoform differ from each other. Additionally, HDAC6 carries also a ubiquitin binding zinc finger domain (ZnF-UBP domain) on its C-terminal. Both HDAC6 and HDAC10 enzymes are primarily located in the cytoplasm, but both have ability to translocate to nucleus upon receiving cellular signals. HDAC6 is primarily involved in organizing the cytoskeleton by deacetylase activities in the cytosol. Furthermore, it has been shown that CD1 of the HDAC6 demonstrates ubiquitin E3 ligase activity [37], and HDAC6 induces aggresomal formation by recognizing misfolded proteins through its ZNF-UBP domain [38].

New findings have demonstrated that HDAC10 exhibits polyamine deacetylase activity rather than histone deacetylase activity [39]. Given that HDAC10 is found in particularly high concentrations in the liver, spleen and kidneys, this enzyme is thought to be responsible for the deacetylation of polyamine building blocks in these organs [39-41]. As HDAC10 is the main subject of this study, it will be analyzed in more detail in Section 1.4.

HDAC11, the only enzyme of class IV, was first identified in 2002 [17]. Class IV was created due to low sequence homology with other classes. HDAC11 is thought to play a role in the

4

modulation of the immune system [42]. Recent studies show that HDAC11 displays a lysine-fatty acid amide hydrolase activity and specifically cleaves myristoyl residues from acylated lysine side chains [43, 44] (see Figure 3).
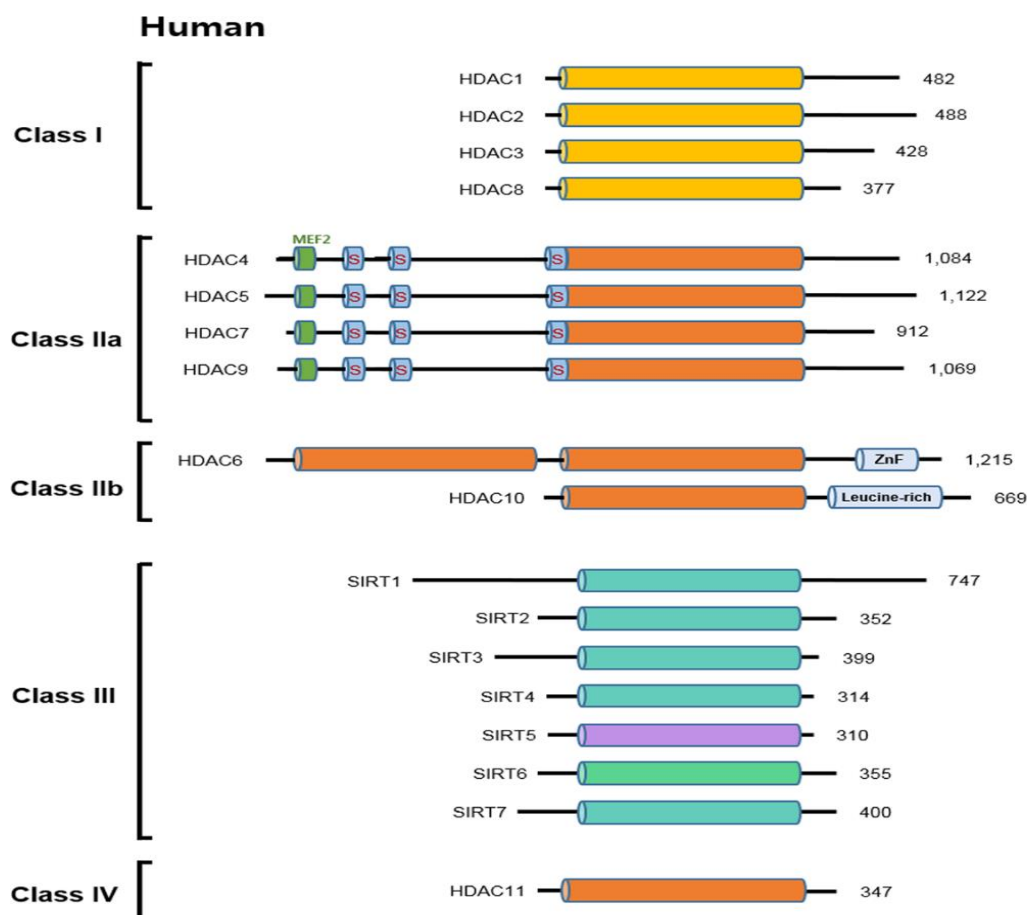
Figure 3: Domain Structure and Classification of Human HDACs: Includes catalytic domains (cylinders), MEF2-binding motifs (short green cylinders), 14-3-3 binding sites (short blue cylinders labeled 'S'), and zinc finger domains (labeled ZnF) and total amino acid counts are shown (adapted from [23]).

1.2. Catalytic Mechanism of Zinc Dependent HDAC Enzymes

The crystal structure of bacterial histone deacetylase-like protein (HDLP) from Aquifex aeolicus provided the first description of the mechanism of zinc-dependent deacetylases. HDLP has 35% sequence homology with human HDAC1. Figure 4 illustrates the catalytic mechanism of lysine deacetylation by HDACs as currently understood based on the crystal structures of human HDAC8. The reaction mechanism begins with a water molecule nucleophilically attacking the carbonyl function of the substrate. The polarity of the carbonyl structure is increased by a hydrogen bond through the hydroxyl group of the tyrosine residue, which is conserved in other isoforms and is numbered 306 in HDAC8. The carbonyl group is also coordinated with the zinc ion. This coordination enhances the activity of the carbonyl group and ensures its proximity to the nucleophilic water molecule. Simultaneously, H143 accepts a

proton from the water molecule, acting as a general base catalyst to activate the water molecule for the nucleophilic attack (see Figure 4A). This allows the formation of a tetrahedral intermediate, as shown in Figure 4B. This tetrahedral intermediate is stabilized by the tyrosine residue 306 and the zinc ion. At this stage, H143, having accepted a proton from the water molecule, acts as a general acid catalyst and donates the proton to the ligand's amide nitrogen atom. As a result (Figure 4C), the acetate group separates from the ligand, while the acetate structure continues to be stabilized by the tyrosine and zinc atoms. Throughout the entire process, H143 acts as both a general base and a general acid catalyst. Meanwhile, H142 serves as an electrostatic catalyst for the negative charge of the acetate intermediate and contributes to the process by simultaneously arranging the position of H143 through steric interactions. The formed acetate is released through the Acetate Release Channel. The protonated lysine is released through the Acetyllysine Channel [45, 46].
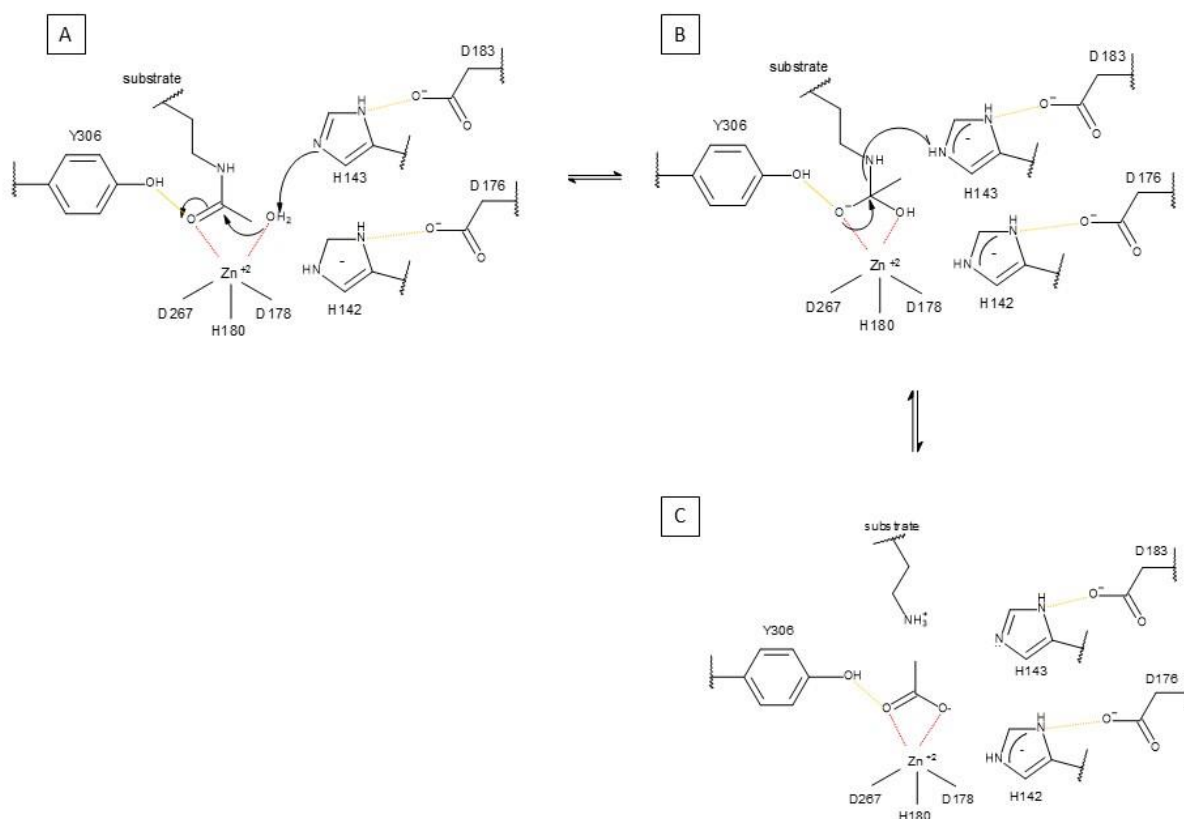
Figure 4: Schematic representation of the catalytic mechanism of lysine deacetylation by HDACs, illustrated for HDAC8 as an example (adapted from [46]).

1.3. HDAC Inhibitors (HDACi): Potential Therapeutic Agents and Their Structural Properties

Histone deacetylase inhibitors (HDACi) have gained attention as potential therapeutic agents due to their ability to target HDACs implicated in various diseases such as neurodegenerative disorders, inflammatory conditions, and cancer [47-51]. By inhibiting HDAC activity, HDACi

promote the accumulation of acetylated histones, leading to altered gene expression patterns [49]. Numerous HDACi have shown promising outcomes in both preclinical and clinical studies, positioning them as potential treatments. However, further research is needed to refine their efficacy and mitigate possible side effects [52, 53].

HDAC inhibitors typically consist of three main structural components: a zinc-binding group (ZBG), a linker, and a capping group (cap). Based on the chemical structure of their zinc-binding moiety, they are generally classified into five major groups: hydroxamic acid derivatives, benzamides (ortho-aminoanilides), cyclic peptides, and carboxylic acid derivatives. Among these groups, till now, there are six approved HDAC inhibitors as depicted in the Figure 5 and as follows:

- **Vorinostat**: A hydroxamic acid derivative approved by the Food and Drug Administration (FDA) in 2006 for treating cutaneous T-cell lymphoma (CTCL) and peripheral T-cell lymphoma (PTCL) [52, 54].

- **Romidepsin**: A cyclic peptide approved by the FDA in 2009 for CTCL and PTCL [54, 55].

- **Belinostat**: A hydroxamic acid derivative approved by the FDA in 2014 for PTCL [54].

- **Chidamide**: An aminobenzamide derivative approved by the China Food and Drug Administration (CFDA) in 2015 for PTCL [56].

- **Panobinostat**: A hydroxamic acid derivative approved by both the FDA and the European Medicines Agency (EMA) in 2015 for multiple myeloma [56, 57]. In 2021, citing lack of feasibility of completing required post marketing trials, Secura Bio, Inc. requested the withdrawal of panobinostat's FDA approval, and in March 2022, the FDA withdrew panobinostat from the US market [58].

- **Givinostat**: A hydroxamic acid derivative approved by the FDA in 2024 for boys aged 6 years and older with all genetic variants of Duchenne muscular dystrophy (DMD) [59].
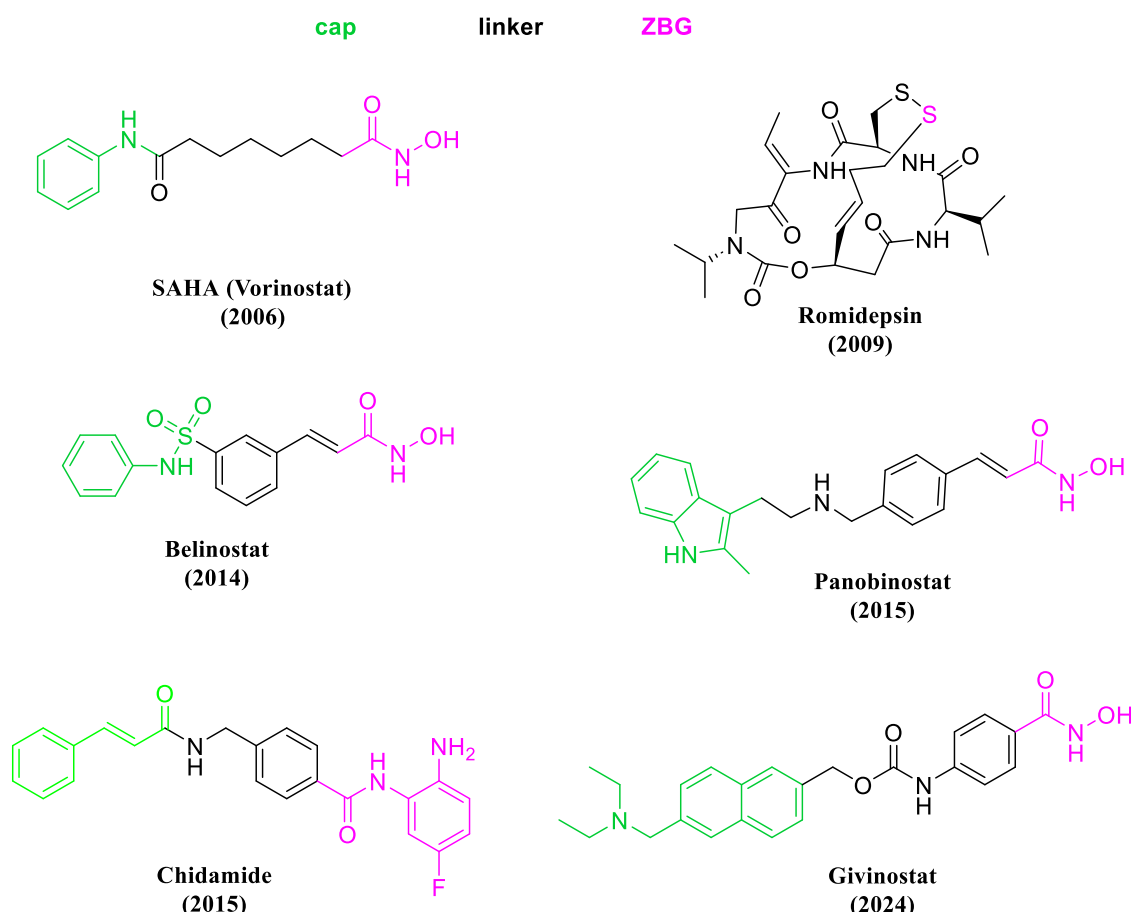
Figure 5: Structures of approved HDAC inhibitors with highlighted pharmacophore features and key structural elements.

However, most of these drugs are considered pan-HDAC inhibitors with limited isoform selectivity, leading to several side effects such as hematological issues (e.g., thrombocytopenia, anemia, and neutropenia) and an increased incidence of cardiac arrhythmias. Additionally, they face challenges like a narrow therapeutic window, suboptimal pharmacokinetic profiles, and drug resistance. Enhancing target selectivity through the development of isoform- or class-specific HDAC inhibitors may help reduce off-target effects. Nevertheless, it remains to be demonstrated in clinical settings whether the benefits of selective HDAC inhibitors can be translated into improved clinical outcomes [60, 61].

1.4. Histone Deacetylase 10 (HDAC10)

Histone deacetylase 10 (HDAC10) was first identified in 2002 by four independent research groups [40, 41, 62, 63]. It shares 55% sequence homology with HDAC6, leading to its classification as a class IIb enzyme. Both HDAC10 and HDAC6 possess two catalytic domains, setting them apart from other classes of histone deacetylases. However, unlike HDAC6, only one catalytic domain in HDAC10 is active, while the other lacks a substrate-binding pocket and remains inactive. This inactive domain likely interacts with the active domain, influencing its

functionality [40, 41, 62, 63]. David Christianson's research group later identified HDAC10 as a polyamine deacetylase (PDAC) due to its high activity toward polyamine substrates, particularly *N*8-acetylspermidine. This aligns with observations that tissues with high polyamine deacetylase activity also exhibit elevated levels of HDAC10 [64].

HDAC10 is broadly expressed in various human tissues, including the kidneys, pancreas, liver, spleen, heart, testis, brain, and placenta [41]. Its distinct preference for deacetylating polyamines, as opposed to lysine residues on proteins, sets it apart from other histone deacetylases [64]. Polyamines are crucial for modulating the activity of biological macromolecules, contributing to the stabilization and packaging of DNA, RNA structural modulation, and the regulation of transcription, translation, and the cell cycle [65-68].

In 2017, the first crystal structure of HDAC10 from zebrafish was revealed with PDB ID:5TD7 [64]. It displayed two arginase-deacetylase folds similar to HDAC6; however, only one of HDAC10's domains is catalytically active, while the smaller domain is inactive and is referred to as a pseudodeacetylase domain [69, 70]. A key feature of HDAC10 is a conserved negatively charged glutamate residue (Glu272 in humans and Glu274 in zebrafish) positioned at the active site. This residue functions as a gatekeeper, facilitating the hydrolysis of positively charged *N*8-acetylspermidine, thus giving HDAC10 a strong affinity for polyamine substrates but minimal activity toward lysine residues [64, 71, 72].

Another distinctive structural feature of HDAC10 is a 3_{10}-helix near the enzyme's active site, comprising four amino acid residues (P^{21}-E^{22}-C^{23}-E^{24} in humans or P^{23}-A^{24}-C^{25}-E^{25} in zebrafish) and also called PE(A)CE motif. This helix limits access to the active site, preventing larger acetylated lysine side chains from reaching the catalytic zinc ion, thereby enhancing the enzyme's selectivity for smaller acetyl polyamines [73].

HDAC10 is involved in various physiological and pathological processes. For instance, knocking out HDAC10 was shown to enhance the activity of regulatory T cells, boosting their immunosuppressive effects [74, 75]. HDAC10 also plays a role in DNA repair, and its involvement in cancer progression has attracted significant interest [76]. In cervical cancer, HDAC10 inhibits matrix metalloproteinases 2 and 9, reducing metastasis [77]. Additionally, HDAC10 is crucial in ovarian and lung cancers, where its elevated levels are essential for tumor cell proliferation. In ovarian cancer, silencing HDAC10 with siRNA makes cells more sensitive to cisplatin, overcoming chemotherapy resistance [78]. Similarly, knocking out HDAC10 in lung cancer cells stops the cell cycle and triggers apoptosis [79, 80]. In neuroblastoma cells,

HDAC10 regulates autophagy. Without HDAC10, there is an accumulation of autophagosomes and lysosomes, likely due to a disruption in their fusion process. In neuroblastoma cells resistant to the chemotherapeutic drug doxorubicin, elevated HDAC10 levels help expel the drug through autophagy. Conversely, inhibiting HDAC10 reverses this resistance and increases the cells' sensitivity to doxorubicin [81].

Given its unique structural and functional properties, HDAC10 represents an attractive target for therapeutic intervention. Research in 2020 demonstrated that inhibitors with bulky capping groups could still be accommodated in the active site, provided they were the appropriate size and shape. This discovery opens up new opportunities for designing specific HDAC10 inhibitors [70]. Ongoing research into HDAC10 inhibitors holds promise for overcoming drug resistance and inhibiting cancer progression. By exploiting HDAC10's narrow active site and substrate specificity, future therapies could provide more effective and targeted treatments for diseases linked to HDAC10 dysregulation.

1.5. Known HDAC10 Inhibitors and Structures

HDAC10 inhibitors, like other HDAC inhibitors, are structured with a zinc-binding group (ZBG), a linker, and a capping group. Tubastatin A, a prominent HDAC inhibitor, and its open analogue DKFZ-480, have been identified as effective against both HDAC6 and HDAC10. These compounds exhibit selectivity indices (SI) of 7 and 40 for HDAC10/6, respectively. Their strong binding affinity for HDAC10 is primarily due to electrostatic interactions between the tertiary amine group and the gatekeeper residue E274 [70, 73, 82]. TH34 has also been highlighted as a promising pan-HDAC inhibitor with activity against HDAC6, HDAC8, and HDAC10 [83]. Recently, DKFZ-748 has been reported as a nanomolar inhibitor of HDAC10, showing exceptional specificity with selectivity indices (SI) of 636 for HDAC10/6 and 2497 for HDAC10/1. DKFZ-748 was developed by modifying SAHA, a well-known pan-HDAC inhibitor, through the incorporation of a methylated amine structure into the alkene linker and making alterations to the capping group (see Figure 6). The addition of this methylated amine, which is protonatable at physiological pH, has been demonstrated to significantly influence the inhibitor's HDAC10 selectivity [84].
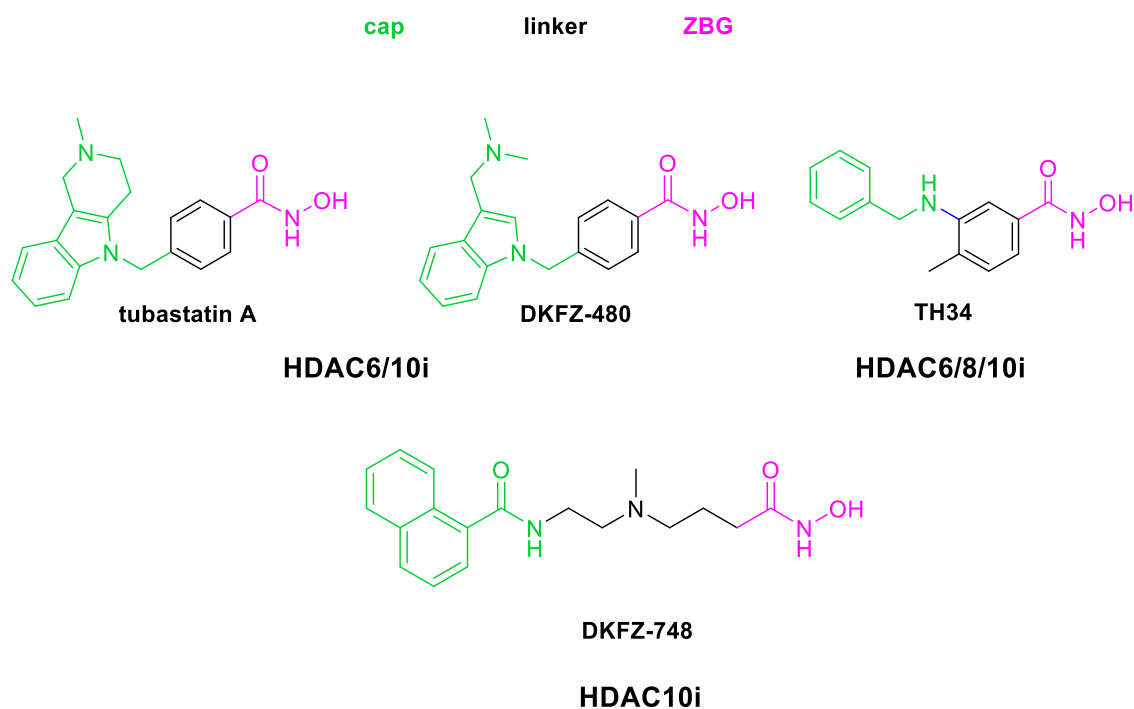
Figure 6: Structures of known HDAC10 inhibitors with highlighted pharmacophore features and key structural elements. Tubastatin A exhibits IC$_{50}$ values of 13 nM for HDAC10 and 100 nM for HDAC6, DKFZ-480 shows IC$_{50}$ values of 4–5 nM for HDAC10 and 158 nM for HDAC6, TH34, an HDAC6/8/10 inhibitor, displays IC$_{50}$ values of 4.6 μM, 1.9 μM, and 7.7 μM respectively, while DKFZ-748 demonstrates IC$_{50}$ values of 5.13 nM for HDAC10 and 3.2 μM for HDAC6 [83, 85].

1.6. PROteolysis TArgeting Chimeras (PROTACs)

In recent years, PROTACs (Proteolysis Targeting Chimeras) have emerged as promising agents for targeting histone deacetylases (HDACs), offering advantages over traditional inhibitors. Bifunctional molecules consist of two functional units, each of which can interact with different target proteins. Some bifunctional molecules act as dual inhibitors, binding separately to two distinct proteins. In contrast, PROTACs are designed to simultaneously bind both a target protein (POI) and an E3 ubiquitin ligase [86, 87].

The mechanism of action of PROTACs involves bringing the POI into close proximity with the E3 ubiquitin ligase, thereby promoting the polyubiquitination of the POI. This results in the protein being recognized and degraded by the proteasome. Unlike traditional HDAC inhibitors, which merely inhibit the enzymatic activity of the target protein, PROTACs degrade the protein, thereby also disrupting protein-protein interactions [88, 89]. Furthermore, due to their catalytic mechanism of action, PROTACs can achieve significant effects at lower concentrations. Their ability to form specific ternary complexes also allows them to exhibit greater cellular selectivity compared to traditional HDAC inhibitors [90-92].

PROTACs mimic the natural protein degradation pathway, the ubiquitin-proteasome system (UPS) [89]. These heterobifunctional molecules have one warhead that binds to the POI, while the other recruits an E3 ubiquitin ligase to form a ternary complex. The E3 ligase facilitates the transfer of ubiquitin to the POI, marking it for degradation. Once polyubiquitination has occurred, the complex dissociates, and the ubiquitinated POI is recognized and degraded by the proteasome. The PROTAC molecule can then bind to another POI and repeat the process, provided the binding to the POI is non-covalent (see Figure 7) [93].
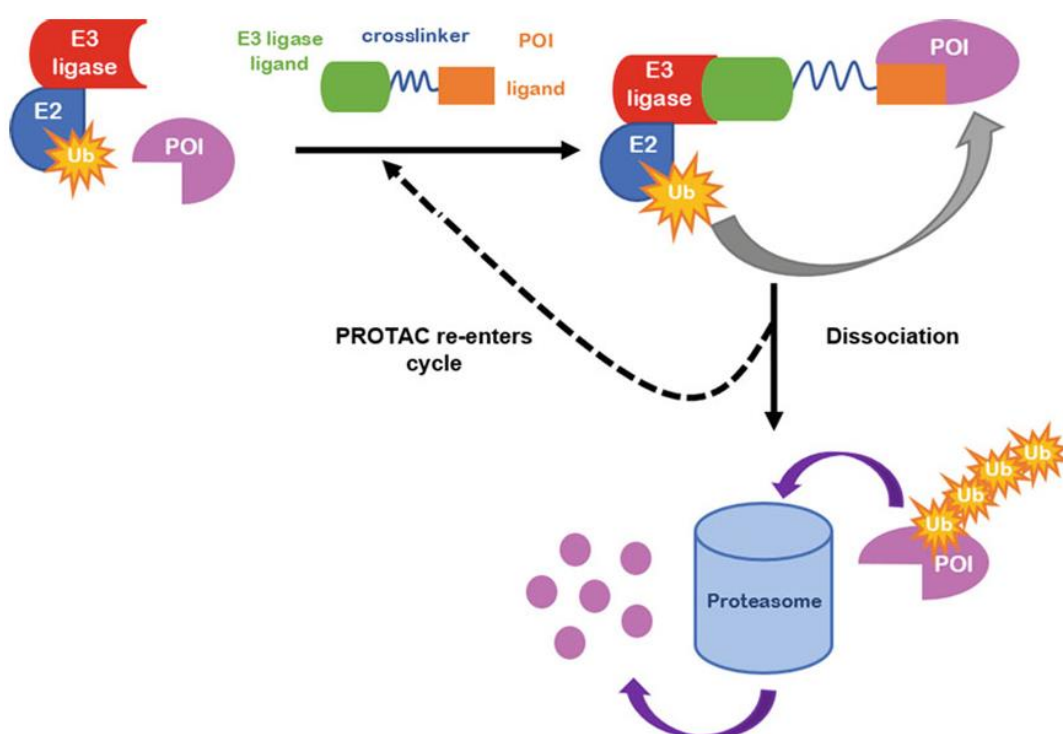
Figure 7: Illustration of PROTAC-induced protein degradation: ternary complex formation, ubiquitination, and proteasomal proteolysis (reproduced from [94]).

In 2018, Yang and colleagues [95] introduced the first HDAC-targeting PROTAC, 9c, which selectively induces the degradation of HDAC6 and utilizes cereblon as the E3 ligase ligand. Subsequently, Smalley and colleagues [96] developed PROTAC 4, which features VHL as the E3 ligase ligand and incorporates a benzamide pharmacophore, selectively targeting HDAC1 and HDAC2 (see Figure 8).
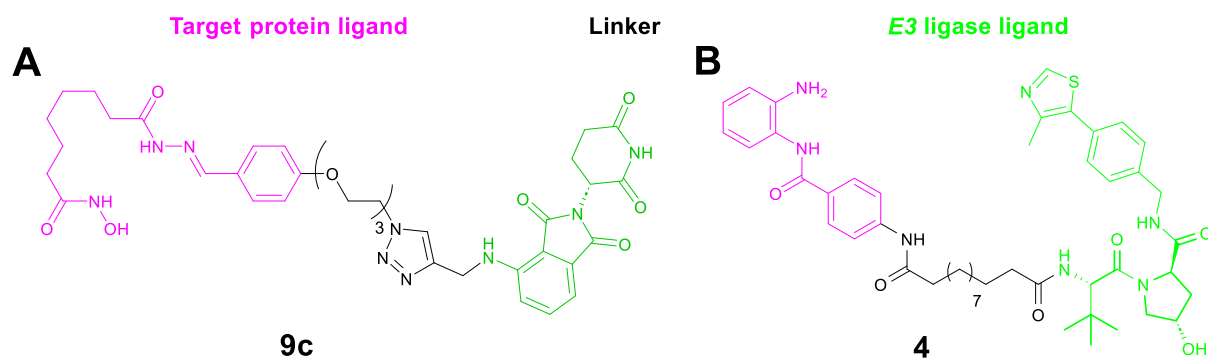
Figure 8: Structures of some representative HDAC-PROTACs with highlighted pharmacophore features and key structural elements.

2.AIM OF THE WORK

This thesis focuses on applying computational techniques, with a particular emphasis on identifying and developing novel inhibitors and degraders for histone deacetylase 10 (HDAC10). The research utilizes a comprehensive computational approach to improve the understanding and optimization of HDAC10 inhibitors.

The study begins with docking simulations to evaluate the interactions of known HDAC10 inhibitors and specially designed focused libraries in HDAC10 crystal structures. This initial analysis assesses how these compounds bind to the enzyme. In this context, the binding poses of N8-acetylspermidine, a well-characterized HDAC10 substrate, and N1-acetylspermidine, which shows small structural and chemical differences compared to N8-acetylspermidine but is not an HDAC10, are also examined through docking simulations

To provide more detailed insights into substrate interactions, molecular dynamics (MD) simulations are employed to analyze the stability of substrates within the zHDAC10 protein over time. Binding free energies for both effective and ineffective substrates are calculated to assess their relative affinities. Decompositional analyses of these binding free energies are applied to identify key factors that influence substrate binding.

In addition to these simulations, newly synthesized compounds are evaluated through zHDAC10 enzymatic assays to determine their binding affinities. Predictions of pIC50 values for planned structural analogues are made to estimate their potency. Selectivity is further examined through docking studies in HDAC1, HDAC6, and HDAC8 isoforms to assess how well the inhibitors differentiate between various HDAC classes.

Finally, protein-protein docking simulations and molecular dynamic studies are conducted to explore interactions between HDAC10, E3 ligases and studied PROTACs, aiming to uncover potential pathways for degradation.

Overall, this thesis integrates CADD methods to advance the discovery and development of specific and effective HDAC10 inhibitors and degraders.

3. METHODS AND MATERIALS

3.1. Computational Methods

Drug discovery is a time and cost-consuming process aims to develop new drug candidates [97]. The process can be relatively facilitated by the use of computational techniques.

The use of computers has already started in the beginning of 80s to investigate drug candidates. From that time on, with the aid of the computers, the drug discovery process has become to be done in a shorter time, less costly and more rationally. Due to these advances, computer-aided drug design (CADD) has attracted the attention of the academic community and the pharmaceutical industry, and today it has become one of the main veins of drug discovery and development studies [98-104]. In fact, the development of some approved and still in use drug substances (such as zanamivir, saquinavir, nefilavir, amprenavir, ritonavir, dorzolamide, tirofiban and captopril) has been carried out with the applications of CADD techniques [100, 105, 106].

Many CADD techniques were applied in that project as well, such as molecular docking, molecular dynamics simulation (MD), co-solvent MD simulation and binding free energy (BFE) calculations. In the sections that follow an overview about these techniques is stated.

3.1.1. Molecular Docking

In the field of molecular modeling, molecular docking is a widely used computational method which was introduced in the early 80s. Molecular docking can be used to model binding modes of a small ligand molecule to protein structure, and the probable interaction among these two at the atomic level. The created model helps us to understand structure-activity relationships. Moreover, the model could be used to predict the strength of the association or binding affinity between small ligand and targeted protein with the scoring functions. But still the scoring functions are challenging and need to be optimized for more reliable results [107]. Protein flexibility is the main problem in mostly used current docking processes. In the mostly used docking processes protein structures as represented as a rigid body or a body with a certain side chain flexibility. In the same processes small ligands are mostly considered as flexible with the aid of advanced algorithms; but, still the protein flexibility problem can be handled by using enhanced techniques such as; induced fit docking (in which protein and ligand treated as flexible), rotamer library (in which side chain rotamer of the protein structures considered)

ensemble docking method (by using multiple protein crystal structures with different conformations when available) and molecular dynamic simulation (in which with the simulation 3-D conformations of the protein could be generated). Yet the techniques are coming with a heavy computational cost [108].

In this work, available crystal structures of the proteins were downloaded from the Protein Databank (PDB;www.rscb.org) [109]. For preparation of the proteins, the protein preparation wizard implementation of the Schrödinger versions 2017.1-2019.1 was used with the following steps: assigning bond orders, adding hydrogen atoms, optimizing the hydrogen bond network, determining the protonation states at pH 7.0 using the Epik tool, and finally performing energy minimization in a restrained manner with an RMSD threshold of 0.3 Å, using the OPLS 2005 or 3e force fields.

After protein preparation, generation of the ligand structures was done using the 2D Sketcher of Schrödinger (versions 2107-2019.1). Subsequently, the LigPrep tool (Schrödinger versions 2017.1-2019.1) was used for the preparation of the ligands. This process involved several steps, including the generation of different protonation states and tautomeric forms at pH 7.0 using the Epik tool. Additionally, stereoisomerism was considered to account for the different possible configurations of chiral centers in the ligands. Afterwards energy minimization was performed using the OPLS force fields 2005 and 3e, ensuring the ligands were in their most stable conformations. To further account for molecular flexibility, 64 conformers for each ligand were generated using the ConfGen tool (Schrödinger versions 2017.1-2019.1).

Preparation of the receptor grid for docking procedure was performed by assigning the co-crystallized ligands as the centroid of the grid box in each PDB crystal structure using the receptor grid preparation module in Schrödinger (version 2019.1).

Lastly, docking of the all generated conformers was done in the Standard Precision mode using Glide (Schrödinger-release 2019.1). A total of 20 poses per ligand conformer were included in the post-docking minimization step, and a maximum of 2 docking poses were generated for each conformer of ligand. Any other settings that are not mentioned was kept as default. The obtained docking poses were visually inspected with the Schrödinger (version 2019.1) and MOE (version 2019.1, Chemical Computing Group, Montreal, Canada) graphical interfaces.

3.1.2. Molecular Dynamic Simulation

Molecular dynamics (MD) is an approach to simulate the dynamic behavior of proteins, ligands, ions, and water molecules with the aid of computers as a function of time. During molecular dynamics simulations, molecular systems are considered as flexible by using Newton's equation of motion.

MD simulations could be used for diverse purposes:

- To study protein flexibility and stability, if protein has different conformations it might be used to determine different protein conformations.
- To identify cryptic or transient pockets in protein structures.
- To map or identify possible binding hot spots on the protein.
- To asses and confirm stability of protein-ligand, protein-protein complexes predicted by docking studies.
- To evaluate the stability of the interactions between protein-ligand structures or protein-protein structures in the docking solutions.
- MD simulations could be used for binding free energy estimation of bound and unbound protein-protein or protein-ligand complexes.

In this work, GPU-based MD simulations were performed by the usage of AMBER18 or AMBER22 program. The *pdb4amber* command was used to analyze and clean PDB files of the protein-ligand complexes to further usage within the tLEaP program. The topology and force field parameters of the ligands were generated with the Antechamber [110] tool of AMBER packages. In the generations of the ligands semi empirical AM1-BCC (Austin Model1 with bond charge correction) atomic charge model were used [111, 112]. Afterwards with the tLEaP module the protein-ligand complexes were structured. In the tLEaP module, the second-generation general AMBER force field (GAFF2) and force field 14 Stony Brook(ff14SB) field were used as ligand and protein force fields respectively [113, 114]. For the catalytic Zn^{2+} the 12-6-4 LJ-type or the 12-6 LJ-type nonbonded ion models were applied [115]. After combining the complexes, they were solvated by TIP3P water model as octahedral box around the protein with 10 Å margin. Then neutralization of the whole systems with Na^+ or Cl^- ions was done. Parameter/topology and coordinate files of the complex systems were saved to use as starting points of the MD simulations.

The solvated and neutralized systems were subjected to two energy minimization steps involving 1000 cycles of steepest descent followed by 2000 cycles of conjugate gradient totaling 3000 cycles of minimization. The first step was for minimization of the solvent

molecules and counter-ions (Na$^+$ and Cl$^-$) in the systems which were done by the constraints application with a force constant of 10 kcal*mol^{-1}*Å^{-2} on to the proteins, ligands and zinc ion and not on solvent and counter-ions. The second minimization step, which is a replica of the first minimization step except without constraints on the proteins, ligands and zinc atoms, were done to minimize the whole system. Later on, the entire system was heated over 100 ps from 0 to 300 K. During the heating step constraints on the solute were used like in the first minimization step. Constant volume periodic boundary was set to equilibrate the temperature of the system by Langevin thermostat using a collision frequency of 2 ps^{-1}. Subsequently, a pressure equilibration routine at 300 K was performed for 200 ps with a constant pressure of 1 bar using constraints as previously described. Ultimately, free molecular dynamic simulations utilizing the Particle Mesh Ewald method with the time step of 2 fs were applied for long 100-500 ns [116]. During these long MDs the system temperature and system pressures were kept at 300 K and at 1 bar, respectively. Implementation of the SHAKE algorithm was done to constrain all bond containing hydrogens. As a results 1000-10000 frames were written for each 100-500 ns long MDs.

The analysis of the created MD trajectories was performed using the cpptraj module in AMBER program. To evaluate to stabilities of the complexes RMSD values of the proteins, ligands and zinc atoms were calculated using cpptraj. Distance calculations were done to check stability of the important interactions between protein-ligand structures. RMSF of the ligand atoms and protein residues were calculated to further examine the stability of the protein-ligand complexes. Also for visual inspection selected representative trajectories were visualized with PyMOL by Schrodinger [117].

3.1.3. Cosolvent Molecular Dynamics (MD)

Cosolvent molecular dynamics (MD) simulations have gained recognition in the scientific literature as valuable computational tools for studying protein surfaces, especially in the context of identifying binding sites and hotspots [118]. In contrast to classical MD simulations, which predominantly use water as the only solvent medium, cosolvent MD offers a different approach, marked by the integration of organic molecules into the aqueous phase. The choice of cosolvents is governed by their different natures and properties, resulting in discernible interactions with the protein surface within the resulting MD trajectories. It is worth noting that numerous methodologies have been developed, each distinguished by differences in simulation times, choice of probe molecules, co-solvent concentrations, and modes of result analysis, specific proteins studied and many other relevant parameters [118-121]. Furthermore, an

important group of studies has been devoted to the investigation of various binding sites. This includes the successful mapping of allosteric and cryptic pockets as well as hotspots related to protein-protein interactions [122-125]. These investigations have not only enabled us to understand the intricacies of protein-ligand interactions, but have also provided insights into the molecular basis of complex biological processes. Such efforts have important implications for drug discovery and modulation of protein functionality, thus underlining the crucial role of co-solvent MD simulations in structural biology and molecular pharmacology.

In this work, GPU-based Cosolvent MD simulations were performed by the usage of AMBER22 program. Using tLEaP, a molecular modeling tool, a thin shell of probe molecules was applied around the protein-ligand complex to explore its surroundings. In our study, five different water mixable probe molecules were used as cosolvent, namely methanol, ethanol, acetamide, trimethylamine and pyridine. Subsequently, a requisite quantity of TIP3P [126] water molecules was appended to the system, ensuring that a ~5% volume-to-volume (v/v) ratio of probe molecules to water was maintained. For each complex and probe molecule, ~5% volume-to-volume (v/v) ratios were prepared as follows:

Methanol-Water Combinations (~5% v/v)

- **HsHDAC8 (PDB ID: 2V5X):** 333 methanol and 14,153 water molecules

- **HsHDAC6 (PDB ID: 5EDU):** 367 methanol and 14,923 water molecules

- **DrHDAC10 (PDB ID: 6WDW):** 389 methanol and 14,104 water molecules

- **DrHDAC10 (PDB ID: 7U69):** 458 methanol and 19,346 water molecules

Ethanol-Water Combinations (~5% v/v)

- **HsHDAC8 (PDB ID: 2V5X):** 205 ethanol and 12,558 water molecules

- **HsHDAC6 (PDB ID: 5EDU):** 248 ethanol and 14,724 water molecules

- **DrHDAC10 (PDB ID: 6WDW):** 241 ethanol and 12,423 water molecules

- **DrHDAC10 (PDB ID: 7U69):** 291 ethanol and 17,841 water molecules

Acetamide-Water Combinations (~5% v/v)

- **HsHDAC8 (PDB ID: 2V5X):** 195 acetamide and 10,411 water molecules

- **HsHDAC6 (PDB ID: 5EDU):** 244 acetamide and 13,035 water molecules

- **DrHDAC10 (PDB ID: 6WDW):** 233 acetamide and 12,048 water molecules

- **DrHDAC10 (PDB ID: 7U69):** 307 acetamide and 16,423 water molecules

Trimethylamine-Water Combinations (~5% v/v)

- **HsHDAC8 (PDB ID: 2V5X):** 76 trimethylamine and 11,012 water molecules

- **HsHDAC6 (PDB ID: 5EDU):** 92 trimethylamine and 13,068 water molecules

- **DrHDAC10 (PDB ID: 6WDW):** 74 trimethylamine and 10,693 water molecules

- **DrHDAC10 (PDB ID: 7U69):** 99 trimethylamine and 14,313 water molecules

Pyridine-Water Combinations (~5% v/v)

- **HsHDAC8 (PDB ID: 2V5X):** 158 pyridine and 13,162 water molecules

- **HsHDAC6 (PDB ID: 5EDU):** 165 pyridine and 13,821 water molecules

- **DrHDAC10 (PDB ID: 6WDW):** 146 pyridine and 11,820 water molecules

- **DrHDAC10 (PDB ID: 7U69):** 215 pyridine and 17,977 water molecules

The topology and force field parameters of the probe molecules were generated with the Antechamber [110] tool of AMBER packages. In the generations of the probe molecules semi empirical AM1-BCC (Austin Model1 with bond charge correction) atomic charge model [111, 112] were used. Additional settings or steps was exactly same as in the previously discussed Molecular Dynamic Simulation please check the Section 3.1.2. In addition to that for each complexes benzhydroxamate or 4-methylpiperidinacyrlhydroxamate moieties of the docked or crystallized ligand were kept in the studied complexes during the cosolvent MD simulations. For each protein and probe pair, three independent 30 ns simulations with different random seeds were carried out resulting in 90 ns of cumulative production simulation time.

For each studied complex, the first three nanoseconds of the three independent simulation runs were considered as the equilibration or adaptation phase for the probe molecules, which were added in the form of a thin shell, and were disregarded. The analysis was then conducted on the spatial distribution of all probe atoms during the remaining 27 nanoseconds. This analysis was carried out by specifying the center of the grid using the center of the protein mass.   Further,

binning the probe atom positions onto a grid with a spacing of 0.5 angstroms (Å) was performed. To achieve this, the cpptraj module from AmberTools 22 was used. The pseudo-PDB of grid points that have density greater than 0.1 fraction of the maximum grid value was used for analysis. MixMD Probeview plugin implemented on the open-source version of the molecular visualization program PyMOL [117, 119] was used for the hotspot mapping, visualization and picturing.

3.1.4. Binding Free Energy Calculations

In general, molecular docking tools are sufficient to predict the binding poses of docked compounds, but accurate ranking and/or scoring of these docking poses requires more sophisticated methods. Compared to molecular docking, binding free energy calculation methods involving molecular dynamics simulations consider solvation effects and conformational flexibility of both protein and ligand [127].

The binding free energy can be calculated by two main approaches: pathway methods and endpoint methods. Pathway methods include free energy perturbations (FEP) [128, 129] and thermodynamic integration (TI) [130, 131]. FEP and TI methods determine the absolute binding free energy through molecular dynamics (MD) simulations, considering factors such as enthalpy changes, entropy changes, conformational flexibility and desolvation effects [132, 133]. Endpoint methods include Molecular Mechanics-Generalized Born/Poisson-Boltzmann Surface Area continuous solvation (MM-GB/PBSA) [134, 135] and Linear Interaction Energy (LIE) [136, 137]. Endpoint methods approximate the binding free energy by evaluating the initial and final states of the system [132]. Several studies have shown that MM-GBSA and MM-PBSA methods are effective in predicting the binding affinity of protein-ligand complexes and obtain satisfactory correlations with experimental data for the congeneric series [138-142].

In the context of binding free energy (BFE) calculations, in this study the AMBER18 program was employed in conjunction with the MMPBSA.py script. Various implicit solvation models were explored, including GB^{HCT} (igb = 1, pbradii mbondi), GB^{OBC} (igb = 2, pbradii mbondi2), GB^{OBC2} (igb = 5, pbradii mbondi2), GBn (igb = 8, pbradii mbondi3), as well as PB_bondi (pbradii bondi) and PB_parse (pbradii parse) [143-147]. These calculations utilized MMGB(PB)SA methods that combine molecular mechanics with solvent models. The binding free energy results were analyzed in four different scenarios:

- A single frame following the first minimization step (Emin1).

- A single frame following the second minimization step (Emin2).

- Frames 1-100 during molecular dynamics (MD) simulations with a 2-frame interval (MD).

- A single frame following the third minimization step after MD (Emin3).

The binding free energies (ΔG_{bind}) for protein-ligand complexes were calculated by means of the difference between the energy of the complex ($G_{complex}$) and the cumulative energies of the protein ($G_{protein}$) and ligand (G_{ligand}) components using Equation (1) [139, 148, 149]:

$$\Delta G_{bind} = G_{complex} - (G_{protein} + G_{ligand}) \ (1)$$

These binding free energies (ΔG_{bind}) can be further elucidated in terms of the gas-phase energy (E_{MM}), free solvation energies (ΔG_{sol}), and entropy ($-T\Delta S$) as defined in Equation (2) [135, 139, 149]:

$$G_{molecule} = E_{MM} + \Delta G_{sol} - T\Delta S \ (2)$$

Internal energy (E_{int}) covers bond, angle and dihedral energies, while electrostatic energy (E_{ele}) describes the interactions between atoms based on their positive and negative charges. Van der Waals (E_{vdw}) interactions cover both short-range and long-range interactions between atoms. Solvation energies are composed of polar solvent contributions ($\Delta G_{PB/GB}$) and non-polar solvent contributions (ΔG_{SA}) as indicated in Equation (3) [135, 139, 148, 149] :

$$\Delta G_{bind} = (E_{int} + E_{ele} + E_{vdw}) + (\Delta G_{PB/GB} + \Delta G_{SA}) - T\Delta S \ (3)$$

Consideration of conformational entropy changes ($-T\Delta S$) is often critical for comprehensive binding free energy determination. However, the inclusion of entropy changes in BFE calculations can significantly increase computational demands without improving accuracy [139, 148-150]. In this study, to relate enthalpies of binding to biological data, the analysis focused only on enthalpy values (ΔH) or both of its components the gas-phase energy (E_{MM}) and free solvation energies (ΔG_{sol}), which are expressed in Equation (4):

$$\Delta H = (E_{MM}) + (\Delta G_{sol}) \ (4)$$

3.1.5. Decompositional Analysis of BFE

Decompositional analysis of BFE is a critical methodology in computational pharmacological research, focusing on the individual contributions of amino acid residues to the overall binding

energy in ligand-protein complexes. This technique is essential for a deeper understanding of the molecular underpinnings of ligand binding and for pinpointing key residues that significantly influence binding affinity. At the heart of this method is the dissection of the total BFE into the specific energy contributions of each protein residue. This calculation encompasses various interaction types, including electrostatic forces and van der Waals interactions. The methodology involves quantitatively determining the influence of each residue on the ligand's binding affinity. Identifying 'hot spots' - residues that play a major role in binding - is particularly valuable for drug development, as these are often the target areas for enhancing ligand interaction [151].

In the field of drug discovery, decompositional analysis can be employed to optimize lead compounds. This approach guides researchers in designing ligands that target critical residues, thereby enhancing the efficacy and specificity of therapeutic agents. In essence, decompositional analysis for BFE offers a detailed view into how individual amino acid residues contribute to ligand-protein binding affinity, playing a key role in elucidating binding mechanisms and aiding in the design of more effective drugs.

The decompositional analyses of binding free energy (BFE) were conducted using the same scenarios, steps, and equations employed in the BFE calculations, with the addition of the command `idecomp=1` in the input files of the MMPBSA.py script. This enabled the calculation of the individual contributions of each residue to the total binding free energy. The analyses were performed using the AMBER18 program and the MMPBSA.py script, consistent with the procedures outlined for the BFE calculations.

3.1.6. Protein-Protein Docking in MOE

This part of the study is mainly devoted to the modeling of ternary complexes based on PROTACs. In this research, the PROTAC Modeling Tools in MOE (Version 2019 and 2020) were used, with particular emphasis on Methods 4b and 5 [152]. Both methods are based on protein-protein docking as the basic modeling approach. The differences between these two methods will be explained in more detail in the following sections.

3.1.7 Method 4b in MOE

For method 4b, two ligand-receptor complexes are required as input structures: E3 ligase (VHL in our studies) with the corresponding warhead and the target protein (HDAC10 in our studies)

with the respective warhead. PROTAC structure is imported in sdf format. All other parameters were adapted from the default settings.

In the first step, as already mentioned, a protein-protein docking is performed between both input ligand-receptor complexes in the absence of the linker moiety of PROTAC. MOE's proprietary protein-protein docking algorithm is used, and a large number of docking poses are generated. In the second step, conformations are generated for the PROTAC structure with LowModeMD, while keeping the two warheads rigid. In the third step, filters, namely Max P-P contact area (default lower than 670 Å2) and Ligand Core RMSD (the default RMSD is 3.5 Å), are applied, and ternary complexes are generated by merging the filtered conformers with the ensemble of protein-protein docking results.

The resulting ternary complexes are then clustered using the hclust_tree function. Two separate clusters are created for proteins and PROTAC based on RMSD calculations. For proteins, RMSD calculations are based on C-alpha atoms with the threshold of 10 Å, while for PROTAC RMSD threshold is 3 Å which is based on heavy atoms after structure superposition.

In selecting the most promising ternary complexes, it is recommended to focus on the cluster containing the largest number of complexes.

3.1.8 Method 5 in MOE

As in Method 4b, the first step in this approach also involves protein-protein docking and the input structures from Method 4b can be used. Once various docking poses are generated, in contrast to Method 4b, there is no explicit search for a suitable PROTAC conformation. Instead, the PROTAC linker is docked directly between the binding pockets of the proteins. To achieve this, the protein complexes are dissolved and the shortest path to bind both proteins is determined by shuffling from oxygen atom to oxygen atom. Finally, the resulting ternary complexes are minimized.

Since the results in Method 5 are not clustered, special attention was paid to two MOE-specific filters: RMSD_RF and ligand_E. These filters help to select the best ternary complexes. The RMSD_RF filter calculates the RMSD of heavy atoms between PROTAC in the final ternary complex and the nearest local energy minimum of PROTAC in the absence of both proteins. The threshold set for this filter is < 2.5 Å. The Ligand_E filter identifies the total force field energy of PROTAC in the ternary complex using the MOE AMBER10: EHT force field. In this case, the threshold is set to < 3600 kcal/mol.

3.1.9 Calculation of Performance Metrics for Classification Models

The efficacy of the classification models was evaluated using several key performance metrics derived from the confusion matrix, including accuracy, precision, sensitivity, specificity, and F1 score. These metrics were calculated as follows:

where TP = true positives, TN = true negatives, FP = false positives, and FN = false negatives.

- **Accuracy**: The proportion of total correct predictions (both true positives and true negatives) out of all predictions made. It was calculated using the formula:

$$\text{Accuracy} = \frac{TP + TN}{TP + FP + TN + FN}$$

- **Precision**: Precision measures the ratio of correctly predicted positive observations (true positives) to all predicted positive observations. It was calculated using the formula:

$$\text{Precision} = \frac{TP}{TP + FP}$$

- **Sensitivity (Recall)**: Sensitivity indicates the model's ability to correctly identify relevant instances of a specific class. It was calculated as:

$$\text{Sensitivity (Recall)} = \frac{TP}{TP + FN}$$

- **Specificity**: Specificity measures the proportion of actual negatives that are correctly identified. It was calculated using the formula:

$$\text{Specificity} = \frac{TN}{FP + TN}$$

- **F1 Score**: The F1 score is the harmonic mean of precision and sensitivity, providing a balance between the two. It is particularly useful in cases of uneven class distribution. It was calculated as:

$$\text{F1 Score} = 2\, x\, \frac{\text{Precision } x \text{ Sensitivity}}{\text{Precision } + \text{ Sensitivity}}$$

These metrics provide a comprehensive assessment of the model's performance in terms of both its ability to detect active compounds (precision, sensitivity) and its overall reliability (accuracy, specificity).

4. RESULTS AND DISCUSSION

4.1. Comparative Analysis of Structural Similarities and Variations Among HDAC Isoforms: HDAC1, HDAC6, HDAC8, and HDAC10

As stated previously, the main aim of this study is to find novel selective HDAC10 inhibitors. Therefore, at the beginning of the project, the similarities and differences between HDAC isoforms; hsHDAC6, hsHDAC8 and hsHDAC1 to drHDAC10 were analyzed. As previously mentioned, among HDACs, HDAC6 differs from the others in that it contains two catalytic domains and HDAC10 has a leucine-rich pseudo-domain in addition to its catalytic domain. However, although HDACs differ, structurally their catalytic domains are conserved, which can be seen in nearly two hundred resolved crystal structures (Protein Data Bank-PDB, rcsb.org) from various organisms [22, 52, 53]. Both the catalytic domain and the pseudo-domain of HDAC10 are surrounded by α-helices while the center consists of eight parallel β-sheets, as in the catalytic domains of other HDAC isoforms and as seen in Figure 9 with the two HDAC10 domains in butterfly wing-like appearance.
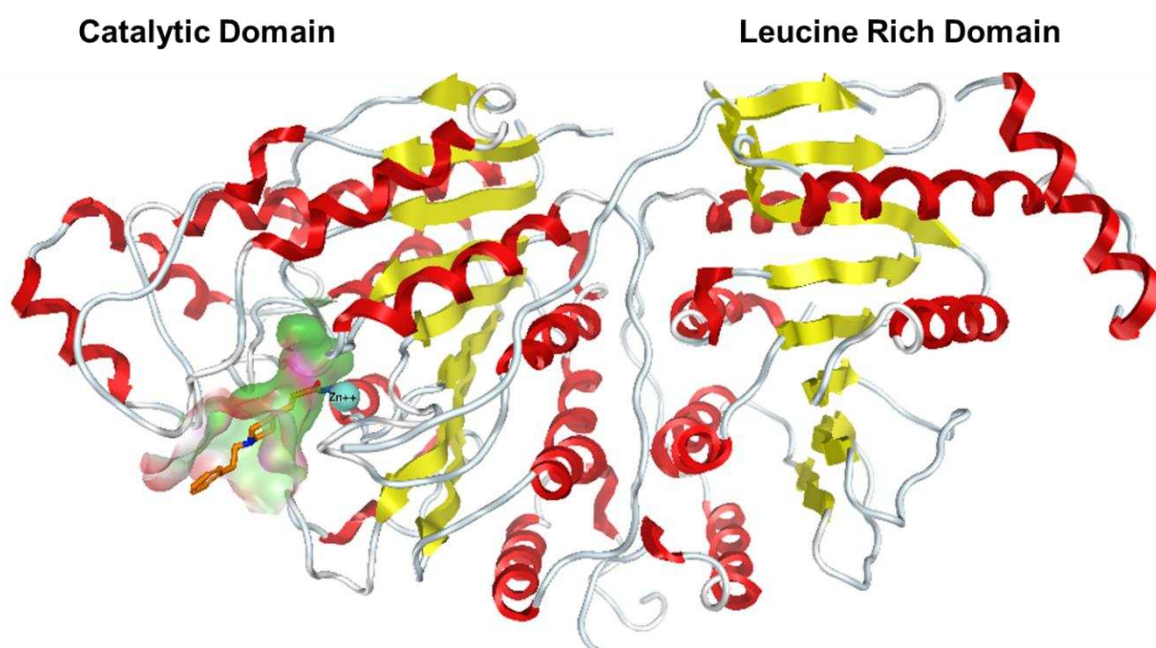
Figure 9: Crystal structure of humanized DrHDAC10 complexed with PZ46 (PDB ID: 7U69) [153]. B-sheets are shown in yellow, α-helices in red, and loops in white. The zinc ion is colored teal, and the ligand is depicted as orange carbon sticks. The active pocket surface is highlighted in green.

In both domains, the β-sheets and α-helices are connected by loops. These loops in the catalytic domain differ in length and structure between different HDAC isoforms [22]. The catalytic zinc ion lies at the base of the catalytic pocket. The pocket is composed of three essential elements; an acetate-binding cavity, a substrate-binding tunnel of approximately 10 Å length and lastly the rim of the catalytic pocket. Also, some HDAC isoforms extend their catalytic domains with

subpockets, such as the foot pocket which is the inner cavity in class I HDACs and the unique side pocket in class I HDAC8 [55].

To conduct the computational studies, the relevant crystallized protein structures were downloaded from the Protein Data Bank; namely DrHDAC10 (PDB ID: 6UHU), HsHDAC6 (PDB ID: 5EDU), HsHDAC8 (PDB ID: 2V5X) and HsHDAC1 (PDB ID: 5ICN). These 3D structures were aligned according to their active binding pockets in the MOE program. The sequence identity and similarity of the catalytic domains and active binding pockets were calculated. Here, in accordance with the phylogenetic classification, the highest sequence identity and similarity values to HDAC10 were assigned to catalytic domain 2 of HsHDAC6 isoform which is 46.6% and 63.0%, respectively. For HsHDAC8, the percent identity and similarity values were calculated as 21.1% and 39.5% for the catalytic domains respectively, while for HsHDAC1 the values were noted as 20.5% and 39.7%, respectively (see Figure 10).
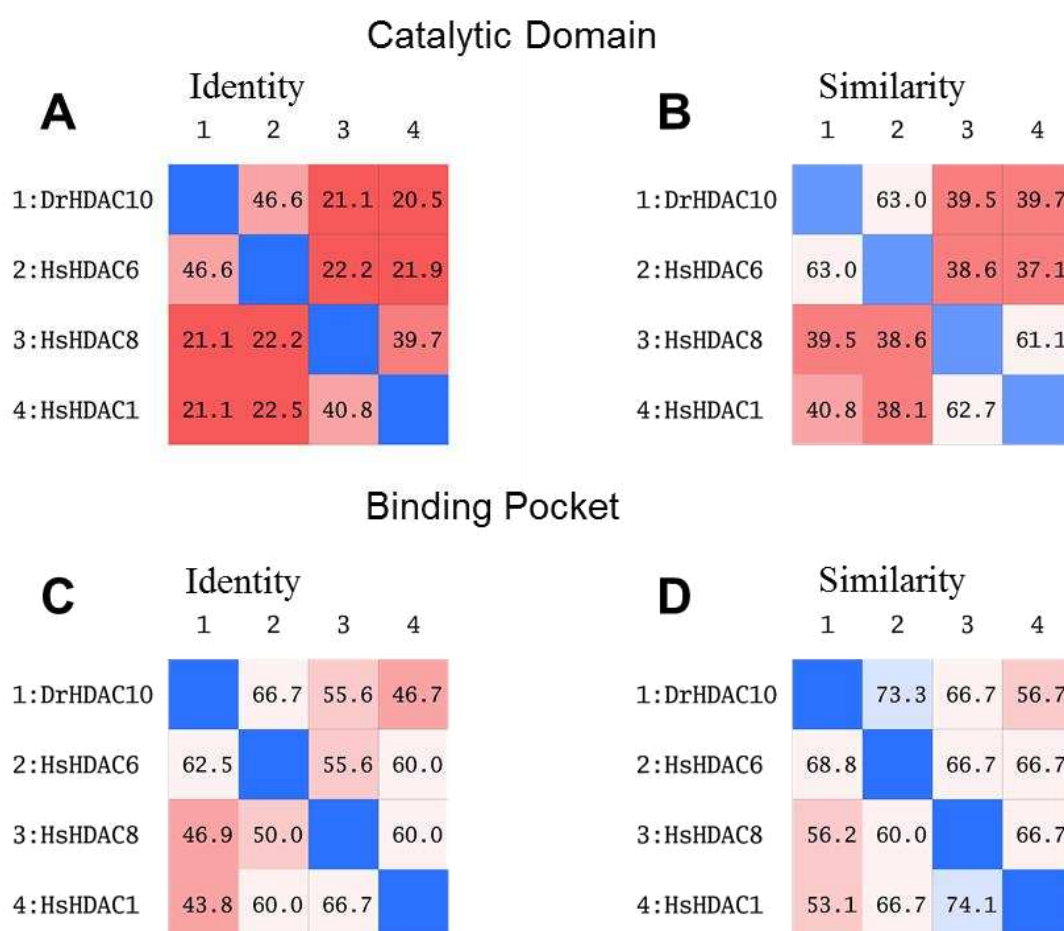
Figure 10: Comparative analysis of sequence identity and similarity between the catalytic domains **(A, B)** and binding pockets **(C, D)** of zebrafish HDAC10 (DrHDAC10) and human HDACs (HsHDAC6, HsHDAC8, HsHDAC1).

Meanwhile, the sequence identity values of the binding pockets calculated with HDAC10 as the reference isoform are 66.7%, 55.6%, and 46.7% for HDAC6, HDAC8, and HDAC1, respectively. The corresponding similarity values are observed to be 73.3%, 66.7%, and 56.7%. Notably, HDAC6, as another member of class IIa HDACs, exhibits an almost 75% similarity, while the other two isoforms, namely HDAC8 and HDAC1, display similarity values above 50%.

Assessments made thus far clearly revealed a challenging task ahead, urging us to conduct a rigorous investigation of the aforementioned binding pockets to attain a clearer characterization and recognition. The binding pockets of HDACs show highly conserved residues; H136, H137, Y307, H176, D174, D267 (residue annotation is given for DrHDAC10 and refers to H610/H142/H140, H611/H143/H141, Y782/Y306/Y264, H651/H180/H178, D649/D178/D176, D742/D267/D264 for HsHDAC6, HsHDAC8 and HsHDAC1 isoforms respectively). Additionally, the C147/C621/C153/C151 and F146/F620/F152/F150 residues in the binding tunnel are conserved among the mentioned HDAC isoforms (see Figure 11A). The seven loops which are part of the active binding show alterations in lengths and positions among the isoforms. Among these mentioned loops (L), L4 and L7 exhibit the least variability between the studied isoforms, while the position and length variation of L1, 2, 3, 5 and 6 is clearly evident in Figure 11B. Furthermore, a one-turn 3_{10}-helix ηA2 (P^{23}ACE), known as the P(E)ACE motif, which is unique to only HDAC10 (Figure 11B). This motif narrows down the binding pocket, aiding HDAC10 in recognizing its natural substrate, N^8-acetylspermidine, unlike other isoforms [64].
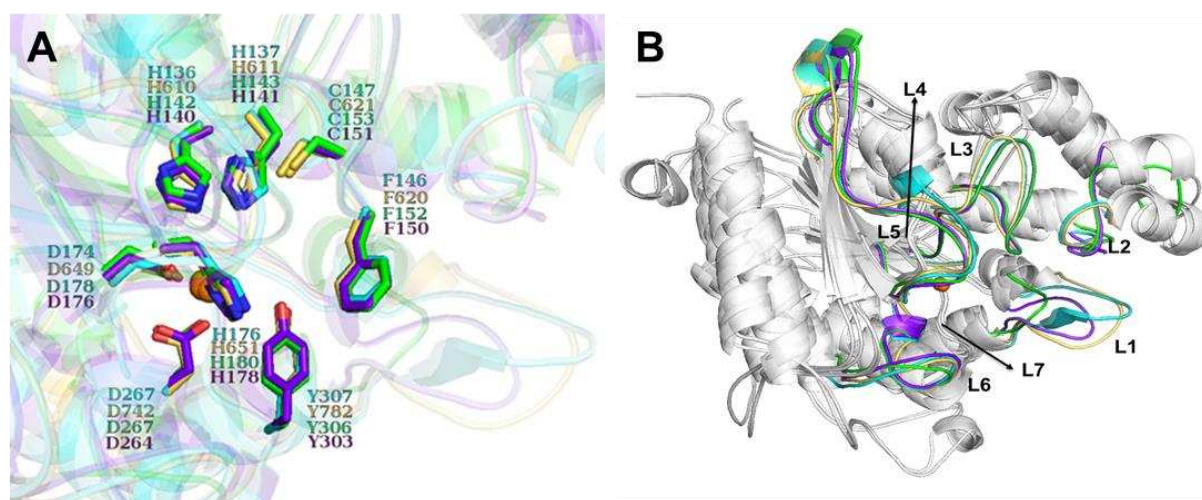
Figure 11: Structural comparison of conserved catalytic residues and binding loops among HDAC isoforms. **A)** Alignment of key catalytic residues (His, Asp, Tyr, Cys, Phe) in the active sites of DrHDAC10, HsHDAC6, HsHDAC8, and HsHDAC1. The conserved positions are highlighted, showing minimal variation among the isoforms. **B)** Overlay of the seven loops (L1–L7) that form the binding pocket across the HDAC isoforms. Loops

L4 and L7 exhibit the least variation, while L1, L2, L3, L5, and L6 show length and positional differences. The unique P(E)ACE motif in HDAC10 (turquoise) is located in the L1 loop, contributing to substrate specificity.

In addition to aforementioned conserved residues in the binding pockets of all studied four isoforms, there are also other amino acids that are non-conserved Figure 12.

The binding pockets of DrHDAC10 and HsHDAC6 share conserved residues like E28/E502, F204/F679, P134/P606, E304/E779, and P273/P746. Meanwhile, the foot pocket [154], common in class I HDACs, is blocked in both by P134/P606 and E304/E779. Mutations like W205/F680, D94/S568, and E274/L749 influence the substrate specificity of these isoforms [64]. Non-conserved residues in the L1 loop (C25/H499, E26/H500, I27/P501) and additional residues in DrHDAC10 (P23, A24) make HDAC10 a polyamine deacetylase (PDAC), not an HDAC, especially with the E274/L749 change in the L6 loop [64]. The E276/G751 mutation in HDAC10 gives it an acidic character, differentiating it from HDAC6. In HDAC6, the Leu749 mutation in L6 and conserved Phe620 in L3, along with His500 and Pro501 in L1, form a hydrophobic patch that stabilizes T-shaped inhibitors specific to HDAC6 [155, 156] (see Figure 12A).

In comparing DrHDAC10 and HsHDAC8, the F204/F207, P273/P273, and D94/D101 pairs are conserved across both isoforms. However, differences in the L1 and L6 loops stand out due to their varying lengths. In HDAC8, these loops are shorter, and mutations like E274/M274, E276/S276, and E28/K33 form a hydrophobic side pocket specific to HDAC8 [157]. For example, the HsHDAC8 L1 loop lacks the P23, A24, C25, E26, and I27 residues found in DrHDAC10. This hydrophobic pocket allows the binding of L-shaped PC34051 and other HDAC8-specific inhibitors. Other notable mutations, like E303/G303 and P134/W141, help form the entrance to the foot pocket in HDAC8 [154] (see Figure 12B).

In the comparison of DrHDAC10 and HsHDAC1, the L2 loop differs in length but conserves D94/D99. The L1 loop of DrHDAC10 includes P23, A24, C25, E26, I27, and E28, while HsHDAC1's L1 loop has G27, H28, P29, and M30, making it shorter, similar to HsHDAC8. Notable mutations include W205/F205, common in HsHDAC isoforms, and the unique F204/Y204 mutation in HsHDAC1. In the L6 loop, mutations such as P273/R270, C273/E276, and E274/L271 are significant. Parallel to HsHDAC8, E304/G300 and P134/L139 mutations are present, but P134/L139 widens the foot pocket entrance in HsHDAC1 [154]. Unlike HsHDAC8, HsHDAC1's L1 loop is longer, and mutations like L271, R270, H28, and P29

prevent the formation of HsHDAC8's side pocket. Additionally, L271 and P29 reduce the distance between L1 and L6, narrowing HsHDAC1's binding tunnel (see Figure 12C).
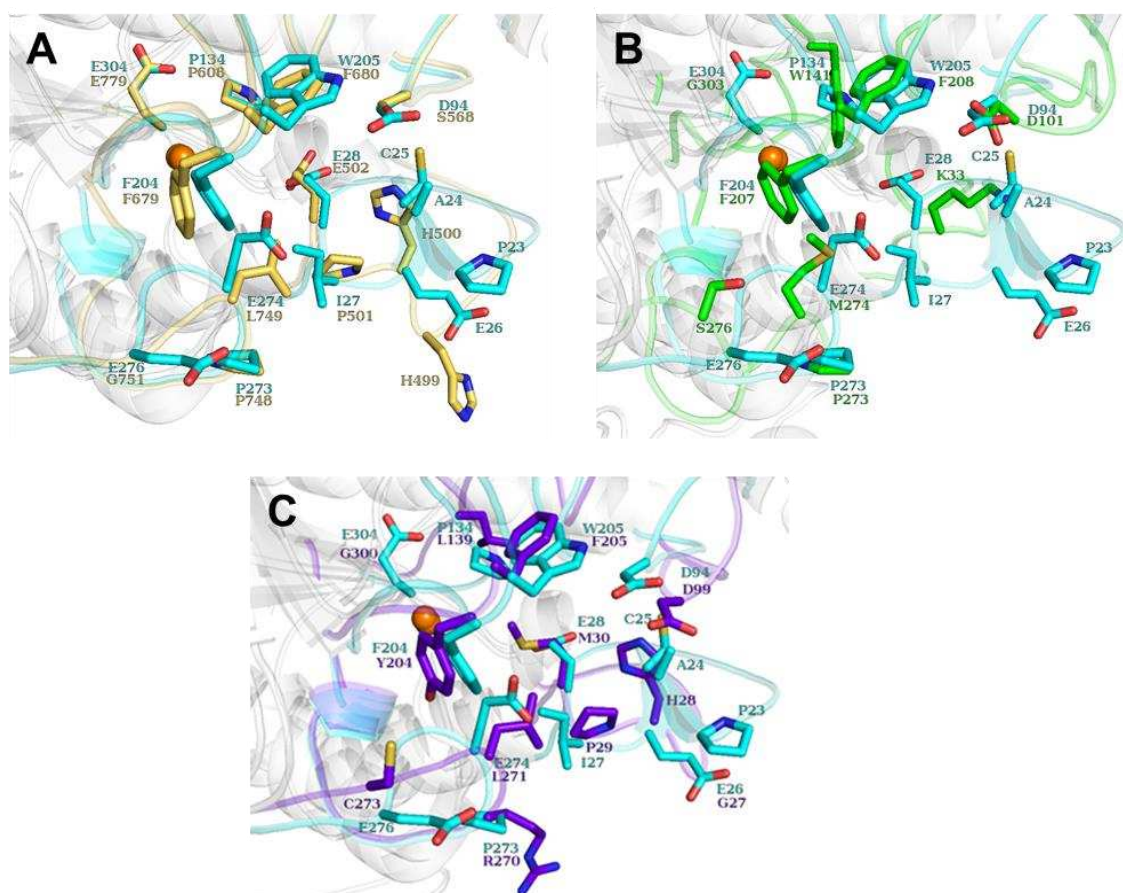
Figure 12: Comparison of binding pocket residues between DrHDAC10 and human HDAC isoforms. **A)** DrHDAC10 vs. HsHDAC6: Conserved residues like F204/F679, P134/P606, and E28/E502 are shown, with significant mutations such as W205/F680 and E274/L749 that influence substrate specificity. **B)** DrHDAC10 vs. HsHDAC8: Conserved residues F204/F207, D94/D101, and P273/P273 are highlighted, with L1 and L6 loop mutations (E274/M274 and E276/S276) forming a hydrophobic side pocket unique to HsHDAC8. **C)** DrHDAC10 vs. HsHDAC1: Variations in loop lengths and mutations such as F204/Y204, W205/F205, and E274/L271, as well as the shorter L1 loop in HsHDAC1, which narrows the binding tunnel compared to DrHDAC10.

Briefly, specific changes have been observed in the DrHDAC10 isoform, including the E274 mutation in Loop 6, the W205 mutation in Loop 3, and the unique P(E)ACE motif in Loop 1. Furthermore, mutations of acidic amino acids like Aspartate and Glutamate have been documented in the distal region of the binding pocket, which are more prevalent in comparison to HsHDAC6, HsHDAC8 and HsHDAC1 isoforms.

4.1.1. Comparative Analysis of Structural Similarities and Variations Among Humanized DrHDAC10 Versus Native DrHDAC10

Till now there is no crystal structure available for human HDAC10 protein, whereas scientists were able to crystallize zebrafish HDAC10 and build humanized zebrafish HDAC10 to mimic human HDAC10 enzymes. The catalytic domains of human and zebrafish HDAC10 possess

63% sequence identity and 79% sequence similarity, respectively [72]. Two mutations in the binding pocket of zebrafish HDAC10, namely A24E and D94A, result in a binding pocket similar to that of human HDAC10 (Figure 13). Mutated DrHDAC10 carrying both mutations is called "humanized" zebrafish HDAC10.
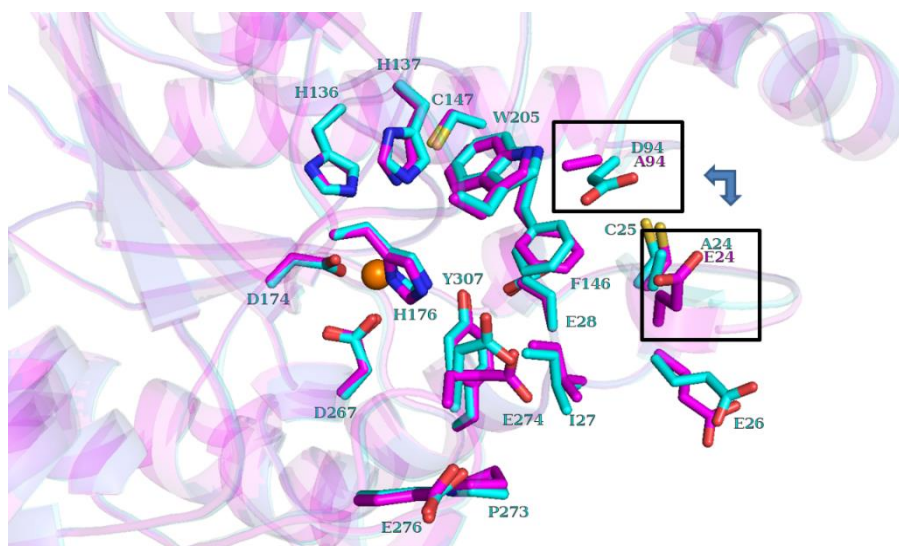
Figure 13: Comparative analysis of humanized (in magenta) vs. native Zebrafish (in cyan) HDAC10.

4.2. Validation of Docking Protocol

4.2.1. Validation with Re-Docking

The available X-ray structures of drHDAC10 and humanized drHDAC10, each complexed with different inhibitors as listed in Table 1 were downloaded from the Protein Data Bank (PDB, www.rcsb.org). Protein preparation was performed following the methods described in the Materials and Methods section, utilizing the Protein Preparation Wizard. The relevant ligands were prepared for docking using LigPrep and ConfGen. The generated conformers were then docked into the prepared protein structures using the program Glide (Schrödinger-release 2019.1) in the Standard Precision mode. This was carried out to validate and assess the docking protocol's ability to accurately reproduce the drHDAC10-inhibitor complexes. The docking of co-crystallized inhibitors was performed using the docking setup outlined in the Materials and Methods section. Subsequently, Root Mean Square Deviation (RMSD) values were calculated for each re-docking solution.

The-top ranked re-docking (the ability to reproduce the binding mode of co-crystallized ligand) poses in all crystal structures resulted in RMSD values below 2.0 Å (Table 1) with the exception of one complex structure (PDB ID 6UIM). When the RMSD values were compared for the top five ranked re-docking poses, it was observed that all values were below 1.78 Å.

31

The lowest RMSD of all re-docking solutions was below 0.9 Å for all ligands. These findings indicate that the employed docking setup effectively predicts the binding mode of various crystallized inhibitors with good accuracy and that the docking setup could be used in further docking studies.

Table 1: RMSD values for re-docking of co-crystallized inhibitors into drHDAC10 and humanized drHDAC10 (adapted from [153] and extended).

PDB IDs	Co-crystallized ligand	Enzyme (Resolution)	RMSD (Å) of top ranked pose	Best RMSD (Å) among top-5 ranked poses	Best RMSD (Å) and docking rank
5TD7	7-[(3-aminopropyl) amino]-1,1,1-trifluoroheptane-2,2-diol	drHDAC10 (2.65 Å)	1.91	1.78	0.89 (119)
6UFN	7-[(3-aminopropyl) amino] heptan-2-one	drHDAC10 (2.70 Å)	1.22	0.84	0.66 (292)
6UFO	7-[(3-aminopropyl) amino]-1-methoxyheptan-2-one	drHDAC10 (2.68 Å)	1.08	1.07	0.51 (283)
6UHV	6-[(3-aminopropyl) amino]-N-hydroxyhexanamide	drHDAC10 (2.53 Å)	1.25	1.15	0.75 (110)
6UHU	5-[(3-aminopropyl) amino] pentylboronic acid	drHDAC10 (2.80 Å)	1.60	1.45	0.72 (166)
6UII	5-[(3-aminopropyl) amino] pentane-1-thiol	drHDAC10 (2.65 Å)	0.81	0.59	0.59 (3)
6UIJ	S-5-[(3-aminopropyl) amino] pentyl} thioacetate	drHDAC10 (2.90 Å)	1.06	1.05	0.51 (117)
6UIL	7-(3-aminopropyl) amino-1,1,1-trifluoroheptan-2-one	drHDAC10 (2.85 Å)	0.79	0.78	0.57 (216)
6UIM	7-(3-aminopropyl) amino-2-oxoheptylthioacetate	drHDAC10 (2.75 Å)	2.93	1.31	0.69 (62)
6VNQ	bishydroxamate	humanized drHDAC10 (2.05 Å)	0.35	0.35	0.32 (16)
6WBQ	hydroxamate	humanized drHDAC10 (2.00 Å)	0.54	0.54	0.54 (1)
6WDV	hydroxamate	humanized drHDAC10 (2.40 Å)	0.53	0.53	0.47 (26)
6WDW	hydroxamate	humanized drHDAC10 (2.20 Å)	0.35	0.39	0.34 (59)
6WDX	hydroxamate	humanized drHDAC10 (2.65 Å)	0.62	0.52	0.36 (30)
6WDY	hydroxamate	humanized drHDAC10 (2.65 Å)	0.62	0.58	0.52 (6)
7KUQ	acetyl-spermidine	humanized drHDAC10 Y307F mutant (2.10 Å)	1.16	0.44	0.24 (55)

PDB ID					
7KUR	acetyl-putrescine	humanized drHDAC10 Y307F mutant (2.10 Å)	0.73	0.73	0.18 (64)
7KUS	acetyl-spermidine	humanized drHDAC10 H137A mutant (2.00 Å)	1.09	1.09	0.62 (128)
7KUT	acetyl-putrescine	humanized drHDAC10 H137A mutant (2.05 Å)	0.69	0.64	0.25 (97)
7U59	Piperidine-4-hydroxamate	humanized drHDAC10 (2.18 Å)	1.04	0.27	0.24 (6)
7U69	Piperidine-4-acrylhydroxamate	humanized drHDAC10 (2.50 Å)	1.25	1.10	0.52 (45)
7U6B	Piperidine-4-acrylhydroxamate	humanized drHDAC10 (2.60 Å)	0.66	0.45	0.39 (79)
7U6A	hydroxamate	humanized drHDAC10 (2.25 Å)	0.90	0.90	0.18 (55)
7U3M	N-methyl piperazine hydroxamate	humanized drHDAC10 (2.10 Å)	1.54	0.45	0.22 (16)

4.2.2. Validation with Cross-Docking

Since in this study enzymatic biological evaluations were carried out using drHDAC10, further cross-docking validations were carried out only in the crystallized drHDAC10 structures.

The top ranked crossdocking poses of all ligands showed RMSD values below 2.5 Å in all PDB structures, with the exception of the cocrystallized ligand in 6UIM which showed higher RMSD in PDB IDs 6UIJ, 6UIL and 6UIM PDBs (see Table 2).

Table 2: RMSD values for cross-docking poses of crystallized drHDAC10 structures.

PDB ID	5TD7	6UFN	6UFO	6UHV	6UHU	6UII	6UIJ	6UIL	6UIM
5TD7 ligand	1.91	1.27	2.37	2.01	2.45	2.11	1.29	1.93	2.11
6UFN ligand	0.98	1.22	0.98	1.18	1.15	1.41	1.24	1.19	1.57
6UFO ligand	2.02	2.20	1.08	1.58	1.66	2.20	2.10	1.51	2.07
6UHV ligand	1.77	1.47	2.22	1.25	2.12	1.34	2.01	1.47	1.87
6UHU ligand	1.51	1.72	1.53	1.60	1.60	1.33	1.13	1.39	1.90
6UII ligand	1.36	1.09	1.61	1.23	1.15	0.81	1.24	1.04	1.07
6UIJ ligand	1.19	1.11	1.96	1.34	1.95	0.69	1.06	1.62	0.67
6UIL ligand	0.75	0.87	0.87	1.18	0.84	2.11	0.86	0.79	1.14
6UIM ligand	2.04	2.32	2.03	1.77	2.39	2.50	2.50	2.70	2.93

4.3. Docking of N^8- and N^1- Acetylspermidines

Recently, Hai and colleagues [39] confirmed that HDAC10 enzymes from both *Danio rerio* (zebrafish) and *Homo sapiens* (human) function as PDACs instead of lysine deacetylases. In the same study, the catalytic efficiency (k_{cat}/K_M) of N^8-acetyl spermidine for hsHDAC10 and drHDAC10 was measured as 2.900±200 and 4.600±300 $M^{-1}s^{-1}$, respectively. Conversely, N^1-acetylspermidine exhibited poor substrate properties with k_{cat}/K_M values of 24±5 and 7±2 $M^{-1}s^{-1}$ for hsHDAC10 and drHDAC10, respectively. This shows a 121-fold and 657-fold selectivity for N8 over N1 for hHDAC10 and zHDAC10, respectively.
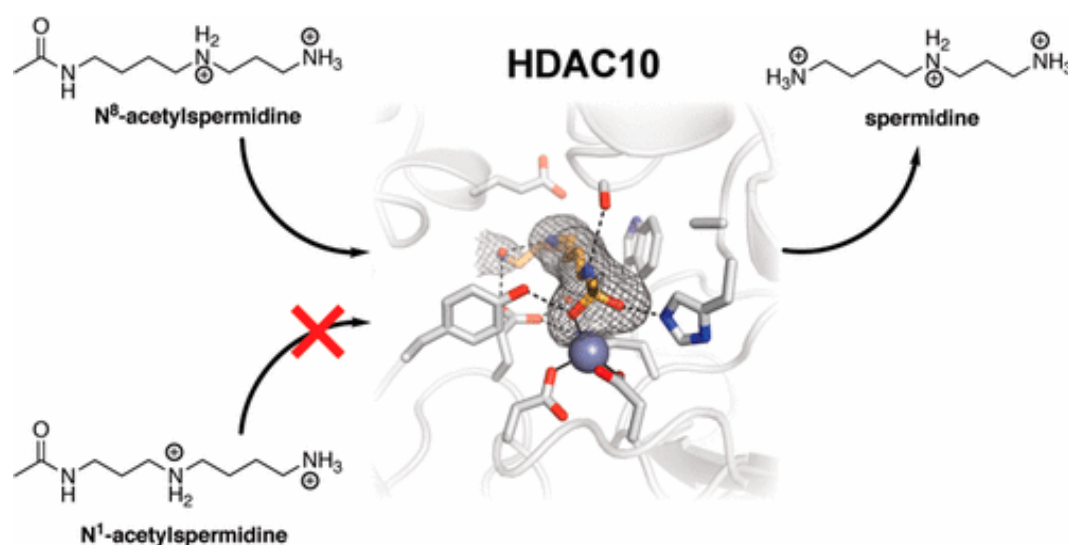
Figure 14: Specificity of cytosolic polyamine deacetylase activity of HDAC10. The enzyme catalyzes the hydrolysis of N^8-acetylspermidine but shows no reactivity towards N^1-acetylspermidine (reproduced from [72]).

In this work, docking studies were performed in an attempt to explain the selectivity of HDAC10 for N^8-acetylspermidine over N^1-acetylspermidine. For docking, the DrHDAC10 crystal structure with the PDB ID: 6UFN was used [158].

In the docking pose of N^8-acetylspermidine (Figure15a), formation of a coordination bond with zinc through the acetyl group and a hydrogen bond with the catalytic Tyr307 was observed. The acetylated N^8 nitrogen atom formed a hydrogen bond with the backbone carbonyl of Gly145. Furthermore, the central protonated nitrogen atom of N^8-acetylspermidine was observed to form ionic bonds with Asp94 and the gatekeeper Glu274 in addition to two π-cation interactions with Trp205, another HDAC10-specific amino acid. Conversely, the other protonated but unacetylated distal N^1 nitrogen was found to make hydrogen bond and ionic interactions with Glu274.

On the other hand, in the docking pose of N^1-acetylspermidine (Figure15b) showed a similar binding mode. The carbonyl group showed a coordination bond with the zinc ion while engaging in a hydrogen bond with Tyr307. The acetylated N^1 nitrogen also formed hydrogen bond with the backbone carbonyl of Gly145. Additionally, similar ionic interactions with Asp94 and the gatekeeper Glu274 were observed as well as the π-cation interactions between the protonated central nitrogen and Trp205 and His176. Furthermore, the distal N^8 nitrogen in this context was found to establish hydrogen bond and salt bridge interactions with Glu274.
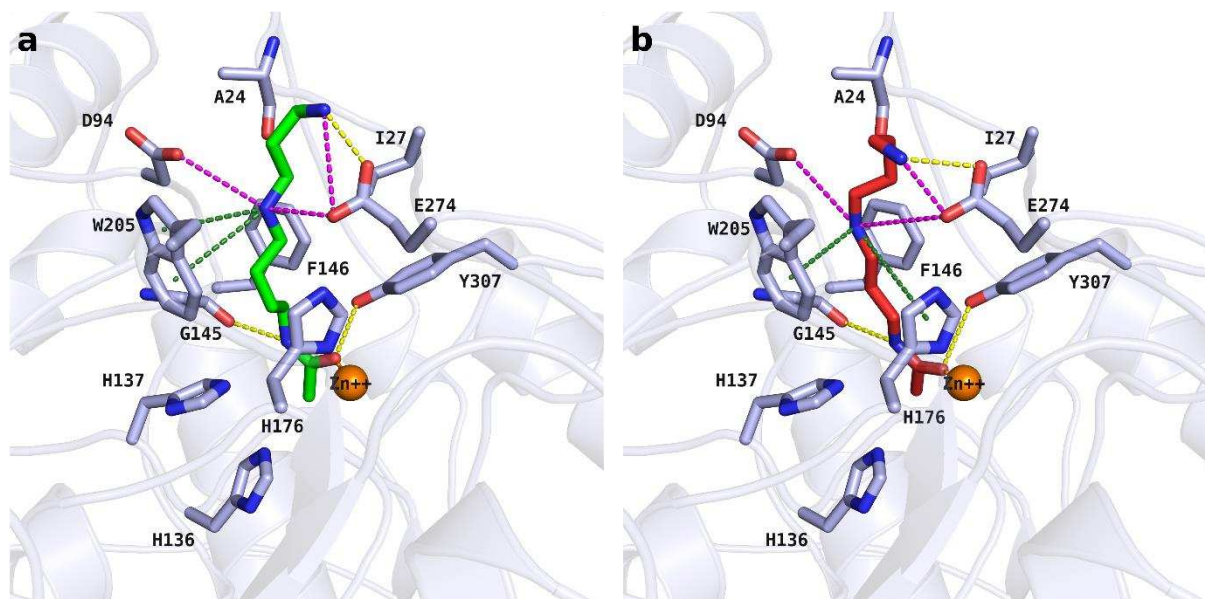
Figure 15: Predicted binding mode in drHDAC10 (PDB ID 6UHU) of acetyl-spermidines, **a)** N^8-acetylspermidine (colored green), **b)** N^1-acetylspermidine (colored red). Side chains of binding site residues are shown as white sticks and the catalytic zinc ion as orange spheres. H-bonds are depicted as yellow-dashed lines, salt bridge interactions are depicted as magenta-dashed lines, π-cation bonds are depicted as green-dashed lines and coordination of the zinc ion by the ligands as orange-dashed lines.

In conclusion, docking studies did not yield any reasonable explanation for the specificity of HDAC10 towards acetylspermidines. It's also noteworthy that the obtained docking scores did not provide a clear distinction (-6.61 and -6.88 for N^8-acetylspermidine and N^1-acetylspermidine, respectively).

Hence further techniques including molecular dynamics simulations and binding free energy calculations using the obtained docking poses were employed.

4.4. MD Simulations and BFE Calculations of Acetyl Spermidines-HDAC10 Complexes: A Comparative Study of N^8 and N^1 Variants

Section 4.3 of the text describes the results of docking studies that yielded binding models for N^8 and N^1 acetyl spermidines. These models were carefully analyzed and created using the drHDAC10 crystal structure coded as 6UFN [158] undergoing a series of three replicas of 100

ns MD simulations. The primary purpose of these simulations was to examine the binding conformation derived from the docking studies and evaluate the stability of the respective ligand-protein complexes.

In the conducted MD simulations, explicit solvent models were used during the simulations, while implicit solvation models were systematically applied in the Binding Free Energy (BFE) calculations. Three replicates of 100 ns MD simulations were performed for each system, with each simulation corresponding to a different compound. Frames from the final 5 ns of each simulation were extracted and used for BFE calculations to ensure that the analysis was based on equilibrated and stable system states.

First BFE Calculation: The "set default pbradii mbondi" setting was applied, optimized for the GB1 solvation model, ensuring compatibility and precision in solvation energy estimates by using frames from the first MD replica for each compound.

Second and Third BFE Calculations: The "set default pbradii mbondi2" setting was used, tailored for the GB2 and GB5 solvation models, enhancing accuracy in these configurations by using frames from the second MD replica for each compound.

Fourth BFE Calculation: The "set default pbradii mbondi3" setting was employed for the GB8 solvation model, ensuring appropriate atomic radii for accurate solvation calculations by using frames from the third MD replica for each compound.

Upon examination of the RMSD graphs derived from molecular dynamics simulations (see Figure 16), it is apparent that both the N^8-acetyl spermidine and the N^1-acetyl spermidine including complexes maintain protein RMSD values below 2 Å throughout the duration of the simulations.

Notably, the N^1 complexes (N^1-acetyl spermidine/HDAC10 complexes) exhibit more pronounced fluctuations compared to the N^8 counterparts. These variations in the RMSD_PRO values for the N^1 complexes could indicate a more dynamic conformational behaviour.

When comparing the RMSD_LIG graphs for N^8 and N^1 complexes (N^8-acetyl spermidine/HDAC10 complexes and N^1-acetyl spermidine/HDAC10 complexes), it is evident that the N^1 ligand tends to have higher RMSD values, suggesting weaker interaction with the active site and a greater flexibility.

The stable RMSD pattern for N^8-acetyl spermidine across suggests a more stable conformation for the ligand within the binding pocket, which could imply a stronger specific ligand-protein interaction.
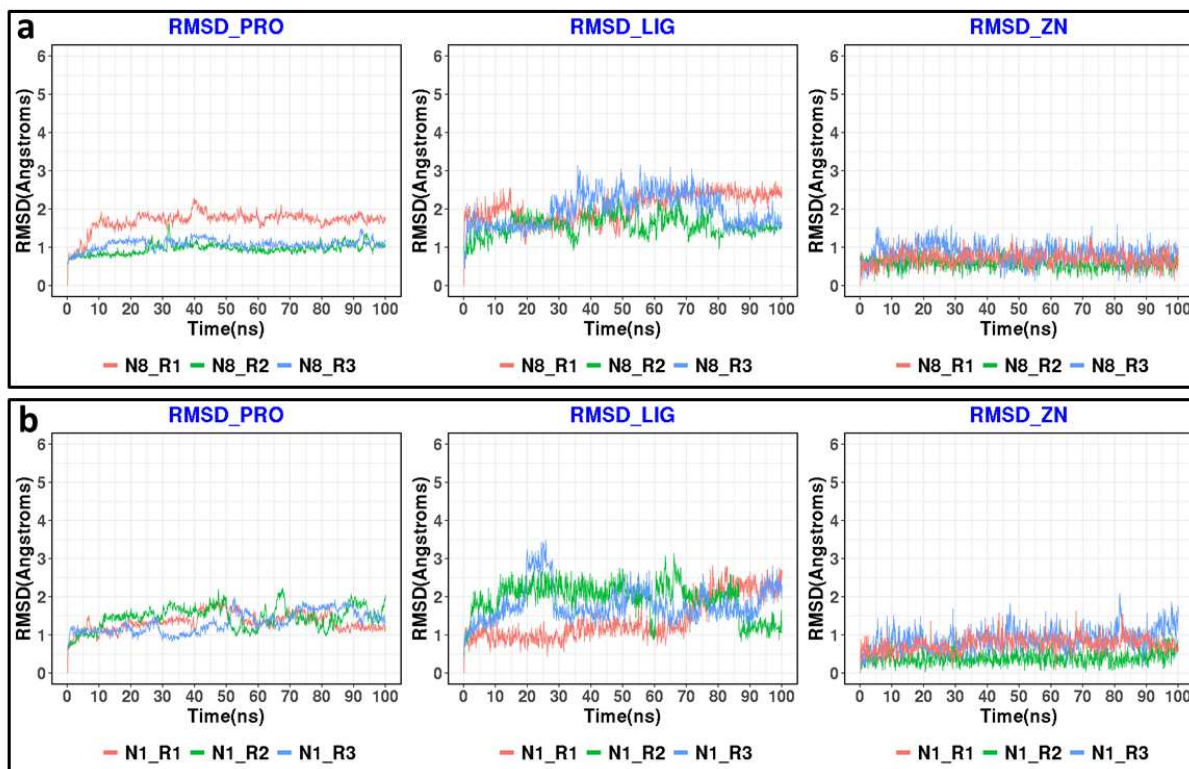
Figure 16: For both N^8 (**a**) and N^1 (**b**) complexes, the RMSD metrics are plotted for distinct elements: protein (PRO), ligand (LIG), and zinc ion (ZN) for three replicates.

The binding mode analysis of the last frames of the MD simulations (N8_R1, N8_R2, and N8_R3) reveals highly similar binding modes for N8-acetyl spermidine in the HDAC10 active site, with consistent interactions and stabilization patterns (see Figures 17c d, and e).

In all three replicas, the ligand maintains key interactions with the active site residues and the zinc ion. The coordination with zinc, the hydrogen bond with G145, and the π-cation interaction with W205 remain stable across the simulations. Notably, the distal N1 nitrogen forms a salt bridge and hydrogen bonds with both D94 and E274, while the middle nitrogen engages in additional hydrogen and ionic interactions with these residues, reinforcing the ligand's stability within the binding pocket.

While slight variations in the ligand's distal geometry are observed—ranging between "n"- and "u"-shaped conformations—these adjustments do not alter the primary interaction network. Instead, they underscore the ligand's flexibility and adaptability to optimize binding within the pocket.

Overall, the obtained binding modes across the replicas collectively suggest a robust and stable interaction network, with consistent engagement of critical residues and the zinc coordination sphere. These results provide a comprehensive understanding of the ligand's behavior and its favorable binding within the HDAC10 active site.

On the other hand, the binding mode analysis of the last frames of the MD simulations for the N1-acetylspermidine/HDAC10 complexes (N1_R1, N1_R2, and N1_R3) reveals consistent retention of the zinc ion coordination and the hydrogen bond with G145 (see Figures 17f, g, and h).

In N1_R1, the distal N8 nitrogen establishes hydrogen and ionic bonds with D94, while the central nitrogen engages in two π-cation interactions with W205, a π-cation bond with H176, and forms salt bridges with both E274 and D94, along with a hydrogen bond with E274.

In N1_R2, the distal N8 nitrogen shifts its orientation towards E274, forming a salt bridge. The central nitrogen continues to interact with W205 and forms hydrogen and ionic bonds with E274, as well as an ionic bond with D94.

In N1_R3, the distal N8 nitrogen maintains a salt bridge with E274, while the central nitrogen interacts with W205 and E274, and additionally forms a π-cation bond with F146.

This analysis highlights consistent interaction patterns, with minor variations in the distal nitrogen's orientation affecting specific residue interactions.
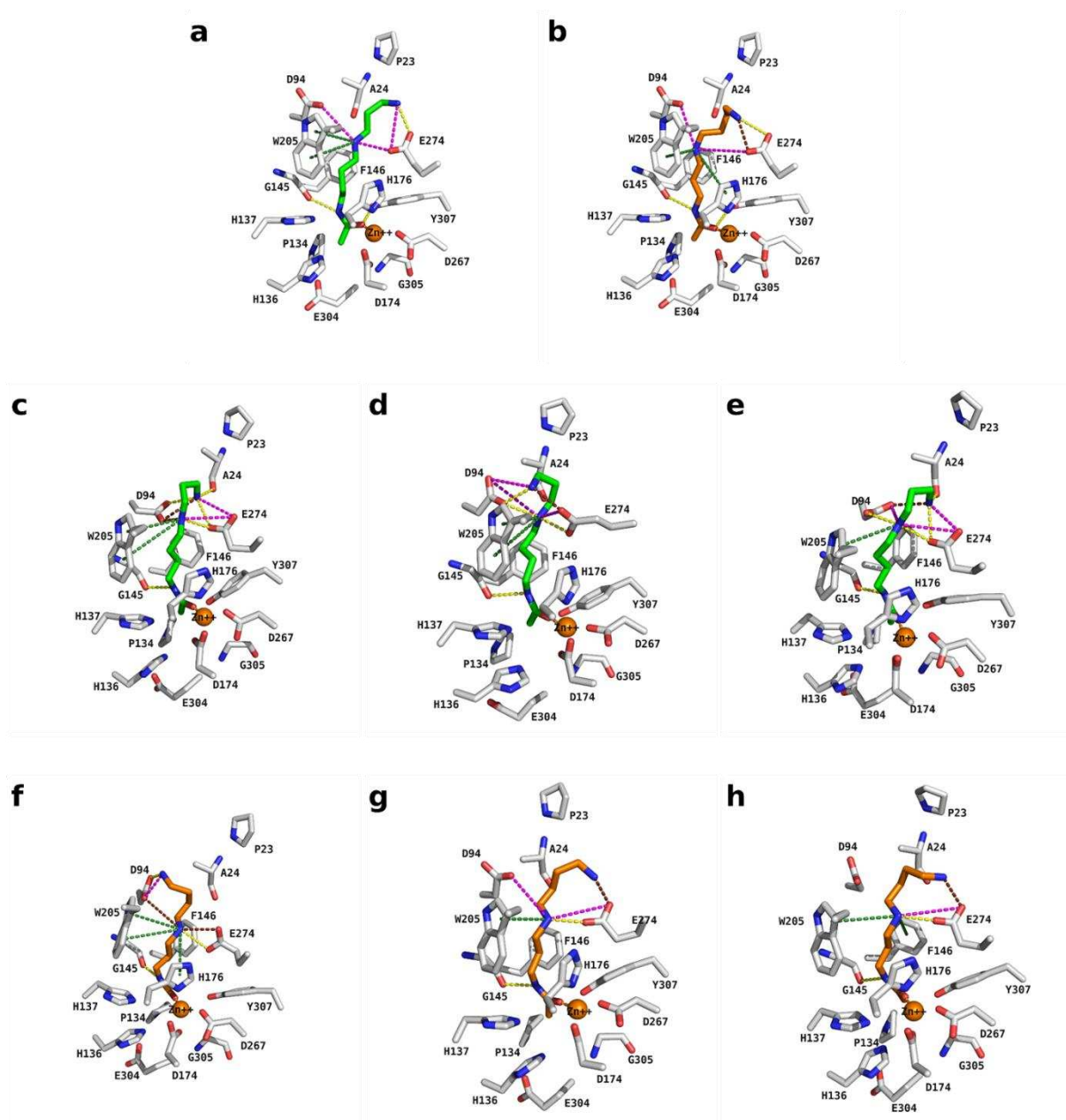
Figure 17: Binding conformations of N^8-acetylspermidine (**a, c–e**) and N^1-acetylspermidine (**b, f–h**) in the HDAC10 active site from docking (**a, b**) and from the last frames of each 100ns MD simulation replicates (**c–h**).

Subsequently, the binding poses observed during the last 5 ns of the MD processes were utilized to calculate the BFE for both acetyl spermidines. The calculated BFE using all implicit solvent models (GB1, GB2, GB5, and GB8) showed that N8-acetylspermidine consistently revealed a more energetically favorable profile than N1-acetylspermidine for each model. For example, in the GB1 and GB2 models, N8-acetylspermidine showed significantly lower total energies than N1-acetylspermidine. This trend was consistent across all models (GB5 and GB8), reinforcing the preference for N8-acetylspermidine (see Figure 18e (TOTAL BFE)).

Finally, to identify which amino acids within the binding pocket are more crucial for binding and to elucidate the reasons behind significant BFE differences among the acetyl spermidine

derivatives, BFE decompositional analyses were performed and presented in tabular form (see figure 18e).

For each used MM-GBSA method, the ligand energy values were significantly in favor of N^8-acetylspermidine (figure 18e).

When examining the contributions of the amino acids within the binding pocket and the catalytic zinc atom to the total binding free energy (BFE), it became apparent that the catalytic zinc ion made a significant contribution to the total energy. This fact is valid for both N^8 and N^1 especially when considering the standard (refer to Figure 18).

The gatekeeper residue E274, along with D94 and A24, were also found to be pivotal in their energy contributions.

A thorough review of the MM-GBSA GB-1 decomposition graph, comparing N^8 and N^1, distinctly shows that the energy contributions from D94, A24, and E274 are significantly greater for N^8 (see Figure 18a).

In the GB2 and GB5 decompositional analyses (see Figure 18b and 18c), contributions from E274 and D94 stand out, with significant differences observed between the energy contributions made by D94 in both graphs. As observed in Figures 17d and g, specifically regarding D94, N^1 forms only an ionic bond with D94 through its central nitrogen atom, whereas the N^8 variant engages in both hydrogen and ionic interactions via its distal and central nitrogen atoms. This explains the significant energy difference between the two.

When examining the comparative GB8 total energy decomposition graph (see Figure 18d), the differences in contributions from D94 and A24 are notable. Considering the relevant binding poses (see Figure 17e and h), it is observed that the N^1 variant does not form any bonds with D94 and A24. In contrast, the N^8 variant establishes a hydrogen bond and an ionic bond with D94 through its central nitrogen atom, while its distal nitrogen atom forms a salt bridge bond with D94 and a hydrogen bond with the backbone atom of A24.

Residues	GB1-N8	Std. Dev	GB1-N1	Std. Dev	GB2-N8	Std. Dev	GB2-N1	Std. Dev	GB5-N8	Std. Dev	GB5-N1	Std. Dev	GB8-N8	Std. Dev	GB8-N1	Std. Dev
P23	0.0249	0.0186	-0.0027	0.0102	0.0504	0.0270	-0.0354	0.0521	0.1032	0.0448	-0.0051	0.0641	-0.0913	0.1464	-0.0133	0.0296
A24	-4.8302	0.5156	-0.5488	0.2211	-1.2213	0.3251	-0.5653	0.1929	-1.2092	0.3790	-0.4454	0.2155	-4.9259	1.1124	-0.3677	0.1498
D94	-13.3678	2.1190	-7.5657	1.3773	-12.1290	1.7212	-0.3527	0.4849	-14.4859	2.0284	-2.7818	3.5669	-8.9275	1.9520	-0.2221	0.5013
P134	-0.2493	0.0653	-0.2313	0.0666	-0.0230	0.0985	-0.0039	0.0723	-0.0039	0.1242	0.0155	0.1189	-0.1863	0.0672	-0.1221	0.0537
H136	0.7577	0.4931	0.4047	0.4432	1.4282	0.6844	1.8050	0.7340	2.5170	0.9483	2.7346	0.9598	0.3152	0.1869	0.6306	0.9634
H137	-0.6263	0.3412	-0.3366	0.4098	-0.6093	0.5175	-0.9054	0.4061	-1.1835	0.5582	-1.5336	0.4922	0.6717	0.6226	0.8546	0.7208
G145	-2.0243	0.5001	-1.8933	0.4260	-1.9541	0.5259	-1.9841	0.5648	-2.0837	0.6587	-2.1882	0.6892	-2.5092	0.8312	-2.9103	0.7670
F146	-2.3941	0.5995	-2.5835	0.3457	-3.4473	0.4448	-3.0071	0.4420	-4.4384	0.4896	-3.7017	0.5126	-1.7300	0.5630	-3.2426	0.4890
D174	1.2787	0.8506	1.2318	0.8908	-0.6487	0.9179	-1.1195	1.0006	-0.7641	1.0598	-1.2505	1.1382	12.0388	1.5491	11.6787	1.2568
H176	-0.1527	0.8074	-0.8645	0.7899	-0.1056	0.7657	-0.7272	0.9453	-0.1819	0.7903	-1.4129	0.9965	4.7943	1.2943	5.2113	1.3005
W205	-3.0702	0.4792	-4.5053	0.8615	-3.4002	0.8007	-3.2367	0.7691	-3.9585	0.9356	-4.3836	1.2007	-3.0177	0.6549	-3.7646	0.8274
D267	0.8416	0.8719	-0.1993	0.5708	-1.6320	0.7435	-2.0026	0.7262	-2.4633	0.8289	-2.4633	0.7720	8.7943	1.8794	9.4056	1.7999
E274	-14.1162	1.3556	-6.7536	0.8060	-10.7714	1.3718	-11.1635	1.8972	-13.2151	1.5961	-11.1199	3.9944	-12.5709	1.4168	-9.1249	1.8980
E304	-0.8337	0.2337	-0.7592	0.2782	-1.1206	0.3486	-1.1927	0.3391	-1.9477	0.4480	-1.9828	0.4096	-0.5628	0.5494	-0.6338	0.4448
G305	-0.1539	0.1140	-0.1225	0.0689	-0.0249	0.0835	-0.0180	0.0758	0.0464	0.1185	-0.0083	0.1281	-0.1907	0.2266	-0.2142	0.1613
Y307	-1.1004	0.3065	-0.8393	0.1547	-0.9850	0.2384	-0.8676	0.2063	-1.2595	0.2453	-1.0395	0.2908	-0.8056	0.3971	-0.7345	0.2885
ZN++	-20.7433	1.7746	-17.2108	1.4479	-16.4697	2.4927	-13.7907	2.9974	-18.7947	2.9176	-16.0073	3.1362	-56.1627	2.1051	-52.8319	2.2407
LIG	-71.4400	2.8874	-55.3114	1.9951	-59.3634	2.3575	-47.7202	2.2627	-57.6942	2.7307	-47.7484	3.1348	-50.4724	4.0776	-38.6285	2.5441
TOTAL BFE	-137.1150	5.4875	-102.2120	3.4946	-116.3027	4.0336	-90.9037	4.2732	-123.1423	4.2909	-96.1085	4.4666	-119.7798	6.9078	-89.6672	4.5827

Figure 18: Binding free energy (BFE) and decomposition analyses for N^8- and N^1-acetylspermidine in the HDAC10 binding pocket using MM-GBSA models (GB1, GB2, GB5, GB8). (**a–d**) Energy contributions from key residues (D94, E274, A24) and zinc ion. (**e**) BFE values and ligand energies with standard deviations.in which N8 consistently displaying lower total energy and higher binding affinity across all models.

In conclusion, in each total energy comparison, N^8 consistently demonstrated a significantly stronger binding energy. It was concluded that the positioning of the central nitrogen atom was a key factor. Firstly, the variation in the position of the central nitrogen atom in the N^8 variant allowed for interactions with D94, which were either not possible or quantitatively and qualitatively weaker in the N^1 variant. Secondly, the difference in the distance between the distal and central nitrogens by one carbon length enabled the N^8 variant to adopt a semi-circular conformation in the distal part of the HDAC10 binding pocket. This conformation, previously described as n- or u-shaped, facilitated the formation of multiple bonds with E274 and D94 through both distal and central nitrogen atoms. Furthermore, this conformation allowed the distal nitrogen atom to form a hydrogen bond with A24, a capability that could not be achieved by the N^1 variant.

These findings highlight the critical role of structural differences in substrate selectivity and activity toward HDAC10, providing a foundation for further exploration of selective inhibitors.

Corroborating this hypothesis, Steimbach et al. have recently illustrated in their research that modifying the SAHA structure, a well-known HDAC pan-inhibitor, by incorporating a protonatable methylated nitrogen atom along its alkyl chain yields aza-SAHA analogues [84]. Up to a critical position, this structural addition enhances activity and selectivity; however, beyond this threshold, there is a strong decrease in HDAC10 activity and selectivity. This observation runs parallel to the fact that among the N^8 and N^1 acetyl spermidine variants, only N^8 is a natural substrate for HDAC10. The N^1 variant's protonatable nitrogen sinks too deeply into the hydrophobic binding pocket, which is considered undesirable. Such observations, among others, elucidate why N^8 acetyl spermidine is preferentially selective towards HDAC10.

4.5. Docking Studies on Non-selective HDAC Inhibitors
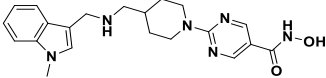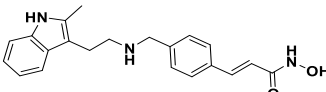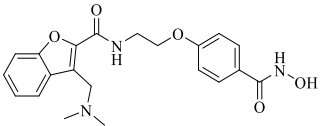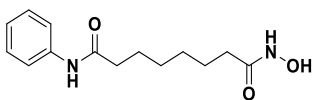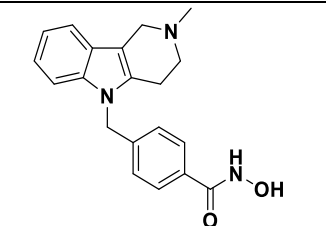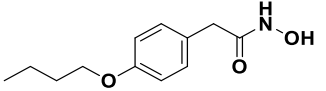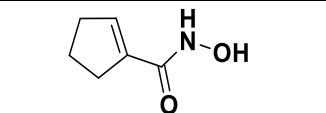
A novel enzymatic assay (see section 7.1.1.3 for details) developed by Daniel Herp was used to evaluate the activity of a series of known HDAC inhibitors against drHDAC10 [155]. Initial screening was conducted at concentrations of 0.1, 1, and 10 μM, and compounds exhibiting over 30% inhibition at 0.1 μM were subsequently tested to determine their HDAC10 IC$_{50}$ values.

Screening of 33 compounds identified strong HDAC10 inhibitory activity in pan-inhibitors **1**, **2**, **3**, HDAC6-selective inhibitors **5** [72] and **7** [159], three cinnamic acid derivatives (**14**, **15**,
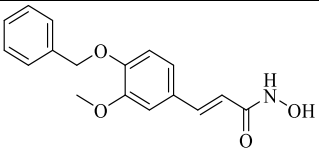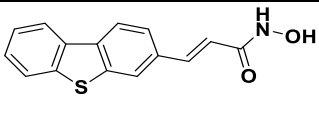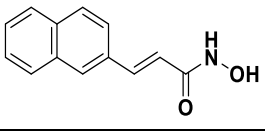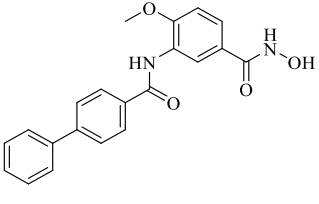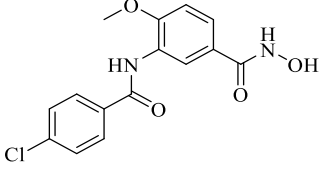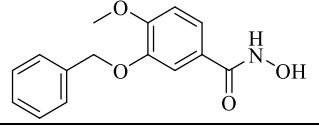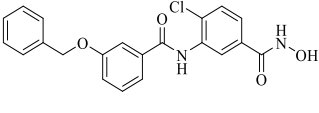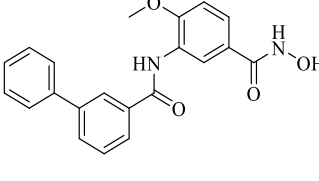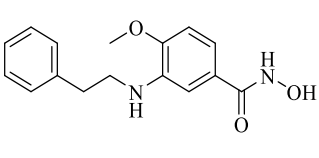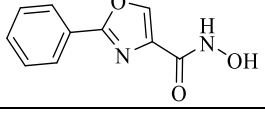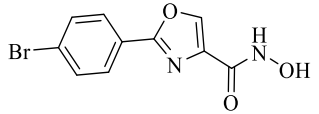
23) [160], and the oxazole compound **31** [161]. The reference pan-inhibitor **4**, included for comparison, showed <10% inhibition at 0.1 μM but still had its IC$_{50}$ value determined. Overall, IC$_{50}$ values ranging from 30 nM to 2000 nM were measured for 10 compounds, while the remaining compounds displayed weaker HDAC10 inhibition (Table 3).
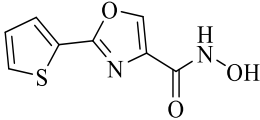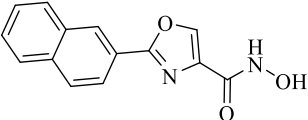
The selectivity profiles of these 10 compounds were evaluated by testing their inhibitory activity against hHDAC1, hHDAC6, and hHDAC8. Non-selective inhibitors (**1-4**) exhibited strong activity against both HDAC1 and HDAC8, while most other compounds showed moderate to weak inhibition of these enzymes. Notably, cinnamic acid derivatives **14** and **23** displayed strong inhibition of HDAC8. All 10 compounds demonstrated significant inhibition of HDAC6, reflecting the structural similarity between HDAC6 and HDAC10.

Table 3: Enzymatic in vitro inhibition of studied compounds (**1-33**) (adapted from [157-159]).

ID	Name/Article ID	Structure	HDAC isoform inhibition % @ c [μM] or IC50 value (nM)			
			*dr*HDAC10	*h*HDAC6	*h*HDAC1	*h*HDAC8
			(NDA-Assay)	(ZMAL)	(ZMAL)	(FDL)
1	quisinostat (**11**)		50 ± 5	182 ± 22	3 ± 0.3	64 ± 3
2	panobinostat (**9**)		51 ± 7	4 ± 0.4	2 ± 0.1	89 ± 6
3	abexinostat (**12**)		134 ± 26	9 ± 0.3	24 ± 2	820 ± 149
4	vorinostat (**6**)		2000 ± 240	104 ± 9	117 ± 6	400 ± 100
5	tubastatin A (**14**)		30 ± 3	34 ± 17	1916 ± 420	1440 ± 120
6	bufexamac (**27**)		26 % @ 0.1 64 % @ 1 >95 % @ 10	n.d.	n.d.	n.d.
7	BRD9757 (**28**)		147 ± 15	455 ± 75	4800 ± 1300	< 10 % @ 100

#	Name	Structure				
8	PCI-34051 (**29**)		14 % @ 0.1 17 % @ 1 70 % @ 10	n.d.	n.d.	n.d.
9	ST70 (**30**)[76]		11 % @ 0.1 51 % @ 1 >95 % @ 10	n.d.	n.d.	n.d.
10	ST71 (**31**)[76]		<10 % @ 0.1 64 % @ 1 > 95 % @ 10	n.d.	n.d.	n.d.
11	TB5 (**32**)[73]		11 % @ 0.1 56 % @ 1 > 95 % @ 10	n.d.	n.d.	n.d.
12	AW12 (**33**)[77]		< 10% @ 0.1 42% @ 1 66% @ 10	n.d.	n.d.	n.d.
13	AW19 (**34**)[78]		11% @ 0.1 19% @ 1 n.d. @ 10	n.d.	n.d.	n.d.
14	TB8 (**35a**)		**185 ± 47**	**95 ± 21**	**1454 ± 470**	**54 ± 9**
15	TB51 (**35b**)		**112 ± 19**	**710 ± 88**	**3630 ± 190**	**705 ± 120**
16	TB53 (**35c**)		12 % @ 0.1 50 % @ 1 81 % @ 10	n.d.	n.d.	n.d.
17	TB54 (**35d**)		11 % @ 0.1 40 % @ 1 67 % @ 10	n.d.	n.d.	n.d.
18	TB76 (**35e**)		26 % @ 0.1 82 % @ 1 83 % @ 10	n.d.	n.d.	n.d.
19	TB77 (**35f**)		18 % @ 0.1 69 % @ 1 > 95 % @ 10	n.d.	n.d.	n.d.
20	TB27 (**35g**)		18 % @ 0.1 24 % @ 1 n.d. % @ 10	n.d.	n.d.	n.d.
21	TB38 (**35h**)		17 % @ 0.1 30 % @ 1			

#	Name	Structure				
			66 % @ 10			
22	TB73 (**36**)	(structure)	< 10 % @0.1 54 % @ 1 56 % @ 10	n.d.	n.d.	n.d.
23	TB75 (**37**)	(structure)	273 ± 58	225 ± 33	2700 ± 200	205 ± 32
24	TH65 (**38a**)	(structure)	< 10 % @0.1 < 10 % @ 1 43 % @ 10	n.d.	n.d.	n.d.
25	TH68 (**38b**)	(structure)	14 % @ 0.1 31 % @ 1 86 % @ 10	n.d.	n.d.	n.d.
26	TH70 (**38c**)	(structure)	11 % @ 0.1 20 % @ 1 n. d. % @ 10	n.d.	n.d.	n.d.
27	TH77 (**38d**)	(structure)	11 % @ 0.1 20 % @ 1 63 % @ 10	n.d.	n.d.	n.d.
28	TH95 (**38e**)	(structure)	< 10 % @0.1 < 10 % @ 1 23 % @ 10	n.d.	n.d.	n.d.
29	TH149 (**38f**)	(structure)	< 10 % @0.1 19 % @ 1 n.d. % @ 10	n.d.	n.d.	n.d.
30	JS18 (**39a**)	(structure)	< 10 % @0.1 45 % @ 1 > 95 % @ 10	n.d.	n.d.	n.d.
31	JS28 (**39b**)	(structure)	400 ± 43	59 ± 9	14470 ± 1100	14370 ± 2950

32	JS35 (**39c**)		< 10 % @0.1 37 % @ 1 > 95 % @ 10	n.d.	n.d.	n.d.
33	JS41 (**39d**)		< 10 % @0.1 34 % @ 1 > 95 % @ 10	n.d.	n.d.	n.d.

After validating the docking procedure through re-docking and cross-docking methods, the docking of the aforementioned compounds (Table 1) were conducted using available crystal structures of drHDAC10 (PDB ID 6UHU) [158], human HDAC6 (PDB ID 5EDU) [69], HDAC1 (PDB ID 5ICN) [162], and HDAC8 (PDB ID 2 V5X) [163] to provide a rationale for the acquired biochemical data. These docking studies aimed to elucidate the observed selectivity profiles of certain hit compounds. Of note, crystal structures of drHDAC6 complexed with hydroxamic acid derivatives demonstrated that these inhibitors might make coordination bond with the catalytic zinc ion in either a mono- or bidentate manner [69, 164-167]. Therefore, two distinct docking approaches were employed in this study to explore plausible binding modes of the hits within the HDAC6 crystal structure.

Docking into hHDAC6 with monodentate zinc coordination manner; involved retrieving the co-crystallized ligand and three water molecules (HOH921, HOH999, and HOH1011) from drHDAC6 crystal structure (PDB ID: 5EF7) [168]. These were inserted into the hHDAC6 crystal structure (PDB ID: 5EDU) [168] prior to the mentioned protein preparation and minimization steps in the Molecular Docking title.

For docking into hHDAC6 with bidentate zinc coordination manner, three water molecules (HOH1015, HOH1006, and HOH1083) were retrieved from drHDAC6 crystal structure (PDB ID: 6CSQ). They were inserted into the HDAC6 crystal structure (PDB ID 5EDU) before the protein preparation and minimization steps mentioned earlier.

The group of pan-HDAC inhibitors, namely abexinostat (**1**), quisinostat (**2**), and panobinostat (**3**), all containing a basic motif in their capping group, demonstrated significant efficacy against HDAC10. The outcomes obtained from docking studies unveiled that the capping moiety of these inhibitors (illustrated in Figure 19) exhibited an ability to engage in salt bridge interactions involving the protonated amine and the gatekeeper residue E274 [73], in addition to hydrophobic interactions with F204 or W205. Furthermore, the zinc binder hydroxamate moiety displayed the classic interactions observed within the lysine binding pocket. These

interactions include a bidentate chelation with the zinc ion and three hydrogen bond interactions with H136, H137, and Y307.
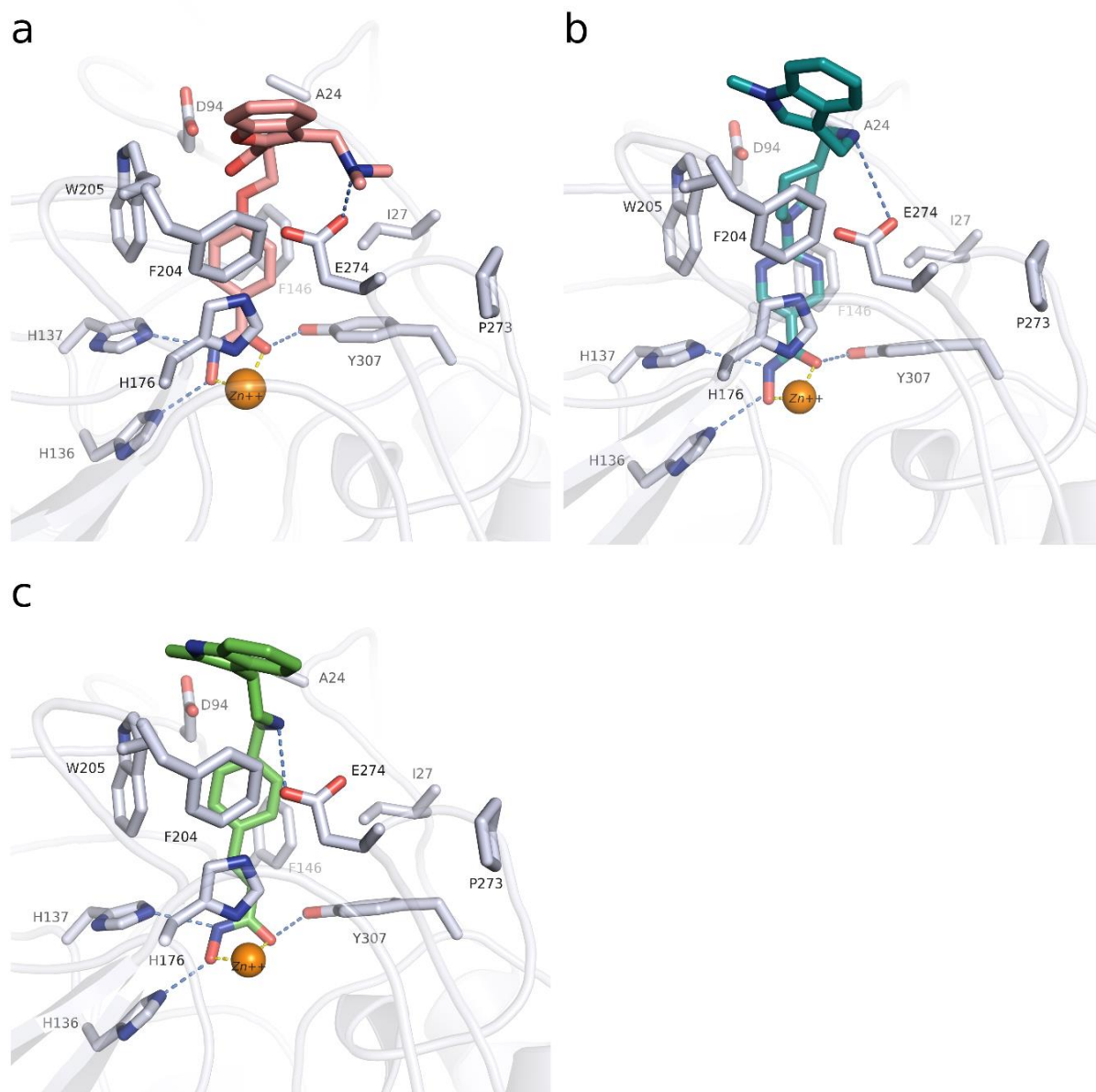
Figure 19: Predicted binding mode in drHDAC10 (PDB ID 6UHU) of pan-inhibitors abexinostat (**1**), quisinostat (**2**) and panobinostat (**3**): **a) 1** (colored salmon), **b) 2** (colored teal), and **c) 3** (colored green). Side chains of binding site residues are shown as white sticks and the catalytic zinc ion as orange spheres. H-bonds and salt bridge interactions are depicted as blue-dashed lines and coordination of the zinc ion by the ligand as yellow-dashed lines (reproduced from [169]).

As previously discussed, multiple previously reported "selective" HDAC6 inhibitors also exhibited significant inhibition of HDAC10. This outcome is understandable given that HDAC6 and HDAC10 are the only members within class IIb of the HDAC family and share a sequence identity of over 45%. Their ligand binding sites show a sequence identity of around 63%. As an example, compound **5** (Tubastatin A) demonstrated almost equal potency in the

nanomolar range against both HDAC6 and HDAC10, while displaying weaker activity against HDAC1 and HDAC8 isoforms. The docking results of compound **5** in drHDAC10 confirm the proposed interactions observed in the crystallized binding mode (PDB ID: 6WBQ) in humanized DrHDAC10. In the crystallized binding pose, the protonated nitrogen atom of Tubastatin A interacts electronically with E274 and E24 [70]. In our docking pose, a salt bridge interaction between the nitrogen atom and E274 was observed. Given the A24E and D94A mutations in the humanized DrHDAC10 structure, the observed docking pose can be considered both successful and consistent. Additionally, bidentate zinc coordination bonds and hydrogen bonds with conserved amino acid residues are other notable similarities. Furthermore, the indole ring of compound **5** exhibited hydrophobic interactions with I27 and W205 (see Figure 20a).

In the case of HDAC6, our docking pose solutions for Tubastatin A (**5**) closely paralleled the crystallized binding mode (PDB ID: 6THV) described in existing literature [170]. In this docking pose, Tubastatin A interacts with the zinc ion through monodentate coordination. The phenyl ring of the linker becomes embedded within the hydrophobic lysine pocket. Simultaneously, the hydrophobic tetrahydro-γ-carboline moiety of capping group is situated against the hydrophobic patch formed by F620, P501, H500, and L749 (see Figure 20b).

Upon investigating HDAC8, docking pose of Tubastatin A (**5)** in this isoform reveals a bidentate zinc coordination, although the hydrophobic capping group remains significantly solvent exposed at the surface of the binding pocket rim. This solvent exposure might contribute to the relatively weaker activity of compound **5** against HDAC8 isoform (see Figure 20c). Conversely, in HDAC1 isoform, the docking pose illustrated that compound **5** is not able to achieve proper chelation of the zinc ion, which explains decreased inhibition activity on this isoform (see Figure 20d).
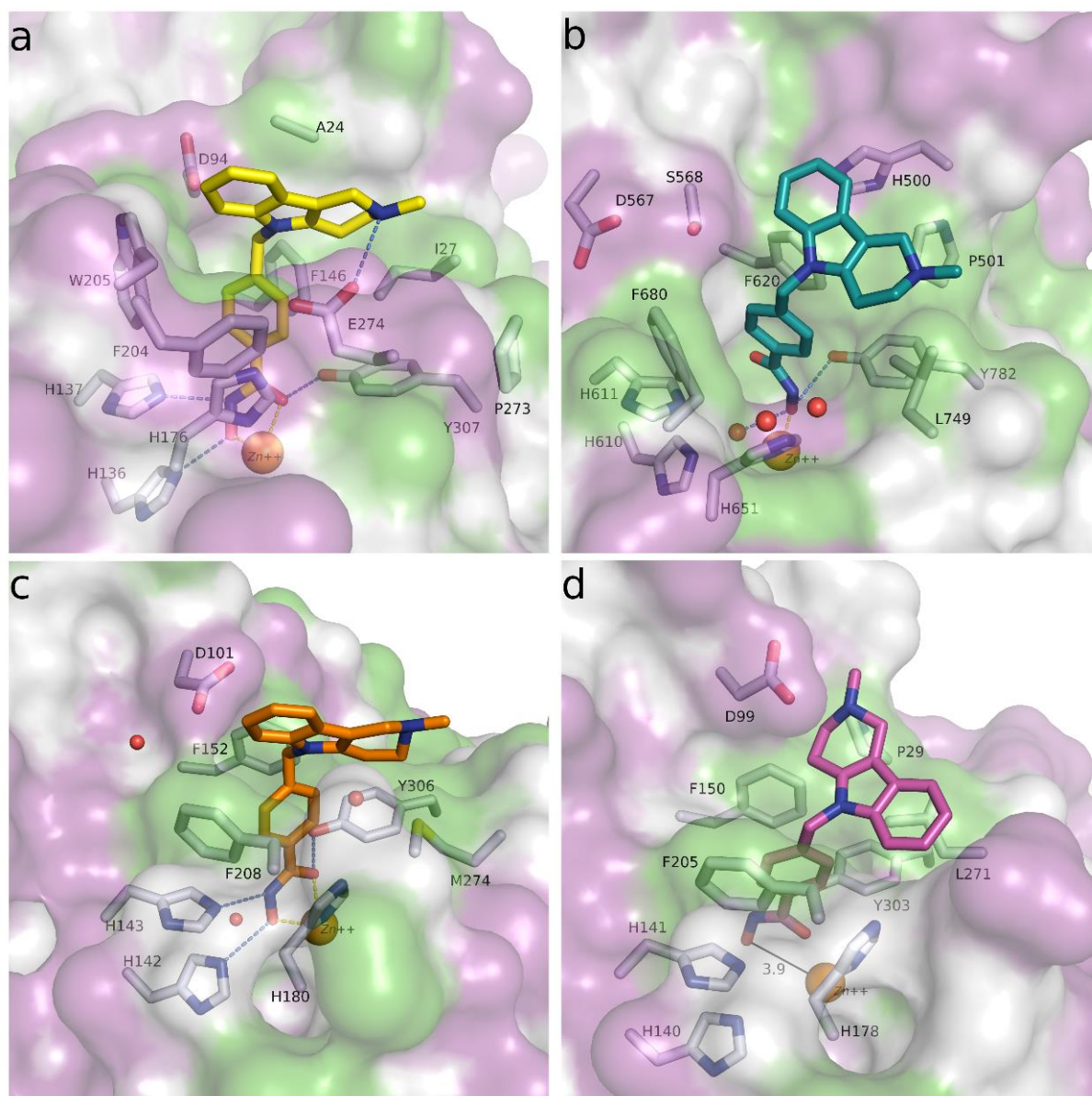
Figure 20: Predicted binding modes of Tubastatin A (**14**) in different HDAC isoforms: **a)** Tubastatin A (yellow sticks) in drHDAC10 (PDB ID 6UHU), **b)** Tubastatin A (teal sticks) in HDAC6 (PDB ID 5EDU), **c)** Tubastatin A (orange sticks) in HDAC8 (PDB ID 2V5X), **d)** Tubastatin A (magenta sticks) in HDAC1 (PDB ID 5ICN). The surface of the protein is colored according to lipophilicity; green for hydrophobic and magenta for hydrophilic. Side chains of binding site residues are shown as white sticks and the catalytic zinc ion as orange spheres. H-bonds and salt bridge interactions are depicted as blue-dashed lines and coordination of the zinc ion by the ligand as yellow-dashed lines. Distances are shown as black lines (reproduced from [169]).

Docking studies provided limited insight into the selectivity of certain previously reported inhibitors toward HDAC6 and HDAC10, such as compound **7** (BRD9757). As exemplified by BRD9757, the inhibitor appears to bind almost indistinguishably across all studied HDAC isoforms, engaging solely with residues that line the highly conserved lysine binding pocket (see Figure 21). Yet, it's important to mention that previous investigations have demonstrated that the selectivity of certain HDAC6 inhibitors is influenced by entropic factors, and the binding of the linker within the lysine pocket of HDAC6 might be influenced by desolvation [171, 172]. Also, it was shown that the interaction between BRD9757 and HDAC6 leads to an

increase in entropy, whereas in the case of HDAC8 binding, it results in a decrease [172]. Therefore, the compounds' selectivity for HDAC10 over HDAC1 and HDAC8 might also be guided by entropic mechanisms as for the other class IIb isoform HDAC6.
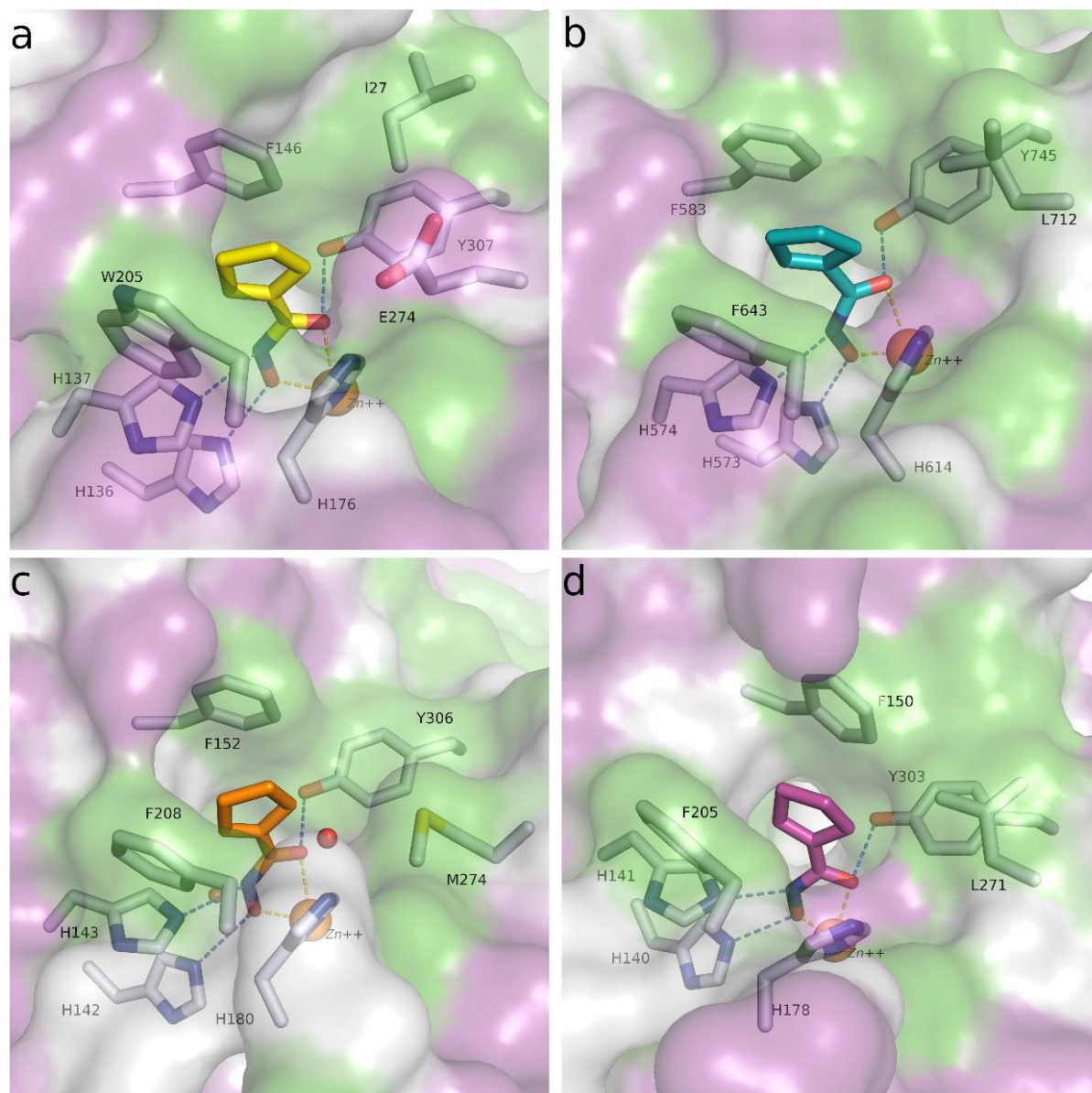
Figure 21: a) Predicted binding mode of BRD9757 (**7**) (yellow sticks) in drHDAC10, **b)** X-ray structure (PDB ID 6CSS) of drHDAC6 in complex with BRD9757 (**7**) (teal sticks), **c)** Predicted binding mode of **BRD9757** (orange sticks) in HDAC8, **d)** Predicted binding mode of BRD9757 (**7**) (magenta sticks) in HDAC1. The surface of the proteins is colored according to lipophilicity; green for hydrophobic and magenta for hydrophilic. Side chains of binding site residues are shown as white sticks and the catalytic zinc ion as orange spheres. H-bonds and salt bridge interactions are depicted as blue-dashed lines and coordination of the zinc ion by the ligand as yellow-dashed lines (reproduced from [169]).

Docking pose of the cinnamic acid-based derivative **23** (TB75) in drHDAC10 shows a bidentate coordination with the catalytic zinc ion and the three common hydrogen bond interactions with conserved two histidine and one tyrosine residues situated at the binding pocket's bottom. The naphthyl capping group becomes nestled within the lysine pocket, forming π-π stacking interactions with W205 and F146 (see Figure 22a). A similar binding mode is observed for TB75 in HDAC6 and HDAC8 isoforms (as seen in Figure 22b and Figure 22c, respectively).

50

In contrast, when considering HDAC1 isoform, where compound **23** only demonstrates weak inhibitory activity, our docking studies reveal that the ligand fails to adequately chelate the zinc ion (illustrated in Figure 22d).
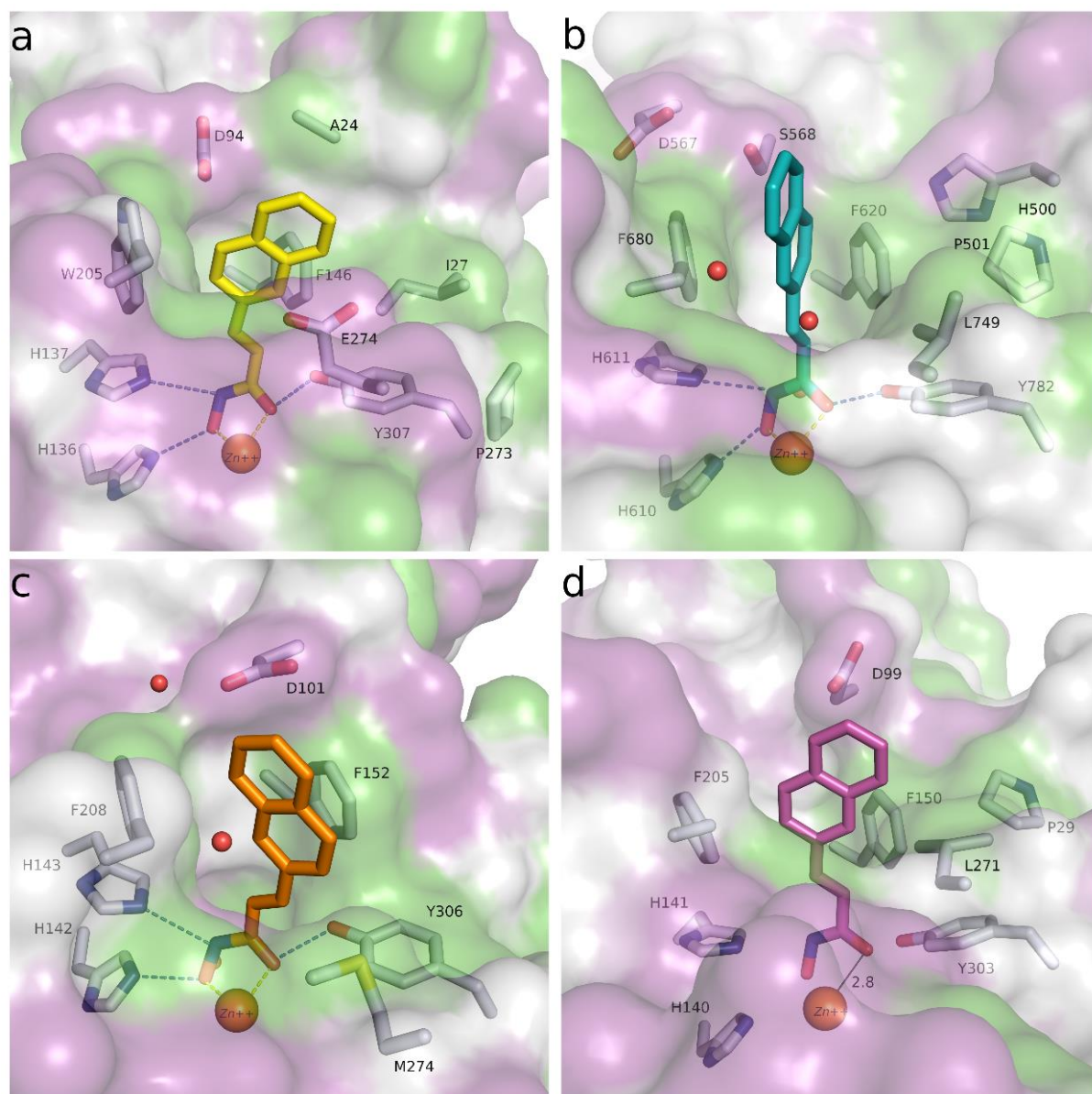
Figure 22: Predicted binding modes of TB75 (**37**) in different HDAC isoforms: **a)** TB75 (yellow sticks) in drHDAC10 (PDB ID 6UHU), **b)** TB75 (teal sticks) in HDAC6 (PDB ID 5EDU), **c)** TB75 (orange sticks) in HDAC8 (PDB ID 2V5X), **d)** TB75 (magenta sticks) in HDAC1 (PDB ID 5ICN). The surface of the proteins is colored according to lipophilicity; green for hydrophobic and magenta for hydrophilic. Side chains of binding site residues are shown as white sticks and the catalytic zinc ion as orange spheres. H-bonds and salt bridge interactions are depicted as blue-dashed lines and coordination of the zinc ion by the ligand as yellow-dashed lines. Distances are shown as black lines (reproduced from [169]).

This scenario mirrors the observations made during the docking of ligands **14** (TB8) and **15** (TB51) into the various HDAC isoforms, as shown in Figure 23. For both drHDAC10 and HDAC6, a bidentate coordination with the zinc ion is evident, and the chlorophenyl moiety finds a suitable placement within the hydrophobic lysine binding pocket (as shown in Figures 23a and 23b, respectively). Conversely, the substantial linker cannot be effectively integrated

into the lysine binding pocket of HDAC1 isoform, thus preventing proper chelation of the zinc ion (illustrated in Figure 23c).
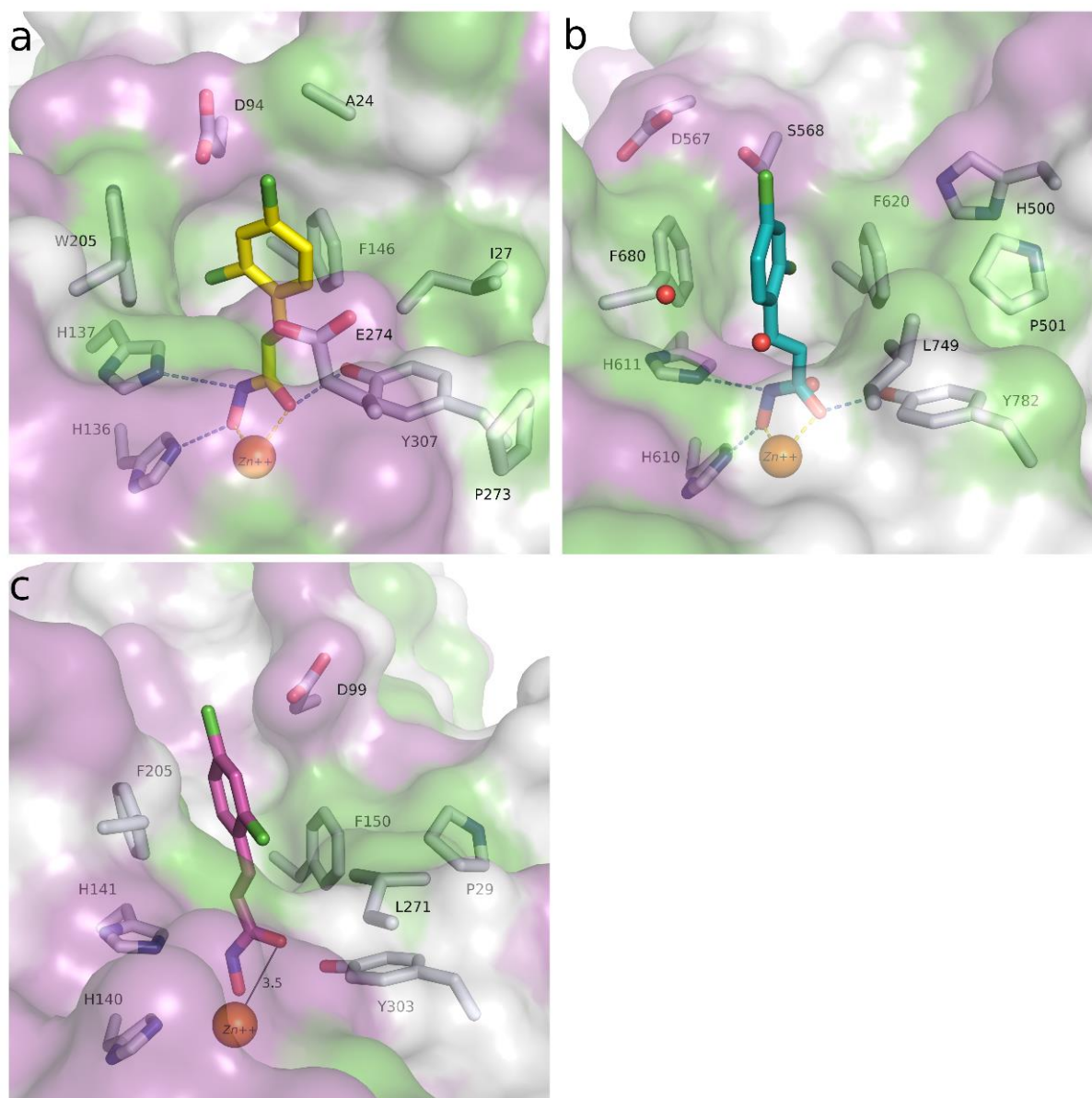
Figure 23: Predicted binding modes of TB51 (**15**) in different HDAC isoforms: **a)** TB51 (**15**) (yellow sticks) in drHDAC10 (PDB ID 6UHU), **b)** TB51 (**15**) (teal sticks) in HDAC6 (PDB ID 5EDU), **c)** TB51(**15**) (magenta sticks) in HDAC1 (PDB ID 5ICN). The surface of the proteins is colored according to lipophilicity; green for hydrophobic and magenta for hydrophilic. Side chains of binding site residues are shown as white sticks and the catalytic zinc ion as orange spheres. H-bonds and salt bridge interactions are depicted as blue-dashed lines and coordination of the zinc ion by the ligand as yellow-dashed lines. Distances are shown as black lines (reproduced from [169]).

Conversely, previously published selective HDAC8 inhibitors, namely m-substituted benzhydroxamate derivatives [157, 173, 174], demonstrated limited inhibitory activity against HDAC10. The docking studies unequivocally reveal that the m-substitution pattern isn't compatible with HDAC10 binding. These docking poses highlight clashes between the p-

substituents (-OCH$_3$ or -Cl) and W205/D94 residues in the HDAC10 binding tunnel (as indicated in Figure 24).

To recapitulate, the findings from the docking studies provide partial insights into the observed inhibitory activity and selectivity profiles of the investigated inhibitors. It's worth noting that alongside these findings, as mentioned earlier, entropic factors also play a significant role in the ligand-protein binding process. In the context of benzhydroxamate derivatives, the inclusion of bulky capping groups at the p-position is effectively accommodated within the binding pockets of both HDAC6 and HDAC10, typically resulting in selectivity against other HDAC subtypes. While the presence of a basic moiety in the capping group, facilitating salt bridge interactions with the gatekeeper E274, might not be a necessity for HDAC10 inhibition, but it could contribute to increased HDAC10 potency. Given the considerable homology between HDAC6 and -10, designing entirely selective HDAC10 inhibitors might be challenging, but instances from the oxazole series have successfully achieved selective inhibition of HDAC6 isoform over HDAC10 isoform.
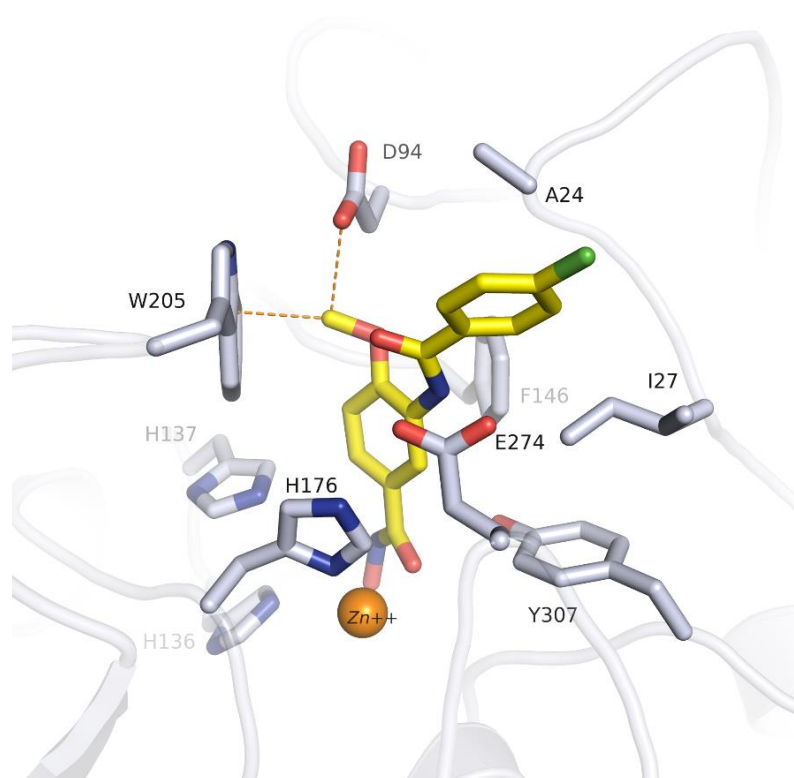
Figure 24: The obtained docking pose of the m-substituted benzhydroxamate TH68 (25) shows clashes with residues in the binding site (reproduced from [169]).

Cinnamic acid derivatives were found to be promising starting points for developing potential selective HDAC10 inhibitors. Bulky groups like o-chlorophenyl and naphthyl moieties can still be effectively accommodated within the lysine binding pocket and the entrance of the active

site cleft. However, these substantial groups are less suitable for binding with HDAC1 isoform, resulting in selectivity over this specific HDAC isoform. Further adaptations might offer potential avenues for creating more potent and selective HDAC10 inhibitors.
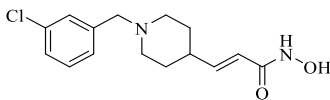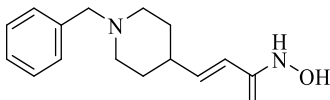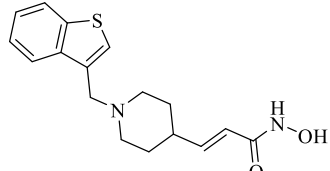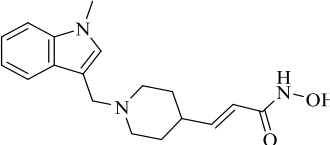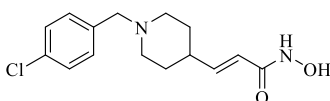
4.6. Design and Docking of Selective HDAC10 inhibitors

Based on the SAR data obtained from our studies with non-selective HDAC10 inhibitors, along with the analysis of the available crystal structures of HDAC10 and the results of docking studies, the initial series of piperidine-4-hydroxamates, *i.e.*, compounds **34-38** were designed as potential HDAC10-selective inhibitors (see Table 4).

Table 4: Enzymatic in vitro inhibition of studied compounds (**34-54**) (adapted from [153, 175]).

ID	Article ID	Structure	HDAC isoform inhibition % @ c [µM] or IC50 value (nM)			
			*dr*HDAC10	*h*HDAC6	*h*HDAC1	*h*HDAC8
			(NDA-Assay)	(ZMAL)	(ZMAL)	(FDL)
34	61a		13 % @ 0.1 20% @ 1 80% @ 10	n.d. % @ 0.1 < 10% @ 1 18 % @ 10	n.d. % @ 0.1 < 10% @ 1 < 10 % @ 10	n.d. % @ 0.1 27 % @ 1 56 % @ 10
35	61b		< 10% @ 0.1 15% @ 1 50% @ 10	n.d. % @ 0.1 21 % @ 1 46 % @ 10	n.d. % @ 0.1 < 10% @ 1 < 10 % @ 10	n.d. % @ 0.1 35 % @ 1 61 % @ 10
36	61c		< 10% @ 0.1 19% @ 1 68% @ 10	n.d. % @ 0.1 < 10 % @ 1 < 10 % @ 10	n.d. % @ 0.1 < 10 % @ 1 29 % @ 10	n.d. % @ 0.1 21 % @ 1 49 % @ 10
37	61d		< 10% @ 0.1 24% @ 1 69% @ 10	n.d. % @ 0.1 < 10 % @ 1 46 % @ 10	n.d. % @ 0.1 11 % @ 1 43 % @ 10	n.d. % @ 0.1 37 % @ 1 70 % @ 10
38	61e		< 10% @ 0.1 < 10% @ 1 27% @ 10	n.d. % @ 0.1 19 % @ 1 65 % @ 10	n.d. % @ 0.1 < 10% @ 1 < 10 % @ 10	n.d. % @ 0.1 42 % @ 1 75 % @ 10
39	61f		< 10% @ 0.1 40% @ 1 67% @ 10	n.d. % @ 0.1 < 10 % @ 1 18 % @ 10	n.d. % @ 0.1 < 10% @ 1 < 10 % @ 10	n.d. % @ 0.1 33 % @ 1 69 % @ 10
40	61g		< 10% @ 0.1 10% @ 1 61% @ 10	n.d. % @ 0.1 < 10 % @ 1 28 % @ 10	n.d. % @ 0.1 < 10% @ 1 < 10 % @ 10	n.d. % @ 0.1 27 % @ 1 70 % @ 10

#	Compound	Structure				
41	66a		64 ± 7	n.d. % @ 0.1 < 10 % @ 1 < 10 % @ 10	n.d. % @ 0.1 < 10 % @ 1 20 % @ 10	1973 ± 309
42	66b		37 ± 5	n.d. % @ 0.1 < 10 % @ 1 11 % @ 10	n.d. % @ 0.1 < 10 % @ 1 11 % @ 10	694 ± 52
43	4a (PZ033)		37 ± 10	210 ± 26	n.d. % @ 0.1 19 % @ 1 49 % @ 10	3500 ± 520
44	4b (PZ039)		106 ± 28	158 ± 21	n.d. % @ 0.1 15 % @ 1 68 % @ 10	3200 ± 410
45	4c (PZ040)		24 ± 5	177 ± 28	n.d. % @ 0.1 16 % @ 1 50 % @ 10	1900 ± 340
46	6b (PZ035)		43 ± 7	280 ± 25	n.d. % @ 0.1 6 % @ 1 54 % @ 10	2400 ± 210
47	10a (PZ046)		11 ± 1	4400 ± 400	16 ± 9 µM	250 ± 50
48	10b (PZ047)		29 ± 6	4800 ± 1100	n.d. % @ 0.1 7 % @ 1 54 % @ 10	420 ± 55
49	10c (PZ048)		20 ± 2	3700 ± 450	3.0 ± 0.2 µM	470 ± 70

50	10d (PZ050)		60 ± 5	n.d. % @ 0.1 / 40 % @ 1 / 83 % @ 10	n.d. % @ 0.1 / 24 % @ 1 / 67 % @ 10	2500 ± 260
51	10e (PZ051)		530 ± 100	n.d. % @ 0.1 / 34 % @ 1 / 89 % @ 10	n.d. % @ 0.1 / 12 % @ 1 / 62 % @ 10	n.d.
52	13a (PZ044)		62 ± 18	1400 ± 140	n.d. % @ 0.1 / 29 % @ 1 / 66 % @ 10	1300 ± 170
53	13b (PZ045)		58 ± 10	2420 ± 530	n.d. % @ 0.1 / 12 % @ 1 / 67 % @ 10	920 ± 170
54	13c (PZ049)		33 ± 3	430 ± 50	9 ± 1 µM	950 ± 260

Docking of the newly designed piperidine hydroxamate derivatives, as expected, showed that the compounds are able to form hydrogen bonds with the conserved two histidine and catalytic tyrosine residues while showing a bidentate coordination of the zinc ion. Additionally, the protonated tertiary amine in the linker undergoes electrostatic interactions with the negatively charged E274 (gatekeeper) and D94 at the opening of the lysine binding pocket. Furthermore, π-cation interactions were observed with the HDAC10-specific W205 residue through the positively charged nitrogen (see Figure 25a). Initially, strong HDAC10 inhibition effects were anticipated due to these binding poses; however, upon a more detailed analysis of the docking pose, it was determined that the positively charged nitrogen atom was located slightly in a lower position than the ideal location. This observation was based on the comparison with the newly reported, experimentally determined binding mode of N^8-acetylspermidine, which is the natural substrate of HDAC10. Since N^1-acetylspermidine shows no binding to HDAC10, it can be deduced that shifting the position of the protonated amine to a lower location would not be well tolerated. Indeed, the docking pose of the aforementioned hydroxamate derivatives show that the position of the protonated amine rather coincides with the expected position of the respective amine in the N^1-acetylspermidine than that of the N^8-analogue, which explains their observed weak HDAC10 inhibitory activity (see Figure 25b).

56
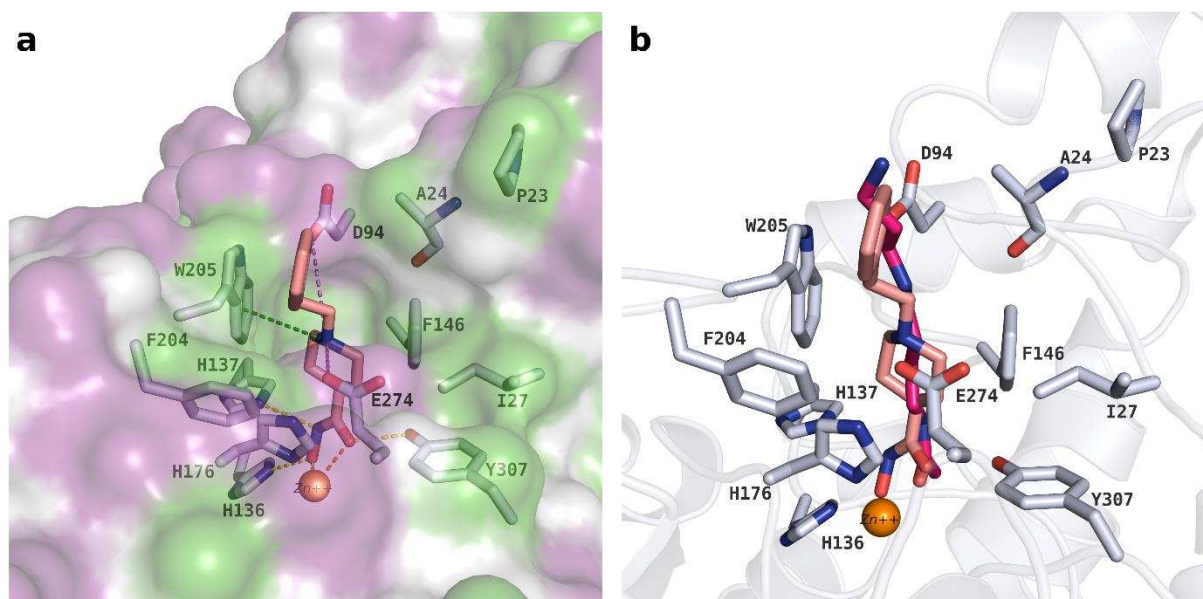
Figure 25: a) Predicted binding mode of **34** (61a) (salmon sticks) in drHDAC10 (PDB ID 6UHU) as a representative of piperidine hydroxamate derivatives **34-38**, **b)** Comparison of the predicted binding mode of compound **34** (salmon sticks) with the experimentally determined binding mode of the natural HDAC10 substrate N^8-acetylspermidine (hot pink sticks) taken from the respective crystal structure (PDB ID: 7KUQ), in which clearly seen how distant two positively charged nitrogen atoms. For the figure **a**, the surface of the proteins is colored according to lipophilicity; green for hydrophobic and magenta for hydrophilic. Binding site residues are shown as white sticks and the catalytic zinc ion as orange spheres. Hydrogen bonds interactions are depicted as yellow-dashed lines, salt bridge as magenta-dashed lines, cation-π interactions as green-dashed lines, and coordination of the zinc ion by the ligand as yellow dashed lines.

Based on the information obtained from docking studies and biological activity investigations of this initial group of piperidine hydroxamate compounds, three novel scaffolds were designed to ensure the optimal placement of the protonated nitrogen atom in the HDAC10 binding pocket. In first scaffold, a second nitrogen is introduced with an ethylene bridge as seen on compounds **41** (66a) and **42** (66b), while in the second scaffold (compounds **47-54**), an acryl moiety was placed between the piperidine ring and zinc-binder hydroxamate moiety. For the last scaffold (compounds **43-46**), the protonatable nitrogen atom and zinc-binder hydroxamate were connected through a benzyl linker (see table 4).

Docking studies were conducted for the two compounds present in the first scaffold to predict drHDAC10 and as well as the selectivity against other studied subtypes namely HDAC1, 6, and 8 (Figure 26a and Figure 27). The docking results of compounds **41** and **42** to the drHDAC10 crystal structure resembled the experimentally determined binding orientation of the HDAC10 substrate N^8-acetylspermidine, showing a similar binding orientation. Additionally, it was observed that the linker regions containing protonated basic amino acids overlapped (Figure 26b).
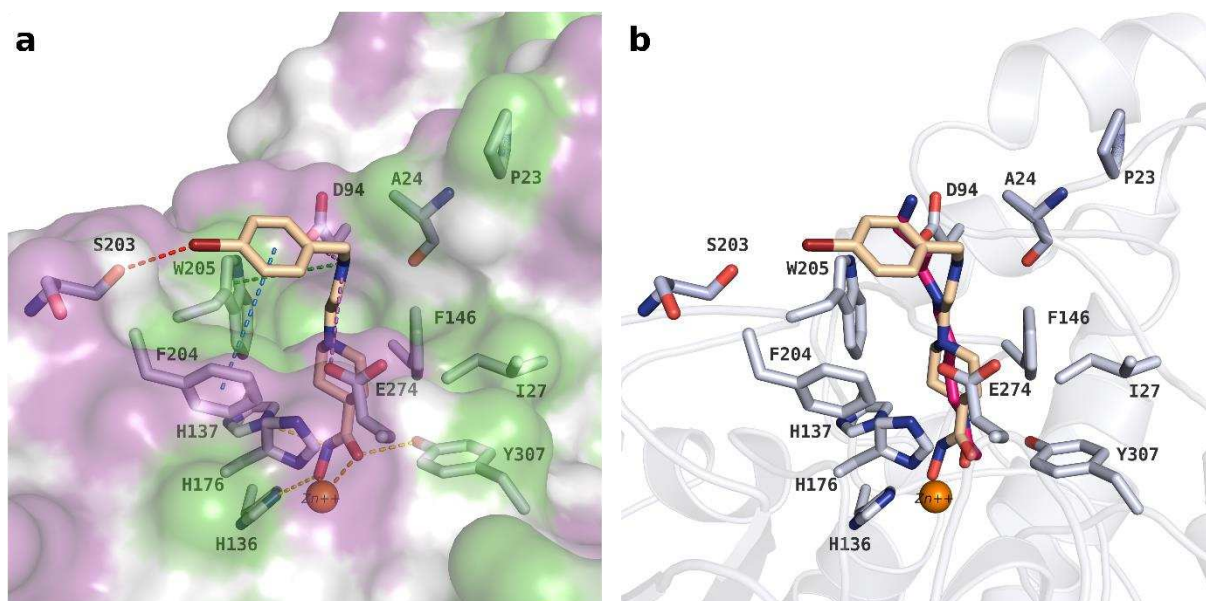
Figure 26: a) Predicted binding mode of compound **42** (wheat sticks) in drHDAC10 (PDB ID 6UHU), representing compounds **41-42**, **b)** Comparison of the predicted binding mode of compound **42** (wheat sticks) with the experimentally determined binding mode of the natural HDAC10 substrate N^8-acetylspermidine (hot pink sticks) from crystal structure PDB ID 7KUQ. The figure highlights the near positioning of the newly introduced nitrogen atom in compound **42** and the positively charged nitrogen atom of N^8-acetylspermidine. For the figure **a)**, the surface of the proteins is colored according to lipophilicity; green for hydrophobic and magenta for hydrophilic. Binding site residues are shown as white sticks and the catalytic zinc ion as orange spheres. Hydrogen bonds interactions are depicted as yellow-dashed lines, salt bridge as magenta-dashed lines, cation-π interactions as green-dashed lines, and coordination of the zinc ion by the ligand as yellow dashed lines.

The hydroxamate moiety present in compounds **41** and **42** chelated the catalytic zinc ion in a bidentate manner, forming typical hydrogen bond interactions with two histidine and tyrosine residues. Meanwhile, the capping group engaged in extensive interactions with amino acid residues situated at the edge of the binding pocket. The protonated amino group was placed in a position that is surrounded by D94, the gatekeeper residue E274, HDAC10 unique W205 and the backbone of the L1 A24, forming two salt bridge interactions and an additional π-cation interaction (Figure 26a). The phenyl group underwent π-π stacking interactions with F204, and in the case of compound **42**, the p-bromo substituent formed an additional halogen bond with the backbone of S203, which might elucidate the higher activity of **42** compared to **41**.

In the docking of HDAC6, (Figure 27a), compound **42** engaged in a bidentate chelation with the zinc ion, and the common hydrogen bond interactions with histidines and tyrosine. However, the capping and linker groups lacked prominent stabilizing interactions, except for a sole hydrogen bond with S568 involving the protonated amine. Particularly, the phenyl moiety in the capping group showed a high solvent exposure, while the linker moiety was also partially exposed to the solvent from the L1-facing side of the binding pocket, indicating limited participation in binding interactions at HDAC6 binding pocket.

58

In contrast, the docking of compound **42** into the crystal structure of HDAC1 generated docking pose (Figure 27b) characterized by a bidentate zinc ion chelation and three common hydrogen bonds with the conserved two histidine and tyrosine residues, facilitated by the hydroxamate moiety. The protonated amine in the linker part established a salt bridge interaction and cation-π interaction with D99 and F205, respectively. Notably, the phenyl group was situated within a hydrophilic sub-pocket, between D99 and N95, at the periphery of the HDAC1 binding site. This positional arrangement implies a possible non-preferred binding orientation. Given the narrower dimensions of HDAC1's acetyl lysine binding pocket, the interaction involving the bulky piperidine moiety might experience reduced favorability relative to its interactions with HDAC8 and HDAC10.

When the focus was shifted to HDAC8 (Figure 27c), a similar pattern of bidentate zinc ion chelation and typical hydrogen bonding with two histidine and tyrosine residues. Importantly, the linker group appeared to form a salt bridge interaction between the protonated amine and D101. Simultaneously, a π-π stacking interaction between the phenyl group and F152 and the hydrophobic capping group was placed into the hydrophobic HDAC8-specific side pocket. These factors may contribute to the notably higher inhibitory efficacy towards HDAC8 compared to HDAC6. In line with these observations, the biological results revealed that the compound exhibited varying degrees of inhibitory activity against HDAC6 and HDAC8. Specifically, at 10 µM, the compound inhibited HDAC6 by 11%, while for HDAC8, the IC_{50} value was determined to be 694 ± 52 nM.
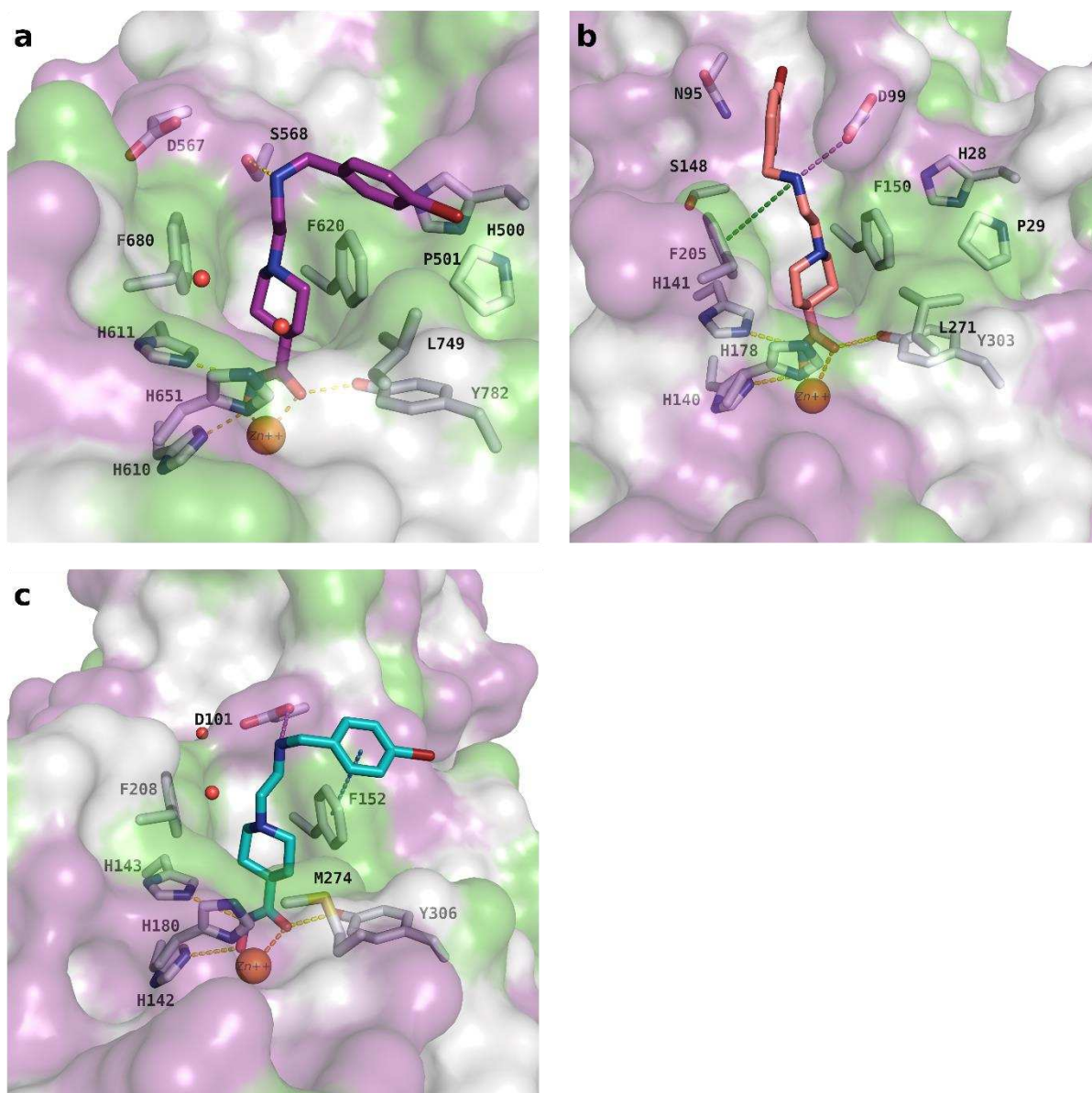
Figure 27: Predicted binding modes of compound **42** in different HDAC isoforms: **a) 42** (purple sticks) in HDAC6 (PDB ID 5EDU), **b) 42** (salmon sticks) in HDAC1 (PDB ID 5ICN), **c) 42** (teal sticks) in HDAC8 (PDB ID 2V5X). The surface of the proteins is colored according to lipophilicity; green for hydrophobic and magenta for hydrophilic. Side chains of binding site residues are shown as white sticks and the catalytic zinc ion as orange spheres. H-bonds and salt bridge interactions are depicted as blue-dashed lines and coordination of the zinc ion by the ligand as yellow-dashed lines. Distances are shown as black lines.

Docking studies conducted on the scaffold including the benzyl moiety (Figure 28a) within HDAC10 unveiled that the protonated nitrogen atom within the linker (represented by compound **45**) is nestled by the side chains of D94, W205, E274 and the main chain carbonyl group of A24 in L1. Compound **45** also shows common hydrogen bonds with conserved histidines and the catalytic tyrosine, along with bidentate zinc coordination. Moreover, the visualization underscores that the protonated nitrogen atom of the representative compound **45** is superimposed with the central nitrogen atom of the experimentally determined binding mode of N^8-acetylspermidine (Figure 28b).

60
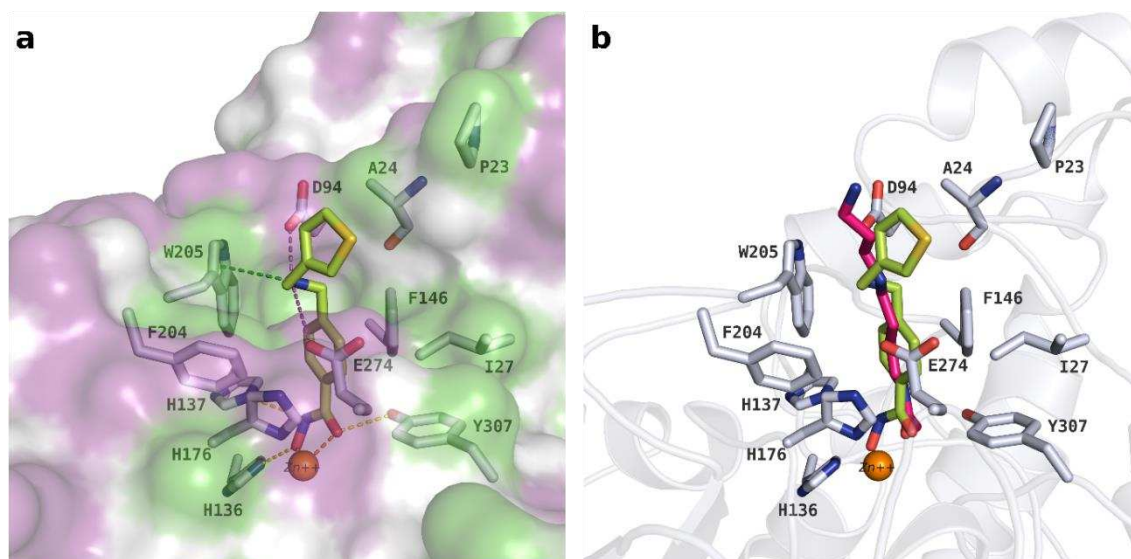
Figure 28: a) Predicted binding mode of compound **45** (lemon sticks) in drHDAC10 (PDB ID 6UHU), **b)** Comparison of the predicted binding mode of compound **45** (lemon sticks) with the experimentally determined binding mode of the natural HDAC10 substrate N^8-acetylspermidine (hot pink sticks) from crystal structure PDB ID 7KUQ. The figure highlights the near positioning of the protonated nitrogen atom in compound **45** and the positively charged nitrogen atom of N^8-acetylspermidine. For the figure **a)**, the surface of the proteins is colored according to lipophilicity; green for hydrophobic and magenta for hydrophilic. Binding site residues are shown as white sticks and the catalytic zinc ion as orange spheres. Hydrogen bonds interactions are depicted as yellow-dashed lines, salt bridge as magenta-dashed lines, cation-π interactions as green-dashed lines, and coordination of the zinc ion by the ligand as yellow dashed lines.

Examination of the docking results of compound **45** in HDAC6, HDAC1 and HDAC8 showed that the compound formed hydrogen bonds with conserved histidines and tyrosine while performing a bidentate zinc chelation over its zinc binder hydroxamate moiety (Figure 29).

In the docking results of compound **45** within HDAC6, along with the previously mentioned common interactions, noteworthy new interactions were evident. Specifically, formation of a unique hydrogen bond between the protonated amine and S568 was accompanied by a cation-π interaction with F608. Additionally, an extra binding characteristic, absent in the initial scaffold, emerged in the form of a π-π interaction between the phenyl moiety of the linker and F620. Moreover, a π-π interaction between the thiophene ring in the capping group and F620 was also observed, marking another distinct feature not present in the initial scaffold. The incorporation of the linker phenyl and the positional placement of the protonated nitrogen atom in the HDAC6 binding site contributed to the establishment of these additional interactions. These newly identified interactions are thought to underlie the potent inhibitory effects exhibited by the representative compound **45** and other analogs from this scaffold on HDAC6 (Figure 29a).

By analyzing the docking pose of compound **45** within the binding pocket of HDAC1 (Figure 29b), it is clear that, similar to compound **42** it engages in cation-π and salt bridge interactions

61

through the protonated nitrogen atom with F208 and D101, respectively. However, the hydrophobic capping group of **45** is positioned within a hydrophilic sub-pocket. This positioning, coupled with the apparent solvent exposure of the ligand, may indicate markedly sub-optimal binding. In light of all these observations, the attenuation of HDAC1 inhibition by **45** is not entirely surprising.

Lastly, inspection of the HDAC8 binding pose (Figure 29c) of compound **45** reveals a similar binding as in HDAC1 with cation-π and salt bridge interactions. The capping group showed heavy solvent exposure, which is postulated as the reason for the decrease in HDAC8 inhibition.
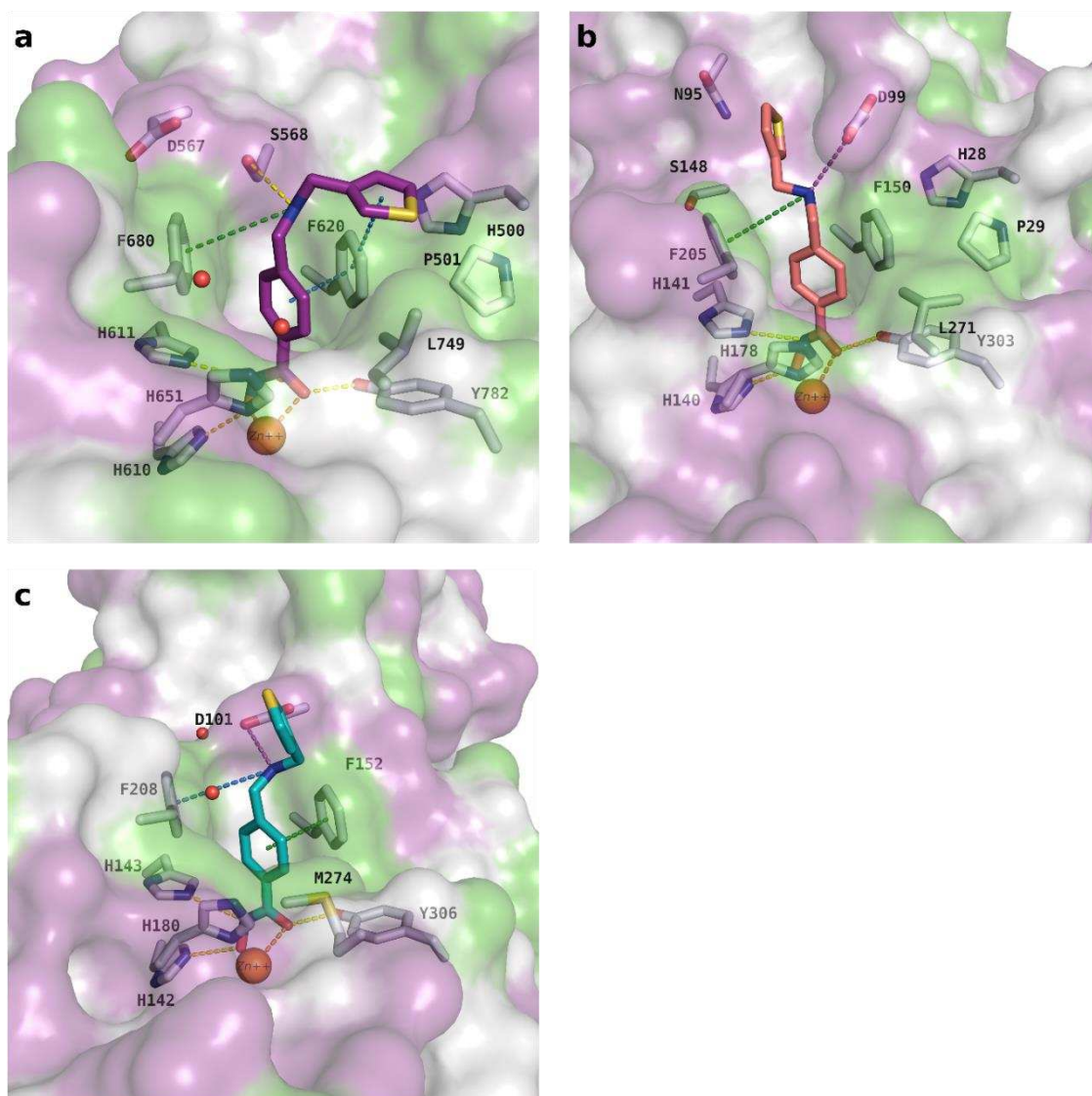
Figure 29: Predicted binding modes of compound **45** in different HDAC isoforms: **a) 45** (purple sticks) in HDAC6 (PDB ID 5EDU), **b) 45** (salmon sticks) in HDAC1 (PDB ID 5ICN), **c) 45** (teal sticks) in HDAC8 (PDB ID 2V5X). The surface of the proteins is colored according to lipophilicity; green for hydrophobic and magenta for hydrophilic. Side chains of binding site residues are shown as white sticks and the catalytic zinc ion as orange spheres. H-bonds and salt bridge interactions are depicted as blue-dashed lines and coordination of the zinc ion by the ligand as yellow-dashed lines. Distances are shown as black lines.

Docking pose of compound **47** (Figure 30a), as a representative of the last scaffold containing piperidine acryl hydroxamate, within the binding pockets of HDAC10 is examined, reveals that the protonated nitrogen is optimally positioned within the binding pocket. This positioning matches exactly the position of the central nitrogen atom in the experimentally determined binding pose of N^8-acetylspermidine (Figure 30b). The protonated nitrogen atom occupies a central position between two acidic amino acids, D94 and E274, forming two salt bridge interactions. In addition, one side of the compound is flanked by the HDAC10-specific residue W205, engaging in π-cation interactions, while the other side is flanked by the backbone carbonyl of A24.
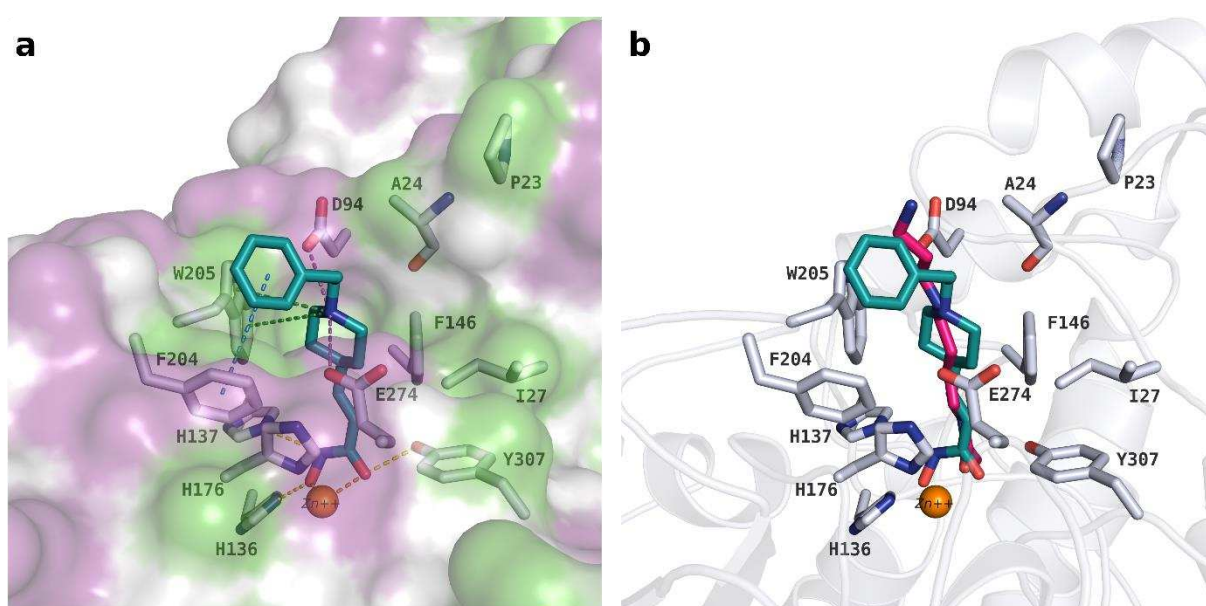
Figure 30: a) Predicted binding mode of compound **47** (teal sticks) in drHDAC10 (PDB ID 6UHU), **b)** Comparison of the predicted binding mode of compound **47** (teal sticks) with the experimentally determined binding mode of the natural HDAC10 substrate N^8-acetylspermidine (hot pink sticks) from crystal structure PDB ID 7KUQ. The figure reveals the superpositioning of the protonated nitrogen of piperidine structure in compound **47** and the positively charged nitrogen atom of N^8-acetylspermidine. For the figure **a)**, the surface of the proteins is colored according to lipophilicity; green for hydrophobic and magenta for hydrophilic. Binding site residues are shown as white sticks and the catalytic zinc ion as orange spheres. Hydrogen bonds interactions are depicted as yellow-dashed lines, salt bridge as magenta-dashed lines, cation-π interactions as green-dashed lines, and coordination of the zinc ion by the ligand as yellow dashed lines.

Evaluating the docking results of compound **47** in HDAC6, HDAC8 and HDAC1, it is clear that common interactions involving two histidine and one tyrosine residues are observed in all the studied isoforms (Figure 31). Notably, in HDAC6 the hydrogen bonding interaction observed with S568 in the previously discussed two scaffolds is absent with compound **47**. The capping group also shows high solvent exposure (Figure 31a). These observations highlight the factors contributing to the reduced HDAC6 inhibitory activity of **47** and compounds bearing the same scaffold, while also explaining the increased selectivity to HDAC10 over HDAC6.

Examination of the HDAC1 binding pose (Figure 31b) shows that the capping group is embedded a hydrophilic sub-pocket as observed with compounds **41** and **45**. This undesirable orientation and solvent exposure of the capping group can be considered as contributing factors to the reduced HDAC1 inhibition.

When the HDAC8 binding pose (Figure 31c) of compound **47** is examined, a striking similarity to the HDAC1 binding pose is observed. Once again, interactions with D101 and F208 are evident and the sensitivity of the structure to solvent exposure is prominently displayed. However, despite the similarities in the docking pose, an IC_{50} inhibition value of 250 nM was measured for HDAC8, which is considered to be inconsistent with the observed docking pose.
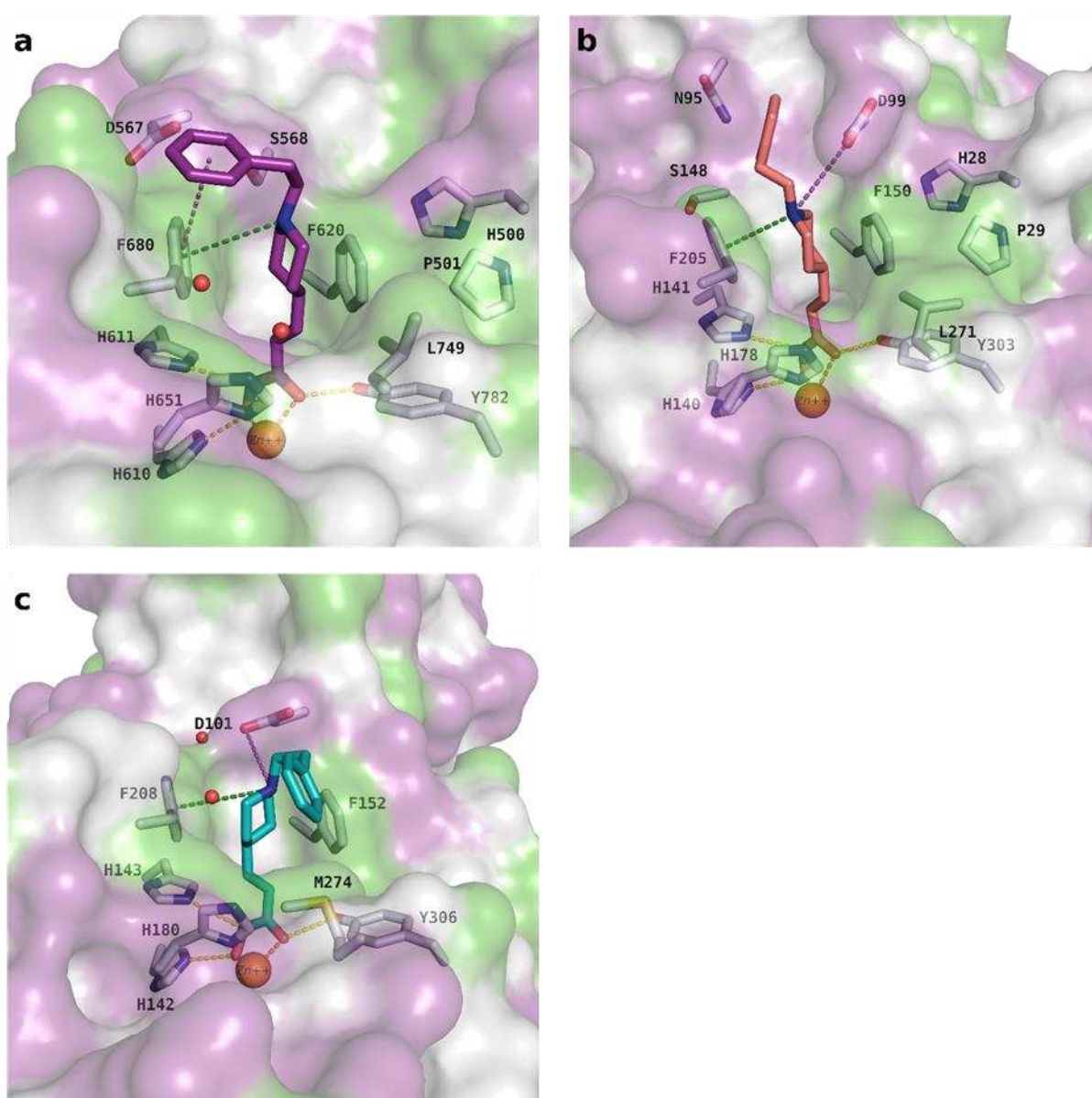
Figure 31: Predicted binding modes of compound **47** in different HDAC isoforms: **a)** **47** (purple sticks) in HDA6 (PDB ID 5EDU), **b)** **47** (salmon sticks) in HDAC1 (PDB ID 5ICN), **c)** **47** (teal sticks) in HDAC8 (PDB ID 2V5X). The surface of the proteins is colored according to lipophilicity; green for hydrophobic and magenta for hydrophilic. Side chains of binding site residues are shown as white sticks and the catalytic zinc ion as orange

spheres. H-bonds and salt bridge interactions are depicted as blue-dashed lines and coordination of the zinc ion by the ligand as yellow-dashed lines. Distances are shown as black lines.

For the purpose of confirming the HDAC10 docking studies, selected potent compounds were successfully crystallized within the binding site of humanized drHDAC10 by our collaborators (PDB IDs: 7U3M, 7U6A, 7U6B, 7U59, and 7U69) [176]. The obtained X-ray structures underscored the accuracy of our computational predictions and reinforces the reliability of the docking approach used in our study. As previously mentioned, there are two differences in the binding pockets of Zebrafish and humanized Zebrafish HDAC10, the later bearing A24E, D94A mutations. Despite these disparities, our docking studies using the Zebrafish crystal successfully predicted the binding poses. This success is a testament to the reliability of our docking methodologies.

Docking of compound, **46**, in the Zebrafish crystal structure (PDB ID: 6UHU) exhibited an RMSD value of 1.4 Å in comparison to its binding conformation in the humanized DrHDAC10 crystal structure (PDB ID: 7U3M) [176]. The docking pose predicted a bidentate zinc coordination, but interestingly, the crystal structure revealed that **46** coordinates the zinc ion in a monodentate manner. This finding is crucial as it highlights the complexity of predicting binding poses, where subtle differences can lead to distinct coordination types, and it is also important to underline that monodentate or bidentate zinc coordination can be difficult to predict through docking studies alone. Nonetheless, the low RMSD value, below 2.0 Å, indicates a significant match between the docking pose and the crystal pose in all aspects other than the ZBG group, which is a hydroxamate group in the compound (Figure 32a).

Upon comparing the experimentally determined binding conformations of compounds **45**, **48**, **41**, and **47** co-crystallized with the humanized drHDAC10 protein (labeled with PDB IDs: 7U6A, 7U6B, 7U59, and 7U69 respectively) [169, 176], with the binding poses derived from docking studies using the drHDAC10 crystal (PDB ID: 6UHU), the RMSD values were calculated to be 2.3 Å, 3.5 Å, 2.3 Å, and 2.6 Å, respectively (see Figure 32b, c, d, e). While these RMSD values are somewhat high, a closer examination of the docking poses and the co-crystallized structures reveals significant matches. For instance, as observed in Figure 31b for compound **45**, when excluding the highly solvent-exposed capping group, which contains an aromatic thiophene moiety, there is a notable degree of congruence between the hydroxamate zinc binder moiety and the benzylamine linker moiety. Excluding this solvent exposed part in the RMSD calculation yielded a much lower value of 0.7 Å. Furthermore, as observed in the

MD studies in following Section 4.7, this capping group exhibits fluctuations throughout the simulation.
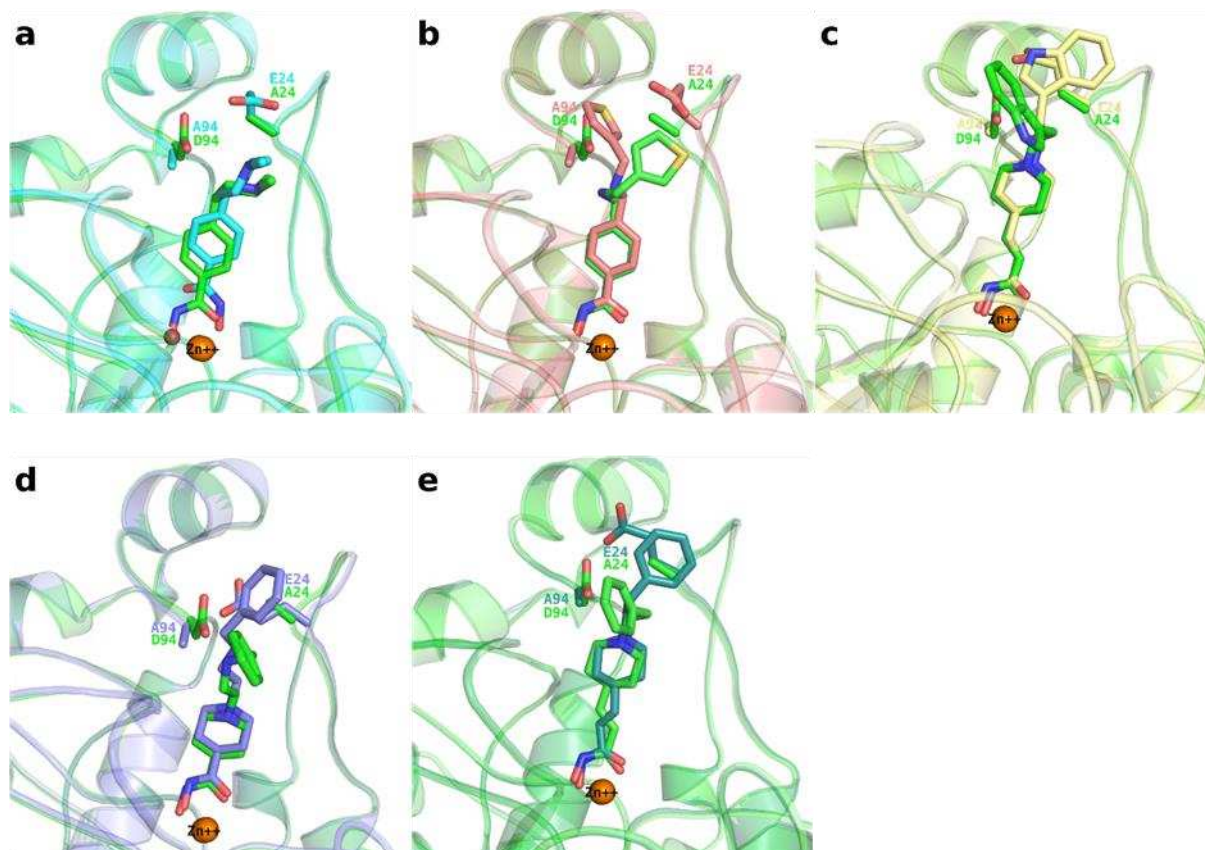
Figure 32: Comparison of the predicted docking poses and experimentally determined binding poses of compounds **46**, **45**, **48**, **41**, and **47** in humanized DrHDAC10 (PDB IDs: 7U3M, 7U6A, 7U6B, 7U59, and 7U69, respectively. The catalytic zinc ions are represented as orange spheres, while water molecules in the relevant binding pockets are shown as small red spheres. Docking solutions for each compound, as well as the DrHDAC10 protein used for docking (PDB ID: 6UHU), are represented as green sticks and cartoons. **a)** Binding pose of co-crystallized **46** and crystallized protein structures of humanized DrHDAC10 are represented as cyan sticks and cartoons. **b)** Binding pose of co-crystallized **45** and crystallized protein structures of humanized DrHDAC10 are represented as salmon sticks and cartoons. **c)** Binding pose of co-crystallized **48** and crystallized protein structures of humanized DrHDAC10 are represented as pale yellow sticks and cartoons. **d)** Binding pose of co-crystallized **41** and crystallized protein structures of humanized DrHDAC10 are represented as purple sticks and cartoons. **e)** Binding pose of co-crystallized **45** and crystallized protein structures of humanized DrHDAC10 are represented as teal sticks and cartoons.

The same scenario applies to other co-crystallized compounds. Additionally, the MD studies of compounds **41**, **47** and **48** in Section 4.8 indicate that the solvent-exposed capping groups are not stable throughout the simulation.

4.7. Validation of MD Protocols

To validate the molecular dynamics (MD) protocol used in our studies, we performed three independent 100 nanosecond MD simulations on humanized drHDAC10 crystal structures (PDB IDs: 7U6B, 7U69, 7U6A and 7U59) using non-identical seed for the velocities. The main purpose of these simulations was two-fold: firstly, to assess the stability of the protein, zinc ions and ligand molecules within the binding pocket and secondly, to verify the suitability of the settings used for these simulations.

Our analysis of the MD simulations revealed several important findings:

-Protein stability: Root-mean-square deviation (RMSD) plots for the used protein structures (Figure 33a, Figure 34a, Figure 35a and Figure 36a) showed that the protein backbone remained stable throughout the simulations, with RMSD values consistently below 1.5 Å.
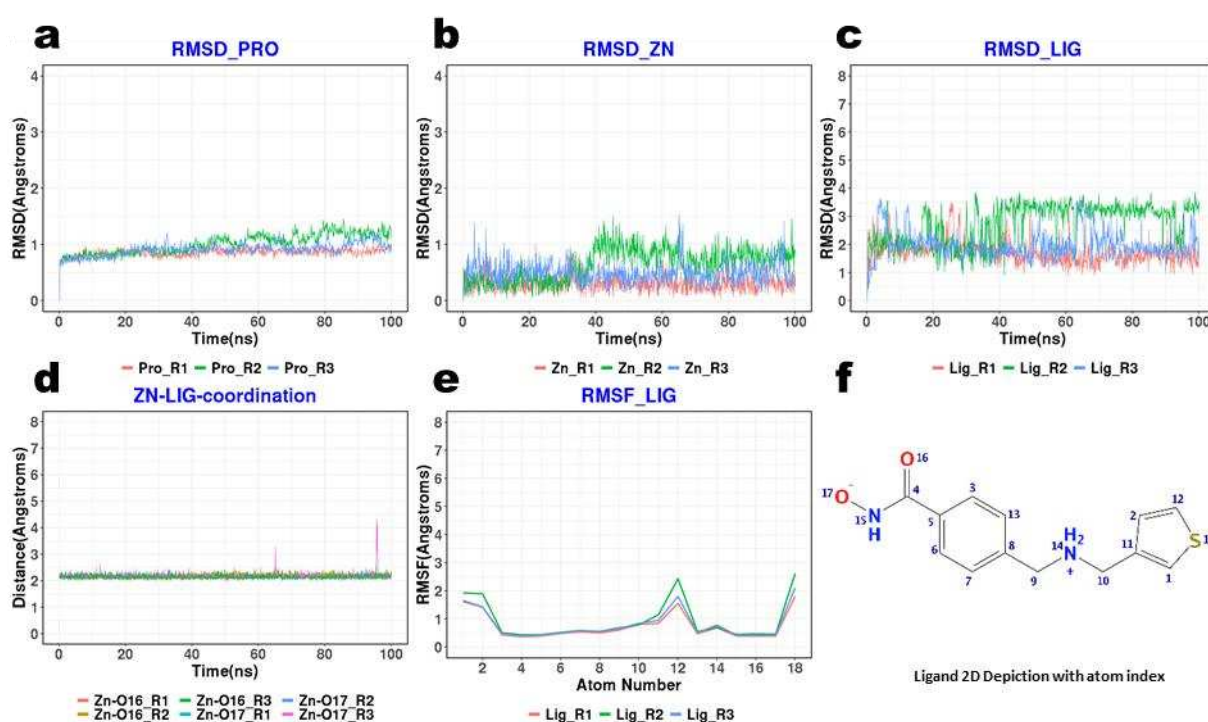
Figure 33: The compilation of data plots from molecular dynamics simulations of the humanized drHDAC10 enzyme complex with the cocrystallized ligand compound **45** (PDB ID 7U6A); **a)** Illustrates RMSD trajectories for the protein's heavy atoms over three replicates of 100 ns simulations. **b)** Illustrates RMSD trajectories for the Zn ion from three 100 ns simulations. **c)** Illustrates RMSD trajectories for the ligand's heavy atoms across three 100 ns simulations. **d)** Illustrates distance tracking between the Zn ion and the oxygen atoms of the ligand's zinc-binding group over three 100 ns simulations. **e)** Illustrates RMSF data for the ligand's heavy atoms from three 100 ns simulations. **f)** Provides a 2D chemical structure of compound **45** with indexed atoms, related to the RMSF plot.

-Zinc ion stability: Similarly, RMSD plots for zinc ions (Figure 33b, Figure 34b, Figure 35b and Figure 36b) revealed that zinc ions exhibited low RMSD values indicating their stability within the binding site.

-Ligand stability: In contrast, the crystallized ligand molecules exhibited higher fluctuations in RMSD plots (Figure 33c, Figure 34c, Figure 35c, and Figure 36c). This behavior was primarily attributed to the flexible capping groups, such as thiophene, indole, and phenyl moieties. As shown in the root-mean-square fluctuation (RMSF) plots (Figure 33e-f, Figure 34e-f, Figure 35e-f, and Figure 36e-f), the RMSF values of the capping groups exceeded 1.0 Å, whereas most other atoms exhibited significantly lower RMSF values. Furthermore, the distances between the hydroxamate group responsible for bidentate zinc coordination in each ligand and zinc ion, shown to be stable throughout the simulations, remained consistent and below 2.5 Å. This was clearly demonstrated by the ZN-LIG coordination plots (Figure 33d, Figure 34d, Figure 35d and Figure 36d), highlighting the stability of the zinc-binding hydroxamates.
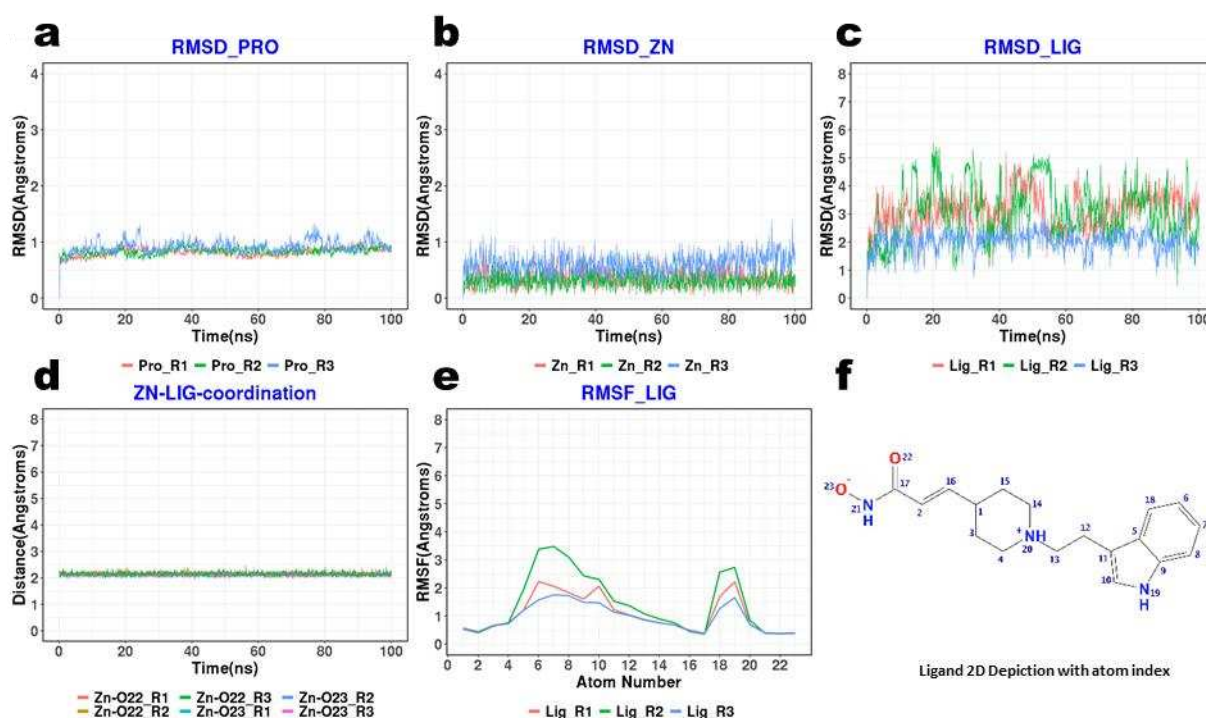
Figure 34: The compilation of data plots from molecular dynamics simulations of the humanized drHDAC10 enzyme complex with the cocrystallized ligand compound **48** (PDB ID 7U6B); **a)** Illustrates RMSD trajectories for the protein's heavy atoms over three replicates of 100 ns simulations. **b)** Illustrates RMSD trajectories for the Zn ion from three 100 ns simulations. **c)** Illustrates RMSD trajectories for the ligand's heavy atoms across three 100 ns simulations. **d)** Illustrates distance tracking between the Zn ion and the oxygen atoms of the ligand's zinc-binding group over three 100 ns simulations. **e)** Illustrates RMSF data for the ligand's heavy atoms from three 100 ns simulations. **f)** Provides a 2D chemical structure of compound **48** with indexed atoms, related to the RMSF plot.
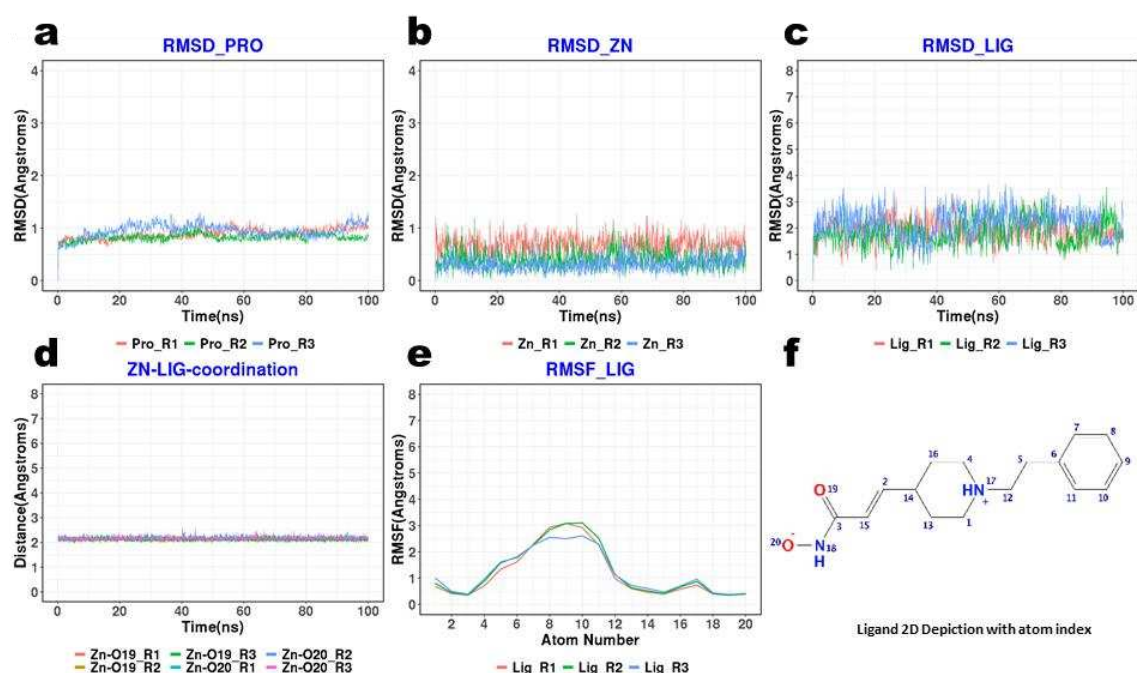
Figure 35: The compilation of data plots from molecular dynamics simulations of the humanized drHDAC10 enzyme complex with the cocrystallized ligand compound **47** (PDB ID 7U69); **a)** Illustrates RMSD trajectories for the protein's heavy atoms over three replicates of 100 ns simulations. **b)** Illustrates RMSD trajectories for the Zn ion from three 100 ns simulations. **c)** Illustrates RMSD trajectories for the ligand's heavy atoms across three 100 ns simulations. **d)** Illustrates distance tracking between the Zn ion and the oxygen atoms of the ligand's zinc-binding group over three 100 ns simulations. **e)** Illustrates RMSF data for the ligand's heavy atoms from three 100 ns simulations. **f)** Provides a 2D chemical structure of compound **47** with indexed atoms, related to the RMSF plot.
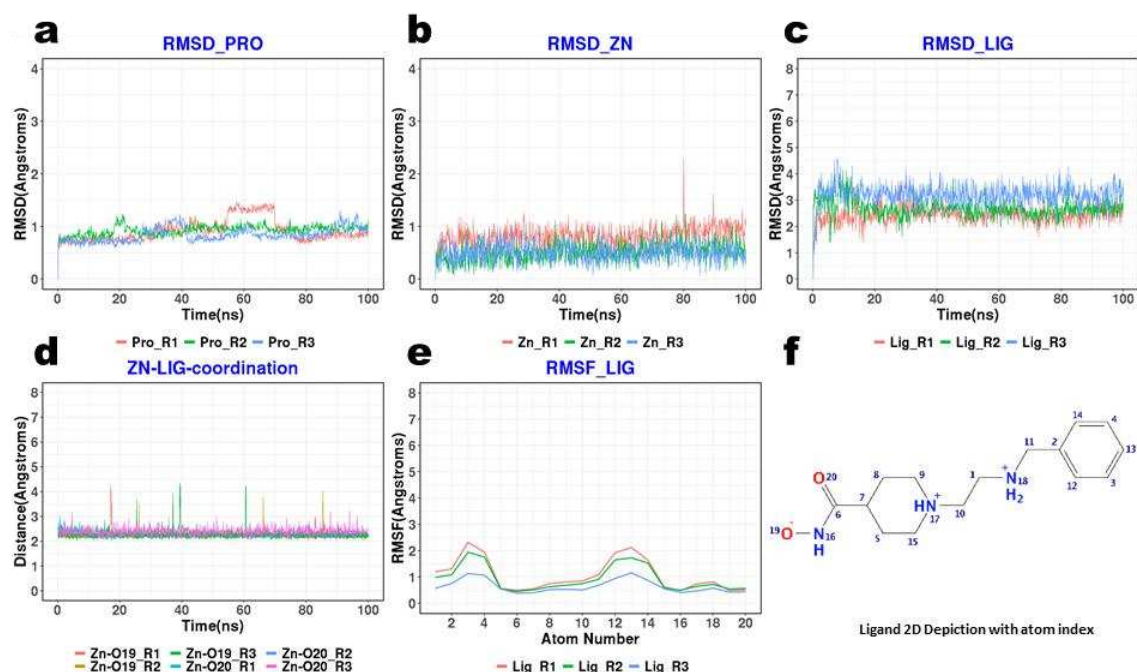
Figure 36: The compilation of data plots from molecular dynamics simulations of the humanized drHDAC10 enzyme complex with the cocrystallized ligand compound **41** (PDB ID 7U59); **a)** Illustrates RMSD trajectories for the protein's heavy atoms over three replicates of 100 ns simulations. **b)** Illustrates RMSD trajectories for the Zn ion from three 100 ns simulations. **c)** Illustrates RMSD trajectories for the ligand's heavy atoms across three 100 ns simulations. **d)** Illustrates distance tracking between the Zn ion and the oxygen atoms of the ligand's zinc-binding group over three 100 ns simulations. **e)** Illustrates RMSF data for the ligand's heavy atoms from three 100 ns simulations. **f)** Provides a 2D chemical structure of compound 41 with indexed atoms, related to the RMSF plot.

69

As a result, the findings are consistent and mutually reinforcing, providing a comprehensive analysis of protein structure stability, zinc atom coordination, and ligand dynamics for each crystal structure.

These results confirm the validity of the used MD protocols and demonstrate their reproducibility. Furthermore, the information obtained from these simulations will be invaluable in our ongoing research, especially in the context of studying complexes obtained through docking experiments.

4.8. BFE Calculation of The Synthesized HDAC10 Inhibitors

BFE calculations were carried out using six distinct parameter configurations and four varied frame settings, as outlined in Section 3.1.4. As an outcome, 24 models were devised. The correlation was assessed by juxtaposing the experimentally determined biological data (pIC_{50}) with the predicted binding free energy values (ΔG) see Figure 37). Regression models were formulated only using compounds with determined HDAC10-IC_{50} values except compounds: **4**, **41**, **42** and **46**, encompassing 20 compounds out of 54 compounds listed in the two tables (table 3 and 4) in previous "4.4." and "4.5." sections. Compounds **41**, **42**, and **46** each carry two nitrogen atoms in positions close to each other. However, at physiological pH, it's challenging to predict which of these two nitrogen atoms will be protonated. Due to this uncertainty in protonation behavior, these compounds were excluded from the studies. On the other hand, compound **4** was removed from the data set because its structure differs significantly from the other compounds under study. This decision was made because its unique structure could potentially affect the performance of the model.

In the assessment of the models, R-squared (R^2) values were utilized as a key metric for evaluation. Models with an R^2 value below 0.4 were excluded from further consideration in the development process. Within this framework, only two models for HDAC10 surpassed this 0.4 benchmark.

(n=20)	Method	R^2	RMSE
Model 0	Glide Docking Score	0.1540	0.4016

(n=20)	Method	R^2	RMSE
Model 1	ΔG_GB1_min1	0.3887	0.3414
Model 2	ΔG_GB1_min2	0.4053	0.3367
Model 3	ΔG_GB1_md1ns	0.3001	0.3653
Model 4	ΔG_GB1_min3	0.2438	0.3797

(n=20)	Method	R^2	RMSE
Model 5	ΔG_GB2_min1	0.3241	0.3590
Model 6	ΔG_GB2_min2	0.4064	0.3364
Model 7	ΔG_GB2_md1ns	0.2824	0.3699
Model 8	ΔG_GB2_min3	0.2015	0.3902

(n=20)	Method	R^2	RMSE
Model 9	ΔG_GB5_min1	0.2874	0.3687
Model 10	ΔG_GB5_min2	0.3832	0.3430
Model 11	ΔG_GB5_md1ns	0.2798	0.3706
Model 12	ΔG_GB5_min3	0.2073	0.3888

(n=20)	Method	R^2	RMSE
Model 13	ΔG_GB8_min1	0.0468	0.4263
Model 14	ΔG_GB8_min2	0.0645	0.4224
Model 15	ΔG_GB8_md1ns	0.0476	0.4262
Model 16	ΔG_GB8_min3	0.0851	0.4177

(n=20)	Method	R^2	RMSE
Model 17	ΔG_PB_b_min1	0.2532	0.3774
Model 18	ΔG_PB_b_min2	0.1661	0.3988
Model 19	ΔG_PB_b_md1ns	0.2132	0.3873
Model 20	ΔG_PB_b_min3	0.1701	0.3978

(n=20)	Method	R^2	RMSE
Model 21	ΔG_PB_P_min1	0.2525	0.3775
Model 22	ΔG_PB_P_min2	0.1484	0.4030
Model 23	ΔG_PB_P_md1ns	0.1139	0.4111
Model 24	ΔG_PB_P_min3	0.1151	0:4108

Figure 37: Comparison of regression models predicting HDAC10 inhibitor activity using binding free energy values (ΔG). Models were evaluated by R^2 and RMSE, using 20 compounds with experimentally determined IC_{50} values, excluding compounds **4, 41, 42** and **46** dues to protonation uncertainty and structural differences.

After the initial evaluation, cross-validation procedures were employed, specifically adopting the leave-one-out methodology. This rigorous approach was instrumental in refining the selection of models, based on a comprehensive consideration of various metrics including R^2, RMSE (root mean square error), XR²LOO (leave-one-out cross-validation), and XRMSE (cross-validated root mean square error). This multifaceted evaluation strategy ensured a robust selection of models, prioritizing those with higher predictive accuracy and reliability. In the analysis of Model 2 (as depicted in Figure 38 A and table 5), one compound was identified as outlier based on its Z-scores, specifically compound **51** (highligtehd as red dash in Figure 38 A), recording a Z-score exceeding 2. The removal of that compound facilitated the creation of Model 25 (as depicted in Figure 38 B and table 5), which demonstrated notable improvements across several key metrics, including R^2, RMSE, XR^2_{LOO} and XRMSE in comparison to Model 2. The Z-score is a statistical measure that quantifies the deviation of the experimentally observed values from those predicted by the model, normalized by the square root of the mean square error of the dataset. In this study, Z-scores were computed for each molecule utilizing the QSAR module in MOE, with any molecule exhibiting a Z-score greater than 2.00 classified as an outlier.

Beyond the statistical identification of outliers based on Z-scores, a more in-depth examination was conducted on compound **51**. This analysis included a scrutiny of its structural

characteristics and IC_{50} value, compared with other compounds in the dataset that share the same scaffold, specifically compounds **47**, **50**, and **54**. For compound **47**, a key distinction from compound **51** is noted: the presence of an ethyl bridge linking the phenyl aromatic structure to the piperidine ring, while compound **51** features a methyl bridge. Compounds **50** and **54**, both derivatives of compound **51**, are characterized by chloro substitutions at the meta and para positions of the phenyl ring, respectively. The IC_{50} values for these three compounds were measured at 11 nM, 60 nM, and 33 nM, respectively. However, the IC_{50} value of compound **51** was measured at 530 nM. Upon this comparative analysis, it was observed that the substantial deviation in the IC_{50} value of compound **51** did not correspond to significant chemical distinctions, thereby confirming its classification as an outlier.

For Model 25, compared to Model 2, an increase in the R-squared value from 0.41 to 0.65 was observed, along with a rise in the cross-validated R-squared value from 0.30 to 0.56. Furthermore, there was a noticeable improvement in the RMSE values, which decreased from 0.34 to 0.24 (for R^2) and from 0.37 to 0.26 (for XR^2). The further internal validation of Model 25 was carried out in the R programming environment, utilizing a range of statistical methods that included Q^2LOOCV (square leave-one-out cross-validation), leave-three-out cross-validation (L3OCV), and threefold cross-validation (3Fold CV). The obtained Q^2 values from these methods were 0.60, 0.60, and 0.59, respectively. Additionally, the RMSE values corresponding to these cross-validation methods were 0.27 for Q^2LOOCV, 0.26 for L3OCV, and 0.27 for 3Fold CV. These results underscore the robustness of Model 25 in terms of both its predictive accuracy (Q^2) and the consistency of its error estimates (RMSE) across different validation methodologies. The table below provides a detailed comparison between Model 2 and Model 25:

Table 5: Comparative performance metrics of Model 2 and Model 25 for HDAC10 binding predictions. The table highlights key evaluation parameters, including R^2, RMSE, XR^2LOO, and XRMSE. Model 25, refined by the removal of outlier compound **51**, demonstrates significant improvements over Model 2, with higher R^2 (0.6469 vs. 0.4053) and cross-validated R^2 (0.5633 vs. 0.2995), as well as lower RMSE values, indicating enhanced predictive accuracy and reliability. lm: linear model, LOOCV: Leave-one out cross validation, Leave_3out CV: Leave-3-out cross validation, 3fold CV: 3fold cross validation. Cross-validation methods (Q^2LOOCV, L3OCV, and 3Fold CV) further validate the robustness of Model 25.

		Moe								100runs		100runs	
Model	Method	Lm		LOOCV		LOOCV		L3OCV		3Fold CV		Outlier	
		R^2	RMSE	XR^2	RMSE	Q^2	RMSE	Q^2	RMSE	Q^2	RMSE		Z Score
Model 2	ΔG_GB1_min2 (n=20)	0.4053	0.3367	0.2995	0.3681							51	3.1507
Model 25	ΔG_GB1_min2 (n=19)	0.6469	0.2358	0.5633	0.2636	0.6041	0.2708	0.6015	0.2648	0.5875	0.2725		

This table succinctly presents the comparison, highlighting the improvements in Model 25 over Model 2 in terms of R-squared, RMSE, cross-validated R-squared, and Q-squared values.
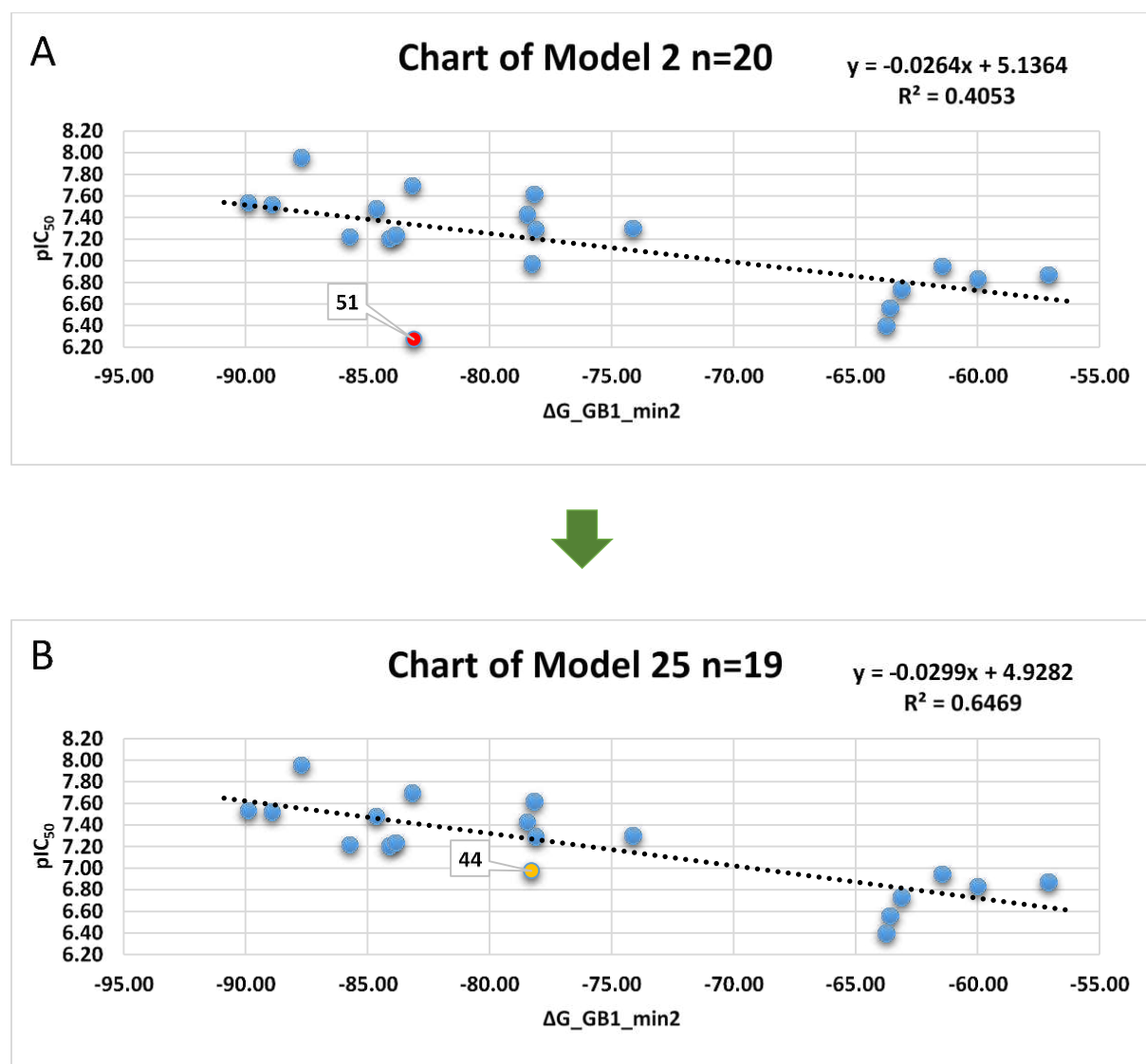
Figure 38: Model refinement process for HDAC10 binding predictions. (**A**) The correlation plots of the model of Model 2, where compound **51** (red filled circle) is identified as an outlier based on its Z-score (> 2). (**B**) The correlation plots of the model of Model 25 after the removal of compound 51, showing improved fit across key metric R^2, and compound **44** is highlighted with yellow filled circle.

The study progressed with a second level of comparison, this time between Model 6 and 26, following the initial analysis that compared Models 2 and 25. This subsequent comparison proved to be quite revealing, as it was built upon the insights gained from the earlier evaluation, thus offering a more in-depth understanding of how the models performed.

Regarding Model 6, as illustrated in Figure 39, compound **51** (highlighted as red dash in Figure 39 A) was flagged as an outlier, having a Z-score of 3.1916 as in the Model2. Model 6 exhibited an R-squared value of 0.41 with an RMSE of 0.34, and a cross-validated R-squared value (XR^2) of 0.30, with an associated RMSE of 0.37.

In response to these findings, Model 26 was formulated, with a specific focus on excluding the outlier. This new model showed marked improvements over Model 6 in several critical areas. Its R-squared value increased significantly from 0.41 to 0.66, and the RMSE decreased from 0.34 to 0.23. Additionally, the cross-validated R-squared value enhanced from 0.30 to 0.57, accompanied by a decrease in RMSE (for XR^2) from 0.37 to 0.26.

To further validate Model 26 internally, various statistical techniques were utilized within the R programming framework. These included Q²LOOCV (square leave-one-out cross-validation), L3OCV (leave-three-out cross-validation), and 3Fold CV (threefold cross-validation). The Q² values achieved were 0.61, 0.61, and 0.60, respectively, with corresponding RMSE values of 0.27 for Q²LOOCV, 0.26 for L3OCV, and 0.27 for 3Fold CV. These results emphasized the reliability and predictive precision of Model 26, as demonstrated through various validation methods.

The following table provides a detailed juxtaposition of Models 6 and 26, spotlighting the substantial advancements made in Model 26 compared to Model 6 in terms of R-squared, RMSE, cross-validated R-squared, and Q-squared values.

Table 6: Comparative performance metrics of Model 6 and Model 26 for HDAC10 binding predictions. The table highlights key evaluation parameters, including R², RMSE, XR²LOO, and XRMSE. Model 26, refined by the removal of outlier compound **51**, demonstrates significant improvements over Model 6, with higher R² (0.6594 vs. 0.4064) and cross-validated R² (0.5722 vs. 0.2953), as well as lower RMSE values, indicating enhanced predictive accuracy and reliability. lm: linear model, LOOCV: Leave-one out cross-validation, Leave_3out CV: Leave-3-out cross-validation, 3Fold CV: 3fold cross-validation. Cross-validation methods (Q²LOOCV, L3OCV, and 3Fold CV) further validate the robustness of Model 26.

| | | Moe | | | | 100runs | | 100runs | | | | | |
| | | Lm | | LOOCV | | LOOCV | | L3OCV | | 3Fold CV | | Outlier | |
Model	Method	R²	RMSE	XR²	RMSE	Q²	RMSE	Q²	RMSE	Q²	RMSE		Z Score
Model 6	ΔG_GB2_min2 (n=20)	0.4064	0.3364	0.2953	0.3695							51	3.1916
Model 26	ΔG_GB2_min2 (n=19)	0.6594	0.2316	0.5722	0.2612	0.6114	0.2683	0.6092	0.2622	0.5972	0.2693		

This detailed comparison not only illustrates the enhancements in Model 26 but also reinforces the importance of outlier identification and model refinement in the development of robust predictive models.
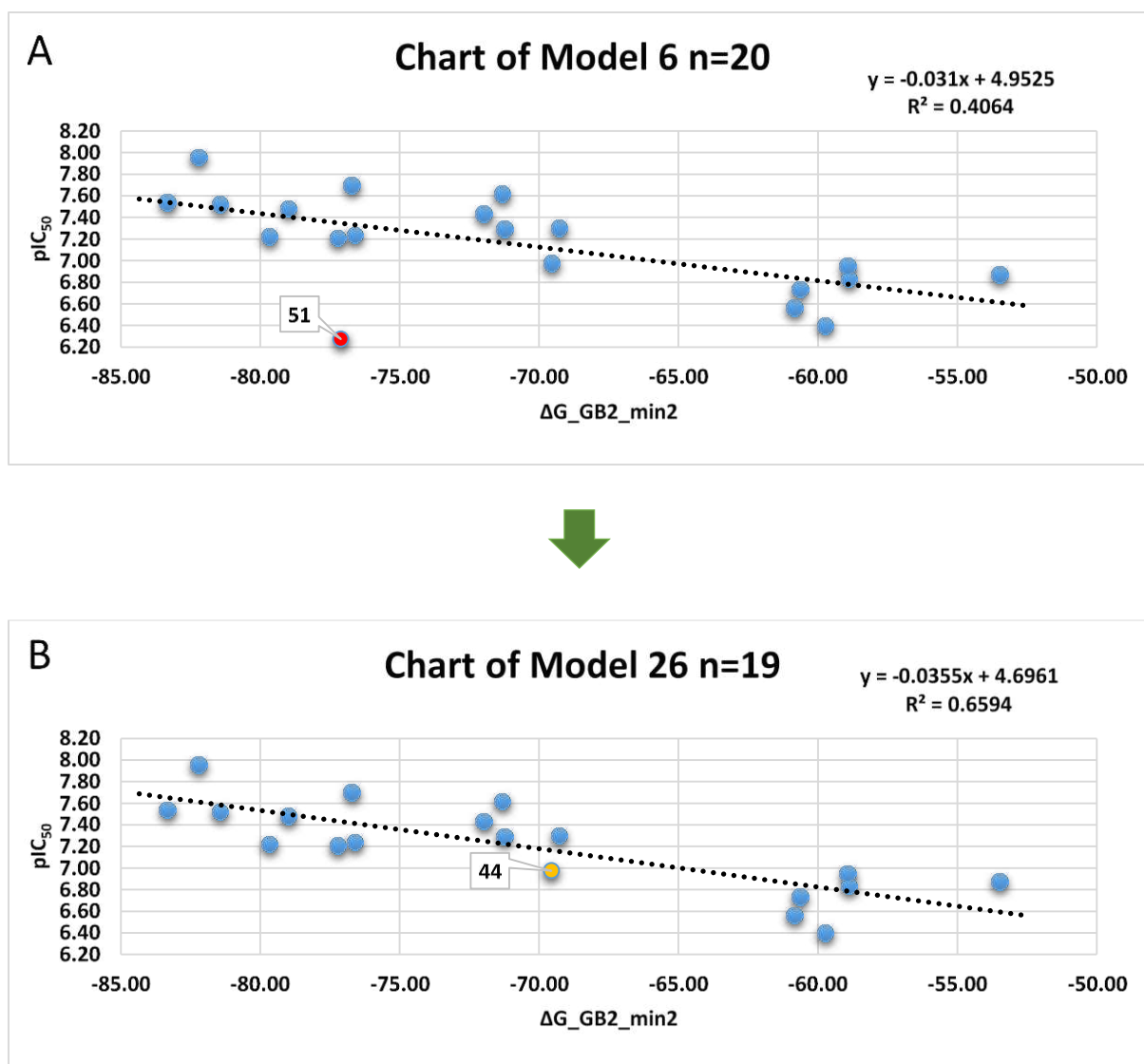
Figure 39: Model refinement process for HDAC10 binding predictions. (A) The correlation plots of the model of Model 6, where compound **51** (red filled circle) is identified as an outlier based on its Z-score (> 2). (B) The correlation plots of the model of Model 25 after the removal of compound **51**, showing improved fit across key metric R², and compound **44** is highlighted with yellow filled circle.

Upon statistical evaluation and internal validation of Models 25 and 26, both have been observed to be successful correlation models. However, beyond the correlation depicted in the graphs of both models, a clear distinction in classification is also apparent. By calculating the x-values (ΔG) where the y-value (pIC_{50}) equals 7 in both correlation equations (Figure 6b and 7b), ΔG threshold values have been determined for compounds with IC_{50} values below and above 100 nM. Compounds with an IC_{50} value above 100 nM, or alternatively, a pIC_{50} value below 7, have been classified as 'less active', while those with an IC_{50} value below 100 nM, or a pIC_{50} value above 7, have been labeled as 'more active'. Classification within the training set for both models has been conducted using the Bayesian classification method, based on the established ΔG threshold values. For Model 25, the ΔG value is calculated at -69.333, while for Model 26, this value is determined to be -64,898 (as shown below).

For model 25:

Correlation equation is: y (pIC$_{50}$) = -0.0299x (ΔG_GB1_min2) + 4.9282

$7 = -0.0299x + 4.9282$

$7 - 4.9282 = -0.0299x$

$2.0718 = -0.0299x$

$x = \dfrac{2.0718}{-0.0299} \approx -69.333$

$x \approx -69.333;$

For model 26:

Correlation equation is: y (pIC$_{50}$) = -0.0355x (ΔG_GB2_min2) + 4.6961

$7 = -0.0355x + 4.6961$

$7 - 4.6961 = -0.0355x$

$2.3039 = -0.0355x$

$x = \dfrac{2.3039}{-0.0355} \approx -64.898$

$x \approx -64.898.$

Consequently, for Model 25 and Model 26, compounds with calculated values of ΔG_GB1_min2 and ΔG_GB2_min2 below −69.333 and −64.898, respectively, are labeled as 'predicted more active'. In contrast, compounds possessing values above these thresholds are designated as 'predicted less active', facilitating classification predictions that are dependent on ΔG values.

Confusion matrices were constructed using classifications based on pIC$_{50}$ values and classification predictions based on calculated ΔG values for Model 25 and Model 26, as shown below.

Table 7: Confusion matrices for Models 25 and 26 in predicting HDAC10 binding activity. Both matrices present the classification of compounds as more active (1) or less active (0). Both Models shows 12 true positives (TP), 7 true negatives (TN), 1 false positive (FP), and 0 false negatives (FN).

Model 25	Predicted More Active (1)	Predicted Less Active (0)
Actual More Active (1)	TP: 12 (True Positives)	FN: 0 (False Negatives)
Actual Less Active (0)	FP: 1 (False Positives)	TN: 7 (True Negatives)

Model 26	Predicted More Active (1)	Predicted Less Active (0)
Actual More Active (1)	TP: 12 (True Positives)	FN: 0 (False Negatives)
Actual Less Active (0)	FP: 1 (False Positives)	TN: 7 (True Negatives)

It was observed that the values in the confusion matrices constructed for both models (25 and 26) are identical. The efficacy of these classification models was quantified using a series of statistical measures derived from these matrices such as accuracy, precision, sensitivity, specificity, and F1 scores. The detailed calculation methods for each parameter are provided in the Materials and Methods section. Here's a summary of the calculated values for both models:

Accuracy: Accuracy represents the proportion of correct predictions among all predictions made. Both models showed an accuracy of **95%**, indicating they are highly reliable in distinguishing between more active and less active compounds.

Precision: Precision measures the ratio of correctly identified positive cases to all predicted positive cases. For both models, the precision was **92.3%**, meaning that when the model predicts a compound as more active, it is correct 92.3% of the time.

Sensitivity (Recall): Sensitivity reflects the model's ability to correctly identify all relevant instances of a specific class. Both models achieved a perfect sensitivity score of **100%**, indicating that they successfully identified all more active compounds.

Specificity: Specificity evaluates the model's ability to correctly identify negative cases. For both models, the specificity was **87.5%**, showing solid performance in correctly identifying less active compounds.

F1 Score: The F1 Score provides a balance between precision and sensitivity. Both models achieved an F1 score of **96%**, indicating that they perform well in both predicting and detecting more active compounds, particularly in cases with an uneven class distribution.

To conclude, Models 25 and 26 demonstrate a strong capacity for prediction, as shown by their high levels of accuracy, precision, and sensitivity, along with notable specificity. The F1 scores reinforce the balanced accuracy of these models in classifying compounds as either more active

or less active. Hence, these models are exceptionally adept at reliably distinguishing between compounds of varying activity levels, making them valuable tools for tasks that demand accurate differentiation between more and less active compounds.

Additionally, it has been observed that compound **44** (highlighted as yellow in Figure 38B and 39B) is a false positive (FP) in the confusion matrices for both models. Upon closer examination of this compound, considering its IC_{50} value along with the standard deviation which is 106 ± 28, the classification of this compound as active in the models can be understood and deemed acceptable. Even though compound **44** remains within the model, this deviation in classification does not significantly detract from the overall effectiveness and reliability of the models.

4.9. External Validation of The QSAR Classification Model

In the application of both classification models (25 and 26) established for HDAC10, newly designed and synthesized compounds containing piperidine acryl hydroxamate structures and their saturated forms, piperidine propyl hydroxamates, were included in the test set. These compounds (**55-88**) were synthesized in house (see table 8). Notably, compounds **49** and **53**, which were evaluated in the previous enzymatic assay, were retested using the updated assay. In the previous assay, the IC_{50} value for compound **49** was measured as 20 nM, whereas in the new assay, it was determined to be 2.66 nM. Similarly, the IC_{50} value for compound **53**, initially measured as 58 nM, was found to be 3.8 nM in the new assay. Despite an 8- to 15-fold difference between the measurements, the ranking of the more potent compounds remained consistent across both assays. Furthermore, the relative activity ratio between the two compounds was preserved in both tests. These findings indicate that the new assay is significantly more sensitive while maintaining consistency in identifying the relative potency of compounds.

Furthermore, further compounds carrying a benzhydroxamic acid moieties, synthesized in house, and tested for activity in the aforementioned new HDAC10 activity assay, were added to the test set (see table 9) [177]. Among these 7 added compounds, 5 of them had IC_{50} values below 100 nM, and only two compounds had IC_{50} values above 100 nM. The compounds in the test set, despite having IC_{50} values determined through the second HDAC10 assay, were classified as more active or less active using the same 100 nM IC50 threshold applied to the training set.
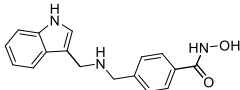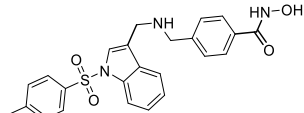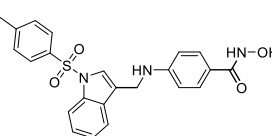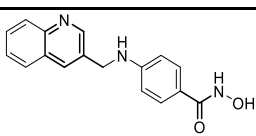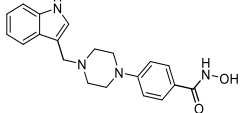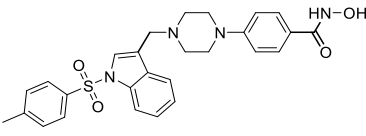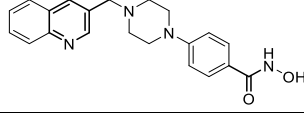
Table 8: Enzymatic in vitro HDAC10 inhibition of studied compounds (**49, 53, 55-88**).

		HDAC10 IC$_{50}$ value (nM) (Abz-Sperm-STFA)			
ID	**IC$_{50}$**	**ID**	**IC$_{50}$**	**ID**	**IC$_{50}$**
49	2.66 ± 0.29	65	1.42 ± 0.22	77	1.66 ± 0.23
53	3.8 ± 0.2	66	1.42 ± 0.17	78	1.23 ± 0.24
55	1.6 ± 0.1	67	9.1 ± 0.6	79	1.16 ± 0.26
56	1.2 ± 0.1	68	0.72 ± 0.02	80	0.86 ± 0.15
57	9.3 ± 0.1	69	6.2 ± 0.19	81	0.96 ± 0.13
58	1.2 ± 0.1	70	5.38 ± 0.47	82	0.78 ± 0.16
59	1.3 ± 0.1	71	6.8 ± 0.1	83	0.64 ± 0.2
60	2.1 ± 0.2	72	1.2 ± 0.1	84	1.91 ± 0.34
61	0.93 ± 0.04	73	1.0 ± 0.1	85	0.89 ± 0.16
62	2.2 ± 0.2	74	0.83 ± 0.17	86	0.81 ± 0.17
63	2.69 ± 0.19	75	0.74 ± 0.02	87	0.55 ± 0.18
64	0.57 ± 0.16	76	1.15 ± 0.13	88	1.06 ± 0.16

To balance the test set, which comprises many active compounds and only two less active ones (compounds **91** and **92**), additional compounds that had not been previously included in the training set were also added. These compounds are known to exhibit less than 50% inhibition at concentrations of 0.1 µM, as listed in Tables 3 and 4 in sections 4.5 (compounds **6**, **8-22**, **24-30**, **32**, **33**) and 4.6 (compounds **34**-**40**). They were incorporated into the test set as weakly active compounds, with the exception of compounds **9** and **10**, which were structurally different from the other compounds.

As a result, the test set consisted of a total of 69 compounds, with 39 compounds categorized as highly active and 30 compounds categorized as less active. Similar to the training set, the more active compounds had IC$_{50}$ values below 100 nM, and the less active ones had values above 100 nM.

Table 9: Enzymatic in vitro inhibition of studied compounds (**89-95**) (adapted from [177]).

ID	ID in Article	Structure	HDAC isoform inhibition % @ c [µM] or IC50 value (nM)			
			*dr*HDAC10	*h*HDAC6	*h*HDAC1	*h*HDAC8
			(Abz-Sperm-STFA)	(FDL2)	(FDL2)	(sLOGO-STFA)
89	1		0.41 ± 0.02	37 ± 12	4500 ± 200	350 ± 20
90	2		4.5 ± 0.3	51 ± 5	n.d. % @ 0.1 22.2 % @ 1 72.8 % @ 10	n.d. % @ 0.1 65.1 % @ 1 97.3 % @ 10
91	3		290 ± 60	53 ± 5	n.d. % @ 0.1 1.3 % @ 1 38.9 % @ 10	n.d. % @ 0.1 49.2 % @ 1 98.9 % @ 10
92	4		110 ± 10	2.5 ± 0.3	n.d. % @ 0.1 51.7 % @ 1 91.4 % @ 10	210 ± 10
93	5		2.0 ± 0.1	73 ± 3	n.d. % @ 0.1 48.4 % @ 1 90.6 % @ 10	74 ± 6
94	6		75 ± 12	n.d. % @ 0.1 7.3 % @ 1 67.2 % @ 10	n.d. % @ 0.1 7.3 % @ 1 67.2 % @ 10	n.d. % @ 0.1 26.9 % @ 1 87.9 % @ 10
95	7		11 ± 1.0	130 ± 10	n.d. % @ 0.1 32.1 % @ 1 79.4 % @ 10	13 % @ 0.1 36 % @ 1 81 % @ 10

Classifications using the ΔG threshold values obtained from the training set were conducted, so for the total 69 compounds docking studies were performed, and then the top scored docking solutions were selected and BFE calculations were performed with GB1 and GB2 MMGBSA methods as for the training set. All the used and calculated values for the test set are tabulated in the supplementary as S1 Table. Confusion matrices were constructed for the models 25 and 26 and their statistical values were calculated.

Table 10: Confusion matrices for Models 25 and 26 in predicting HDAC10 binding activity for the Test Set compounds For Model 25, the classification results show 39 true positives (TP), 0 false negatives (FN), 12 false positives (FP), and 18 true negatives (TN). In contrast, Model 26 also identifies 39 TP and 0 FN but reduces the false positives to 7 and increases true negatives to 23. This side-by-side comparison illustrates that Model 26 has enhanced accuracy in distinguishing fewer active compounds compared to Model 25.

Test of Model 25	Predicted More Active (1)	Predicted Less Active (0)
Actual More Active (1)	TP: 39 (True Positives)	FN: 0 (False Negatives)
Actual Less Active (0)	FP: 12 (False Positives)	TN: 18 (True Negatives)

Test of Model 26	Predicted More Active (1)	Predicted Less Active (0)
Actual More Active (1)	TP: 39 (True Positives)	FN: 0 (False Negatives)
Actual Less Active (0)	FP: 7 (False Positives)	TN: 23 (True Negatives)

The statistical measures derived from the confusion matrices for Model 25 and Model 26 are as follows, respectively:

- **Accuracy:** 82.6%, 89.8%

- **Precision:** 76.5%, 84.8%

- **Recall (Sensitivity):** 100%, 100%

- **Specificity**: 60%, 76.7%

- **F1 Score:** 86.7%, 91.8%

Comparing the two models, Model 26 shows an improvement in almost every statistical measure, indicating a more precise and reliable predictive ability. The increased specificity in Model 26 suggests a better distinction between more active and less active compounds, while the higher precision and F1 score indicate a better balance between the precision and recall of the model. Overall, Model 26 is demonstrated to be the superior model in terms of predictive accuracy and reliability.

In a further examination, it was noted that among the false positives (FP), 7 compounds were common to both Model 25 and Model 26, specifically compounds **34**, **35**, **36**, **37**, **38**, **39**, and **40**. In addition to these, Model 25 incorrectly predicted compounds **12**, **13**, **27**, **28**, and **91** as more active than they should be. When investigating the FP compounds common to both models, it is observed that they all possess piperidine hydroxamate structures. As previously discussed in docking studies, the nitrogen atom capable of protonation in these structures is positioned further than the optimal location (see section 4.5 Figure 22). However, the used models did not predict the decrease in activity of these compounds. As seen in the N^8 and N^1

acetyl spermidine case study (see Section 4.4), it is thought that BFE calculations based on frames obtained from longer MD simulations might distinguish these activities, but this would be costly in terms of time and computational resources.

Consequently, following the external validation of Models 25 and 26, it has been observed that Model 26, demonstrating superior performance, can serve as a classification model for modelling studies of novel HDAC10 inhibitors. This application is particularly effective when combined with a careful visual examination of the obtained docking solutions, enabling Model 26 to act as an efficient post filtering method in these and future screening or modelling studies.

4.10. Docking of The Test Set Compounds

Docking studies for the compounds in the test set were conducted using the DrHDAC10 crystal structure (PDB ID: 6UHU), employing the same settings as those used for compounds in the training set.

In this section, some representative highly active compounds from the test set were chosen to investigate their docking poses within the HDAC10 binding pocket and to evaluate their selectivity profiles. This analysis mirrored the ones conducted on representative compounds in the training set, involving docking to other HDAC subtypes, namely hsHDAC1 (PDB ID: 5ICN), hsHDAC6 (PDB ID: 5EDU), and hsHDAC8 (PDB ID: 2V5X). This method was employed to enhance the understanding of molecular interaction variances across different HDAC subtypes and to assess the binding affinity and specificity of these compounds for particular HDAC isoforms.

The predicted binding modes of the novel inhibitors **61** and **68** within HDAC10 isoform offer valuable insights into their pronounced inhibitory effects on DrHDAC10 as depicted in Figures 40a and 40b. In particular, the hydroxamate zinc linker moiety forms hydrogen bonds with the side chains of the amino acids Y307, H136 and H137, while showing bidentate chelation with the catalytic zinc ion, as expected. The piperidine-acryl or -propyl segments in the linker moieties of compounds **61** and **68** occupy the hydrophobic lysine binding site. Additionally, the protonated amine exhibits dual salt bridge/electrostatic interactions with the side chains of D94 and the gatekeeper residue E274, and engages in cation-π interactions with HDAC10 unique W205. These interactions are similar to those observed in polyamine substrates and other potent inhibitors of HDAC10, as reported in various studies and previous sections [72, 153, 169]. Furthermore, for **68**, an extra π-π interaction was identified between the distal naphthalene group, serving as a capping unit, and the side chain of F204, as shown in Figure 40b.
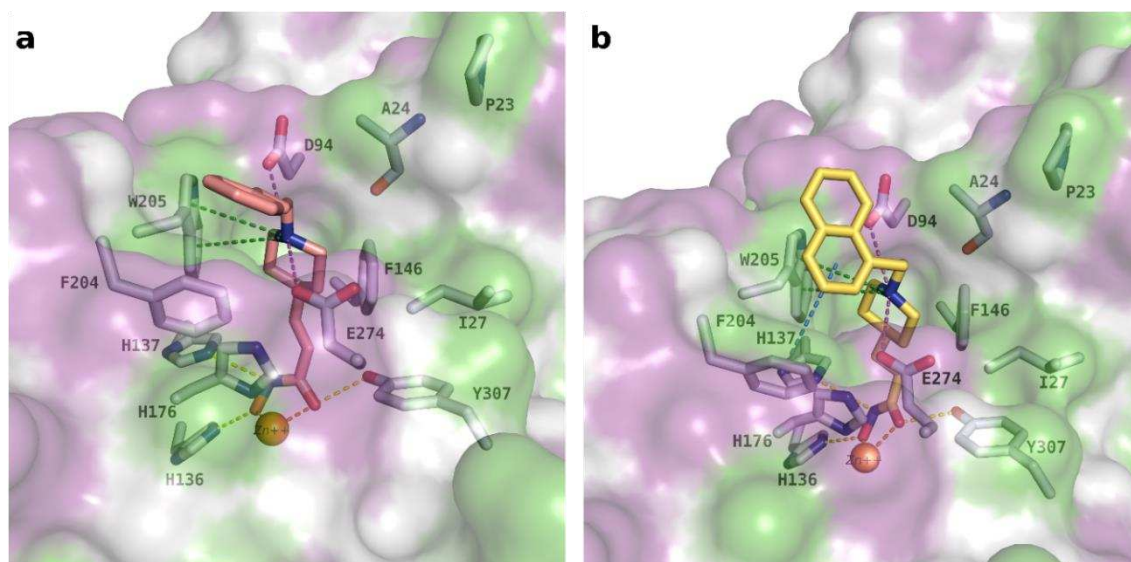
Figure 40: The predicted binding modes of compounds **a) 61** (represented by salmon-colored sticks) and **b) 68** (represented by pale yellow-colored sticks) within the drHDAC10 isoform (PDB ID: 6UHU). The enzyme's surface is color-coded to indicate lipophilicity, with green representing hydrophobic regions and magenta for hydrophilic areas. The side chains of amino acids at the binding site are displayed in white, while the catalytic zinc ion is depicted as an orange sphere. Interactions such as hydrogen bonds are shown with yellow dashed lines, salt bridge and electrostatic interactions with magenta dashed lines, π-π interactions with blue dashed lines, cation-π interactions with green dashed lines, and the coordination of the zinc ion by the ligand is illustrated with orange dashed lines.

In order to understand the weak activity of compound **61** against HDAC1, 6, and 8, docking studies were carried out in these HDAC isoforms as mentioned before. These studies revealed binding patterns where the compound **61** demonstrates bidentate chelation with the catalytic zinc ion, with interactions of the linker group in the lysine binding channel similar to those seen with drHDAC10. The primary difference lies in the behavior of the protonated piperidine-N. For drHDAC10, this protonated amine is located at the lysine binding tunnel's entrance, surrounded by a high concentration of electronegative residues, a distinctive feature of HDAC10. Here, it forms electrostatic interactions with the side chains of E274, the gatekeeper residue, and D94, which is more deeply embedded in the binding pocket in HDAC10 isoform, along with a cation-π interaction with W205. Conversely, in HDAC1, 6, and 8, the lysine binding tunnel entrance is primarily lined with neutral hydrophobic residues. It is also noteworthy that, in drHDAC10, the piperidine group is completely enclosed by the residues at the tunnel entrance, whereas in the other HDAC isoforms, it is partially exposed, as shown in Figure 41.
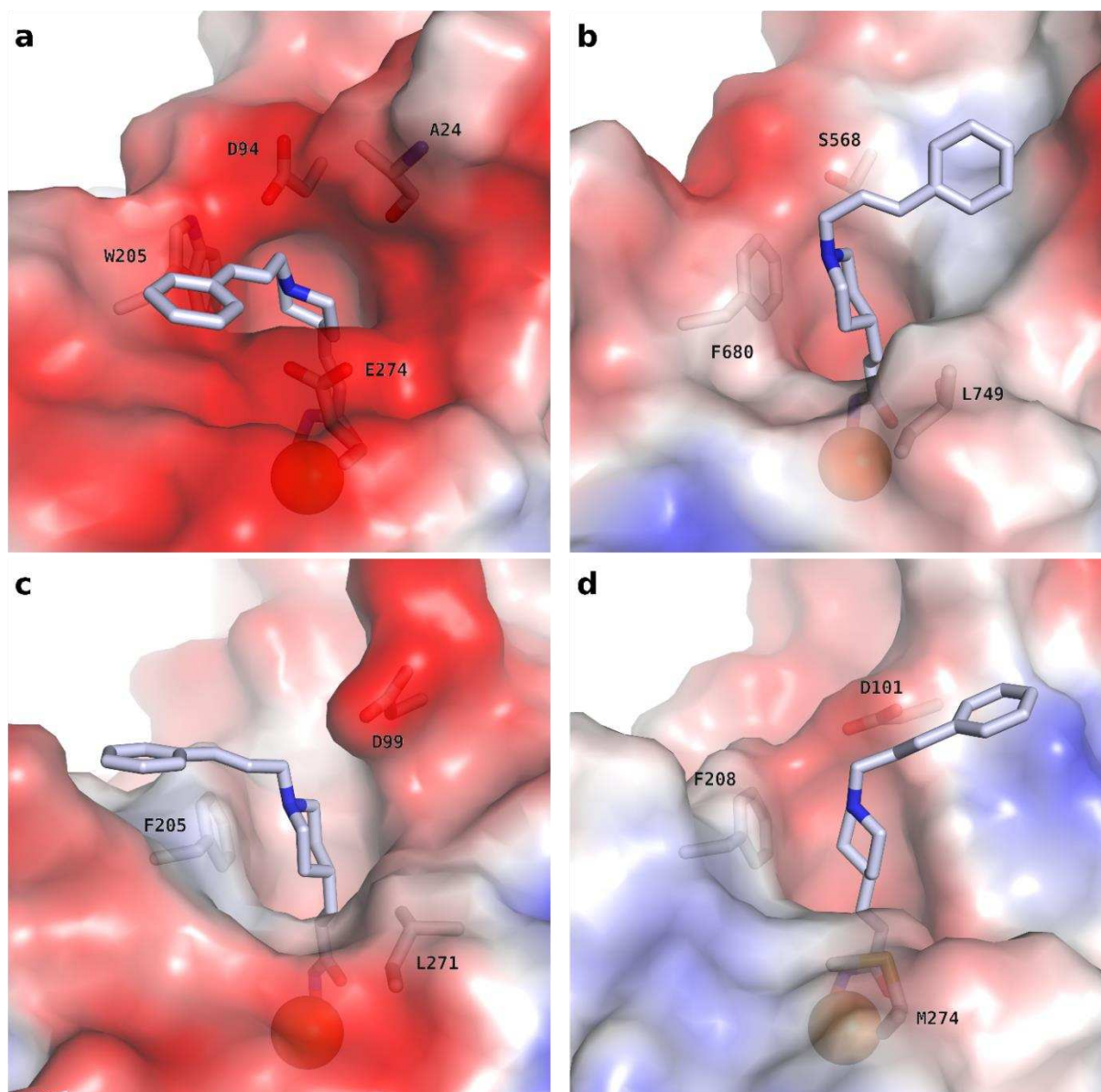
Figure 41: Illustration of the predicted binding modes of compound **61** in various HDAC isoforms; **a) 61** in drHDAC10 (PDB ID 6UHU), **b) 61** in hHDAC6 (PDB ID 5EDU), **c) 61** in hHDAC1 (PDB ID 5ICN), and **d) 61** in hHDAC8 (PDB ID 2V5X. The proteins' surfaces are color-coded to reflect the electrostatic potential, ranging from red (indicating negatively charged areas) to blue (for positively charged regions). The side chains of the amino acids at the binding sites are displayed as white sticks, and the catalytic zinc ion is represented by an orange sphere.

The predicted binding modes of compounds carrying amino acid moieties as terminal capping groups (**74**, **75**, **87** and **88**), show similar interactions to those seen with **61** in drHDAC10. In addition, the docking poses of these compounds show that the capping groups containing amino acid moieties form additional salt bridge interactions between the protonated primary amines and the side chain of D94. Moreover, for **74** and **87**, both having *S* configuration, an additional hydrogen bond is formed between the amide-NH of the amino acid terminal group and the side chain of D94 (see Figure 42).
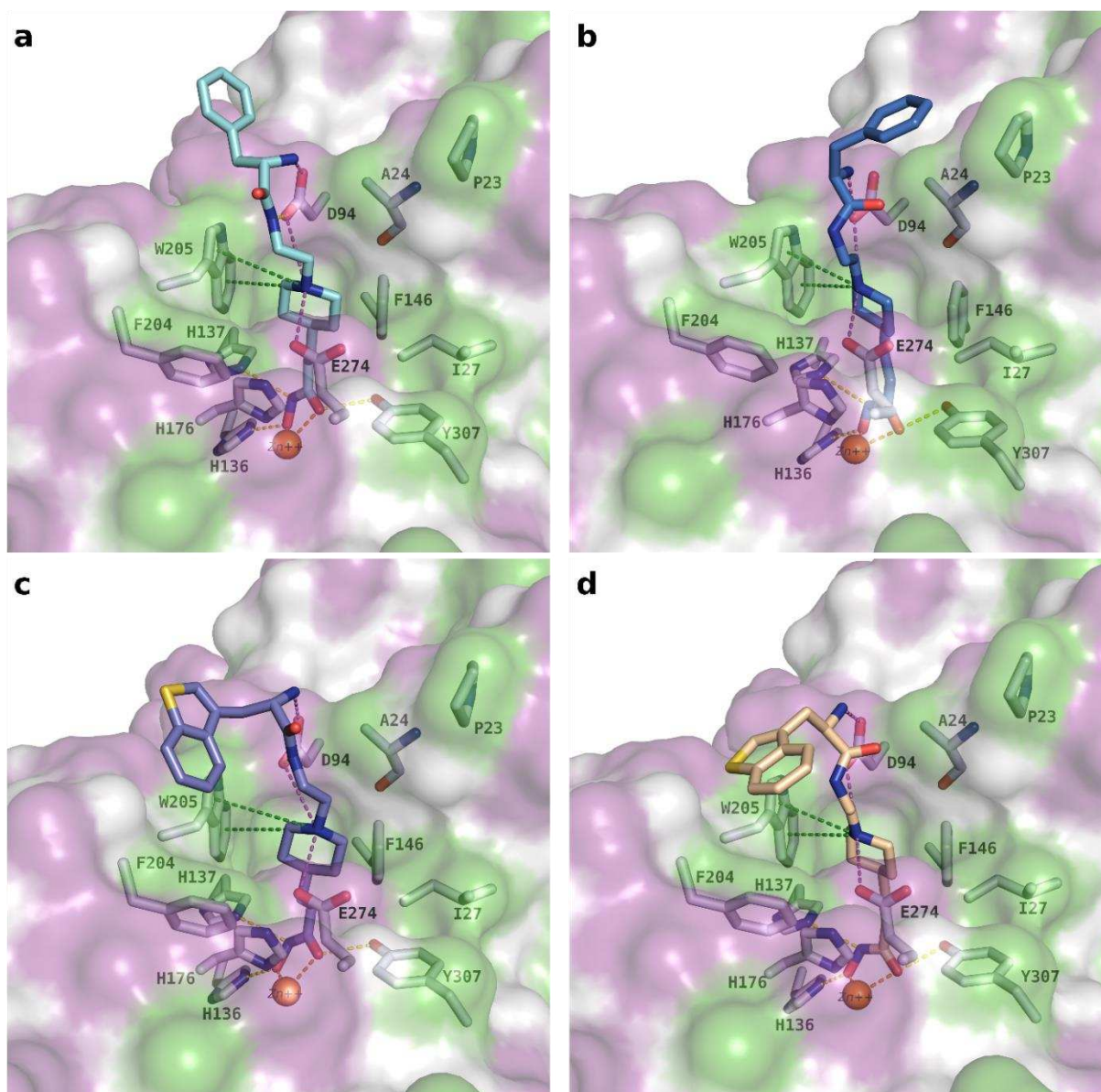
Figure 42: Illustration of the predicted binding modes of the compounds **a) 74** (represented by turquoise sticks), **b) 75** (represented by pale yellow sticks), **c) 87** (represented by purple sticks) and **d) 88** (represented by wheat color sticks) within drHDAC10 (PDB ID: 6UHU). The protein surfaces are color-coded to reflect lipophilicity, with green indicating hydrophobic regions and magenta for hydrophilic areas. The side chains of the amino acids at the binding sites are visualized as white structures, and the catalytic zinc ion is highlighted as an orange sphere. Interactions such as hydrogen bonds are shown with yellow dashed lines, salt bridges and electrostatic interactions with magenta dashed lines, π-π interactions with blue dashed lines, cation-π interactions with green dashed lines, and the coordination of the zinc ion by the ligand is depicted with orange dashed lines.

In the study of HDAC inhibitors involving the benzhydroxamate derivatives synthesized by Amer Tarawneh (Figures 43, 44, and 45), the docking analyses revealed that the phenyl part of the linker consistently occupies the hydrophobic lysine binding pocket across all examined isoforms. Furthermore, in the cases of DrHDAC10, HsHDAC8, and HsHDAC1, hydrogen bond interactions were noted with the conserved residues H136/142/140, H137/143/141, and Y307/306/303, respectively. In contrast, for HsHDAC6, the hydroxyl oxygen was found to form a water-mediated hydrogen bond with the conserved histidine residues H610 and H611.

The predicted binding conformation of compound **89** within the active site of DrHDAC10, as shown in Figure 43a, provides insight into the compound's remarkable inhibitory activity against HDAC10. In addition to forming hydrogen bonds with the conserved tyrosine and histidines, compound **89** also forms π-π stacking interactions with F204. More importantly, in its protonated state, the amine function of **93** forms dual salt bridge interactions with D94 and the gatekeeper residue E274, while also exhibiting cation-π interactions with the other HDAC10 specific W205 residue. These binding characteristics are consistent with those observed for potent and selective HDAC10 inhibitors and polyamine substrates as mentioned before.

HDAC6, a class IIa member, differs from HDAC10 in its binding pocket due to mutations like D94/S568 and E274/L749. These variations lead to a different docking result for compound **89** in HDAC6, showing only a single hydrogen bond with S568 (see Figure 43b). This could account for the approximately 90-fold higher selectivity of HDAC10 over HDAC6, as seen in Table 9 in section "4.9.".

In class I HDAC members HDAC1 and HDAC8, the gatekeeper residue at the lysine binding tunnel's entrance is different (E274 in HDAC10 is replaced by in L271 HDAC1 and M274 in HDAC8). This change results in the loss of a salt bridge interaction with the protonated amine function of the compound **89** in the binding tunnel of the studied class I HDAC isoforms. The absence of this salt bridge interaction, combined with the positional differences of the D101/D99 amino acids in comparison to HDAC10's D94, leads to a conformational change in the linker portion. This alteration appears to result in compound **89** adopting an 'L'-shaped binding pose in the HDAC8 and HDAC1 isoforms. Such positioning leads to the loss of π-π interactions, observed in the HDAC10 binding pose, through the capping group, and renders the hydrophobic capping group evidently more exposed to the solvent. The exposed capping groups are likely another cause of reduced activity in both class I isoforms. Furthermore, the narrower binding pocket in HDAC1, resulting from the E274/L271 variation, could create steric hindrance for the linker and capping group of **89**. This might explain the relatively greater loss of activity in this isoform compared to HDAC8 as depicted in Figures 43c and 43d.
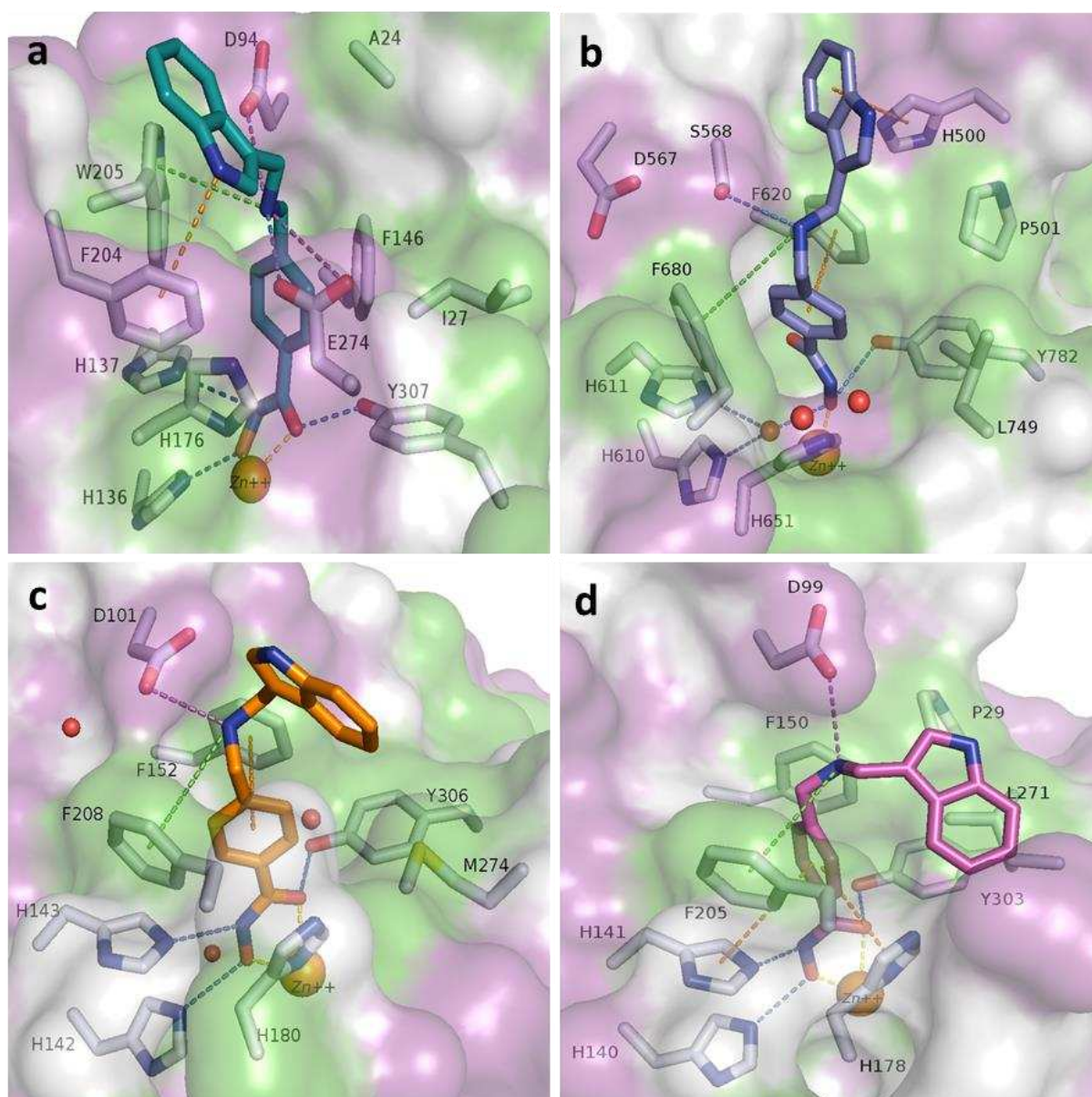
Figure 43: Illustration of the predicted binding modes of compound **89** in various HDAC isoforms. **a) 89** (represented in teal sticks) in drHDAC10 (PDB ID 6UHU), **b) 89** (represented in violet sticks) in HDAC6 (PDB ID 5EDU), **c) 89** (represented in orange sticks) in HDAC8 (PDB ID 2V5X), and **d) 89** (represented in magenta sticks) in HDAC1 (PDB ID 5ICN). The surface of the proteins is color-coded to reflect lipophilicity, with green indicating hydrophobic regions and magenta for hydrophilic areas. The side chains of the amino acids at the binding sites are displayed as white sticks, and the catalytic zinc ion is highlighted as an orange sphere. Interactions such as hydrogen bonds are shown with blue dashed lines, salt bridges with magenta dashed lines, π-π interactions with orange dashed lines, cation-π interactions with green dashed lines, and the coordination of the zinc ion by the ligand is depicted with yellow dashed lines (reproduced from [177]).

Comparable findings were noted for the DrHDAC10 bindings of compounds **93** and **94**, characterized by a piperazine linker, distinct from the amino methyl linker in **89**. In these cases, the protonated piperazine-NH engaged in dual salt bridge interactions with D94 and E274, as well as cation-π interactions with W205. Furthermore, the capping groups of these compounds exhibited π-π interactions with W205 within the HDAC10 binding pocket, akin to those observed with **89**. Additionally, one of the oxygens in the sulphonamide structure of **94** establishes a hydrogen bond with the N207 amino acid (see Figure 44).

87
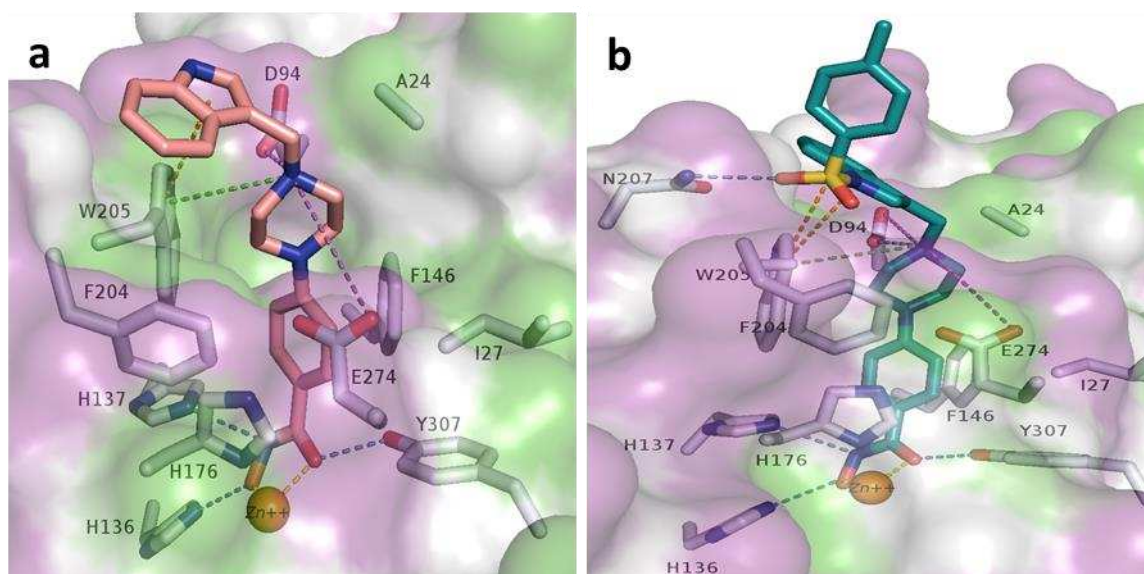
Figure 44: Illustration of the predicted binding modes of compounds in drHDAC10 (PDB ID 6UHU). **a) 93** (represented in peach sticks) and **b) 94** ((represented in teal sticks). The surface of the proteins is color-coded to reflect lipophilicity, with green indicating hydrophobic regions and magenta for hydrophilic areas. The side chains of the amino acids at the binding sites are displayed as white sticks, and the catalytic zinc ion is highlighted as an orange sphere. Interactions such as hydrogen bonds are shown with blue dashed lines, salt bridges with magenta dashed lines, π-π interactions with orange dashed lines, cation-π interactions with green dashed lines, and the coordination of the zinc ion by the ligand is depicted with yellow dashed lines (reproduced from [177]).

Compounds that lack a basic amino group, such as **91** and **92**, demonstrated a notable reduction in HDAC10 inhibitory activity. This reduction can be linked to the absence of salt bridge interactions with D94 and E274, as well as the cation-π interaction with W205 in HDAC10, interactions that were present in the other compounds discussed in this report. As expected, the only interaction observed in these cases was a hydrogen bond between the NH-group and D94, as depicted in Figures 45b and 45c. These observations underscore the significance of the protonated nitrogen and its strategic placement in enhancing binding interactions with HDAC10.

Upon examining the binding position of **90** which features a capping group of N-tosyl indole instead of indole capping group of **89**, it is observed that the π-π interaction formed by the indole ring of **89** with W205 shifts to the phenyl ring of the tosyl structure in **90**. While the other interactions remain the same for both compounds, there is a notable increase in solvent exposure for the tosyl moiety of the capping group of **90**, which explains the 11-fold decrease in activity (see table 9). For a comparative view of the binding positions, see Figures 45a for **90** and 43a for **89**.
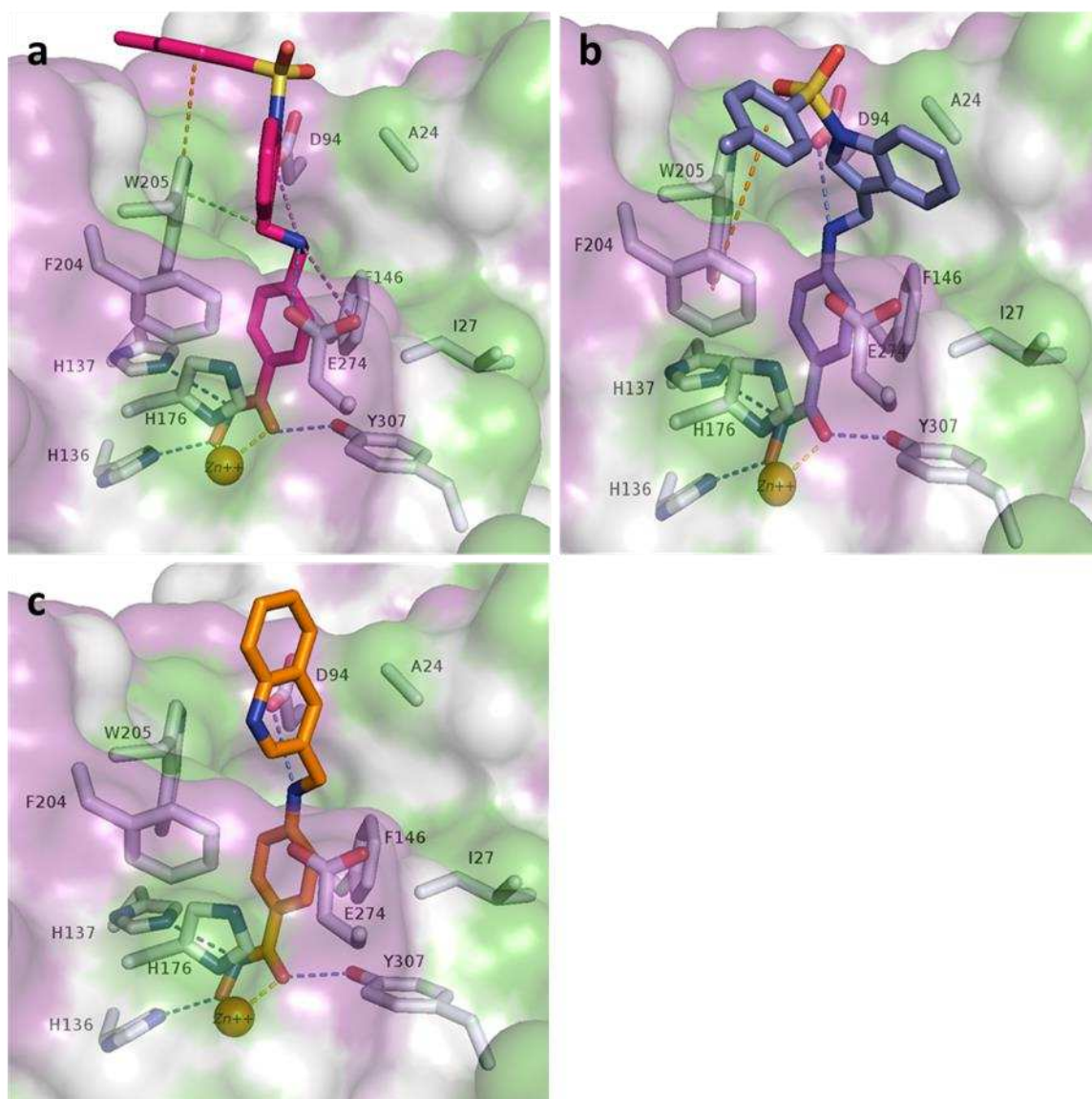
Figure 45: Illustration of the predicted binding modes of compounds **90 ,91** and **92** in drHDAC10 (PDB ID 6UHU), **a) 90** (represented in magenta sticks), **b) 91** (represented in violet sticks), **c) 92** (represented in orange sticks) .The surface of the proteins is color-coded to reflect lipophilicity, with green indicating hydrophobic regions and magenta for hydrophilic areas. The side chains of the amino acids at the binding sites are displayed as white sticks, and the catalytic zinc ion is highlighted as an orange sphere. Interactions such as hydrogen bonds are shown with blue dashed lines, salt bridges with magenta dashed lines, π-π interactions with orange dashed lines, cation-π interactions with green dashed lines, and the coordination of the zinc ion by the ligand is depicted with yellow dashed lines. (reproduced from

The *in vitro* data (Table 9 in section "4.9.") indicate that the placement of the tosyl moiety on the indole capping group results in reduced HDAC10 inhibitory activity. Specifically, **90** exhibits a roughly 10-fold decrease in HDAC10 inhibition compared to **89**. Furthermore, **95** shows a decrease in activity by almost 38-fold relative to its unsubstituted analog, **94**. Our docking studies show that the hydrophobic tosyl moiety does not engage in interactions with the edge of the HDAC10 binding site and remains fully exposed to the solvent. This latter aspect may account for the observed decrease in HDAC10 inhibitory activity of **95** compared to **94**.

4.11. Molecular Dynamics Simulation of The Synthesized Test Set Compounds

The stability of the predicted binding modes obtained from the molecular docking studies on selected hit compounds, specifically **74**, **75** and **89** was evaluated using molecular dynamics simulations. These simulations were repeated in triplicate, each 100 ns, and were performed on the crystal structure of drHDAC10 with the PDB ID: 6UHU.

Analysis of the protein RMSD plots revealed that the protein structures of the studied compound complexes remained stable, with RMSD values consistently below 1.5 Å throughout the 100 ns simulations (see Figures 46a, 47a, and 48a).

Additionally, the catalytic zinc atom within each complex exhibited stability, maintaining RMSD values below 1.5 Å in every replicate (see Figures 46b, 47b and 48b).

In a similar way, the bidentate chelations between the catalytic zinc atom and the zinc-binding groups of the compounds were sustained throughout the 100 ns MD simulations for each compound. These chelations, involving the two oxygen atoms of the zinc-binding groups, maintained a distance of approximately 2Å between the oxygen atom and the zinc ion (see Figures 46d, 47d and 48d).

The capping group consistently emerges as the primary source of fluctuations across all compounds, as indicated by the RMSD_LIG (see Figures 46c, 47c and 48c) and RMSF_LIG plots (see Figures 46e, 47e and 48e). This region exhibits higher flexibility and dynamic behavior, with RMSF values exceeding 2 Å, particularly in solvent-exposed areas. In contrast, regions like the Zinc Binding Group (ZBG) and linker demonstrate more stable interactions, maintaining lower RMSF values (<1.5 Å). The increased mobility of the capping group, especially in compounds like **75** and **89**, contributes to the instability and variability in binding poses, as seen in higher RMSD values and notable fluctuations in replicates. Compounds **74** and **75**, which are stereoisomers, were compared in terms of their RMSD and RMSF graphs (see Figures 48c, 49c and 48e, 49e). The analysis revealed that the S-isomer, compound **74**, exhibits lower RMSD values and is more stable compared to the R-isomer, compound **75**. The findings highlight the capping group's role in driving ligand instability and its impact on the overall dynamics within the binding pocket. However, as a result, no significant difference was observed in HDAC10 inhibitory activity (see table 8).
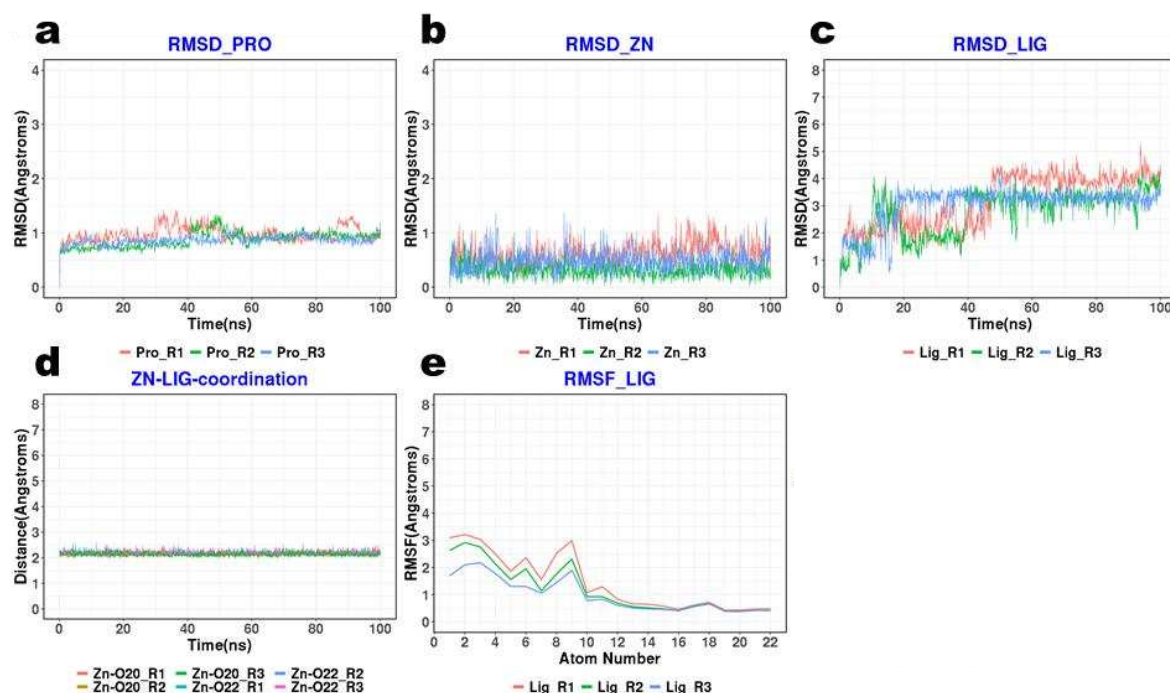
Figure 46: The compilation of data plots from molecular dynamics simulations of the predicted binding mode of compound **89** in drHDAC10 (PDB ID 6UHU); **a)** Illustrates RMSD trajectories for the protein's heavy atoms over three replicates of 100 ns simulations. **b)** Illustrates RMSD trajectories for the Zn ion from three 100 ns simulations. **c)** Illustrates RMSD trajectories for the ligand's heavy atoms across three 100 ns simulations. **d)** Illustrates distance tracking between the Zn ion and the oxygen atoms of the ligand's zinc-binding group over three 100 ns simulations. **e)** Illustrates RMSF data for the ligand's heavy atoms from three 100 ns simulations.
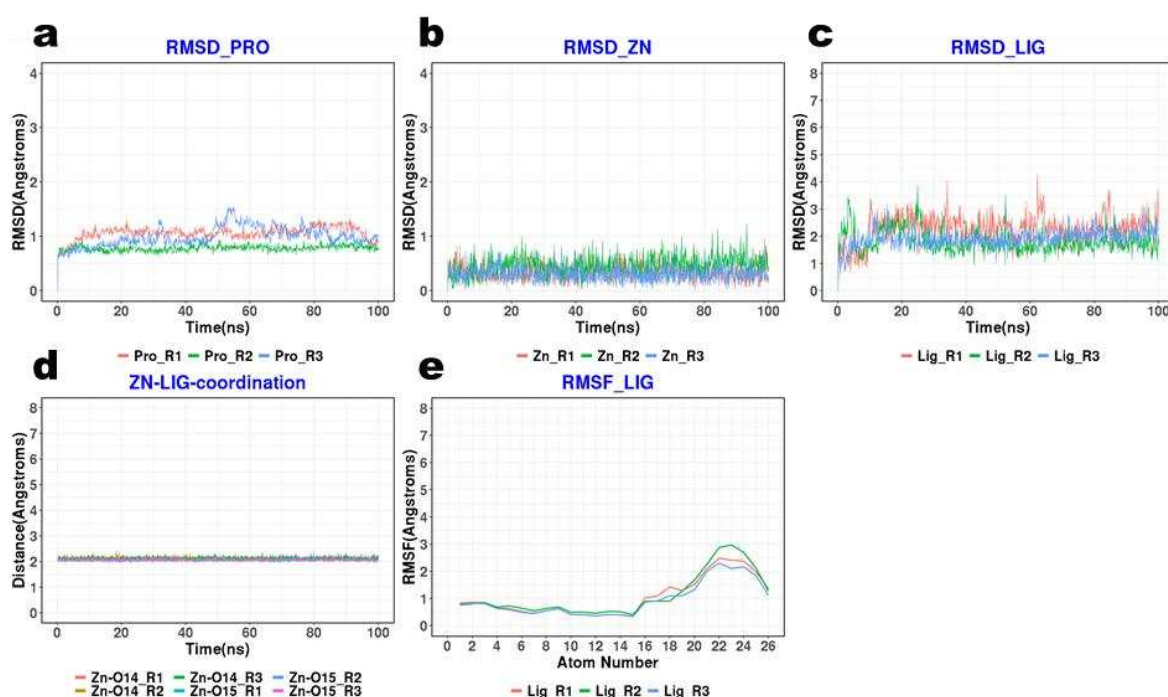
Figure 47: The compilation of data plots from molecular dynamics simulations of the predicted binding mode of compound **74** in drHDAC10 (PDB ID 6UHU); **a)** Illustrates RMSD trajectories for the protein's heavy atoms over three replicates of 100 ns simulations. **b)** Illustrates RMSD trajectories for the Zn ion from three 100 ns simulations. **c)** Illustrates RMSD trajectories for the ligand's heavy atoms across three 100 ns simulations. **d)** Illustrates distance tracking between the Zn ion and the oxygen atoms of the ligand's zinc-binding group over three 100 ns simulations. **e)** Illustrates RMSF data for the ligand's heavy atoms from three 100 ns simulations.
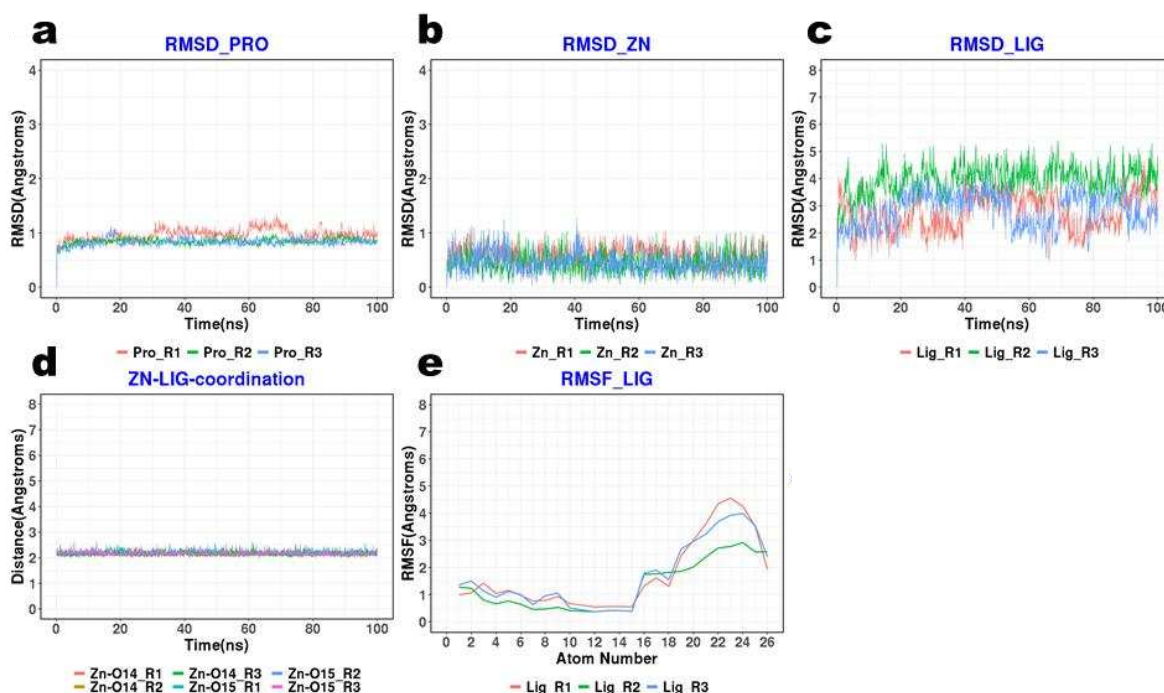
Figure 48: The compilation of data plots from molecular dynamics simulations of the predicted binding mode of compound **75** in drHDAC10 (PDB ID 6UHU); **a)** Illustrates RMSD trajectories for the protein's heavy atoms over three replicates of 100 ns simulations. **b)** Illustrates RMSD trajectories for the Zn ion from three 100 ns simulations. **c)** Illustrates RMSD trajectories for the ligand's heavy atoms across three 100 ns simulations. **d)** Illustrates distance tracking between the Zn ion and the oxygen atoms of the ligand's zinc-binding group over three 100 ns simulations. **e)** Illustrates RMSF data for the ligand's heavy atoms from three 100 ns simulations.

Clustering the MD trajectories based on the ligand RMSD revealed three distinct clusters for each of the inhibitors **74**, **75**, and **89**.

For compound **74** (S-isomer), the clusters have occupancies of 63%, 29%, and 8%, respectively (Figure 49a). Here, the main variation occurs in the orientation of the solvent-exposed phenyl ring of the phenylalanine moiety, while the amide and primary amine groups consistently adopt the same orientation in all clusters, allowing interactions with the D94 side chain. In contrast, for compound **75** (R-isomer), the three clusters show more pronounced deviations in the positioning of the phenylalanine capping group, with respective occupancies of 32%, 30%, and 28% (Figure 49b), highlighting significant changes in binding poses compared to the S-isomer.

For compound **89**, upon examining these clusters (Figure 49c), the indole capping group is observed to occupy one of two hydrophobic regions at the rim of the binding pocket. In two of the clusters, with occupancies of 53% and 20%, the indole group engages in hydrophobic interactions with residues I27, A28, and P29. In the third cluster, which has a 27% occupancy, the capping group is positioned between residues F204 and W205. Despite showing significant fluctuations, the indole capping group remains well-accommodated at the entrance of the lysine

binding pocket of HDAC10, where it forms stabilizing hydrophobic interactions with nearby residues.
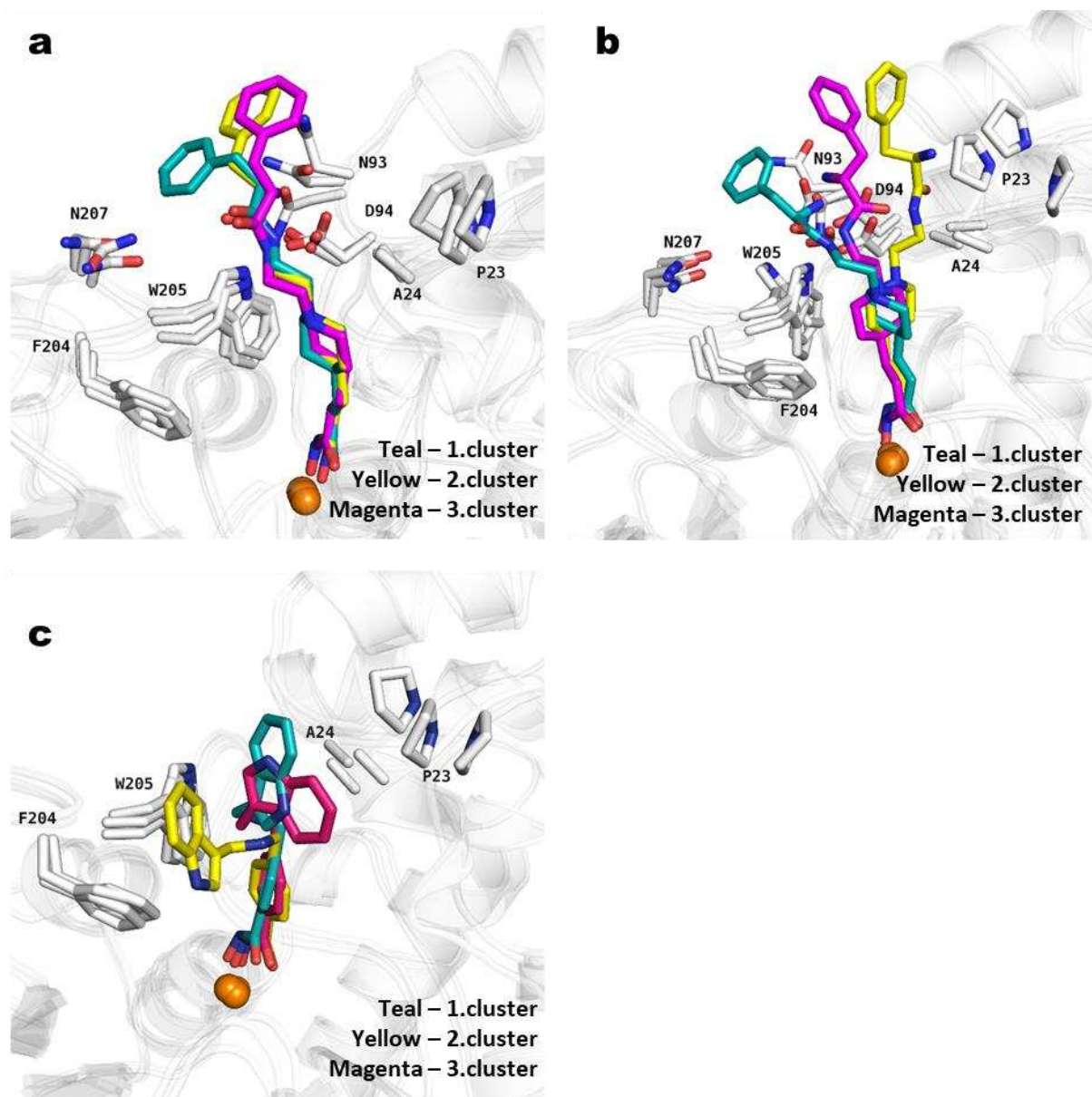
Figure 49: Representative poses of the obtained three clusters with the highest occupancy from the results of 3 MD replicas for each studied compound. **a)** For compound **74**, teal sticks for the first cluster (occupancy 63%), yellow sticks for the second cluster (occupancy 29%) and magenta sticks for the third cluster (occupancy 8%); **b)** For compound **75**, teal sticks for the first cluster (occupancy 38%), yellow sticks for the second cluster (occupancy 32%) and magenta sticks for the third cluster (occupancy 30%); **c)** For compound **89**, teal sticks for the first cluster (occupancy 53%), yellow sticks for the second cluster (occupancy 27%) and magenta sticks for the third cluster (occupancy 20%). The side chains of amino acids at the relevant binding site are shown as white sticks, while the catalytic zinc ion is depicted as orange spheres.

4.12. Cosolvent MDs

In accordance with the details given in the Materials and Methods section 3.1.3, cosolvent MD studies were performed by selectively retaining a fraction of co-crystallized or docked ligands in the binding pockets of protein-ligand complexes. We aimed to identify any additional sub-

pockets, as well as hydrophobic or hydrophilic patches or sites within the central or outer regions of HDAC10 binding pockets through cosolvent molecular dynamics studies.

As mentioned, only the benzhydroxamate fractions of the ligands that docked into the binding pockets of HDAC8, HDAC6, and HDAC10 crystal structure (PDB ID: 6WDW) were kept in the binding pocket (Figure 50a, Figure 50b and Figure 50c, respectively). Instead, in the HDAC10 crystal structure PDB ID: 7U69, the *N*-methylpiperidine acryl hydroxamate fraction of the co-crystallized ligand was retained (Figure 50d). It is also important to note that there are variations in the conformations of the side-chain of the E24 residues across the two investigated HDAC10 crystal structures as seen in the Figures 50c-d.
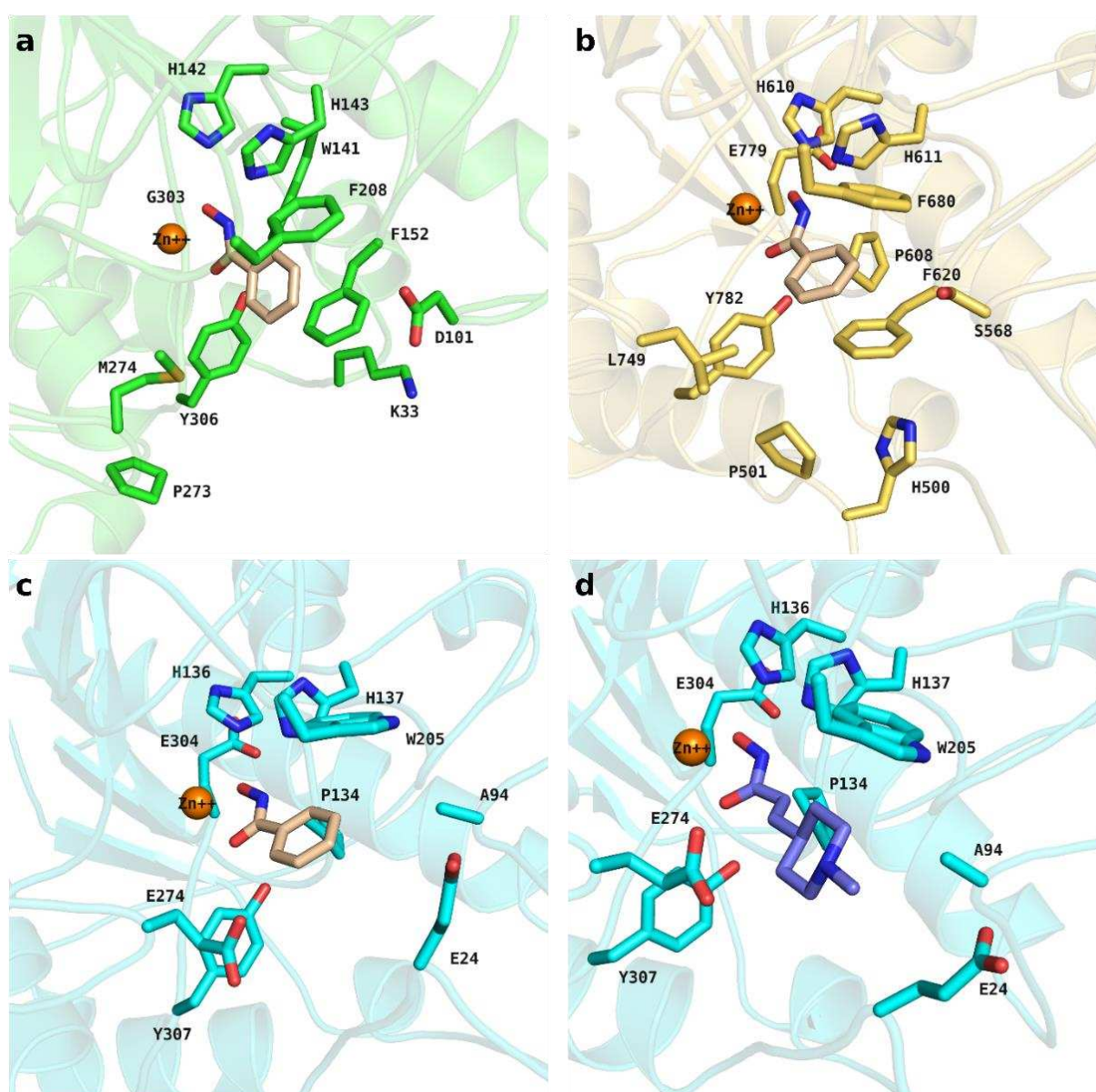
Figure 50: Initial binding complexes of HDAC isoforms before solvent and cosolvent addition in MD simulations. **a)** HDAC8 (green) with benzhydroxamate fraction of the docked ligand (wheat) and key residues, **b)** HDAC6 (yellow) showing the benzhydroxamate fraction of the ligand (wheat) and important residues, **c)** HDAC10 (PDB ID: 6WDW) (cyan) with the benzhydroxamate fraction of the co-crystallized ligand (wheat) and key residues,

94

including E24, **d)** HDAC10 second structure (cyan) with N-methylpiperidine acryl hydroxamate fraction (purple) and distinct E24 conformation. Orange spheres represent zinc ions at the catalytic sites.

The rationale for employing this methodology originated from the observation that, the hydrophobic cap groups of the studied inhibitors tend to demonstrate instability during MD studies. Our primary objective was to investigate the existence of any additional pockets or hotspots within these binding sites where these capping groups could be directed and stabilized. If feasible, our goal was to refine the structural targeting to enhance both specificity and potency for HDAC10 inhibition.

Cosolvent MD simulations were conducted for HDAC10 isoform using AMBER22. Trajectories obtained from these simulations were subjected to mapping using PyMOL MixMD. We utilized two different crystal structures with the corresponding Protein Data Bank (PDB) identifiers, 6WDW and 7U69.

To validate our approach, the same method with the same settings was further applied on two specific HDAC isoforms for which secondary hydrophobic sites were previously identified: HDAC8 (PDB ID: 2V5X) and HDAC6 (PDB ID: 5EDU). HDAC8 has been documented in the literature to have a hydrophobic side pocket [178], while HDAC6 is known to contain aforementioned hydrophobic patch made up by F620, P501, H500 and L749 [155].

As mentioned in Materials and Methods section (Section 3.1.3), five different probe molecules were used as co-solvents. In general alcohols, for example methanol and ethanol are used for mapping hydrophobic sites and hydrogen bond acceptor/ hydrogen bond donor (HBA/HBD) interactions over their alkyl and hydroxyl pharmacophore features [179, 180]. While acetamide was used to map hydrophobic sites through the methyl pharmacophore feature of acetamide, HBA through its carbonyl oxygen and HBD through its amide-NH2 group [179]. Another probe molecule used was the triethylamine structure, which was identified in the Schrödinger 2021-1 release database as having a small hydrophobic mapping role. It was used to map hydrophobic sites through three ethyl groups surrounding the nitrogen atom. The final probe molecule used was pyridine, a weak base that is more water soluble than the benzene ring system. In the literature, pyridine is labeled as 6-membered aromatic (more soluble) for its mapping role [180], and in this study, it was used for the mapping of hydrophobic, and/or possible π-π, π -cation interaction sites. After cosolvent MD simulations, mapping of hotspots was performed using the MixMD Probeview plugin implemented in the open-source version of the molecular visualization program PyMOL.

As a result of methanol cosolvent MD simulations, two distinct hotspots were identified in the region commonly referred to as the 'foot pocket'. This pocket extends deep into the interior of the protein structure while carrying the gatekeeper W141, and G303, at the entrance. These hotspots are depicted as two separate magenta meshes, serving as visual representations of their locations within the binding pocket (Figure 51a). Two additional hotspots are detected as magenta meshes, one is near the M274 residue in the distal part of binding tunnel and the other one is far from the binding pocket at the outer surface of the protein.

To provide further supporting evidence and enhance visual comprehension, we conducted a transfer of the binding pose of an N-alkyl hydroxamate compound (shown as purple stick in Figure 51a) known to partially occupy the HDAC8 foot pocket. This transfer was performed from the crystallized complex of smHDAC8 (PDB ID: 6FU1) to the hsHDAC8 (PDB ID: 2V5X) structure utilized in our cosolvent studies.

In the transfer process, we initially aligned the two crystal structures by aligning their backbone atoms within the protein structures. Subsequently, we transferred the crystallized N-alkyl hydroxamate structure. This procedure allowed us to superimpose and align the relevant structural information, aiding in our analysis of the HDAC8 foot pocket in the context of our cosolvent studies.

Cosolvent MD simulations of the HDAC6 isoform resulted in the mapping of two distinct hotspots within the binding pocket of HDAC6, along with the identification of various hotspots of varying sizes or scales located away from the binding pocket. These hotspots are visually depicted as magenta meshes in Figure 51b.

To confirm our findings and provide visual explanations, we utilized Tubastatin A, a compound that has been documented as a selective inhibitor of HDAC6 in the literature. The binding poses of Tubastatin A (shown as teal stick in Figure 51b) in DrHDAC6 (PDB ID: 6THV), as crystallized in the protein structure, was transferred to the binding pocket of HsHDAC6.

In the 6THV crystal structure and our docking studies (see Title 4.4.), it was demonstrated that tetrahydro-γ-carboline moiety of capping group of Tubastatin A forms hydrophobic interactions with the aforementioned hydrophobic patch. The utilization of methanol as a probe molecule allowed us to recognize and map the hydrophobic patch in hsHDAC6. This mapping was confirmed by observing the overlap of the hotspots with the mentioned capping group portion and the encirclement of this hotspot by the amino acids F620, P501, H500, and L749, which constitute the hydrophobic patch.

When examining the methanol occupancy grid mapping of both cosolvent studies of humanized DrHDAC10 (PDB IDs: 6WDW and 7U69) crystal structures, numerous hotspots of varying sizes were found in locations far from the binding pocket and beyond the reach of ligands bound within the binding pocket. These hotspots are depicted as magenta meshes (see Figure 51c-d).
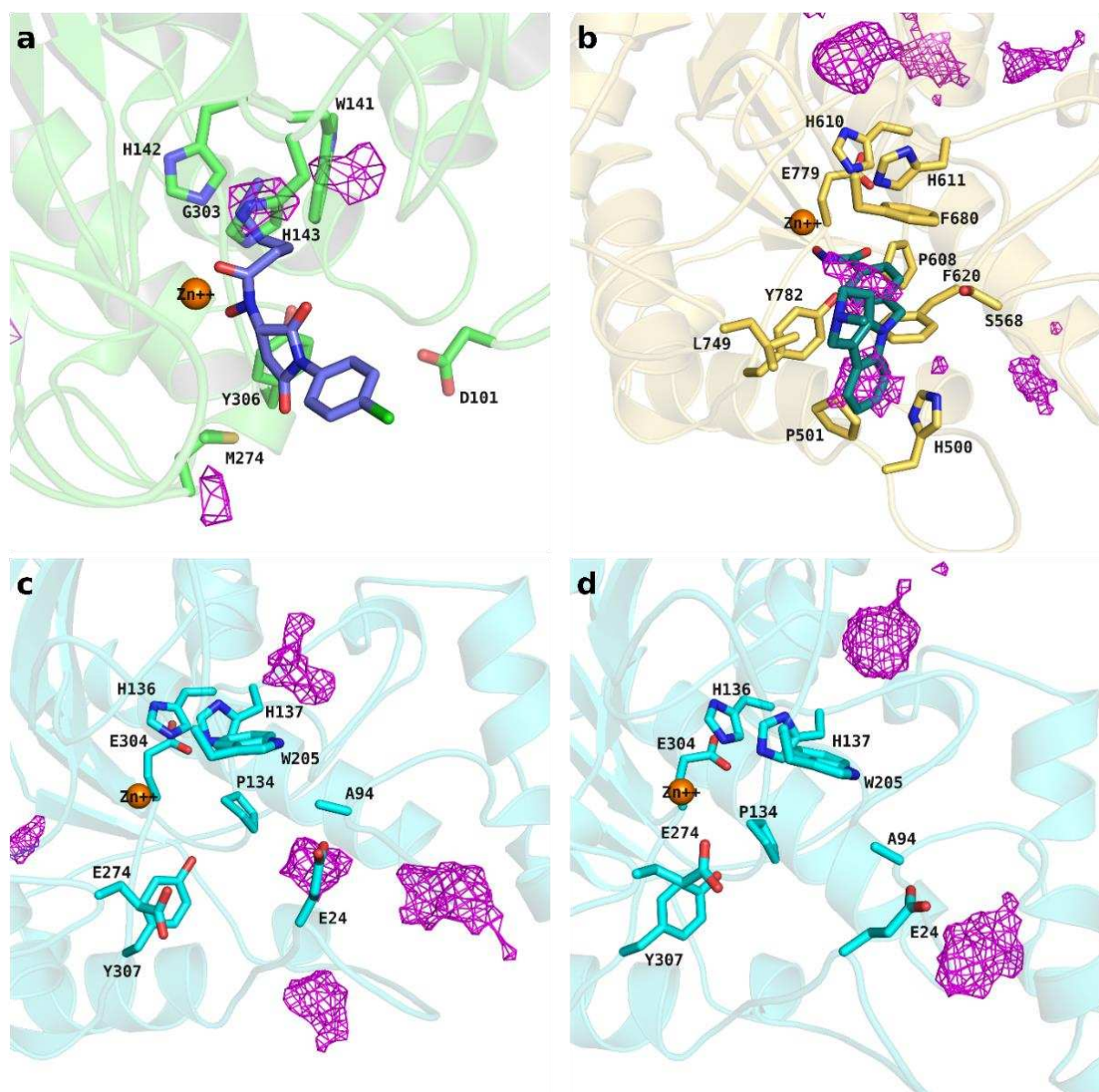
Figure 51: Mapping of hotspots identified through Methanol Cosolvent Molecular Dynamics (MD) simulations in HDAC isoforms. **a)** HDAC8 (PDB ID: 2V5X) showing hotspots (magenta meshes) in the 'foot pocket' and distal regions, along with N-alkyl hydroxamate (purple sticks, PDB ID: 6FU1). Key residues such as H142, H143, W141, G303, and M274 are highlighted in green. **b)** HDAC6 (PDB ID: 5EDU) with hotspots (magenta meshes) overlapping Tubastatin A (teal sticks, PDB ID: 6THV) in the hydrophobic patch. Key residues including H610, E779, F620, P501, and L749 are shown in yellow. **c, d)** HDAC10 structures (PDB IDs: 6WDW and 7U69) showing methanol-identified hotspots (magenta meshes) distant from the binding pocket, with key residues H136, E304, E274, and Y307 highlighted in cyan. Orange spheres denote zinc ions at catalytic sites.

In parallel with the methanol mapping studies, a portion of the class I HDAC-specific foot pocket was detected in HDAC8 by using the ethanol probe molecule. These hotspot locations are depicted as orange mesh (see Figure 52a). Similar to the methanol studies, the N-alkyl

hydroxamate structure (seen as purple sticks) was transferred from the crystallized complex of smHDAC8 (PDB ID: 6FU1) to demonstrate the overlap between the alkyl structure located in a portion of the foot pocket and the detected hotspot. Other hotspots were also observed on the outer surface of the loops comprising the binding pocket of the HsHDAC8 isoform.

HDAC6 co-solvent MD simulations with ethanol probe molecule resulted in the mapping of the hotspot located in the distal region of the binding pocket, which matches the hydrophobic patch of HDAC6 mentioned earlier, as well as the detection of several hotspots of different sizes or scales located away from the binding pocket. These hotspots are visually shown as orange mesh in Figure 52b. It was clearly observed that the phenyl ring in the hydrophobic tetrahydro-γ-carboline capping group of Tubastatin A aligned with the hot spot detected in the binding pocket. In conclusion, the mapping of the hydrophobic patch (F620-P501-H500-L749) and its location within HDAC6 was successfully accomplished using an ethanol probe molecule as cosolvent. This is noted as evidence that cosolvent studies can detect and map even small patches that may affect the binding pose and possible additional pockets as intended.

In the ethanol occupancy grid maps obtained from cosolvent studies with both humanized DrHDAC10 crystal structures, several hotspots of various sizes were observed in locations far from the binding pocket, beyond the reach of ligands, hence unlikely to affect the binding pose. These hot spots are illustrated as orange mesh in Figures 52c-d.
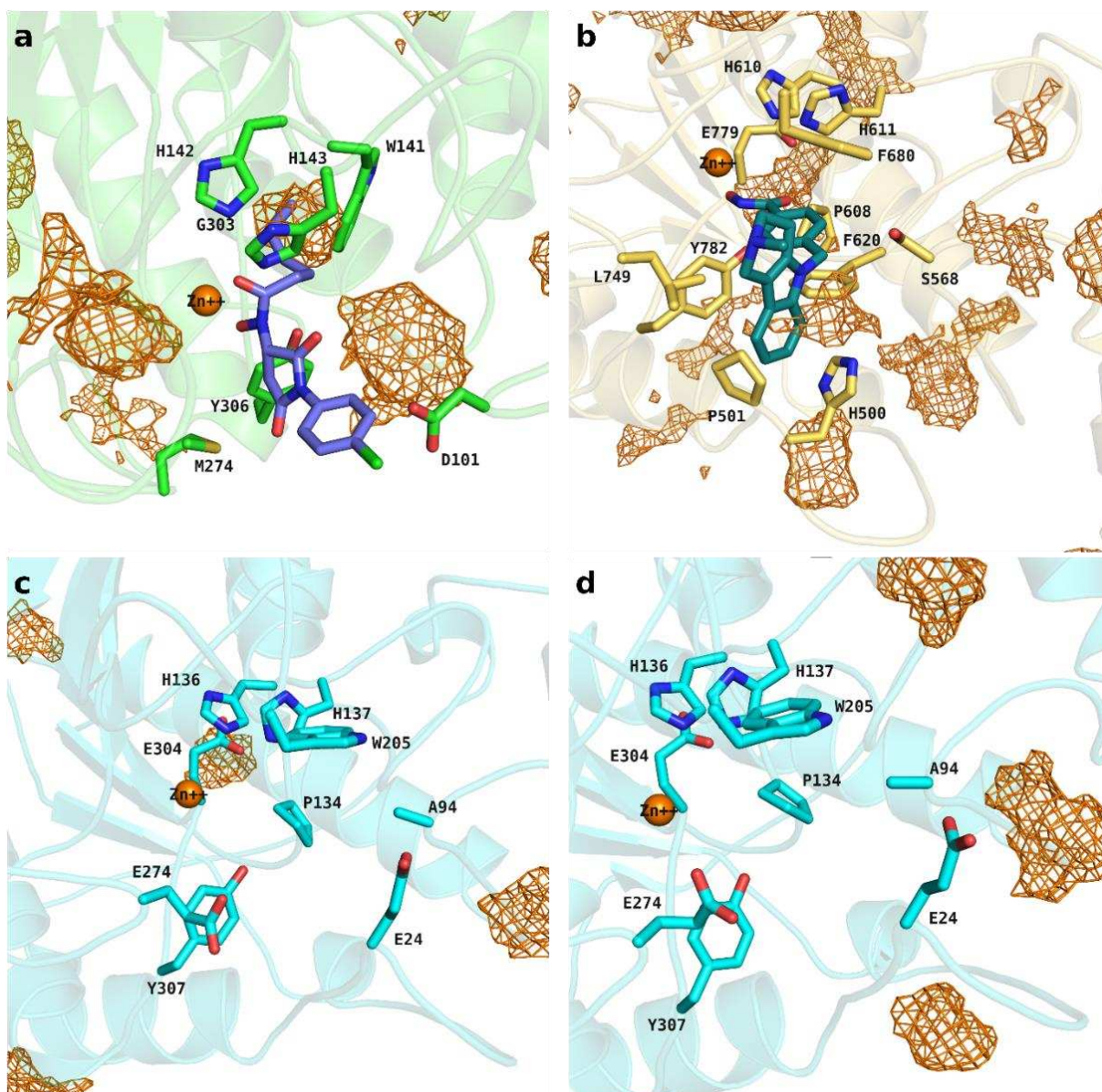
Figure 52: Mapping of hotspots identified through Ethanol Cosolvent Molecular Dynamics (MD) simulations in HDAC isoforms. **a)** HDAC8 (PDB ID: 2V5X) showing hotspots (orange meshes) in the 'foot pocket' and outer surface loops. The N-alkyl hydroxamate (purple sticks, PDB ID: 6FU1) transferred from smHDAC8 illustrates the overlap with the detected hotspot in the foot pocket. **b)** HDAC6 (PDB ID: 5EDU) displaying a hotspot (orange meshes) within the distal hydrophobic patch (F620, P501, H500, L749) and additional hotspots located away from the binding pocket. Tubastatin A (teal sticks, PDB ID: 6THV) was transferred to confirm the alignment of its phenyl ring within the mapped hotspot. **c, d)** HDAC10 structures (PDB IDs: 6WDW and 7U69) showing ethanol-identified hotspots (orange meshes) in locations far from the binding pocket, unlikely to influence ligand binding. Orange spheres represent zinc ions at the catalytic sites.

As mentioned earlier, in Cosolvent MD studies, another probe molecule used is acetamide. Acetamide hotspots are shown here as red meshes in the grid occupancy maps obtained in the co-solvent molecular dynamic study of each complex. In these HDAC8 2V5X, HDAC6 5EDU and HDAC10 6WDW crystals, as mentioned earlier, the phenyl hydroxamate structure was left as part of the active ligands in the complexes and hotspots were detected in the central regions of the binding pockets. These hotspots correspond to hydrogen bonding interactions involving the amino acid side chains D101 (HDAC8), S568 (HDAC6), and E274 (HDAC10) with the

99

acetamide structure, as well as hydrophobic interactions between the hydrophobic side of the binding pocket and the methyl group of acetamide. These hotspots are larger and more widespread in HDAC8 (see Figure 53a) and HDAC10 (see Figure 53c) crystals, whereas HDAC6 (see Figure 53b) exhibits a less intense and smaller hotspot around S568 residue. Additionally, there were some variations in the size and number of small hotspots observed on the surfaces of the protein structures in all the examined crystal structures except for HDAC8. However, these hotspots were disregarded since they were determined to be unrelated to the location and binding pose of the binding pocket, as discussed previously.

Lastly, when analyzing the 7U69 coded HDAC10 crystal structure, a distinct situation emerged, which is not surprising given the unique circumstances. As previously noted, in the complex created for co-solvent molecular dynamics studies, the methylphenylacrylhydroxamate structure was retained within this crystal structure. Currently, this structure exhibits electronic interactions through the protonated piperidine nitrogen with E274 and π-cation interactions with W205. Consequently, unlike other complexes, the acetamide structure did not aggregate in the central part of the already occupied binding pocket by protonated piperidine. As a result, grid occupancy hotspots did not form in this location (see Figure 53d).
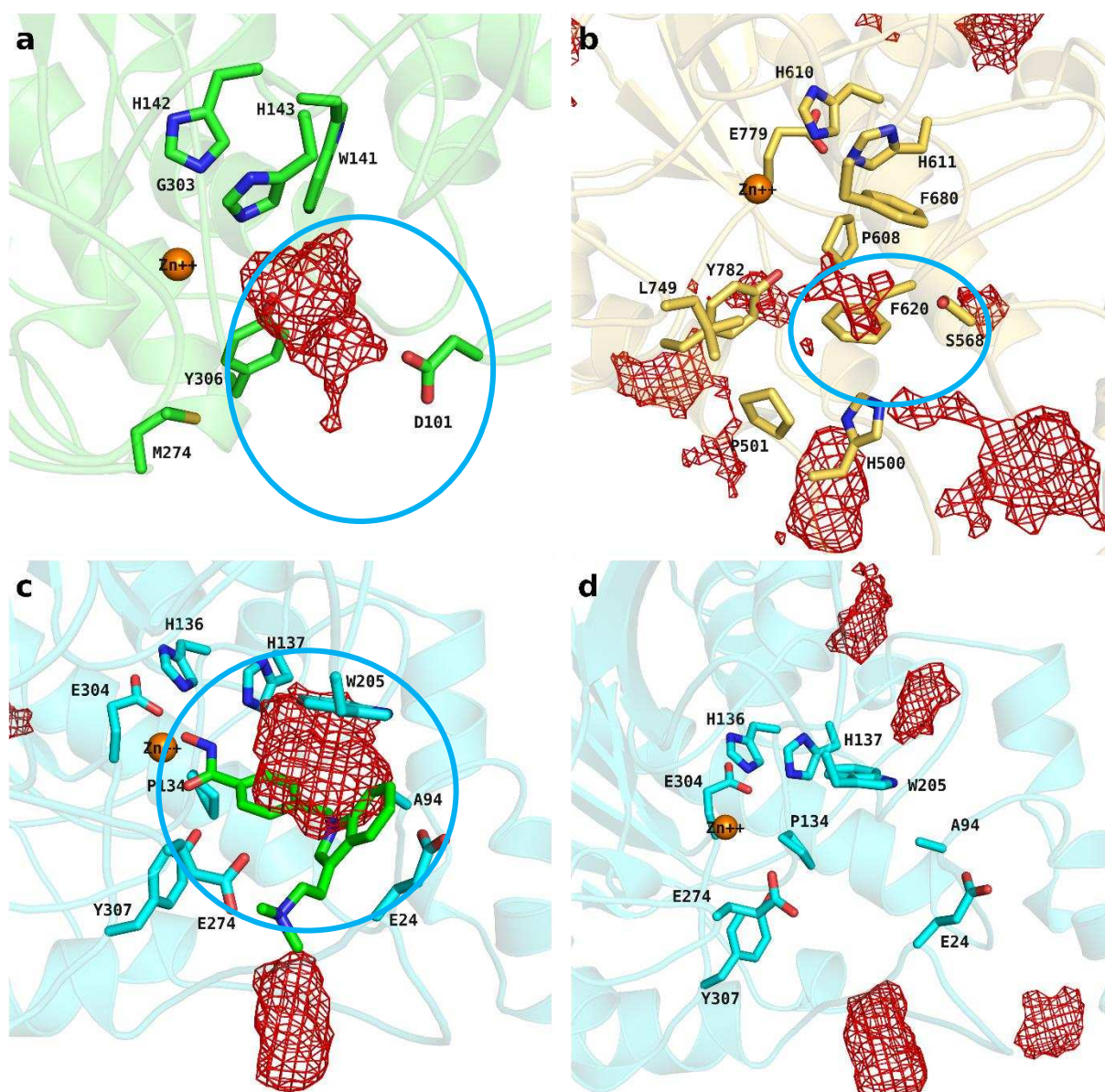
Figure 53: Mapping of hotspots identified through Acetamide Cosolvent Molecular Dynamics (MD) simulations in HDAC isoforms. **a)** HDAC8 (PDB ID: 2V5X) showing widespread acetamide hotspots (red meshes) in the central binding pocket, interacting with D101 through hydrogen bonding and hydrophobic interactions with the methyl group of acetamide, **b)** HDAC6 (PDB ID: 5EDU) displaying smaller hotspots (red meshes) around S568 within the binding pocket, indicating moderate hydrogen bonding and hydrophobic interactions. **c)** HDAC10 (PDB ID: 6WDW) with significant hotspots (red meshes) in the binding pocket center, showing interactions with E274 and W205, aligned with the crystallized dimethylaminoethylindole phenyl hydroxamate structure (light green sticks). **d)** HDAC10 (PDB ID: 7U69) with acetamide hotspots located away from the central binding pocket. Orange spheres represent zinc ions at the catalytic sites.

Triethylamine was used as the fourth co-solvent probe molecule. As a result of the triethylamine co-solvent dynamics simulations conducted with HsHDAC8 (PDB ID: 2V5X) and the phenyl hydroxamate ligand fragment, a substantial and clear hotspot corresponding to the unique side pocket specific to the HDAC8 isoform was obtained. The alignment of this side pocket with the structure crystallized with SmHDAC8 and the selective "L"-shaped HDAC8 inhibitor (PDB ID: 6HQY), previously referred to in the literature as PCI34051 (shown as teal sticks), confirmed its location (see Figure 54a). As a result, a portion of the HDAC8 binding pocket

and the HDAC8-specific hydrophobic side pocket were successfully determined using the triethylamine probe molecule as a co-solvent.

As a result of using triethylamine as the co-solvent probe molecule in HDAC6 co-solvent studies, hot spots were observed on the outer surfaces of the HsHDAC6 (PDB ID: 5EDU) in various including the previously mentioned HDAC6-specific hydrophobic patch. These hotspots are shown as blue meshes in Figure 54b. Although no clear and distinct hotspot mapping was obtained as in the HDAC8 isoform, it is clear that a hotspot marking part of the HsHDAC6 binding pocket, and the region of the hydrophobic patch area overlaps with the hydrophobic capping group of the Tubastatin A (shown as teal stick) transferred from the DrHDAC6 crystal (PDB ID: 6THV). In other words, determination of the hydrophobic patch and its location, as targeted in the co-solvent studies, was also possible in this HDAC isoform by using triethylamine as the co-solvent probe molecule.

Unlike the triethylamine studies with HsHDAC8 (PDB ID: 2V5X) and HDAC6 (PDB ID: 5EDU) crystals, no triethylamine grid occupation hotspots were observed near or related to binding pocket in both humanized DrHDAC10 (PDB IDs: 6WDW and 7U69, respectively) crystal structures used. Instead, in both crystals, hotspots of different sizes and locations were observed on protein surfaces, shown as blue meshes (Figure 54c-d). These are in line with the previously mentioned co-solvent MD results of humanized DrHDAC10 crystal structures using ethanol and methanol probe molecules.
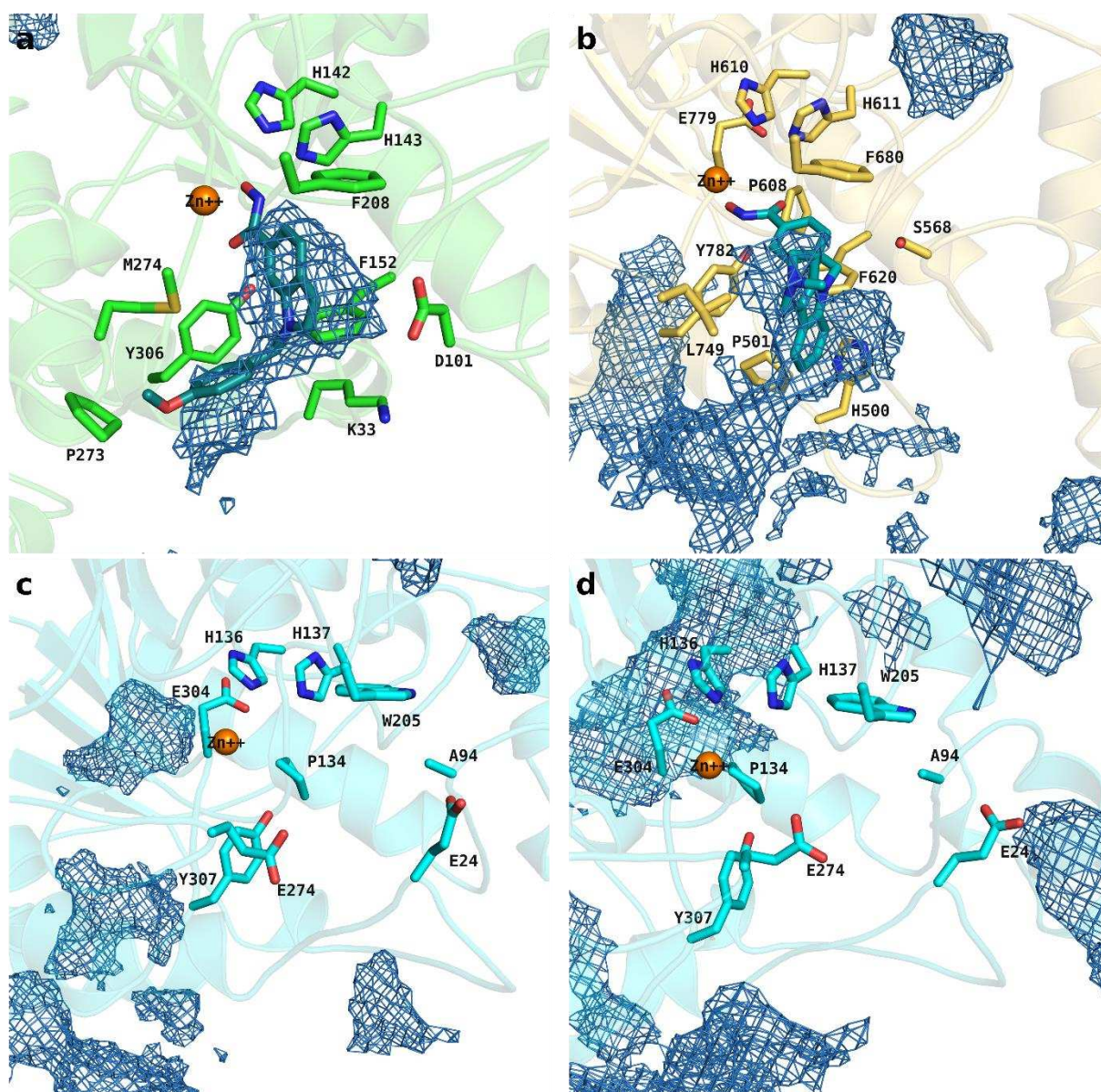
Figure 54: Mapping of hotspots identified through Triethylamine Cosolvent Molecular Dynamics (MD) simulations in HDAC isoforms. **a)** HDAC8 (PDB ID: 2V5X) showing significant hotspots (blue meshes) within the binding pocket and the HDAC8-specific hydrophobic side pocket. The alignment with the selective HDAC8 inhibitor PCI34051 (teal sticks, PDB ID: 6HQY) confirms hotspot locations corresponding to the hydrophobic linker and capping group, **b)** HDAC6 (PDB ID: 5EDU) showing hotspots (blue meshes) partially overlapping the hydrophobic patch and binding pocket. The hydrophobic capping group of Tubastatin A (teal sticks, PDB ID: 6THV) aligns with the mapped hotspot, indicating the successful identification of the targeted hydrophobic patch, **c)** HDAC10 structures (PDB ID: 6WDW) showing triethylamine-identified hotspots (blue meshes) primarily on the protein surface and away from the binding pocket, consistent with other cosolvent studies using ethanol and methanol, **d)** HDAC10 (PDB ID: 7U69) showing similar hotspot locations, suggesting a lack of relevant interactions within the HDAC10 binding pocket for this probe.

Pyridine is the fifth and the last probe molecule used in co-solvent studies. Examining the results of pyridine co-solvent MD simulations for HsHDAC8 (PDB ID: 2V5X), it is clear that the pink mesh representations of the pyridine occupancy grids clearly highlight the class I HDAC-specific foot pocket and the HDAC8 isoform-specific side pocket. (see Figure 55a).

In the pyridine co-solvent studies conducted with the HsHDAC6 complex, alongside some pyridine occupancy hotspots located away from the protein's binding pocket, attention is drawn to a large, T-shaped pyridine density hotspot that aligns with a portion of the HDAC6 binding pocket, as well as the previously mentioned HDAC6-specific hydrophobic patch (F620-P501-H500-L749). These hotspots are shown as pink meshes in Figure 55b. An examination of the structures of HDAC6 selective inhibitors such as Ricolinostat, Citarinostat, Tubastatin A, WT161, Tubacin, TO-317, HPB, HPOB, ACY-1083 and Nexturastat A, these HDAC6 selective inhibitors have a common feature, which is the presence of branching in the linker moiety and/or the capping group [167, 181]. These inhibitors can be described as having a Y- or T-shaped geometry. The experimentally detected binding pose of TO-317 in the binding pocket of the DrHDAC6 protein is available in the PDB database with PDB ID: 7JOM. This binding pose was transplanted into the binding pocket of the HsHDAC6 protein used in the cosolvent studies, and there is a clear alignment between the transplanted binding pose of the TO-317 ligand, shown as cyan sticks, and the hot spot obtained from the cosolvent studies, shown as pink mesh (see Figure 55b).

Analyzing the pyridine occupancy grid hotspots generated through co-solvent molecular dynamics with a pyridine probe molecule, it was found that in the first studied humanized DrHDAC10 crystal structure (PDB ID: 6WDW), there were some hotspots, shown as a pink mesh, corresponding to surface regions of the HDAC10 protein. More importantly, pyridine hotspots, also shown as pink mesh, were found around amino acids W205, A94 and E24 of the HDAC10 binding pocket and overlapping with the capping group of the co-crystallized ligand. The mentioned hotspots were observed as a result of hydrogen bond interactions between the pyridine probe molecules and the gatekeeper E274 during the cosolvent MD simulations. Additionally, π-π interactions occurred between the pyridine ring and the tryptophan ring, and in some cases, the partially positively charged nitrogen atom in the pyridine ring engaged in ionic interactions with side chain of E24 and backbone of A94. These hotspots, also correspond to the positioning of the hydrophobic linker and capping group of the dimethylaminoethylindole structure crystallized in the 6WDW structure and shown as light green sticks (see Figure 55c).

When pyridine hotspot mapping of another humanized DrHDAC10 crystal structure (PDB ID: 7U69) was examined, it was noted that no hotspots were observed close to the target binding pocket. Instead, pyridine hotspots were identified on the surface areas of the HDAC10 protein, shown as pink meshes (see Figure 55d). The absence of hotspots in the 7U69 HDAC10 crystal, observed in the other HDAC10 crystal structure (PDB ID: 6WDW), is consistent with the

mapping results obtained with the acetamide probe molecule. The reason for the absence of hot spots in 7U69 crystal structure is due to the protonated nitrogen atom of the methylpiperidine acryl hydroxamate ligand fraction t forming ionic bonds with E274, E24 as well as π-cation interactions with W205. These aforementioned interactions prevented the pyridine probe molecule from localizing in this area (see Figure 55c-d).
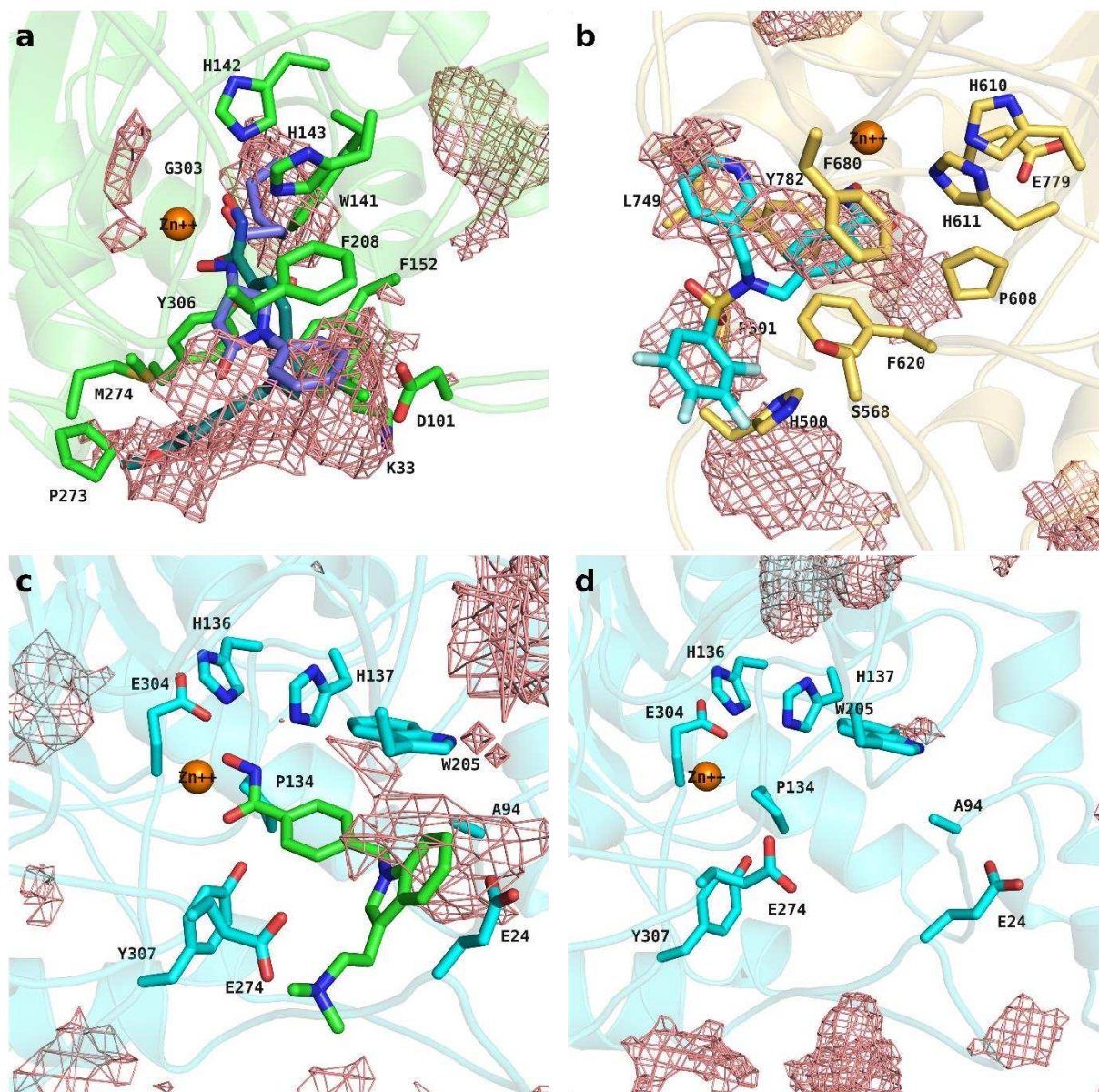
Figure 55: Mapping of hotspots identified through Pyridine Cosolvent Molecular Dynamics (MD) simulations in HDAC isoforms. **a)** HDAC8 (PDB ID: 2V5X) showing pyridine-identified hotspots (pink meshes) in the foot pocket and HDAC8-specific side pocket. The N-alkyl hydroxamate structure (purple sticks, PDB ID: 6FU1) aligns with hotspots under H142 and H143, while the selective HDAC8 inhibitor PCI34051 (teal sticks, PDB ID: 6HQY) overlaps with hotspots in the side pocket. **b)** HDAC6 (PDB ID: 5EDU) with a prominent T-shaped pyridine density hotspot (pink meshes) that aligns with the binding pocket and HDAC6-specific hydrophobic patch (F620, P501, H500, L749). The transplanted binding pose of the HDAC6-selective inhibitor TO-317 (cyan sticks, PDB ID: 7JOM) shows alignment with the hotspot in the binding pocket. **c)** HDAC10 (PDB ID: 6WDW) with hotspots (pink meshes) near W205, A94, and E24, overlapping the capping group of the co-crystallized ligand. The hotspots align with the dimethylaminoethylindole structure (light green sticks) from the 6WDW crystal. **d)** HDAC10 (PDB

ID: 7U69) showing pyridine hotspots (pink meshes) on the protein surface, with no hotspots near the binding pocket due to interactions between the ligand's protonated nitrogen and key residues, preventing pyridine localization in this area**.**

In summary, from the co-solvent studies using different probe molecules, both studies using ethanol and methanol probe molecules enabled the detection of the foot pocket specific to class I HDACs for the HDAC8 isoform as a member of this class, while for the HDAC6 isoform using ethanol and methanol as probe molecules, it was possible to map the hydrophobic patch mentioned in the literature. When acetamide was used as a probe molecule, amino acids capable of forming hydrogen bonds, such as D101 and S568, were identified, along with parts of the binding pockets in HDAC8 and HDAC6.

The use of triethylamine as a co-solvent clearly mapped part of the HDAC8 binding pocket and the HDAC8-specific side pocket, while HDAC6 isoform showed hotspots corresponding to part of the HDAC6 binding pocket and the previously mentioned hydrophobic patch. Finally, in cosolvent molecular dynamics studies using the pyridine probe molecule, the foot pocket and a side pocket were detected in the HDAC8 isoform, while in the HDAC6 isoform a hotspot resembling the letter "T" was detected, including the hydrophobic patch, and corresponding part of the binding pocket.

Co-solvent MD studies using five different probe molecules were generally successful in detecting regions such as the foot pocket and side pocket known to exist in the HDAC8 isoform and the hydrophobic patch known to exist in the HDAC6 isoform, providing validation of the method used.

After successfully mapping and validating the method, the same approach was applied to map the HDAC10 isoform using two humanized DrHDAC10 crystal structures (PDB IDs: 6WDW and 7U69) while retaining the benzhydroxamate and 4-methylpiperidin acryl hydroxamate ligand fractions in the respective binding pockets. Only in the co-solvent studies with the 6WDW crystal structure, some successful mappings were achieved in the binding pocket. When the acetamide probe molecule was used, a hotspot was detected which was related to the gatekeeper E274 and other HDAC10 specific residue W205, in the HDAC10 binding pocket. Additionally, when the pyridine probe molecule was used as co-solvent, a mapping is obtained that also shows part of the binding pocket, with a hotspot along W205, which directs attention to amino acids E274, W205, E24 and A94.

Nevertheless, none of the HDAC10 cosolvent MD mapping studies were able to pinpoint a side pocket or hydrophobic/hydrophilic patch that could be targeted to improve the stability of the

capping group and boost HDAC10 selectivity and activity. The co-solvent studies, on the other hand, underscored the notion of developing inhibitors that could engage with the acidic region created by gatekeeper E274 along with, E24, W205, and A94 within the HDAC10 binding pocket, thereby enhancing HDAC10 selectivity and activity.

4.13. Modeling Ternary Complexes of HDAC10-PROTACs

4.13.1. Workflow for Modelling Ternary Complexes

In this modeling study, HDAC10 PROTACs synthesized by Dr. Fereshteh Mahmoudi from Sippl research group were employed to model ternary complexes comprising the catalytic active domain of the HDAC10 protein, HDAC10 PROTAC, and pVHL. The first set of HDAC10-PROTAC structures was created by linking the VHL ligand to the 4th position of the phenyl ring in the capping group of **47** (PZ46), one of the our most potent HDAC10 inhibitors, using an amide functional group. This linkage was carried out by using alkane linker structures with carbon numbers ranging from 2 to 6, providing diversity and yielding **PROTAC1, PROTAC2, PROTAC3, PROTAC4** and **PROTAC5,** degrader structures. The second set was formed by replacing the phenyl ring in the first set with a methylene bridge, resulting in **PROTAC6, PROTAC7, PROTAC8, PROTAC9** and **PROTAC10,** degraders. The compounds in both sets exhibited high HDAC10 inhibition with IC$_{50}$ values ranging from 0.76 to 4.5 nM. Among the tested compounds, **PROTAC6, PROTAC7, PROTAC8, PROTAC9** and **PROTAC10** from the second set exhibited significantly higher HDAC10 degradation than the others, with degradation levels of 70% or more. These compounds were identified as strong degraders. **PROTAC1** and **PROTAC2** from the first set were classified as moderate degraders, showing approximately 50% and 30% degradation, respectively. In contrast, **PROTAC3, PROTAC4** and **PROTAC5** from the first set showed no degradation and were labelled as non-degradants. This assessment was carried out by Andreas Mieland and Elena Weis from the research group of Professor Oliver Krämer, our collaborating group at the University of Mainz, Germany. The biodegradation assay method used for this evaluation is detailed in the appendix. It is also noteworthy that although the replacement of the phenyl ring with a methylene bridge did not significantly affect the inhibition values, it had a notable effect on the degradation values (see Figure 56).
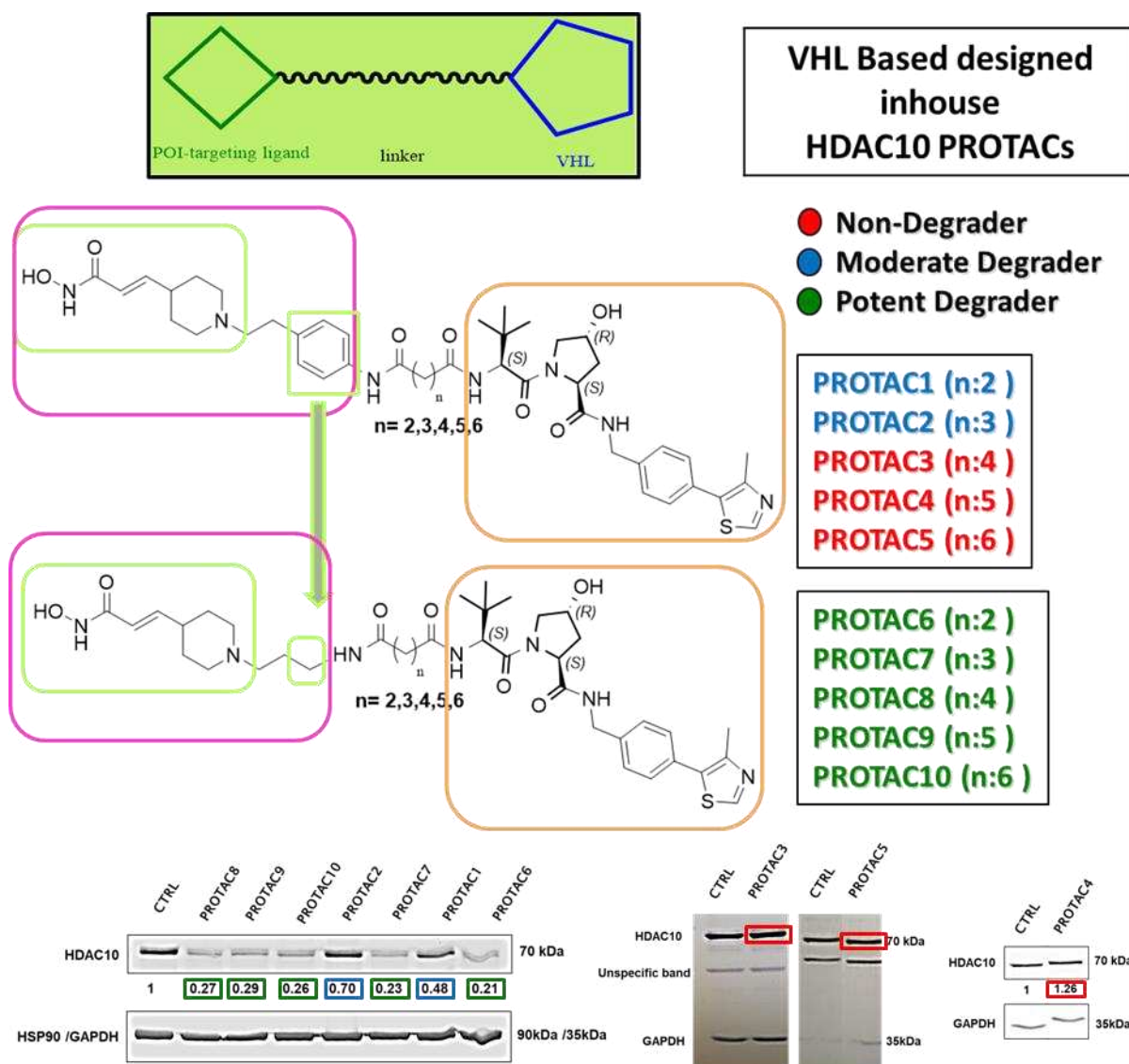
Figure 56: The figure showcases the design, synthesis, and evaluation of HDAC10 PROTACs. The top section shows the PROTAC structure with different linkers used to create two sets of compounds. The middle section categorizes PROTACs based on degradation performance: strong degraders (green), moderate degraders (blue), and non-degradants (red). The bottom section presents Western blot analysis, confirming HDAC10 degradation levels for each compound. Strong degraders (**PROTAC6, PROTAC7, PROTAC8, PROTAC9** and **PROTAC10**) significantly degraded HDAC10, while moderate (**PROTAC1** and **PROTAC2**) and non-degradants (**PROTAC3, PROTAC4** and **PROTAC5**) showed lower or no degradation.

In the development of PROTACs, the modeling of ternary complexes can play a particularly instrumental role. Various software, methodologies, and procedures are now available for this purpose [31]. The approach adopted in this study for HDAC10-PROTACs, along with the programs utilized, is depicted in Figure 57 and explained in the sections 3.1.6-3.1.8 in details.

Workflow: modeling ternary complexes

- Protein Preparation Wizard (Schrödinger/2021)

Preparation of pVHL and POI (HDAC10) →

Protein-protein docking →
- PROTAC modeling tools in MOE (version 2020/2019)
- Method 4B
- Method 5
- RMSD RF, ligand_E and visual inspection

Selection of ternary complexes →

RMSD-calculations →
- MOE (version 2020/2019)
- Sequence and structural alignment

MD-simulations (500ns) →
- AMBER22
- Trajectory Analyses, RMSD, RMSF and distance calculations

Docking of Degradars
- Glide SP Docking (Schrödinger/2021)

Figure 57: Approach to modeling the ternary complexes of HDAC10-PROTACs and the programs used in the process.

Modeling of the ternary complexes was done with the VHL protein, HDAC10 protein and aforementioned FM degraders. Crystal structure of the VHL protein was downloaded from Protein Data Dank with the PDB ID: 5T35 which is a ternary complex including pVHL as protein degrader, BRD4 BD2 as POI and the PROTAC MZ1 [182]. For the HDAC10 protein humanized DrHDAC10 crystal with the PDB ID:7U69 was used which includes the HDAC10 inhibitor compound **47** (PZ46) [153].

After downloading the corresponding protein structures, protein preparations were done in the Schrodinger/2021 software with the usage protein preparation wizard. Subsequently, protein-protein dockings were done with the PROTAC modeling tools in the MOE (MOE versions 2019/2020) first using Method 4B which was the superior Method among the PROTAC modeling tools in the MOE packages according to literature. However, visual inspection showed that the bidentate zinc coordination in the crystal structure used was not present in the formed ternary complex, so another method, Method 5, was used as an alternative.

4.13.2. Selection of The Ternary Complexes

Between 283-285 ternary complexes were generated for all studied PROTACs as a result of Method 5. These outputs are further filtered by the consideration of the RMSD_RF and Ligand_E values in Method 5, serving as the primary criteria for further filtering. Additionally, a secondary filtering based on visual inspections was applied, examining the interactions shown by the ligand warheads in the used crystal structures and the C-C bond angles and lengths within the alkane structures used as linkers. In accordance with all the aforementioned restrictions, the final ternary complexes fulfilling the specified conditions were selected: 0 for **PROTAC1,** 3 for **PROTAC2**, 1 for **PROTAC3**, 2 for **PROTAC4**, 4 for **PROTAC5**, 3 for **PROTAC6**, 5 for **PROTAC7**, 1 for **PROTAC8**, 3 for **PROTAC9**, and 0 for **PROTAC10**. No consensus was found among the ternary complexes obtained for the different PROTACs. Consequently, the modeling results pertaining to **PROTAC6**, which is among the strongest degraders and features the shortest linker moiety among the FM PROTACs used in the modeling studies, were subjected to further advanced modeling investigations (see Figure 58).

PROTAC	Total number of ternary complexes	Selected ternary complexes	P-P Dock Pose	Degradation Activity
PROTAC1	283	0	-	Moderate
PROTAC2	283	3	111, 138, 144	Moderate
PROTAC3	283	1	53	No
PROTAC4	283	2	111, 230	No
PROTAC5	285	4	58, 97, 152, 224	No
PROTAC6	**283**	**3**	**7, 26, 152**	Strong
PROTAC7	283	5	19, 32, 96, 111, 187	Strong
PROTAC8	284	1	187	Strong
PROTAC9	284	3	89, 97, 152,	Strong
PROTAC10	285	0	-	Strong

RMSD_RF [Å]:
- o RMSD of PROTAC in final ternary complex ↔ nearest local minimum after minimization without proteins

ligand_E [kcal/mol]:
- o total forcefield energy of PROTAC conformation in the ternary complex

visual inspection:
- o protein-ligand interactions
- o bond lengths of the linker

Figure 58: Summary of ternary complex selection and degradation activity of PROTACs: The table shows the total number of ternary complexes generated, selected complexes, corresponding protein-protein docking poses, and degradation activity for each PROTAC. Highlighting PROTAC6 as a strong degrader with unique docking poses (7, 26, 152), among others evaluated.

Examination of the complex models of PROTAC6 reveals three distinct ternary structures with various positioning, protein-protein and protein-PROTAC interactions. In these P-P docking solutions, ternary complexes are superimposed over the larger protein, POI (HDAC10), showcasing the different positions of s VHL and PROTAC6 within the complexes.

RMSD values were calculated for the VHL proteins depicted in these figures, or alternatively, for all proteins within the complexes, including HDAC10 and VHL proteins. P-P Docking

poses 152 and 7 show RMSD values of 55.5 Å and 14.2 Å for the VHL structure with respect to the top-ranked result from the MOE PROTAC modeling tool, P-P Docking pose 26. Upon analysis of these results and figures, it is apparent that P-P docking poses 26 and 7 exhibit closer proximity to each other, while pose 152 deviates significantly from them. Additionally, while it is clear that the PROTAC6 in P-P docking pose 152, differs distinctly in orientation from both the PROTAC6 in P-P docking pose 26 and the PROTAC6 in P-P docking pose 7s, it is also observed that the orientations of PROTAC6s in P-P docking poses 26 and 7 are more similar to each other but still exhibit differences (see Figure 59).
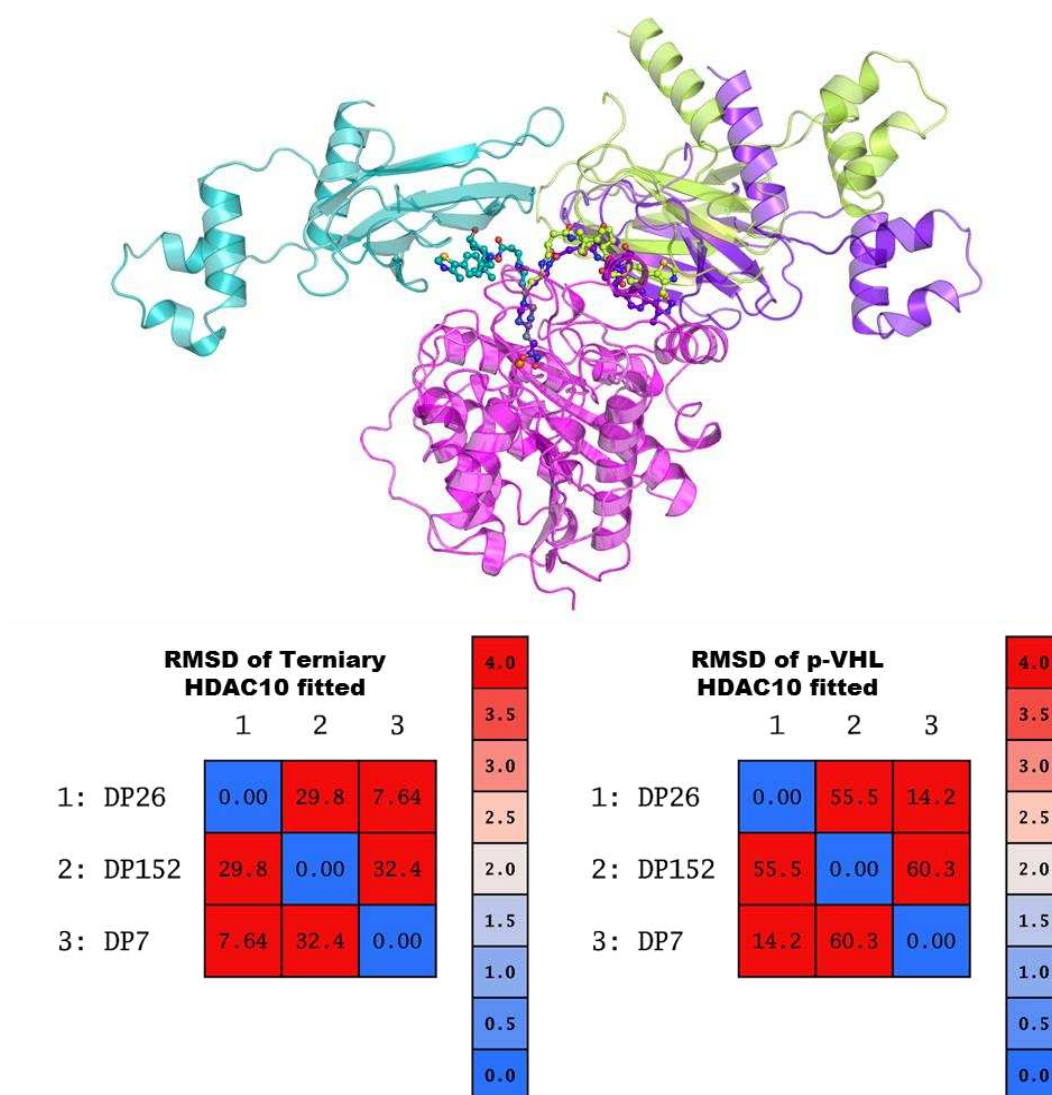
Figure 59: Distinct Ternary Structures and RMSD Analysis of PROTAC6: Superimposed models of HDAC10 (pink) with VHL proteins in docking poses 26 (lemon green), 7 (purple), and 152 (teal) reveal varying orientations and interactions of PROTAC6 within the complexes. RMSD heatmaps show structural deviations among the ternary complexes and VHL proteins, highlighting the closer similarity between poses 26 and 7 compared to pose 152.

4.13.3. MD-Simulations of The Selected Ternary Complexes

As a subsequent procedure, the stability of the selected modeled ternary complexes, specifically PROTAC6_26, PROTAC6_152, and PROTAC6_7, was assessed using molecular dynamics simulations with AMBER22 program as in the previous studies.

For analysis RMSD, RMSF and distance calculations were computed separately for HDAC10 and VHL proteins, after fitting to the C-alpha atoms of the respective protein. RMSD calculations for the catalytic zinc ion were performed by aligning the alpha carbon atoms of the HDAC10 proteins, thus undergoing a fitting process to HDAC10. For the RMSD calculations of PROTAC and the ternary complex, the alignment was performed on the alpha carbon atoms of the ternary complex proteins. As a last step, the stability of some key interactions made by the VHL and HDAC warheads within their respective binding pockets, and whether these warheads remain in these pockets, were assessed by examining the distances between the atoms that form these bonds, and the variations in these distances. These combined computations were conducted to gain a more detailed and comprehensive understanding of the stability of the proteins, the stability of PROTAC, and ultimately, the stability of the ternary complex.

In MD simulations of the PROTAC6_26 ternary complex, the HDAC10 protein was observed to consistently maintain RMSD values below or around 2 Å. The RMSD profile of the catalytic zinc ion is significantly stable at about 1 Å, while the VHL peaks at 4 Å but generally remains between 1.5-3 Å. The overall complex RMSD values show fluctuations between 4 and 8 Å beyond the first 100 ns (see Figure 60a). The RMSF values of HDAC10 are stable, in agreement with RMSD stability, except for a residue near position 330 (see Figure 60a, b). Conversely, the RMSF of VHL shows high values around amino acids 161-181, explaining the high values and fluctuations in the RMSD plot (see Figure 60a, c). This total examination leads us to the conclusion that each protein structure is internally stable, but that the individual proteins making up the whole complex undergoes significant positional shifts relative to each other.

When the PROTAC RMSD plot is examined (see Figure 60d), it is observed that the RMSD values for the PROTAC increase to around 3.5 Å at the beginning of the simulation and increase after 110 ns reaching values as high as 5 Å.

In the analysis of hydrogen bond distances involving the VHL warhead with H110, H115, S111, and Y98 through atoms N(13)H, O(19)H, O19, and O15, a consistently stable profile around 2 Å is noted for the bond with H115. The other interactions show distance values fluctuating between 2 and 4.5 Å, and occasionally peaking at 6 Å (see Figure 60e). All in all, we could observe that the warhead majorly maintained its interactions within the VHL-pocket.

Meanwhile, the hydroxamate moiety of the HDAC10 warhead lost its interaction with the zinc ion within the course of the MD-simulation (O45's zinc coordination distance peaked ranged between 6-8 Å, and O46 fluctuated within 7-8 Å). These variations indicate disrupted interactions between the HDAC warhead and HDAC protein in the PROTAC6_26 ternary complex. This complex, was hence excluded from further studies.
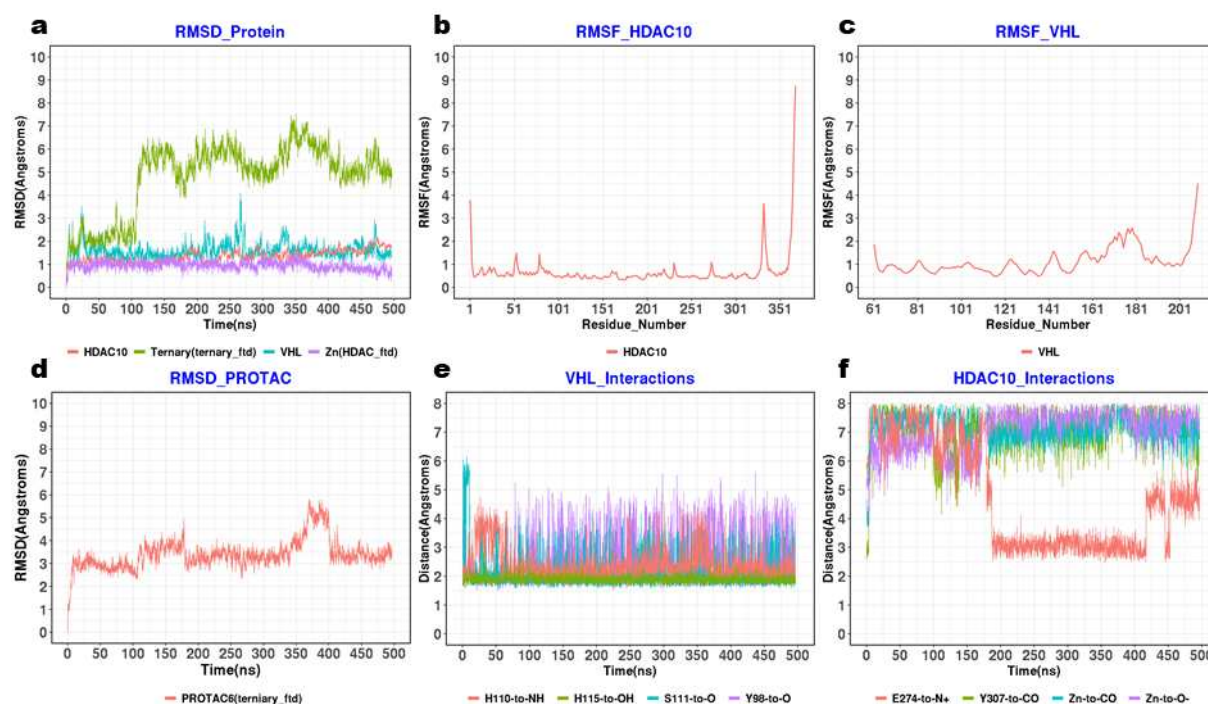
Figure 60: Molecular Dynamics Simulation Analysis of PROTAC6_26: **a)** RMSD profiles of proteins, **b)** RMSF plot of HDAC10, **c)** RMSF plot of VHL, **d)** RMSD plot of PROTAC, **e)** Distance measurements of VHL interactions and **f)** Distance measurements of HDAC10 interactions.

Examination of the graphs from the 500 ns MD simulation of the PROTAC6_7 ternary complex shows that the HDAC10 protein maintains an RMSD range of 1-2 Å. The catalytic zinc atom, shows stability below 1 Å throughout the MD simulation. The RMSD values for the VHL protein fluctuate between 1-4 Å, averaging around 2 Å with a plateau of up to 5 Å between 300-400 ns, then returning to the initial profile in the last 100 ns. The HDAC10 RMSF plot reflects the RMSD values and remains below 2 Å except for a residue around position 330 (See Figure 61a, b). The VHL RMSF plot, although showing higher values than HDAC10, remains below 2 Å except in the range 161-181, which consists of small α-helices between the two flexible loops (See Figure 61a, b, c). This explains the fluctuations and high plateaus in the VHL RMSD plot. The RMSD value for the whole protein complex, initially hovers around 2 Å, jumps to 5 Å and fluctuates between 2-5 Å during the first 200 ns. It then rises to a plateau of 8.5 Å at 250 ns, followed by a fluctuating profile between 4.5-7 Å (See Figure 61a). Overall, the stability assessment is similar to the previous complex: Both protein structures are individually stable,

but the ternary complex does not retain this stability, indicating positional changes and different ternary complex conformations.

When examining the PROTAC RMSD graph for the PROTAC6_7 ternary complex (see Figure 61d), it is observed that the RMSD value gradually increases to approximately 2.5 Å within the first 100 ns of the MD simulation and remains around this value until 250 ns. At 250 ns, the RMSD briefly reaches 6 Å before returning to 3 Å between 250-300 ns. Towards the end of the MD simulation, the RMSD stabilizes between 3-4 Å. This PROTAC RMSD pattern closely resembles the ternary RMSD trend in the protein RMSD plot.

The distances of VHL-containing interactions fluctuate over time in the range 2 to 6 Å (H110-to-NH, H115-to-OH, S111-to-O, Y98-to-O), with most interactions remaining relatively constant, but there are occasional spikes indicating transient changes in interaction distances, except for H115-to-OH, which remains constant around 2 Å (See Figure 61e).

The distances for interactions involving HDAC10 (E274-to-NH, Y307-to-CO, Zn-to-CO, Zn-to-O) also show fluctuations over time. The Zn-to-CO and Zn-to-O interactions are particularly stable, while E274-to-NH and Y307-to-CO show more variability but an overall stable profile. These data indicate that the two warheads remain bound in their respective binding pockets (See Figure 61f).

Overall, the PROTAC6_7 ternary complex obtained from MOE was found to be unstable and evolved into a different positional arrangement. However, throughout the MD simulation, both warhead structures maintained their interactions with the respective proteins and remained stable within their binding pockets.
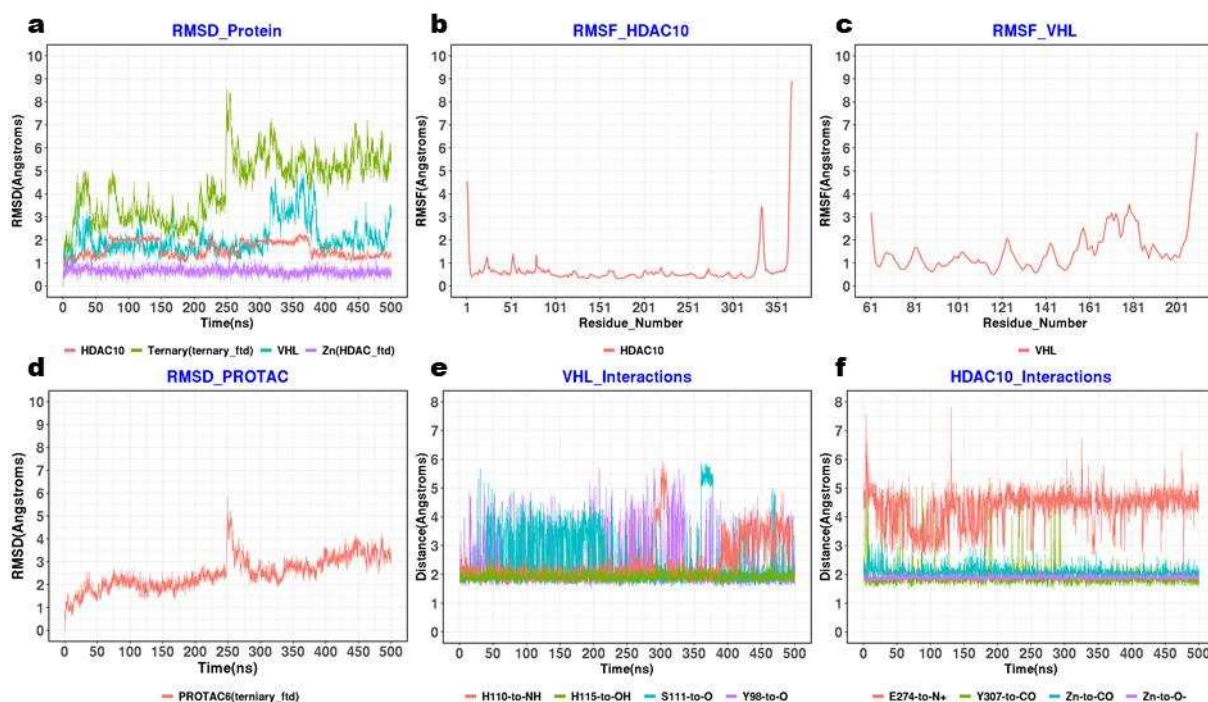
Figure 61: Molecular Dynamics Simulation Analysis of PROTAC6_7: **a)** RMSD profiles of proteins, **b)** RMSF plot of HDAC10, **c)** RMSF plot of VHL, **d)** RMSD plot of PROTAC, **e)** Distance measurements of VHL interactions and **f)** Distance measurements of HDAC10 interactions.

The conformational changes PROTAC6_7 ternary complex during the 500 ns MD simulation was analyzed, with HDAC10 proteins superimposed for visualization (Figure 62). During the first 100 ns, the VHL protein exhibited a slight shift (Figure 62a). Between 100-200 ns, it maintained this new position (Figure 62b), but significant rearrangement occurred from 200-300 ns (Figure 62c). Minor adjustments were noted between 300-400 ns (Figure 62d), while stability was maintained from 400-500 ns (Figure 62e). The major positional shifts and significant changes from the beginning to the end of the 500 ns MD simulation are highlighted in Figure 62f.
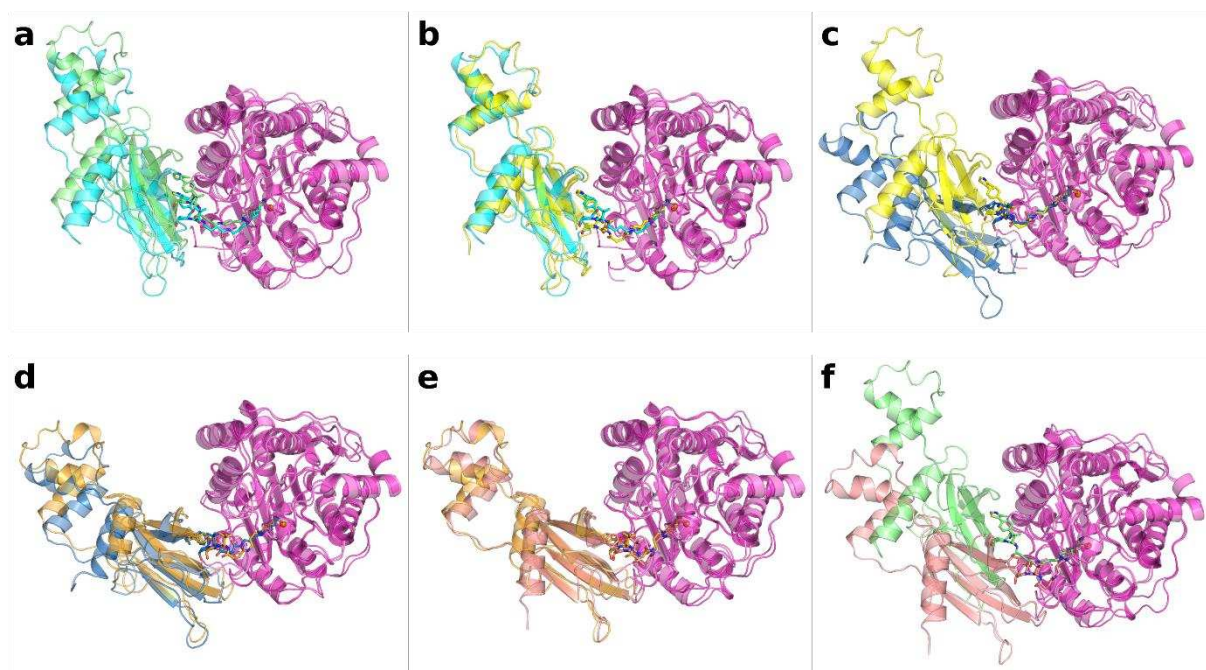
Figure 62: Positional Evolution of VHL in the PROTAC6_7 Ternary Complex During 500 ns MD Simulation: **a)** VHL positions before MD (green) and at 100 ns (cyan), **b)** VHL positions at 100 ns (cyan) and at 200 ns (yellow), **c)** VHL positions at 200 ns (yellow) and at 300 ns (blue), **d)** VHL positions at 300 ns (blue) and at 400 ns (orange), **e)** VHL positions at 400 ns (orange) and at 500 ns (peach), **f)** VHL positions compared between before MD (green) and 500 ns (peach). The HDAC10 protein within the ternary complex is indexed and kept fixed throughout the simulation, shown in pink and purple.

The initial arrangement of the PROTAC6_7 ternary complex (0 ns) solution from the aforementioned Method 5 and the arrangement obtained at the end of the 500 ns MD simulation have been examined in detail and are depicted in Figure 63, where protein-protein and PROTAC-protein interactions are also illustrated.

The initial ternary complex is shown in Figure 63a. The left part of the image highlights interactions between VHL and HDAC10, focusing on salt bridges (Arg107-Glu187, Arg107-Glu186, Arg108-Glu186) and a hydrogen bond (Gln96-Lys91). The middle image presents these interactions in 2D, differentiating hydrogen bonds, salt bridges, and hydrophobic interactions. The right image illustrates interactions between the PROTAC6 and both proteins, including cation-π (HDAC10: Trp205), hydrogen bonds (HDAC10: His136, His137, Tyr307, Glu274; VHL: Arg69, Tyr98, His110, Ser111, His115, Asn67, Ser68, Tyr112), metal coordination (HDAC10: catalytic zinc ion), and π-π interactions (HDAC10: Tyr183; VHL: Tyr98).

The final ternary complex arrangement after the 500 ns MD simulation is shown in Figure 63b. The salt bridge interaction now includes only Arg69-Glu24, while the hydrogen bonds are changed to include Gln73-Hid201, Gln73-Ser203, Arg108-Gln202, and Gln96-Lys90. The middle 2D representation in Figure 18b highlights the updated interactions, differentiating

116

hydrogen bonds, salt bridges, and hydrophobic interactions. The right section illustrates the evolved interactions between the PROTAC6 and both proteins, including conserved cation-π (HDAC10: Trp205), hydrogen bonds (HDAC10: His136, His137, Tyr307 conserved; Asn93, Asn207 new; VHL: Tyr98, Ser111, His115 conserved; Arg69, His110 lost; Arg107 new), conserved metal coordination (HDAC10: catalytic zinc ion), π-π interactions (HDAC10: Tyr183 lost; VHL: Tyr98 conserved), and a newly formed ionic interaction between HDAC10 Glu274 and the protonated nitrogen of the HDAC10 warhead, which developed from a water-mediated hydrogen bond during MD simulation.

The final arrangement shows that some interactions are preserved, some are lost, and new interactions were formed, highlighting the dynamic nature of the ternary complex and the shift of the protein-protein interaction surface throughout the MD simulation.
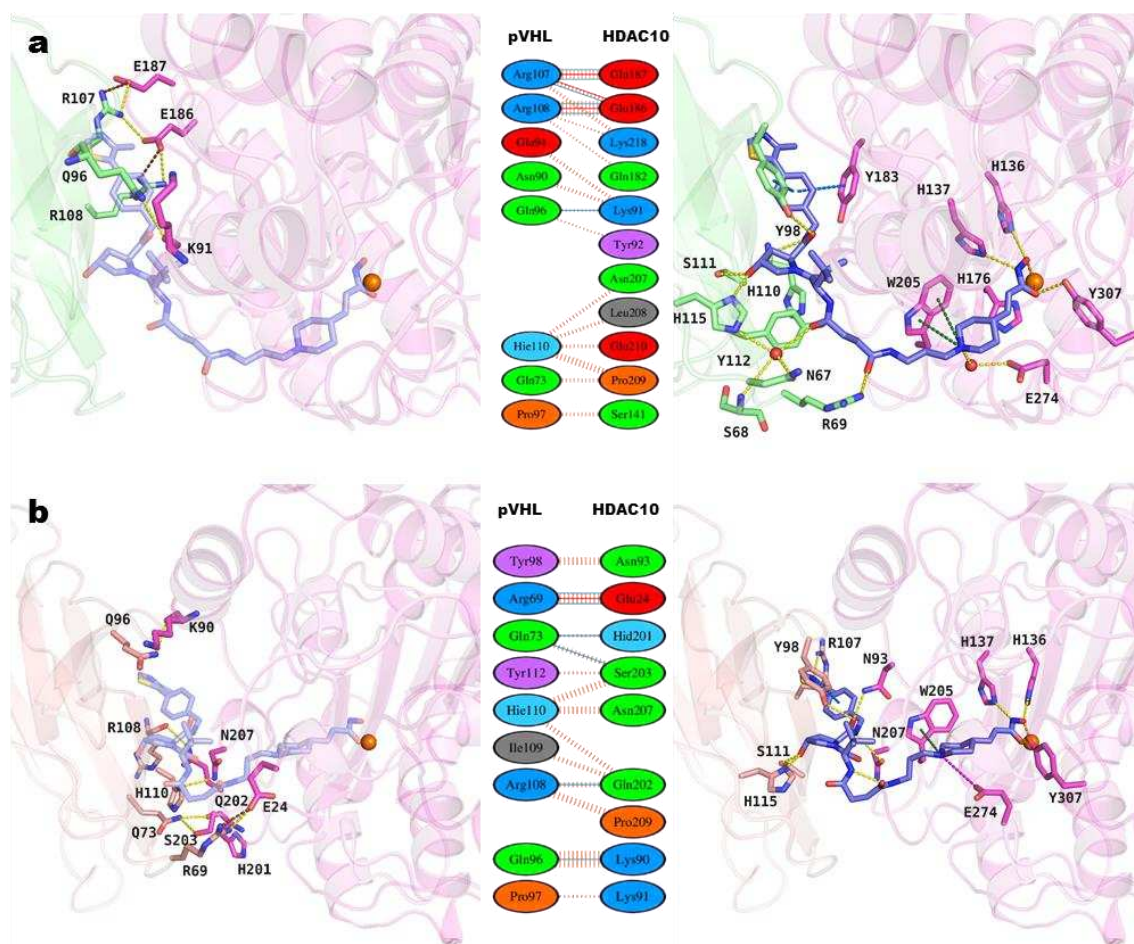
Figure 63: Configuration of PROTAC6_7 Ternary Complex before MD and at 500 ns MD Simulation: **a)** Before MD: Left—protein-protein interactions between VHL and HDAC10 with salt bridges and hydrogen bonds. Middle—2D interaction map. Right—PROTAC6 interactions with both proteins, **b)** 500 ns: Left—updated protein-protein interactions with salt bridges and hydrogen bonds. Middle—2D interaction map. Right—PROTAC6 interactions with proteins, showing conserved and modified connections. Brown dashed lines indicate salt bridges; yellow indicates hydrogen bonds; green shows cation-π; orange represents metal coordination; blue indicates π-π; magenta shows ionic interactions for the 3D figures. Red lines indicate salt bridges; blue lines show hydrogen bonds; yellow dashed lines represent hydrophobic interactions for the 2D figures.

Finally, the RMSD, RMSF, and distance graphs obtained from the 500 ns MD simulation of the PROTAC6_152 ternary complex were analyzed (Figure 64). As observed with the PROTAC6_7 complex, both VHL and HDAC10 proteins remained stable with RMSD values around 2 Å. The catalytic zinc ion also displayed stability below 1 Å throughout the simulation (Figure 64a). The HDAC10 RMSF graph indicates stability around 1 Å, while the VHL RMSF graph shows a stable profile except for residues 161-181 (Figure 64b, 64c).

However, the ternary complex RMSD remained stable at approximately 4 Å for the first 150 ns, then increased reaching peaks around 9 Å between 200-250 ns. Afterward, it dropped back to around 4 Å and stabilized between 7-8 Å post 400 ns. This indicates that while each protein is individually stable, significant conformational changes occured within the ternary complex (Figure 64a).

Examination of the PROTAC RMSD plots revealed a similar pattern to the ternary complex RMSD graph. The RMSD value of the PROTAC structure was around 2 Å for the first 150 ns, fluctuated up to 9 Å, and stabilized around 6 Å post 350 ns (Figure 64d).

Detailed analysis of interaction distances shows VHL interactions mostly stable around 2-3 Å, with occasional spikes up to 6 Å, while HDAC10 interactions remain stable around 2 Å except Glu274 to protonated nitrogen, which showed fluctuations up to 5 Å indicating the potential formation of a water mediated hydrogen bond (Figure 64e-f).
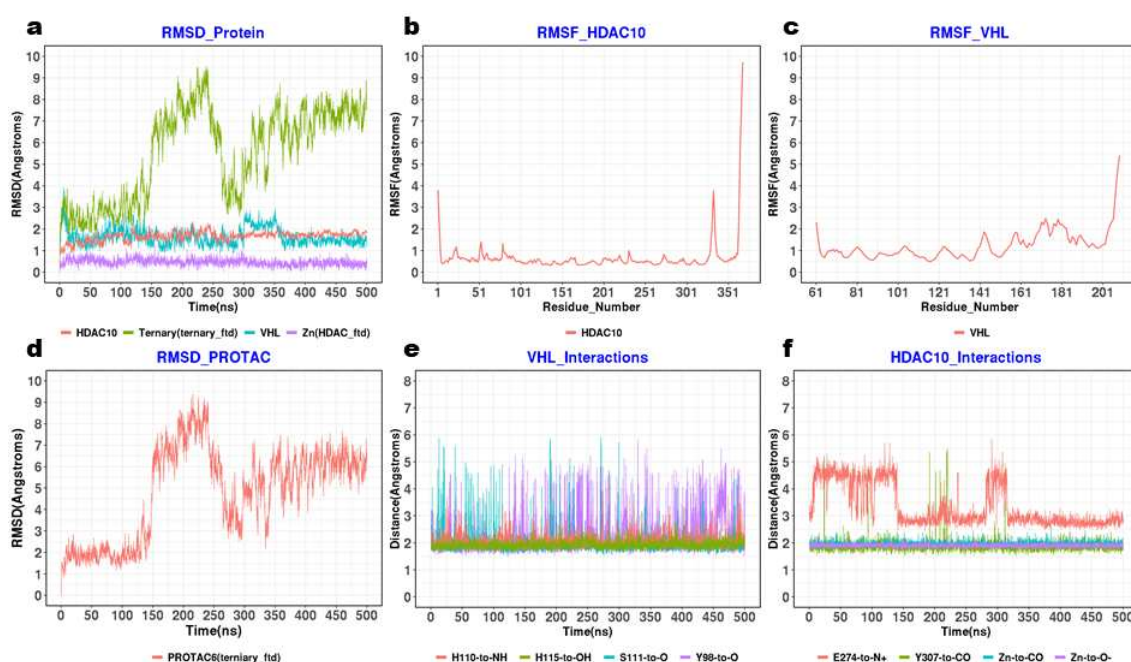
Figure 64: Molecular Dynamics Simulation Analysis of PROTAC6_152: **a)** RMSD plot of proteins, **b)** RMSF plot of HDAC10, **c)** RMSF plot of VHL, **d)** RMSD plot of PROTAC, **e)** Distance measurements of VHL interactions and **f)** Distance measurements of HDAC10 interactions.

The conformational changes of the PROTAC6_152 ternary complex during the 500 ns MD simulation was analyzed by superimposing the HDAC10 proteins for visualization (Figure 65). In the first 100 ns, the VHL protein exhibited a stable profile (Figure 65a). Between 100-200 ns, it showed significant movement (Figure 65b). The VHL protein then returned to its original position during the rearrangement from 200-300 ns (Figure 65c). Between 300-400 ns, a dynamic shift to a different ternary complex conformation was noted (Figure 65d), and this new arrangement was maintained from 400-500 ns (Figure 65e). Finally, major positional shifts and significant changes from the beginning to the end of the 500 ns MD simulation were highlighted (Figure 65f).
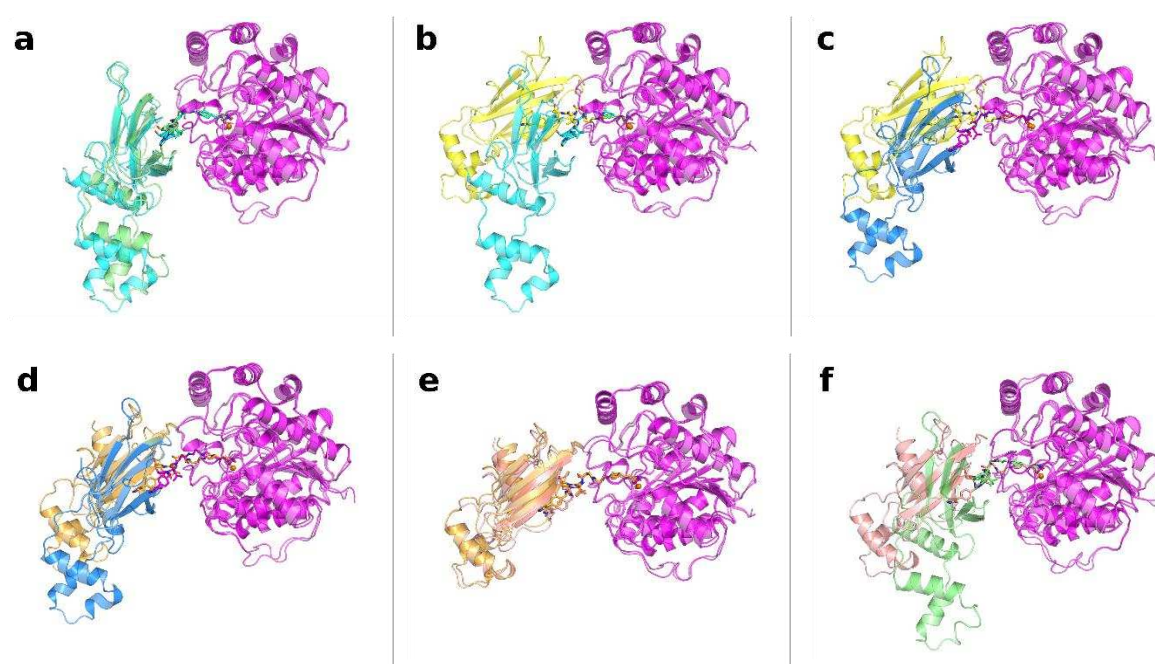
Figure 65: Positional Evolution of VHL in the PROTAC6_152 Ternary Complex During 500 ns MD Simulation: **a)** VHL positions before MD (green) and at 100 ns (teal), **b)** VHL positions at 100 ns (teal) and at 200 ns (yellow), **c)** VHL positions at 200 ns (yellow) and at 300 ns (blue), **d)** VHL positions at 300 ns (blue) and at 400 ns (orange), **e)** VHL positions at 400 ns (orange) and at 500 ns (peach), **f)** VHL positions compared between before MD (green) and at 500 ns (pink). The HDAC10 protein within the ternary complex is indexed and kept fixed throughout the simulation, shown in pink and purple.

The structure of the PROTAC6_152 ternary complex obtained from Method 5 (before MD) and after 500 ns MD simulation is detailed in Figure 66. This figure shows the interactions between the VHL and HDAC10 proteins as well as the interactions between PROTAC6 and both proteins, highlighting the variations that occur throughout the simulation.

In the initial ternary arrangement (Figure 66a, left), protein-protein interactions between VHL and HDAC10 include salt bridges (Arg107-Glu26, Asp92-Lys232, Glu94-Lys232), hydrogen

bonds (Asn67-Ser203, Arg69-Asn207, Arg69-Gln202, Arg108-Thr21, Gln96-Glu276), and additional hydrophobic interactions shown in the center of the figure (middle).

After a 500 ns MD simulation (Figure 66b), the initial salt bridges disappeared, with a new salt bridge forming between Glu70 and Lys90. Similarly, the initial hydrogen bonds were lost, while new hydrogen bonds formed between Arg69-Pro206 and Tyr112-Glu24.

When examining the right side of Figure 66a, initial key interactions between PROTAC6 and both proteins are highlighted. These include cation-π interactions (HDAC10: Trp205), hydrogen bonds (HDAC10: His136, His137, Tyr307, Asn207; VHL: Tyr98, His110, Ser111, His115), metal coordination bonds (HDAC10: catalytic zinc ion), π-π interactions (VHL: Tyr98), and ionic interactions (HDAC10: Glu274). When the right sides of Figures 66a and 66b are compared, conserved interactions such as Trp205(cation-π), His136, His137, and Tyr307 can be observed, along with new interactions like Tyr112 and Trp205. While the metal coordination bonds remain intact, a new ionic interaction involving Glu24 is also identified.

Based on these findings, it is clear that both warheads demonstrate stable binding in their respective binding pockets.

Overall, while the warheads in both binding pockets remain stably bound, the binding surfaces and conformations of the two proteins exhibit significant changes throughout the molecular dynamics (MD) simulation.
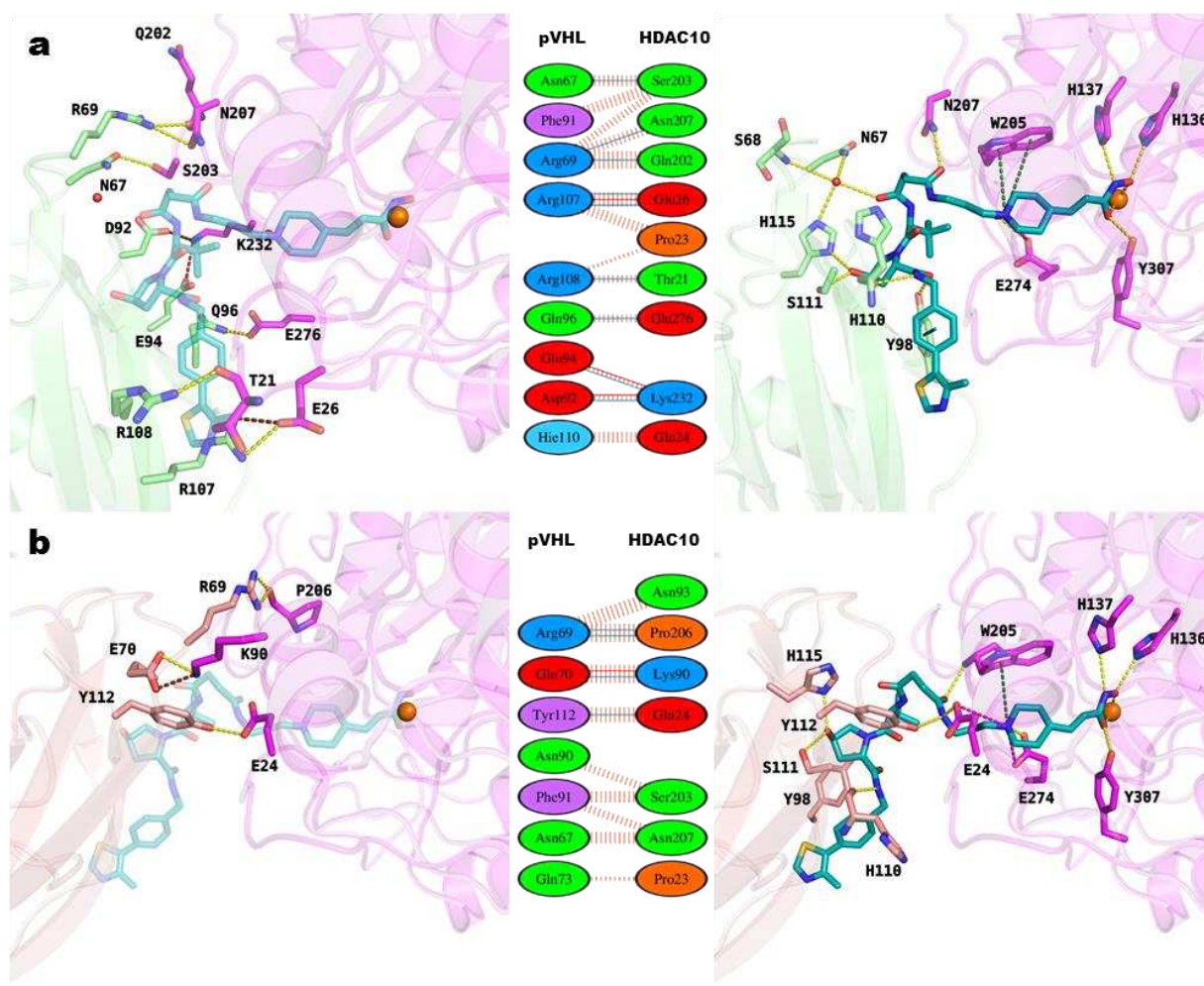
Figure 66: Configuration of PROTAC6_152 Ternary Complex before MD and at 500 ns MD Simulation: **a)** Before MD: Left—protein-protein interactions between VHL and HDAC10 with salt bridges and hydrogen bonds. Middle—2D interaction map. Right—PROTAC6 interactions with both proteins, **b)** 500 ns: Left—updated protein-protein interactions with salt bridges and hydrogen bonds. Middle—2D interaction map. Right—PROTAC6 interactions with proteins, showing conserved and modified connections. Brown dashed lines indicate salt bridges; yellow indicates hydrogen bonds; green shows cation-π; orange represents metal coordination; blue indicates π-π; magenta shows ionic interactions for the 3D figures. Red lines indicate salt bridges; blue lines show hydrogen bonds; yellow dashed lines represent hydrophobic interactions for the 2D figures.

As a final result, it was observed that two of the three studied ternary complexes maintained the interactions of the warheads with both VHL protein and HDAC10 during 500 ns of MD simulations. Considering the accepted fact that plasticity in PROTAC ternary structures is expected and acceptable [183], it can be concluded that the solutions PROTAC6_7, PROTAC6_152 from method 5, and their evolved ternary complexes represent possible ternary

complex conformations. In the next phase of the study, given the fact that different PROTACs can induce the same ternary complex conformation (for the same POI and E3 ligase proteins) and the same protein-protein interactions, and considering that an appropriate docking method was not used in MOE Method 5, we will proceed by conducting docking studies in grid structures separately obtained from these four ternary complex conformations (PROTAC6_7 before MD, PROTAC6_7 last frame of MD, PROTAC6_152 before MD and PROTAC6_152 last frame of MD) for strong, medium, and ineffective degraders. In these four binding modes, active degraders are expected to provide suitable binding modes for strong and medium-level degrader structures in principle.

4.13.4 Docking studies of HDAC10-PROTACs

Docking studies were conducted in the same manner as protein-ligand studies (see section 3.1.1). Initially, a no-constraint docking approach was attempted, but since no docking results were obtained, four H-bond constraints were applied: two from the POI structures (His136, Tyr307) and two from the VHL protein (His110, Ser111). Since the binding pockets of both warheads and their binding modes are known from crystal structures, the main focus of this study is to observe whether the PROTACs with the linker structures can fit in the predicted protein-protein arrangements of the four aforementioned ternary complex structures.

Analyzing the docking results obtained from the grid of PROTAC6_152 from Method 5 (before MD) (see Table 11), strong degraders PROTAC7, PROTAC6, and PROTAC9 produced docking poses (see Figures 67a, 67c, and 67d, respectively), respectively, indicating successful docking results. However, PROTAC8 and PROTAC10 did not produce any docking results. For moderate degraders, PROTAC2 showed a docking pose (see Figure 67b) with a worse score than strong degraders, where part of the VHL ligand did not overlap, indicating docking failure to reproduce the warhead's binding mode. Similarly, the moderate degrader PROTAC1 and non-degraders yielded no docking solutions. In Figure 67, the binding pose of PROTAC6 obtained from Method 5 was used for comparison. Overall, the success rate was 60% for strong degraders and 0% for moderate degraders.

Table 11 : Glide Docking Scores for Degraders in ternary complexes obtained before MD and at 500 ns of MD Simulations of Pose 152. N.D. indicates scores not determined.

PROTAC6_P–P Dock pose152 Docking Results of Schrödinger	Before MD	Glide Docking Score	MD last 500 ns	Glide Docking Score
Strong Degraders	PROTAC7	–17.675	PROTAC7	–17.291
	PROTAC6	–16.024	PROTAC6	–16.224
	PROTAC8	N.D.	PROTAC8	N.D.
	PROTAC9	–16.742	PROTAC9	N.D.
	PROTAC10	N.D.	PROTAC10	N.D.
Moderate–Degraders	PROTAC2	–13.303	PROTAC2	N.D.
	PROTAC1	N.D.	PROTAC1	N.D.
Non–Degraders	PROTAC3	N.D.	PROTAC3	N.D.
	PROTAC4	N.D.	PROTAC4	N.D.
	PROTAC5	N.D.	PROTAC5	N.D.

In the docking studies using the ternary complex PROTAC6_152 obtained after 500 ns MD simulation (see Table 11), only two out of the 5 strong degraders, namely PROTAC7 and PROTAC6, produced docking poses (see Figures 68a and 68b, respectively) with docking scores of -17.291 and -16.224, respectively. In Figure 68, the binding pose of PROTAC6 in the last frame of the 500 ns molecular dynamics simulation, is shown for comparison. No docking poes were obtained for moderate and non-degraders.
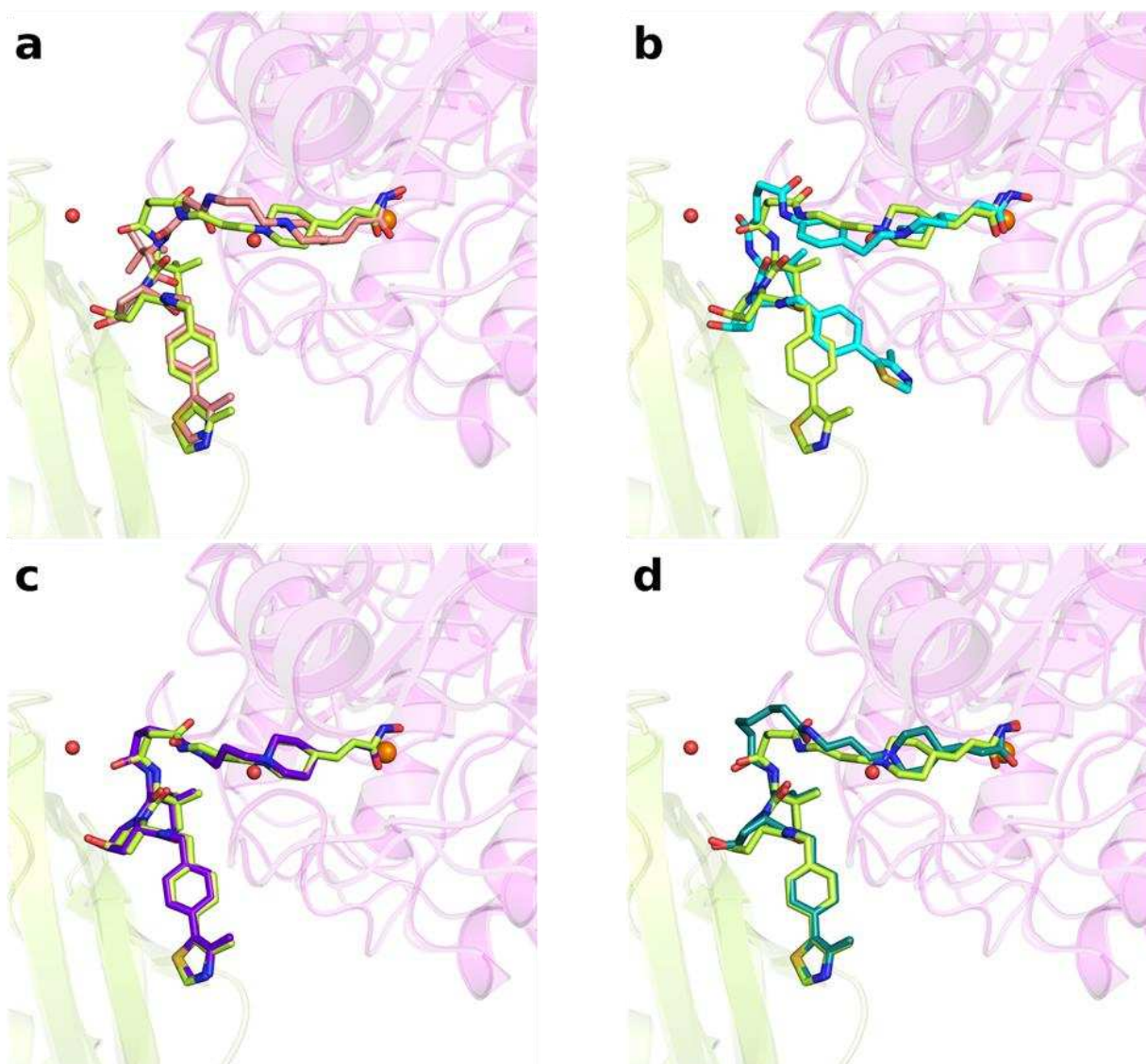
Figure 67: Superimposed Docking Poses for Strong and Moderate Degraders in the Ternary Complex of PROTAC6_152 Grid, obtained prior to MD simulation (from MOE). **a)** PROTAC7 (salmon sticks), **b)** PROTAC2 (cyan sticks), **c)** PROTAC6 (purple sticks) and **d)** PROTAC9 (teal sticks). All poses are compared to the reference PROTAC6 pose (lime green) from the ternary complex. The ternary complex includes HDAC10 (pink cartoons) and the VHL protein (lime green cartoons). The orange sphere represents the catalytic zinc ion, while the red spheres indicate the positions of water molecules.
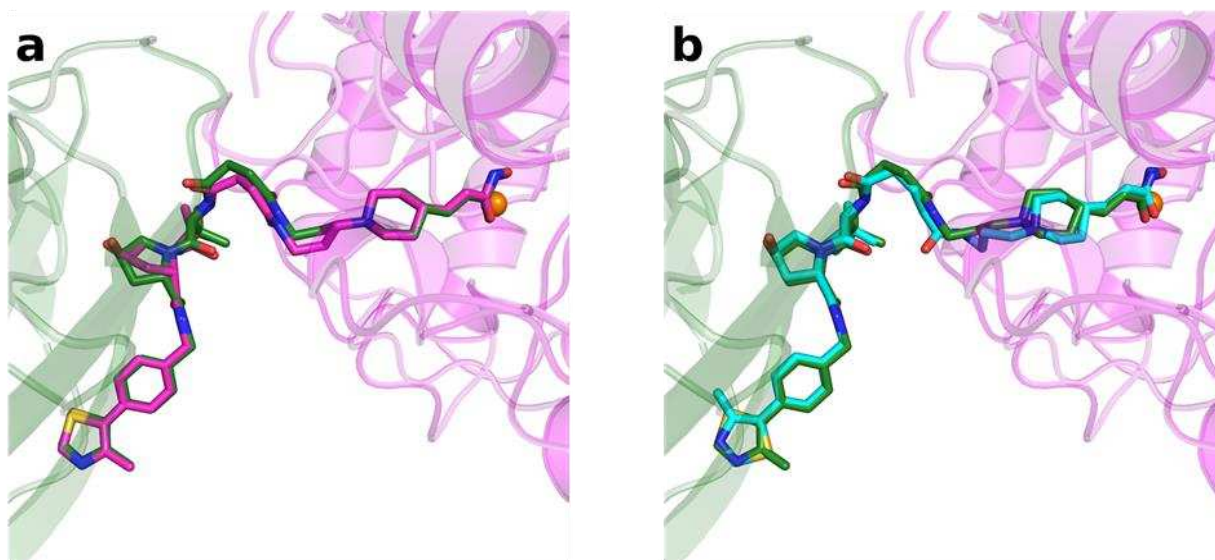
Figure 68: Superimposed Docking Poses for Strong and Moderate Degraders in the Ternary Complex structure obtained after 500 ns MD simulation (PROTAC6_152 Grid). **a)** PROTAC7 (magenta sticks) and **b)** PROTAC6 (cyan sticks. All poses are compared to the reference PROTAC6 pose (forest green) from the ternary complex. The ternary complex includes HDAC10 (pink cartoons) and the VHL protein (forest green cartoons). The orange sphere represents the catalytic zinc ion.

Examining the docking results obtained using from the grid of PROTAC6_7 before MD (refer to Table 12), it was observed that nearly all strong degraders, except for PROTAC6, generated docking poses (see Figures 69c, 69d, 69e, and 69f, respectively), with docking scores of between -17.126 and -20.096, demonstrating successful docking results. Among the moderate degraders, PROTAC2 yielded a docking pose (see Figure 69a) with a docking score of -17.649, while PROTAC1 did not produce any results. As anticipated, most of the non-degraders did not result in any docking solutions, except for PROTAC3, which had a docking score of -13.913 (see Figure 69b). Overall, the success rate for strong degraders was 80%, while for moderate degraders, it was 50%. Additionally, there was one false positive solution among the non-degraders, specifically PROTAC3.

When using the ternary complex that PROTAC6_7 evolved into after 500 ns MD simulation (refer to Table 12) for docking studies, all strong degraders -PROTAC7, PROTAC6, PROTAC8, PROTAC9, and PROTAC10- produced docking poses (see Figures 70a, 70c, 70d, 70e, and 70f, respectively) with docking scores of -17.320, -14.653, -16.022, -17.464, and -18.345, respectively. Among the moderate degraders, only PROTAC2 generated a docking pose (see Figure 70b) with an equally good docking score. As expected, there were no docking solutions for non-degraders. In this scenario, the success rate was 100% for strong degraders and 50% for moderate degraders, with no false positives.

Table 12: Glide Docking Scores for Degraders in ternary complexes obtained before MD and at 500 ns of MD Simulations of Pose 7. N.D. indicates scores not determined.

PROTAC6_P–P Dock pose7 Docking Results of Schrödinger	Before MD	Glide Docking Score	MD last 500 ns	Glide Docking Score
Strong Degraders	PROTAC7	–17.126	PROTAC7	–17.320
	PROTAC6	N.D.	PROTAC6	–14.653
	PROTAC8	–17.305	PROTAC8	–16.022
	PROTAC9	–20.096	PROTAC9	–17.464
	PROTAC10	–18.667	PROTAC10	–18.345
Moderate–Degraders	PROTAC2	–17.649	PROTAC2	–18.427
	PROTAC1	N.D.	PROTAC1	N.D.
Non–Degraders	PROTAC3	–13.913	PROTAC3	N.D.
	PROTAC4	N.D.	PROTAC4	N.D.
	PROTAC5	N.D.	PROTAC5	N.D.
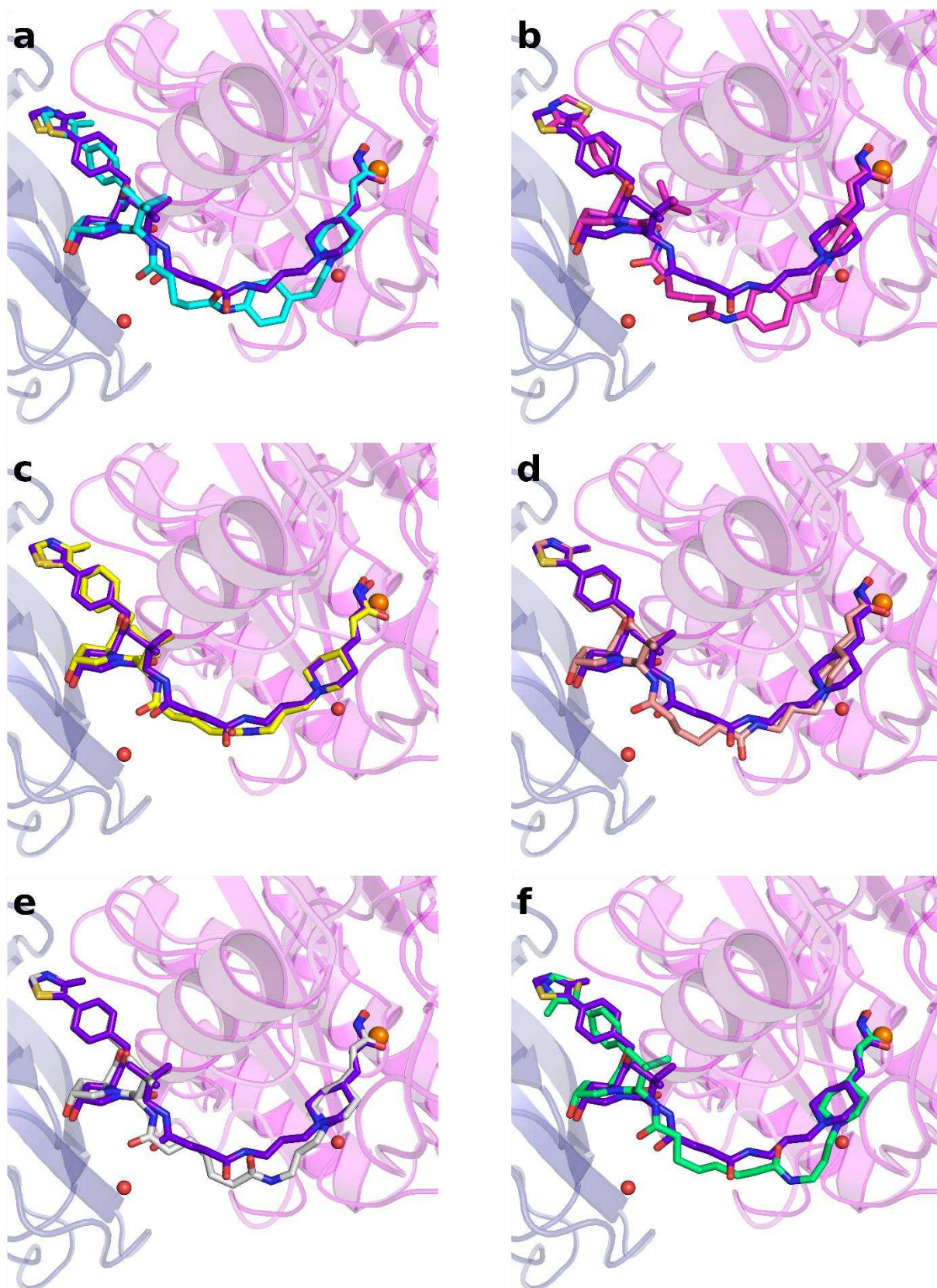
Figure 69: Superimposed Docking Poses for Strong, Moderate, obtained prior to MD simulation (from MOE in 0 ns in the PROTAC6_7 Grid. **a)** PROTAC2 (cyan sticks), **b)** PROTAC3 (magenta sticks), **c)** PROTAC7 (yellow sticks), **d)** PROTAC8 (salmon sticks), **e)** PROTAC9 (white sticks) and f) PROTAC10 (pale green sticks). All poses are compared to the reference PROTAC6 pose (purple sticks). The ternary complex includes HDAC10 (pink cartoons) and the VHL protein (blue cartoons). The orange sphere represents the catalytic zinc ion, while the red spheres indicate the positions of water molecules.
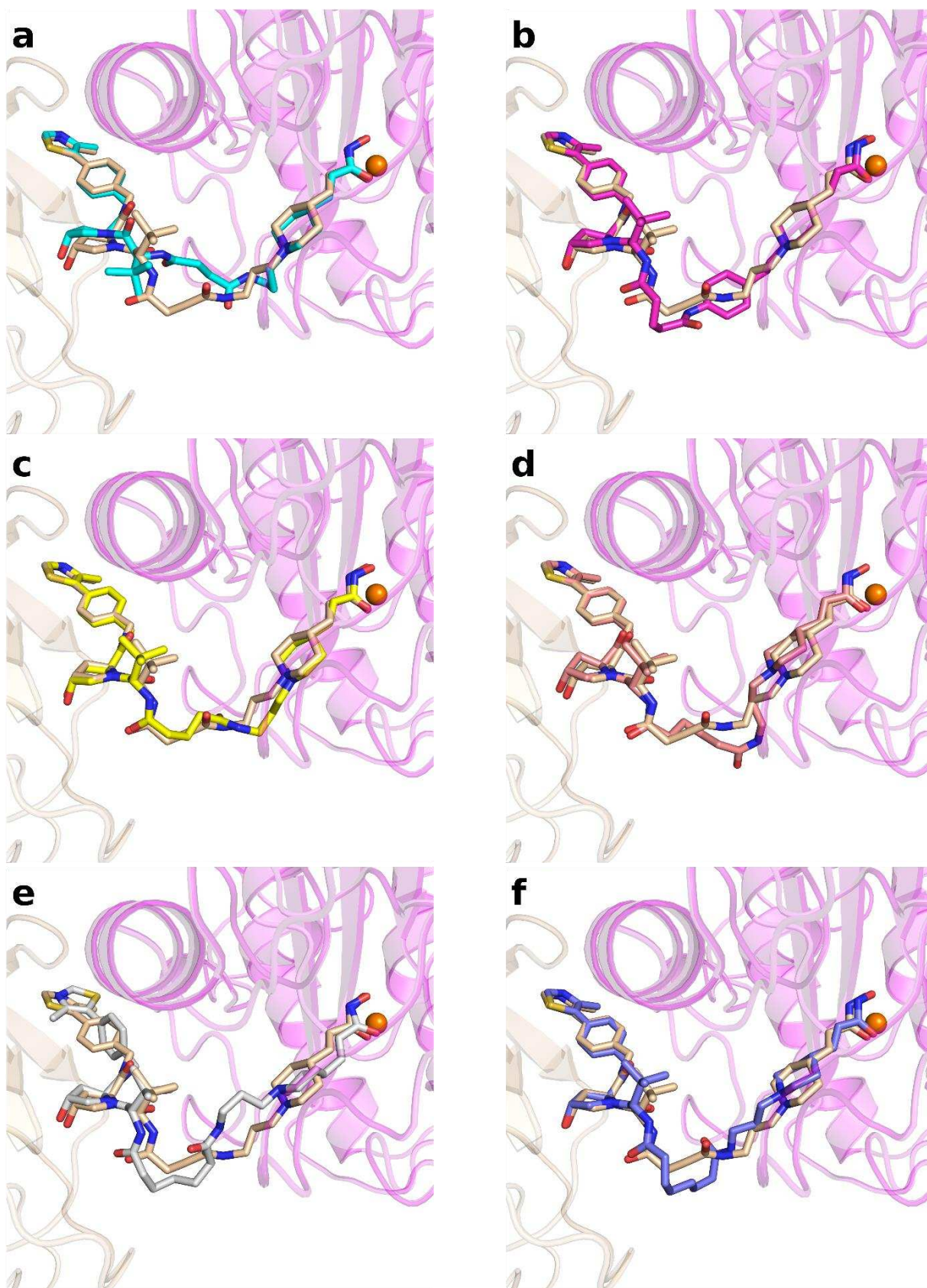
Figure 70: Superimposed Docking Poses for Strong and Moderate Degraders at 500 ns in the PROTAC6_7 Grid. **a)** PROTAC7 (cyan sticks), **b)** PROTAC2 (magenta sticks), **c)** PROTAC6 (yellow sticks), **d)** PROTAC8 (salmon sticks), **e)** PROTAC9 (white sticks) and **f)** PROTAC10 (purple sticks). All poses are compared to the reference PROTAC6 pose (wheat sticks). The ternary complex includes HDAC10 (pink cartoons) and the VHL protein (blue cartoons). The orange sphere represents the catalytic zinc ion.

In evaluating the docking studies conducted across the four different ternary complex models, it was generally observed that active degraders produced successful docking results, while inactive compounds did not yield any docking poses, with the exception of PROTAC3 (pose7, 0ns). This partially reinforces the validity of the modeling approach and provides a feedback mechanism that affirms the ability to distinguish between active and inactive compounds. However, among the ternary complex models studied, the PROTAC6_7 ternary complex, which evolved after 500 ns, stood out as the most effective model. This structure consistently produced favorable docking results for strong degraders, such as PROTAC7, PROTAC6, PROTAC8, PROTAC9, and PROTAC10, while correctly not yielding any docking poses for inactive compounds.

Given these findings, the PROTAC6_7 model at 500 ns has emerged as the most promising model for future research. It holds significant potential as a guide for the design of novel HDAC10 degraders involving the VHL protein, as it has proven capable of differentiating between active and inactive compounds.

5. CONCLUSION

This study focused on molecular modeling studies on selective inhibitors and degraders for HDAC10, a class IIb histone deacetylase with polyamine deacetylase activity. Given the time and cost challenges of drug discovery, advanced computational techniques such as molecular docking, molecular dynamics (MD), and binding free energy (BFE) calculations were employed to guide the design of selective HDAC10 inhibitors and degraders.

Structural analyses have already identified unique features of HDAC10, such as the P(E)ACE motif, the gatekeeper residue E274, and the HDAC10-specific W205, essential for binding small acetylated polyamines. Docking studies showed the importance of salt bridges between E274 and inhibitors, as seen with Tubastatin A, an HDAC6-selective inhibitor, which also interacts with E274. New compounds **(41–88, 90-91, 94-96)** were designed, including piperidine-acryl-hydroxamate, propyl-acryl-hydroxamate, and benzyl-linked hydroxamate linkers, improving selectivity and activity with IC_{50} values around or below 100 nM. Crystallization studies with humanized HDAC10 confirmed the accuracy of the predicted docking poses.

Further 100 ns MD studies in triplicates validated the stability of the predicted docking poses stability, however showing the flexibility of the capping groups. Rescoring the obtained dockings poses using 1-ns MD simulations produced 2 good correlation models (Model 2 and model 6). Statistical validation also identified two robust classification models -model 25 and model 26, which are able to differentiate between active and less active HDAC10 inhibitors. These models were used to predict pIC_{50} values and filter modified compounds, with external validation confirming model 26 as the superior tool. Despite some minor misclassifications, model 26 effectively guided the design of new selective HDAC10 inhibitors.

Co-solvent MD studies, which were validated by identifying binding pockets in HDAC8 and HDAC6, did not reveal new targetable regions or subpockets in HDAC10. However, they highlighted key residues E274, W205, and A94, reinforcing that targeting these residues is crucial for inhibitor design.

In the final part, a ternary complex model was developed using VHL-based PROTAC degraders to predict HDAC10 degradation activity. This model could distinguish between active and inactive degraders using docking the PROTACs into models generated for the HDAC10-VHL complex. The grid files generated from the developed ternary model can be utilized in docking

studies, enabling the pre-screening of new VHL-based HDAC10 degraders in a practical, time-efficient, and cost-effective manner.

In conclusion, the study provides a comprehensive framework using computational tools to design and optimize selective HDAC10 inhibitors and degraders, laying the groundwork for future therapeutic developments.

6. REFERENCES

1. Yan, M.S., C.C. Matouk, and P.A. Marsden, *Epigenetics of the vascular endothelium.* J Appl Physiol (1985), 2010. **109**(3): p. 916-26.
2. Turner, B.M., *The adjustable nucleosome: an epigenetic signaling module.* Trends Genet, 2012. **28**(9): p. 436-44.
3. Bhaumik, S.R., E. Smith, and A. Shilatifard, *Covalent modifications of histones during development and disease pathogenesis.* Nat Struct Mol Biol, 2007. **14**(11): p. 1008-16.
4. Torano, E.G., et al., *The Impact of External Factors on the Epigenome: In Utero and over Lifetime.* Biomed Res Int, 2016. **2016**: p. 2568635.
5. Campos, E.I. and D. Reinberg, *Histones: annotating chromatin.* Annu Rev Genet, 2009. **43**: p. 559-99.
6. Allis, C.D. and T. Jenuwein, *The molecular hallmarks of epigenetic control.* Nat Rev Genet, 2016. **17**(8): p. 487-500.
7. Li, E., *Chromatin modification and epigenetic reprogramming in mammalian development.* Nat Rev Genet, 2002. **3**(9): p. 662-73.
8. Pang, M. and S. Zhuang, *Histone deacetylase: a potential therapeutic target for fibrotic disorders.* J Pharmacol Exp Ther, 2010. **335**(2): p. 266-72.
9. Chen, P.J., et al., *Epigenetic modifications by histone deacetylases: Biological implications and therapeutic potential in liver fibrosis.* Biochimie, 2015. **116**: p. 61-9.
10. Miremadi, A., et al., *Cancer genetics of epigenetic genes.* Hum Mol Genet, 2007. **16 Spec No 1**: p. R28-49.
11. Kim, Y.Z., *Altered histone modifications in gliomas.* Brain Tumor Res Treat, 2014. **2**(1): p. 7-21.
12. Eslaminejad, M.B., N. Fani, and M. Shahhoseini, *Epigenetic regulation of osteogenic and chondrogenic differentiation of mesenchymal stem cells in culture.* Cell J, 2013. **15**(1): p. 1-10.
13. Tang, J., H. Yan, and S. Zhuang, *Histone deacetylases as targets for treatment of multiple diseases.* Clin Sci (Lond), 2013. **124**(11): p. 651-62.
14. Seto, E. and M. Yoshida, *Erasers of histone acetylation: the histone deacetylase enzymes.* Cold Spring Harb Perspect Biol, 2014. **6**(4): p. a018713.
15. Park, S.Y. and J.S. Kim, *A short guide to histone deacetylases including recent progress on class II enzymes.* Exp Mol Med, 2020. **52**(2): p. 204-212.
16. Frye, R.A., *Characterization of five human cDNAs with homology to the yeast SIR2 gene: Sir2-like proteins (sirtuins) metabolize NAD and may have protein ADP-ribosyltransferase activity.* Biochem Biophys Res Commun, 1999. **260**(1): p. 273-9.
17. Gao, L., et al., *Cloning and functional characterization of HDAC11, a novel member of the human histone deacetylase family.* J Biol Chem, 2002. **277**(28): p. 25748-55.
18. Li, G., Y. Tian, and W.G. Zhu, *The Roles of Histone Deacetylases and Their Inhibitors in Cancer Therapy.* Front Cell Dev Biol, 2020. **8**: p. 576946.
19. Leipe, D.D. and D. Landsman, *Histone deacetylases, acetoin utilization proteins and acetylpolyamine amidohydrolases are members of an ancient protein superfamily.* Nucleic Acids Res, 1997. **25**(18): p. 3693-7.
20. Yoshida, M., et al., *Chemical and structural biology of protein lysine deacetylases.* Proc Jpn Acad Ser B Phys Biol Sci, 2017. **93**(5): p. 297-321.
21. Chen, L., et al., *Duration of nuclear NF-kappaB action regulated by reversible acetylation.* Science, 2001. **293**(5535): p. 1653-7.
22. Ropero, S. and M. Esteller, *The role of histone deacetylases (HDACs) in human cancer.* Mol Oncol, 2007. **1**(1): p. 19-25.

23.   Ito, K., *Impact of post-translational modifications of proteins on the inflammatory process.* Biochem Soc Trans, 2007. **35**(Pt 2): p. 281-3.

24.   Gregoretti, I.V., Y.M. Lee, and H.V. Goodson, *Molecular evolution of the histone deacetylase family: functional implications of phylogenetic analysis.* J Mol Biol, 2004. **338**(1): p. 17-31.

25.   Jeltsch, A., *Epigenetic Targets in Drug Discovery. Edited by Wolfgang Sippl and Manfred Jung.* ChemBioChem, 2009. **10**(17): p. 2801-2801.

26.   Kim, J.Y., et al., *HDAC1 nuclear export induced by pathological conditions is essential for the onset of axonal damage.* Nat Neurosci, 2010. **13**(2): p. 180-9.

27.   Takami, Y. and T. Nakayama, *N-terminal region, C-terminal region, nuclear export signal, and deacetylation activity of histone deacetylase-3 are essential for the viability of the DT40 chicken B cell line.* J Biol Chem, 2000. **275**(21): p. 16191-201.

28.   Waltregny, D., et al., *Histone deacetylase HDAC8 associates with smooth muscle alpha-actin and is essential for smooth muscle cell contractility.* FASEB J, 2005. **19**(8): p. 966-8.

29.   Kelly, R.D.W., et al., *Histone deacetylase (HDAC) 1 and 2 complexes regulate both histone acetylation and crotonylation in vivo.* Sci Rep, 2018. **8**(1): p. 14690.

30.   Sun, Z., et al., *Deacetylase-independent function of HDAC3 in transcription and metabolism requires nuclear receptor corepressor.* Mol Cell, 2013. **52**(6): p. 769-82.

31.   Chakrabarti, A., et al., *HDAC8: a multifaceted target for therapeutic interventions.* Trends Pharmacol Sci, 2015. **36**(7): p. 481-92.

32.   Aramsangtienchai, P., et al., *HDAC8 Catalyzes the Hydrolysis of Long Chain Fatty Acyl Lysine.* ACS Chem Biol, 2016. **11**(10): p. 2685-2692.

33.   Verdin, E., F. Dequiedt, and H.G. Kasler, *Class II histone deacetylases: versatile regulators.* Trends Genet, 2003. **19**(5): p. 286-93.

34.   Muslin, A.J. and H. Xing, *14-3-3 proteins: regulation of subcellular localization by molecular interference.* Cell Signal, 2000. **12**(11-12): p. 703-9.

35.   Nishino, T.G., et al., *14-3-3 regulates the nuclear import of class IIa histone deacetylases.* Biochem Biophys Res Commun, 2008. **377**(3): p. 852-6.

36.   Kao, H.Y., et al., *Isolation of a novel histone deacetylase reveals that class I and class II deacetylases promote SMRT-mediated repression.* Genes Dev, 2000. **14**(1): p. 55-66.

37.   Zhang, M., et al., *HDAC6 deacetylates and ubiquitinates MSH2 to maintain proper levels of MutSalpha.* Mol Cell, 2014. **55**(1): p. 31-46.

38.   Kawaguchi, Y., et al., *The deacetylase HDAC6 regulates aggresome formation and cell viability in response to misfolded protein stress.* Cell, 2003. **115**(6): p. 727-38.

39.   Hai, Y., et al., *Histone deacetylase 10 structure and molecular function as a polyamine deacetylase.* Nature Communications, 2017. **8**.

40.   Guardiola, A.R. and T.P. Yao, *Molecular cloning and characterization of a novel histone deacetylase HDAC10.* J Biol Chem, 2002. **277**(5): p. 3350-6.

41.   Tong, J.J., et al., *Identification of HDAC10, a novel class II human histone deacetylase containing a leucine-rich domain.* Nucleic Acids Res, 2002. **30**(5): p. 1114-23.

42.   Yanginlar, C. and C. Logie, *HDAC11 is a regulator of diverse immune functions.* Biochimica et Biophysica Acta (BBA) - Gene Regulatory Mechanisms, 2018. **1861**(1): p. 54-59.

43.   Kutil, Z., et al., *Histone Deacetylase 11 Is a Fatty-Acid Deacylase.* ACS Chem Biol, 2018. **13**(3): p. 685-693.

44.   Moreno-Yruela, C., et al., *Histone Deacetylase 11 Is an epsilon-N-Myristoyllysine Hydrolase.* Cell Chem Biol, 2018. **25**(7): p. 849-856 e8.

45.   Porter, N.J. and D.W. Christianson, *Structure, mechanism, and inhibition of the zinc-dependent histone deacetylases.* Curr Opin Struct Biol, 2019. **59**: p. 9-18.

46.   Gantt, S.M., et al., *General Base-General Acid Catalysis in Human Histone Deacetylase 8.* Biochemistry, 2016. **55**(5): p. 820-32.

47.   Bates, S.E., *Epigenetic Therapies for Cancer.* N Engl J Med, 2020. **383**(7): p. 650-663.

48.   Falkenberg, K.J. and R.W. Johnstone, *Histone deacetylases and their inhibitors in cancer, neurological diseases and immune disorders.* Nat Rev Drug Discov, 2014. **13**(9): p. 673-91.

49.   Ediriweera, M.K., K.H. Tennekoon, and S.R. Samarakoon, *Emerging role of histone deacetylase inhibitors as anti-breast-cancer agents.* Drug Discov Today, 2019. **24**(3): p. 685-702.

50.   Bolden, J.E., M.J. Peart, and R.W. Johnstone, *Anticancer activities of histone deacetylase inhibitors.* Nat Rev Drug Discov, 2006. **5**(9): p. 769-84.

51.   Li, Y. and E. Seto, *HDACs and HDAC Inhibitors in Cancer Development and Therapy.* Cold Spring Harb Perspect Med, 2016. **6**(10).

52.   Marks, P.A. and R. Breslow, *Dimethyl sulfoxide to vorinostat: development of this histone deacetylase inhibitor as an anticancer drug.* Nat Biotechnol, 2007. **25**(1): p. 84-90.

53.   West, A.C. and R.W. Johnstone, *New and emerging HDAC inhibitors for cancer treatment.* J Clin Invest, 2014. **124**(1): p. 30-9.

54.   Rashidi, A. and A.F. Cashen, *Belinostat for the treatment of relapsed or refractory peripheral T-cell lymphoma.* Future Oncol, 2015. **11**(11): p. 1659-64.

55.   Grant, C., et al., *Romidepsin: a new therapy for cutaneous T-cell lymphoma and a potential therapy for solid tumors.* Expert Rev Anticancer Ther, 2010. **10**(7): p. 997-1008.

56.   Gao, S., et al., *Preclinical and Clinical Studies of Chidamide (CS055/HBI-8000), An Orally Available Subtype-selective HDAC Inhibitor for Cancer Therapy.* Anticancer Agents Med Chem, 2017. **17**(6): p. 802-812.

57.   Greig, S.L., *Panobinostat: A Review in Relapsed or Refractory Multiple Myeloma.* Target Oncol, 2016. **11**(1): p. 107-14.

58.   Food, U.S. and A. Drug, *Withdrawal of Approval of NDA 205353 for FARYDAK (Panobinostat) Capsules, 10 mg, 15 mg, and 20 mg*, in *Federal Register*. 2022. p. 15249-15250.

59.   Lamb, Y.N., *Givinostat: First Approval.* Drugs, 2024. **84**(7): p. 849-856.

60.   Ho, T.C.S., A.H.Y. Chan, and A. Ganesan, *Thirty Years of HDAC Inhibitors: 2020 Insight and Hindsight.* J Med Chem, 2020. **63**(21): p. 12460-12484.

61.   Chen, R., et al., *The application of histone deacetylases inhibitors in glioblastoma.* J Exp Clin Cancer Res, 2020. **39**(1): p. 138.

62.   Fischer, D.D., et al., *Isolation and characterization of a novel class II histone deacetylase, HDAC10.* J Biol Chem, 2002. **277**(8): p. 6656-66.

63.   Kao, H.Y., et al., *Isolation and characterization of mammalian HDAC10, a novel histone deacetylase.* J Biol Chem, 2002. **277**(1): p. 187-93.

64.   Hai, Y., et al., *Histone deacetylase 10 structure and molecular function as a polyamine deacetylase.* Nat Commun, 2017. **8**: p. 15368.

65.   Bloomfield, V.A., *DNA condensation by multivalent cations.* Biopolymers, 1997. **44**(3): p. 269-82.

66.   Yoo, J. and A. Aksimentiev, *The structure and intermolecular forces of DNA condensates.* Nucleic Acids Res, 2016. **44**(5): p. 2036-46.

67.   Oguro, A., et al., *Two stems with different characteristics and an internal loop in an RNA aptamer contribute to spermine-binding.* J Biochem, 2017. **161**(2): p. 197-206.

68.   Ivanov, I.P., J.F. Atkins, and A.J. Michael, *A profusion of upstream open reading frame mechanisms in polyamine-responsive translational regulation.* Nucleic Acids Res, 2010. **38**(2): p. 353-9.

69. Hai, Y. and D.W. Christianson, *Histone deacetylase 6 structure and molecular basis of catalysis and inhibition.* Nat Chem Biol, 2016. **12**(9): p. 741-7.

70. Herbst-Gervasoni, C.J., et al., *Structural Basis for the Selective Inhibition of HDAC10, the Cytosolic Polyamine Deacetylase.* ACS Chem Biol, 2020. **15**(8): p. 2154-2163.

71. Shinsky, S.A. and D.W. Christianson, *Polyamine Deacetylase Structure and Catalysis: Prokaryotic Acetylpolyamine Amidohydrolase and Eukaryotic HDAC10.* Biochemistry, 2018. **57**(22): p. 3105-3114.

72. Herbst-Gervasoni, C.J. and D.W. Christianson, *X-ray Crystallographic Snapshots of Substrate Binding in the Active Site of Histone Deacetylase 10.* Biochemistry, 2021. **60**(4): p. 303-313.

73. Geraldy, M., et al., *Selective Inhibition of Histone Deacetylase 10: Hydrogen Bonding to the Gatekeeper Residue is Implicated.* J Med Chem, 2019. **62**(9): p. 4426-4443.

74. Wang, M., et al., *A Novel Role for Histone Deacetylase 10 (HDAC10) in the Regulation of PD-L1 Expression and Immune Tolerance Mediated By Antigen Presenting Cells (APCs).* Blood, 2017. **130**: p. 3561.

75. Dahiya, S., et al., *HDAC10 deletion promotes Foxp3(+) T-regulatory cell function.* Sci Rep, 2020. **10**(1): p. 424.

76. Kotian, S., et al., *Histone Deacetylases 9 and 10 Are Required for Homologous Recombination*.* Journal of Biological Chemistry, 2011. **286**(10): p. 7722-7726.

77. Song, C., et al., *Histone deacetylase (HDAC) 10 suppresses cervical cancer metastasis through inhibition of matrix metalloproteinase (MMP) 2 and 9 expression.* J Biol Chem, 2013. **288**(39): p. 28021-33.

78. Islam, M.M., et al., *HDAC10 as a potential therapeutic target in ovarian cancer.* Gynecologic Oncology, 2017. **144**(3): p. 613-620.

79. Shan, C., et al., *4-hydroxyphenylpyruvate dioxygenase promotes lung cancer growth via pentose phosphate pathway (PPP) flux mediated by LKB1-AMPK/HDAC10/G6PD axis.* Cell Death & Disease, 2019. **10**(7): p. 525.

80. Yang, Y., et al., *HDAC10 promotes lung cancer proliferation via AKT phosphorylation.* Oncotarget, 2016. **7**(37): p. 59388-59401.

81. Oehme, I., et al., *Histone deacetylase 10 promotes autophagy-mediated cell survival.* Proc Natl Acad Sci U S A, 2013. **110**(28): p. E2592-601.

82. Butler, K.V., et al., *Rational design and simple chemistry yield a superior, neuroprotective HDAC6 inhibitor, tubastatin A.* J Am Chem Soc, 2010. **132**(31): p. 10842-6.

83. Kolbinger, F.R., et al., *The HDAC6/8/10 inhibitor TH34 induces DNA damage-mediated cell death in human high-grade neuroblastoma cell lines.* Arch Toxicol, 2018. **92**(8): p. 2649-2664.

84. Steimbach, R.R., et al., *Aza-SAHA Derivatives Are Selective Histone Deacetylase 10 Chemical Probes That Inhibit Polyamine Deacetylation and Phenocopy HDAC10 Knockout.* J Am Chem Soc, 2022. **144**(41): p. 18861-18875.

85. Lambona, C., et al., *Histone deacetylase 10: A polyamine deacetylase from the crystal structure to the first inhibitors.* Curr Opin Struct Biol, 2023. **82**: p. 102668.

86. Sun, X., et al., *PROTACs: great opportunities for academia and industry.* Signal Transduct Target Ther, 2019. **4**: p. 64.

87. Churcher, I., *Protac-Induced Protein Degradation in Drug Discovery: Breaking the Rules or Just Making New Ones?* J Med Chem, 2018. **61**(2): p. 444-452.

88. Pettersson, M. and C.M. Crews, *PROteolysis TArgeting Chimeras (PROTACs) - Past, present and future.* Drug Discov Today Technol, 2019. **31**: p. 15-27.

89. Cecchini, C., et al., *From Conception to Development: Investigating PROTACs Features for Improved Cell Permeability and Successful Protein Degradation.* Front Chem, 2021. **9**: p. 672267.

90. Zengerle, M., K.H. Chan, and A. Ciulli, *Selective Small Molecule Induced Degradation of the BET Bromodomain Protein BRD4.* ACS Chem Biol, 2015. **10**(8): p. 1770-7.

91. Schwalm, M.P., et al., *Tracking the PROTAC degradation pathway in living cells highlights the importance of ternary complex measurement for PROTAC optimization.* Cell Chem Biol, 2023. **30**(7): p. 753-765 e8.

92. Webb, T., C. Craigon, and A. Ciulli, *Targeting epigenetic modulators using PROTAC degraders: Current status and future perspective.* Bioorg Med Chem Lett, 2022. **63**: p. 128653.

93. Bondeson, D.P., et al., *Catalytic in vivo protein knockdown by small-molecule PROTACs.* Nat Chem Biol, 2015. **11**(8): p. 611-7.

94. Darwish, S., *Dissertation MLU 2022: Title of the Thesis (if available).* 2022, Martin Luther University Halle-Wittenberg.

95. Yang, K., et al., *Development of the first small molecule histone deacetylase 6 (HDAC6) degraders.* Bioorg Med Chem Lett, 2018. **28**(14): p. 2493-2497.

96. Smalley, J.P., et al., *Optimization of Class I Histone Deacetylase PROTACs Reveals that HDAC1/2 Degradation is Critical to Induce Apoptosis and Cell Arrest in Cancer Cells.* J Med Chem, 2022. **65**(7): p. 5642-5659.

97. Sabe, V.T., et al., *Current trends in computer aided drug design and a highlight of drugs discovered via computational techniques: A review.* European Journal of Medicinal Chemistry, 2021. **224**.

98. Jorgensen, W.L., *The many roles of computation in drug discovery.* Science, 2004. **303**(5665): p. 1813-8.

99. Van Drie, J.H., *Computer-aided drug design: the next 20 years.* J Comput Aided Mol Des, 2007. **21**(10-11): p. 591-601.

100. Baig, M.H., et al., *Computer Aided Drug Design: Success and Limitations.* Curr Pharm Des, 2016. **22**(5): p. 572-81.

101. Kubinyi, H., *Success Stories of Computer-Aided Design*, in *Computer Applications in Pharmaceutical Research and Development*. 2006. p. 377-424.

102. Warr, W.A., *A CADD-alog of strategies in pharma.* J Comput Aided Mol Des, 2017. **31**(3): p. 245-247.

103. Stahl, M., W. Guba, and M. Kansy, *Integrating molecular design resources within modern drug discovery research: the Roche experience.* Drug Discov Today, 2006. **11**(7-8): p. 326-33.

104. Muegge, I., A. Bergner, and J.M. Kriegl, *Computer-aided drug design at Boehringer Ingelheim.* J Comput Aided Mol Des, 2017. **31**(3): p. 275-285.

105. Hartman, G.D., et al., *Non-peptide fibrinogen receptor antagonists. 1. Discovery and design of exosite inhibitors.* J Med Chem, 1992. **35**(24): p. 4640-2.

106. Pai, V.B. and M.C. Nahata, *Nelfinavir mesylate: a protease inhibitor.* Ann Pharmacother, 1999. **33**(3): p. 325-39.

107. Saikia, S. and M. Bordoloi, *Molecular Docking: Challenges, Advances and its Use in Drug Discovery Perspective.* Curr Drug Targets, 2019. **20**(5): p. 501-521.

108. Huang, S.Y., *Comprehensive assessment of flexible-ligand docking algorithms: current effectiveness and challenges.* Brief Bioinform, 2018. **19**(5): p. 982-994.

109. Berman, H.M., et al., *The Protein Data Bank.* Nucleic Acids Res, 2000. **28**(1): p. 235-42.

110. Wang, J., et al., *Automatic atom type and bond type perception in molecular mechanical calculations.* J Mol Graph Model, 2006. **25**(2): p. 247-60.

111. Jakalian, A., D.B. Jack, and C.I. Bayly, *Fast, efficient generation of high-quality atomic charges. AM1-BCC model: II. Parameterization and validation.* J Comput Chem, 2002. **23**(16): p. 1623-41.

112.   Jakalian, A., et al., *Fast, efficient generation of high-quality atomic Charges. AM1-BCC model: I. Method.* Journal of Computational Chemistry, 2000. **21**(2): p. 132-146.

113.   He, X.B., et al., *A fast and high-quality charge model for the next generation general AMBER force field.* Journal of Chemical Physics, 2020. **153**(11).

114.   Maier, J.A., et al., *ff14SB: Improving the Accuracy of Protein Side Chain and Backbone Parameters from ff99SB.* Journal of Chemical Theory and Computation, 2015. **11**(8): p. 3696-3713.

115.   Li, P., L.F. Song, and K.M. Merz, Jr., *Parameterization of highly charged metal ions using the 12-6-4 LJ-type nonbonded model in explicit water.* J Phys Chem B, 2015. **119**(3): p. 883-95.

116.   Toukmaji, A., et al., *Efficient particle-mesh Ewald based approach to fixed and induced dipolar interactions.* Journal of Chemical Physics, 2000. **113**(24): p. 10913-10927.

117.   *The PyMOL Molecular Graphics System, Version 2.0 Schrödinger,LLC.*

118.   Ghanakota, P. and H.A. Carlson, *Driving Structure-Based Drug Discovery through Cosolvent Molecular Dynamics.* Journal of Medicinal Chemistry, 2016. **59**(23): p. 10383-10399.

119.   Graham, S.E., N. Leja, and H.A. Carlson, *MixMD Probeview: Robust Binding Site Prediction from Cosolvent Simulations.* Journal of Chemical Information and Modeling, 2018. **58**(7): p. 1426-1433.

120.   Guvench, O. and A.D. MacKerell, *Computational Fragment-Based Binding Site Identification by Ligand Competitive Saturation.* Plos Computational Biology, 2009. **5**(7).

121.   Alvarez-Garcia, D. and X. Barril, *Molecular Simulations with Solvent Competition Quantify Water Displaceability and Provide Accurate Interaction Maps of Protein Binding Sites.* Journal of Medicinal Chemistry, 2014. **57**(20): p. 8530-8539.

122.   Ghanakota, P. and H.A. Carlson, *Moving Beyond Active-Site Detection: MixMD Applied to Allosteric Systems.* Journal of Physical Chemistry B, 2016. **120**(33): p. 8685-8695.

123.   Ghanakota, P., et al., *Large-Scale Validation of Mixed-Solvent Simulations to Assess Hotspots at Protein-Protein Interaction Interfaces.* Journal of Chemical Information and Modeling, 2018. **58**(4): p. 784-793.

124.   Tan, Y.S., et al., *The Application of Ligand-Mapping Molecular Dynamics Simulations to the Rational Design of Peptidic Modulators of Protein-Protein Interactions.* Journal of Chemical Theory and Computation, 2015. **11**(7): p. 3199-3210.

125.   Tan, Y.S., et al., *Using Ligand-Mapping Simulations to Design a Ligand Selectively Targeting a Cryptic Surface Pocket of Polo-Like Kinase 1.* Angewandte Chemie-International Edition, 2012. **51**(40): p. 10078-10081.

126.   Jorgensen, W.L., et al., *Comparison of Simple Potential Functions for Simulating Liquid Water.* Journal of Chemical Physics, 1983. **79**(2): p. 926-935.

127.   Heinzelmann, G. and M.K. Gilson, *Automation of absolute protein-ligand binding free energy calculations for docking refinement and compound evaluation.* Sci Rep, 2021. **11**(1): p. 1116.

128.   Zwanzig, R.W., *High-Temperature Equation of State by a Perturbation Method .1. Nonpolar Gases.* Journal of Chemical Physics, 1954. **22**(8): p. 1420-1426.

129.   Zwanzig, R.W., *High-Temperature Equation of State by a Perturbation Method .2. Polar Gases.* Journal of Chemical Physics, 1955. **23**(10): p. 1915-1922.

130.   Straatsma, T.P. and H.J.C. Berendsen, *Free-Energy of Ionic Hydration - Analysis of a Thermodynamic Integration Technique to Evaluate Free-Energy Differences by Molecular-Dynamics Simulations.* Journal of Chemical Physics, 1988. **89**(9): p. 5876-5886.

131. Straatsma, T.P., H.J.C. Berendsen, and J.P.M. Postma, *Free-Energy of Hydrophobic Hydration - a Molecular-Dynamics Study of Noble-Gases in Water.* Journal of Chemical Physics, 1986. **85**(11): p. 6720-6727.

132. Bhati, A.P., et al., *Rapid, Accurate, Precise, and Reliable Relative Free Energy Prediction Using Ensemble Based Thermodynamic Integration.* Journal of Chemical Theory and Computation, 2017. **13**(1): p. 210-222.

133. Fratev, F. and S. Sirimulla, *An Improved Free Energy Perturbation FEP plus Sampling Protocol for Flexible Ligand-Binding Domains.* Scientific Reports, 2019. **9**.

134. Srinivasan, J., et al., *Continuum solvent studies of the stability of RNA hairpin loops and helices.* Journal of Biomolecular Structure & Dynamics, 1998. **16**(3): p. 671-+.

135. Kollman, P.A., et al., *Calculating structures and free energies of complex molecules: Combining molecular mechanics and continuum models.* Accounts of Chemical Research, 2000. **33**(12): p. 889-897.

136. Hansson, T., J. Marelius, and J. Aqvist, *Ligand binding affinity prediction by linear interaction energy methods.* Journal of Computer-Aided Molecular Design, 1998. **12**(1): p. 27-35.

137. Aqvist, J., C. Medina, and J.E. Samuelsson, *A new method for predicting binding affinity in computer-aided drug design.* Protein Eng, 1994. **7**(3): p. 385-91.

138. Bulbul, E.F., et al., *Application of Ligand- and Structure-Based Prediction Models for the Design of Alkylhydrazide-Based HDAC3 Inhibitors as Novel Anti-Cancer Compounds.* Pharmaceuticals (Basel), 2023. **16**(7).

139. Bulbul, E.F., et al., *Docking, Binding Free Energy Calculations and In Vitro Characterization of Pyrazine Linked 2-Aminobenzamides as Novel Class I Histone Deacetylase (HDAC) Inhibitors.* Molecules, 2022. **27**(8).

140. Simoben, C.V., et al., *Binding Free Energy (BFE) Calculations and Quantitative Structure-Activity Relationship (QSAR) Analysis of Schistosoma mansoni Histone Deacetylase 8 (smHDAC8) Inhibitors.* Molecules, 2021. **26**(9).

141. Wichapong, K., et al., *Application of Docking and QM/MM-GBSA Rescoring to Screen for Novel Myt1 Kinase Inhibitors.* Journal of Chemical Information and Modeling, 2014. **54**(3): p. 881-893.

142. Slynko, I., et al., *Identification of Highly Potent Protein Kinase C-Related Kinase 1 Inhibitors by Virtual Screening, Binding Free Energy Rescoring, and in vitro Testing.* ChemMedChem, 2016. **11**(18): p. 2084-94.

143. Feig, M., et al., *Performance comparison of generalized born and Poisson methods in the calculation of electrostatic solvation energies for protein structures.* Journal of Computational Chemistry, 2004. **25**(2): p. 265-284.

144. Hawkins, G.D., C.J. Cramer, and D.G. Truhlar, *Pairwise Solute Descreening of Solute Charges from a Dielectric Medium.* Chemical Physics Letters, 1995. **246**(1-2): p. 122-129.

145. Hawkins, G.D., C.J. Cramer, and D.G. Truhlar, *Parametrized models of aqueous free energies of solvation based on pairwise descreening of solute atomic charges from a dielectric medium.* Journal of Physical Chemistry, 1996. **100**(51): p. 19824-19839.

146. Mongan, J., et al., *Generalized Born model with a simple, robust molecular volume correction.* Journal of Chemical Theory and Computation, 2007. **3**(1): p. 156-169.

147. Onufriev, A., D. Bashford, and D.A. Case, *Exploring protein native states and large-scale conformational changes with a modified generalized born model.* Proteins, 2004. **55**(2): p. 383-94.

148. Karaman, B. and W. Sippl, *Docking and binding free energy calculations of sirtuin inhibitors.* Eur J Med Chem, 2015. **93**: p. 584-98.

149. Genheden, S. and U. Ryde, *The MM/PBSA and MM/GBSA methods to estimate ligand-binding affinities.* Expert Opin Drug Discov, 2015. **10**(5): p. 449-61.

150. Hou, T., et al., *Assessing the performance of the molecular mechanics/Poisson Boltzmann surface area and molecular mechanics/generalized Born surface area methods. II. The accuracy of ranking poses generated from docking.* J Comput Chem, 2011. **32**(5): p. 866-77.

151. Chaudhary, N. and P. Aparoy, *Application of per-residue energy decomposition to identify the set of amino acids critical for in silico prediction of COX-2 inhibitory activity.* Heliyon, 2020. **6**(10): p. e04944.

152. Drummond, M.L., et al., *Improved Accuracy for Modeling PROTAC-Mediated Ternary Complex Formation and Targeted Protein Degradation via New In Silico Methodologies.* J Chem Inf Model, 2020. **60**(10): p. 5234-5254.

153. Zeyen, P., et al., *Identification of histone deacetylase 10 (HDAC10) inhibitors that modulate autophagy in transformed cells.* Eur J Med Chem, 2022. **234**: p. 114272.

154. Luo, Y. and H. Li, *Structure-Based Inhibitor Discovery of Class I Histone Deacetylases (HDACs).* Int J Mol Sci, 2020. **21**(22).

155. Herp, D., et al., *First Fluorescent Acetylspermidine Deacetylation Assay for HDAC10 Identifies Selective Inhibitors with Cellular Target Engagement.* Chembiochem, 2022. **23**(14): p. e202200180.

156. He, G., et al., *Discovery of selective HDAC6 inhibitors capped by flavonoid or flavonoid-analogous moieties as anti-cancer therapeutics simultaneously harboring anti-proliferative and immunomodulatory activities.* Bioorg Chem, 2022. **129**: p. 106146.

157. Marek, M., et al., *Characterization of Histone Deacetylase 8 (HDAC8) Selective Inhibition Reveals Specific Active Site Structural and Functional Determinants.* J Med Chem, 2018. **61**(22): p. 10000-10016.

158. Herbst-Gervasoni, C.J. and D.W. Christianson, *Binding of N(8)-Acetylspermidine Analogues to Histone Deacetylase 10 Reveals Molecular Strategies for Blocking Polyamine Deacetylation.* Biochemistry, 2019. **58**(49): p. 4957-4969.

159. Wagner, F.F., et al., *Potent and selective inhibition of histone deacetylase 6 (HDAC6) does not require a surface-binding motif.* J Med Chem, 2013. **56**(4): p. 1772-6.

160. Bayer, T., et al., *Synthesis, Crystallization Studies, and in vitro Characterization of Cinnamic Acid Derivatives as SmHDAC8 Inhibitors for the Treatment of Schistosomiasis.* ChemMedChem, 2018. **13**(15): p. 1517-1529.

161. Senger, J., et al., *Synthesis and Biological Investigation of Oxazole Hydroxamates as Highly Selective Histone Deacetylase 6 (HDAC6) Inhibitors.* J Med Chem, 2016. **59**(4): p. 1545-55.

162. Watson, P.J., et al., *Insights into the activation mechanism of class I HDAC complexes by inositol phosphates.* Nat Commun, 2016. **7**: p. 11262.

163. Vannini, A., et al., *Substrate binding to histone deacetylases as shown by the crystal structure of the HDAC8-substrate complex.* EMBO Rep, 2007. **8**(9): p. 879-84.

164. Miyake, Y., et al., *Structural insights into HDAC6 tubulin deacetylation and its selective inhibition.* Nat Chem Biol, 2016. **12**(9): p. 748-54.

165. Porter, N.J., et al., *Histone Deacetylase 6-Selective Inhibitors and the Influence of Capping Groups on Hydroxamate-Zinc Denticity.* J Med Chem, 2018. **61**(17): p. 8054-8060.

166. Osko, J.D., et al., *Exploring Structural Determinants of Inhibitor Affinity and Selectivity in Complexes with Histone Deacetylase 6.* J Med Chem, 2020. **63**(1): p. 295-308.

167. Porter, N.J., et al., *Unusual zinc-binding mode of HDAC6-selective hydroxamate inhibitors.* Proc Natl Acad Sci U S A, 2017. **114**(51): p. 13459-13464.

168. Hai, Y. and D.W. Christianson, *Histone deacetylase 6 structure and molecular basis of catalysis and inhibition.* Nature Chemical Biology, 2016. **12**(9): p. 741-+.

169. Herp, D., et al., *First Fluorescent Acetylspermidine Deacetylation Assay for HDAC10 Identifies Selective Inhibitors with Cellular Target Engagement.* Chembiochem, 2022. **23**(14).

170. Shen, S., et al., *Structural and in Vivo Characterization of Tubastatin A, a Widely Used Histone Deacetylase 6 Inhibitor.* ACS Med Chem Lett, 2020. **11**(5): p. 706-712.

171. Osko, J.D. and D.W. Christianson, *Structural determinants of affinity and selectivity in the binding of inhibitors to histone deacetylase 6.* Bioorg Med Chem Lett, 2020. **30**(8): p. 127023.

172. Porter, N.J., F.F. Wagner, and D.W. Christianson, *Entropy as a Driver of Selectivity for Inhibitor Binding to Histone Deacetylase 6.* Biochemistry, 2018. **57**(26): p. 3916-3924.

173. Heimburg, T., et al., *Structure-Based Design and Synthesis of Novel Inhibitors Targeting HDAC8 from Schistosoma mansoni for the Treatment of Schistosomiasis.* J Med Chem, 2016. **59**(6): p. 2423-35.

174. Heimburg, T., et al., *Structure-Based Design and Biological Characterization of Selective Histone Deacetylase 8 (HDAC8) Inhibitors with Anti-Neuroblastoma Activity.* J Med Chem, 2017. **60**(24): p. 10188-10204.

175. Herp, D., *Entwicklung eines In-vitro-Aktivitätstestsystems und selektiver Hemmstoffe für die Histondesacetylase 10*, M. Jung, Editor. 2020, Universität Freiburg.

176. Zeyen, P., et al., *Identification of histone deacetylase 10 (HDAC10) inhibitors that modulate autophagy in transformed cells.* European Journal of Medicinal Chemistry, 2022. **234**.

177. Tarawneh, A., et al., *Efficacy of a New Selective Indole-Based Histone Deacetylase 10 Inhibitor in Targeted Anticancer Therapy.* SSRN Electronic Journal.

178. Simoben, C.V., et al., *A Novel Class of Schistosoma mansoni Histone Deacetylase 8 (HDAC8) Inhibitors Identified by Structure-Based Virtual Screening and In Vitro Testing.* Molecules, 2018. **23**(3).

179. Alvarez-Garcia, D. and X. Barril, *Molecular simulations with solvent competition quantify water displaceability and provide accurate interaction maps of protein binding sites.* J Med Chem, 2014. **57**(20): p. 8530-9.

180. Lexa, K.W., G.B. Goh, and H.A. Carlson, *Parameter choice matters: validating probe parameters for use in mixed-solvent simulations.* J Chem Inf Model, 2014. **54**(8): p. 2190-9.

181. Olaoye, O.O., et al., *Unique Molecular Interaction with the Histone Deacetylase 6 Catalytic Tunnel: Crystallographic and Biological Characterization of a Model Chemotype.* J Med Chem, 2021. **64**(5): p. 2691-2704.

182. Gadd, M.S., et al., *Structural basis of PROTAC cooperative recognition for selective protein degradation.* Nat Chem Biol, 2017. **13**(5): p. 514-521.

183. Zhao, H., *Structural Basis of Conformational Dynamics in the PROTAC-Induced Protein Degradation.* ChemMedChem, 2024. **19**(14): p. e202400171.

7. SUPPLEMENTARY

Table 13: The docking scores, binding free energy results, and prediction results of the training set for HDAC10 QSAR models.

ID	pIC$_{50}$	Glide Docking Score	Predicted PIC$_{50}$ Model 25	Predicted PIC$_{50}$ Model 26	GB1_min2 Model 25	GB2min2 Model 26	1_or_0 according to pIC$_{50}$	Predicted 1_or_0 Model 25	Predicted 1_or_0 Model 26
1	7.3028	-9.3633	7.1456	7.1536	-74.1295	-69.2745	1	1	1
2	7.2941	-9.7980	7.2645	7.2234	-78.1047	-71.2412	1	1	1
3	6.8719	-10.0857	6.6365	6.5936	-57.1087	-53.4872	0	0	0
5	7.5214	-9.6288	7.5880	7.5852	-88.9190	-81.4419	1	1	1
7	6.8333	-8.8028	6.7232	6.7851	-60.0088	-58.8855	0	0	0
14	6.7331	-7.9102	6.8165	6.8478	-63.1281	-60.6541	0	0	0
15	6.9500	-8.2826	6.7664	6.7868	-61.4526	-58.9335	0	0	0
23	6.5635	-8.3047	6.8304	6.8546	-63.5903	-60.8451	0	0	0
31	6.3986	-8.8092	6.8351	6.8157	-63.7476	-59.7478	0	0	0
43	7.4318	-9.9876	7.2755	7.2498	-78.4710	-71.9861	1	1	1
44	6.9747	-10.0211	7.2696	7.1635	-78.2733	-69.5530	0	1	1
45	7.6198	-9.9620	7.2670	7.2260	-78.1864	-71.3153	1	1	1
47	7.9586	-8.9416	7.5524	7.6124	-87.7285	-82.2081	1	1	1
48	7.5376	-10.4583	7.6170	7.6523	-89.8875	-83.3322	1	1	1
49	7.6990	-10.3107	7.4162	7.4179	-83.1751	-76.7243	1	1	1
50	7.2218	-10.4695	7.4930	7.5224	-85.7422	-79.6717	1	1	1
51*	6.2725	-10.1326			-83.0984	-77.1063	none		
52	7.2076	-10.3081	7.4440	7.4351	-84.1021	-77.2085	1	1	1
53	7.2366	-9.2886	7.4363	7.4141	-83.8474	-76.6162	1	1	1
54	7.4815	-10.1893	7.4603	7.4985	-84.6490	-78.9976	1	1	1

Table 14: The docking scores, binding free energy results, and prediction results of the test set for HDAC10 QSAR models.

ID	pIC$_{50}$	Glide Docking Score	Predicted PIC$_{50}$ Model 25	Predicted PIC$_{50}$ Model 26	GB1_min2 Model 25	GB2min2 Model 26	1_or_0 according to pIC$_{50}$	Predicted 1_or_0 Model 25	Predicted 1_or_0 Model 26
6	<7.0000	-7.6182	6.8029	6.8123	-62.6724	-59.6541	0	0	0
8	<7.0000	-4.6481	5.2254	4.9321	-9.9376	-6.6525	0	0	0
11	<7.0000	-8.6683	6.6519	6.6213	-57.6246	-54.2677	0	0	0
12	<7.0000	-9.4415	7.1015	6.7871	-72.6540	-58.9431	0	1	0
13	<7.0000	-8.6005	7.3142	6.9055	-79.7658	-62.2801	0	1	0
16	<7.0000	-7.6893	6.7413	6.7398	-60.6136	-57.6095	0	0	0
17	<7.0000	-7.8479	6.7951	6.7667	-62.4115	-58.3684	0	0	0
18	<7.0000	-7.7292	6.7821	6.8004	-61.9778	-59.3184	0	0	0
19	<7.0000	-8.9399	6.6856	6.6916	-58.7502	-56.2504	0	0	0
20	<7.0000	-7.7314	6.6701	6.5833	-58.2309	-53.1982	0	0	0
21	<7.0000	-8.4774	6.9013	6.8734	-65.9610	-61.3750	0	0	0
22	<7.0000	-8.5133	6.8080	6.7931	-62.8413	-59.1130	0	0	0
24	<7.0000	-7.3459	6.8850	6.7953	-65.4162	-59.1739	0	0	0
25	<7.0000	-7.6307	6.9416	6.9135	-67.3085	-62.5057	0	0	0
26	<7.0000	-7.8664	6.6983	6.6043	-59.1742	-53.7900	0	0	0
27	<7.0000	-7.3464	7.1491	6.8672	-74.2448	-61.2006	0	1	0
28	<7.0000	-7.7208	7.1351	6.7572	-73.7786	-58.0991	0	1	0
29	<7.0000	-7.8526	6.8016	6.6539	-62.6295	-55.1880	0	0	0
30	<7.0000	-7.3586	6.6505	6.5827	-57.5788	-53.1807	0	0	0
32	<7.0000	-7.5523	6.6416	6.5827	-57.2801	-53.1817	0	0	0
33	<7.0000	-7.4970	6.8120	6.7676	-62.9766	-58.3918	0	0	0
34	<7.0000	-9.4589	7.4319	7.4740	-83.6989	-78.3053	0	1	1
35	<7.0000	-9.4762	7.3154	7.3260	-79.8033	-74.1353	0	1	1
36	<7.0000	-10.3892	7.5127	7.5912	-86.3998	-81.6096	0	1	1
37	<7.0000	-9.6877	7.3392	7.3290	-80.6004	-74.2195	0	1	1
38	<7.0000	-8.3014	7.6908	7.7480	-92.3534	-86.0307	0	1	1
39	<7.0000	-9.4676	7.5172	7.5682	-86.5508	-80.9620	0	1	1
40	<7.0000	-9.5155	7.5179	7.5948	-86.5728	-81.7116	0	1	1

55	8.7959	-9.1659	7.6356	7.5353	-90.5087	-80.0332	1	1	1
56	8.9208	-9.4210	7.6363	7.5851	-90.5337	-81.4384	1	1	1
57	8.0315	-9.1684	7.6305	7.5900	-90.3387	-81.5754	1	1	1
58	8.9208	-10.4711	7.6712	7.6420	-91.6985	-83.0430	1	1	1
59	8.8861	-9.3338	7.5874	7.6284	-88.8968	-82.6575	1	1	1
60	8.6778	-9.2010	7.5586	7.4688	-87.9336	-78.1588	1	1	1
61	9.0315	-10.6161	7.6033	7.5562	-89.4290	-80.6236	1	1	1
62	8.6576	-10.2074	7.5722	7.4158	-88.3897	-76.6660	1	1	1
63	8.5702	-10.2996	7.4896	7.3250	-85.6295	-74.1066	1	1	1
64	9.2441	-7.9919	7.7290	7.8606	-93.6314	-89.2047	1	1	1
65	8.8477	-9.7898	7.4039	7.4820	-82.7638	-78.5315	1	1	1
66	8.8477	-7.7396	7.6105	7.4872	-89.6710	-78.6775	1	1	1
67	8.0410	-9.3413	7.5641	7.5752	-88.1187	-81.1587	1	1	1
68	9.1427	-9.5498	7.5209	7.6006	-86.6752	-81.8754	1	1	1
69	8.2076	-9.2956	7.6507	7.6658	-91.0151	-83.7136	1	1	1
70	8.2692	-9.2743	7.0741	7.6223	-71.7380	-82.4875	1	1	1
71	8.1675	-10.1910	7.6052	7.6169	-89.4929	-82.3347	1	1	1
72	8.9208	-9.9481	7.7470	7.6393	-94.2314	-82.9660	1	1	1
73	9.0000	-9.9254	7.7613	7.6636	-94.7098	-83.6516	1	1	1
74	9.0809	-9.6039	7.9070	7.8941	-99.5804	-90.1480	1	1	1
75	9.1308	-9.9427	8.0642	7.8431	-104.8362	-88.7121	1	1	1
76	8.9393	-10.7287	7.8924	7.8739	-99.0949	-89.5790	1	1	1
77	8.7799	-10.1288	7.4446	8.1131	-84.1238	-96.3229	1	1	1
78	8.9101	-10.2416	7.9542	7.9266	-101.1605	-91.0651	1	1	1
79	8.9355	-10.1416	8.1747	7.7176	-108.5300	-85.1741	1	1	1
80	9.0655	-10.3737	7.8036	7.8103	-96.1239	-87.7856	1	1	1
81	9.0177	-10.1579	7.7368	7.7176	-93.8920	-85.1731	1	1	1
82	9.1079	-9.5260	7.8538	7.8541	-97.8048	-89.0212	1	1	1
83	9.1938	-9.8241	8.0189	8.0237	-103.3217	-93.8004	1	1	1
84	8.7190	-9.8241	8.3356	8.3854	-113.9093	-103.9982	1	1	1
85	9.0506	-9.4910	7.4343	7.6015	-83.7806	-81.8997	1	1	1

86	9.0915	-10.2601	7.6008	7.6098	-89.3469	-82.1342	1	1	1
87	9.2596	-9.4469	7.6301	8.4244	-90.3258	-105.0963	1	1	1
88	8.9747	-10.0649	7.8336	7.7470	-97.1297	-86.0029	1	1	1
89	9.3872	-10.4695	7.3132	7.2859	-79.7323	-73.0046	1	1	1
90	8.3468	-9.7381	7.4006	7.2746	-82.6530	-72.6860	1	1	1
91	6.5376	-8.1982	7.1346	6.9483	-73.7594	-63.4880	0	1	0
92	6.9586	-8.7151	6.9356	6.9034	-67.1092	-62.2221	0	0	0
93	8.6990	-10.9976	7.4555	7.4078	-84.4884	-76.4398	1	1	1
94	7.1249	-10.0136	7.4337	7.2911	-83.7600	-73.1506	1	1	1
95	7.9586	-10.6655	7.5949	7.5590	-89.1494	-80.7034	1	1	1

7.1. Biological Evaluation

7.1.1. Enzymatic in vitro HDAC activity assay

7.1.1.1. HDAC1 and HDAC6 ZMAL Assays

Human recombinant HDAC1 and HDAC6 enzymes were obtained from BPS Bioscience (catalog no. 50051 for HDAC1 and catalog no. 50006 for HDAC6). The assay was performed using the substrate ZMAL (Z-(Ac)Lys-AMC) at a concentration of 126 µM as seen Figure S1a. A total volume of 60 µL per well was prepared, containing 52 µL of enzyme solution in incubation buffer (50 mM Tris-HCl, pH 8.0, 137 mM NaCl, 2.7 mM KCl, 1 mM MgCl2, and 1 mg/mL BSA), 3 µL of increasing concentrations of inhibitors in DMSO, and 5 µL of the fluorogenic substrate ZMAL. The reaction mixture was incubated at 37 °C for 90 minutes.

After incubation, 60 µL of stop solution, including 5 µL Trichostatin A (33 µM) and 10 µL trypsin (6 mg/mL) in trypsin buffer (50 mM Tris-HCl, pH 8.0, 100 mM NaCl), was added to the wells, followed by a 30-minute incubation at 37 °C. Fluorescence was measured using a POLARstar OPTIMA plate reader with an excitation wavelength of 390 nm and an emission wavelength of 460 nm.

An enzyme-free blank, a DMSO control, and a 100% conversion control were included in the experiment. The percentage of inhibition was calculated using a formula that accounts for the fluorescence intensity of the controls. IC_{50} values were determined by nonlinear regression analysis with Origin 2019b software.

7.1.1.2. HDAC8 FDL Assay

The HDAC8 assay was carried out by Patrik Zeyen (AG Medicinal Chemistry MLU) using the Fluor-de-Lys (FDL) drug discovery kit from Enzo Life Sciences (BML-KI178). The enzyme (hHDAC8) was obtained from cooperation partners (C. Romier, Strasbourg) as shown in Figure S1b.

The reaction mixture consisted of 15 µL of enzyme solution, 10 µL of inhibitor at increasing concentrations, and 25 µL of FDL substrate solution. It was incubated for 90 minutes at 37 °C in a ½ AreaPlate-96 F microplate. Following this, 50 µL of developer solution was added, and the plate was incubated for an additional 45 minutes at 30 °C.

Fluorescence was measured similarly to the HDAC1 and HDAC6 assays. An enzyme-free blank, a DMSO control, and a 100% conversion control were also included. Percent inhibition and IC50 values were calculated using the same methods as those used for the ZMAL-Trypsin

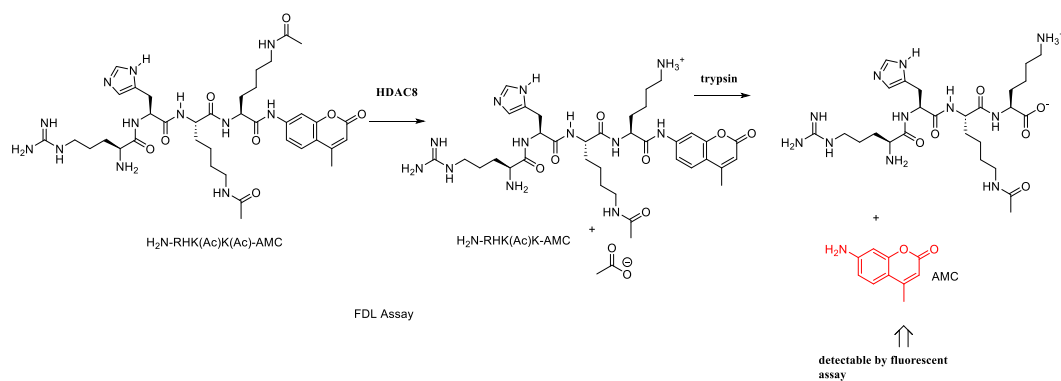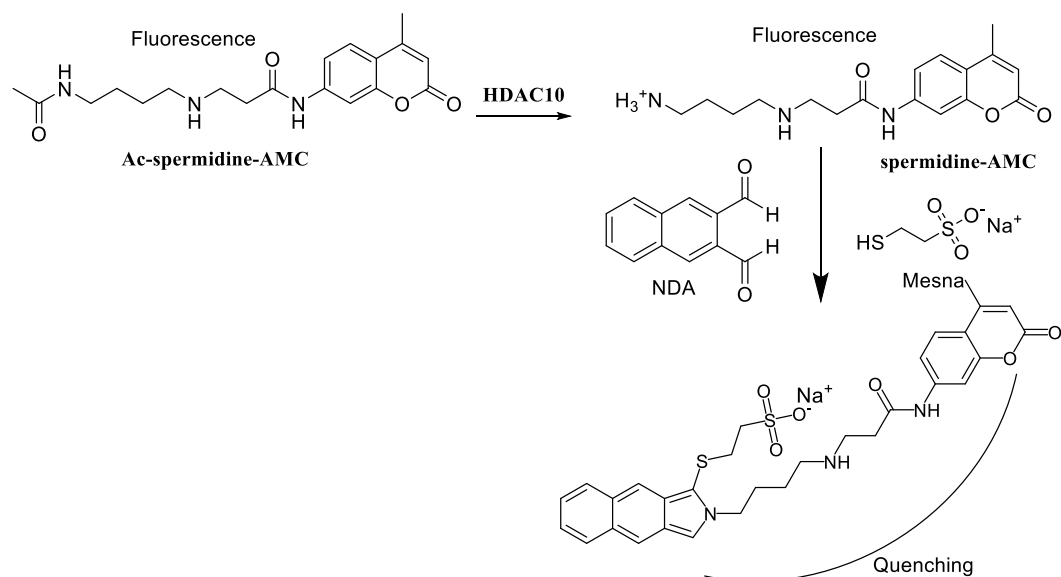assay.

a.
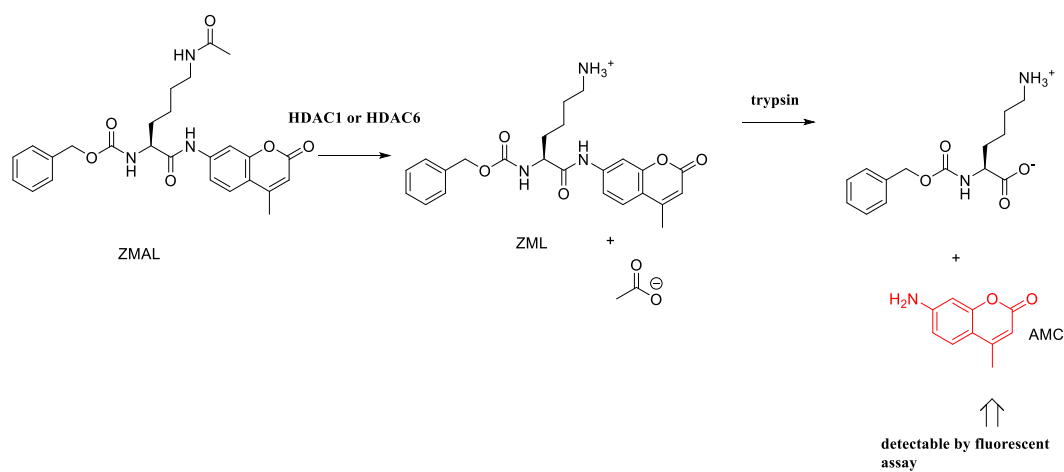
b.

c.

Figure 71: HDAC activity measurement mechanism based on fluorescence-based assay (for compounds **1- 54**).

146

7.1.1.3. HDAC10 NDA Assay

The HDAC10 assay utilized Ac-spermidine-AMC as the substrate as shown in Figure S1c. The assay buffer contained 20 mM Na2HPO4, pH 7.9, 100 mM NaCl, 0.25 mM EDTA, 10% (v/v) glycerol, 10 mM Mesna, and 0.01% (v/v) TWEEN 20.

The stop solution was prepared with 5 µL NDA (16 mM), 5 µL Quisinostat (0.1 mM), and 190 µL borate buffer (100 mM boric acid, pH 9.5) per well. The enzyme solution (0.0054 mg/mL) was freshly prepared in assay buffer immediately before use.

The assay was conducted by Daniel Herp (AG Pharmaceutical Chemistry, Univ. of Freiburg) in black OptiPlateTM-96 F microplates. Assay components were added to each well, including blanks, positive and negative controls, and test compounds. The plate was incubated for 25 minutes at 25 °C before measuring the fluorescence.

Fluorescence was detected using a POLARstar plate reader with an excitation wavelength of 330 nm and an emission wavelength of 390 nm. Conversion rates with and without the inhibitor were calculated, and IC_{50} values were determined using nonlinear regression with Origin 2019b software.

7.1.1.4. HDAC1 and HDAC6 FDL2 Assays

HDAC1 and HDAC6 activities were measured by Matthes Zessin (AG Enzymology MLU) using a discontinuous assay as shown in Figure S2a. For HDAC1, the enzyme was incubated at 37°C for 90 minutes, while HDAC6 was incubated at room temperature for 30 minutes. The substrate used was Ac-RHKK(Ac)-AMC, at a concentration of 20 µM for HDAC1 and 5 µM for HDAC6. The enzyme concentrations were 10 nM for HDAC1 and 1 nM for HDAC6. Inhibitors were prepared in 9% DMSO (v/v), resulting in a final DMSO concentration of 3% (v/v) in a 21 µL reaction volume.

After incubation, 21 µL of stop solution (containing 1 mg/mL Trypsin and 20 µM SAHA) was added, followed by an additional incubation at room temperature for 45-60 minutes. The buffer used for the reactions consisted of 20 mM HEPES (pH 7.4), 140 mM NaCl, 10 mM KCl, 1 mM TCEP, and 0.2 mg/mL BSA. The fluorescence intensity was measured every 10 seconds for a total of 10 measurements, and the average signal was used for analysis. Fluorescence was detected using the EnVision 2104 Multilabel Reader (PerkinElmer, Waltham, USA) with an excitation wavelength of 380 nm and an emission wavelength of 430 nm, using black 384-well plates.

7.1.1.5. HDAC8 sLOGO-STFA Assay

HDAC8 activity was measured by Matthes Zessin (AG Enzymology MLU) using a continuous assay with sLOGO-STFA as the substrate as shown in Figure S2b. The substrate and inhibitor were used at concentrations of 50 µM and 2 nM, respectively. For HDAC1 and HDAC6, the inhibitor concentrations were 10 nM and 1 nM, respectively, dissolved in 12% (v/v) DMSO, yielding a final DMSO concentration of 3% (v/v) in a 40 µL reaction volume. The buffer solution consisted of 20 mM HEPES (pH 7.4), 140 mM NaCl, 10 mM KCl, 1 mM TCEP, and 0.2 mg/mL BSA. Sixty measurements were taken at 1-minute intervals, and the slope from the linear portion of the graph was used for calculations. Fluorescence intensity was recorded at an excitation wavelength of 320 nm and an emission wavelength of 430 nm in black 384-well plates using the EnVision 2104 Multilabel Reader (PerkinElmer, Waltham, USA).
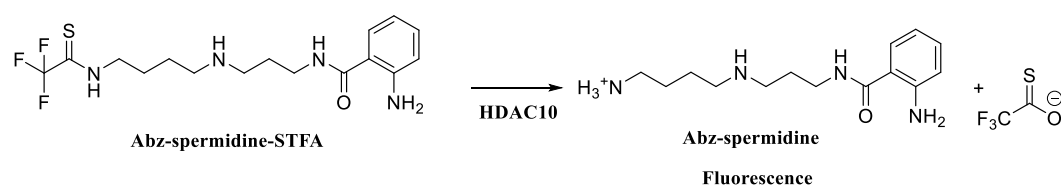
a.
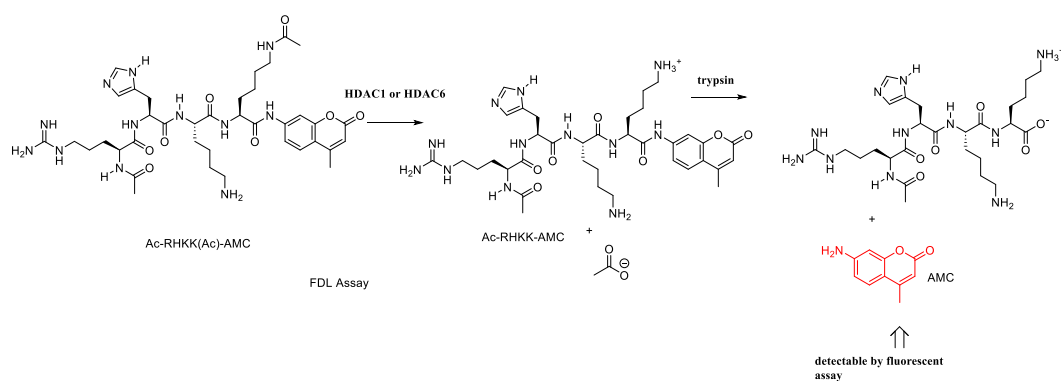
b.
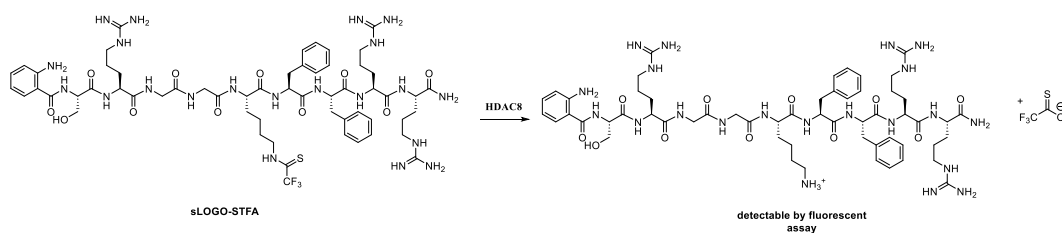
c.

Figure 72: HDAC activity measurement mechanism based on fluorescence-based assay (for compounds **49, 53, 55-96**).

7.1.1.6. HDAC10 Abz-spermidine-STFA Assay

The expressed and purified HDAC10 enzyme, at a concentration of 5 nM, was incubated at room temperature with a 50 µM substrate (Abz-Sperm-STFA) in a buffer containing 20 mM HEPES (pH 7.4) and 0.5 mg/mL BSA as shown in Figure S2c. The inhibitors were dissolved in 12% (v/v) DMSO, resulting in a final DMSO concentration of 3% (v/v). Fluorescence measurements were taken 50 times at 1-minute intervals, and the slope from the linear region of the graph was used for calculations. Fluorescence intensity was recorded using black 384-well plates at an excitation wavelength of 320 nm and an emission wavelength of 430 nm on the EnVision 2104 Multilabel Reader (PerkinElmer, Waltham, USA). The assay was carried out by Matthes Zessin (AG Enzymology MLU).

7.1.2. Cellular Assay and Degradation

Cellular and degradation assays were conducted in collaboration by Melisa Halilovic (AG Prof. Krämer at the Institute of Toxicology, University of Medicine Mainz, Germany). The HDAC degradation activity of the designed degraders was evaluated using two acute leukemia cell lines: RS4-11 (acute lymphoblastic leukemia) and MV4-11 (acute myeloid leukemia).

The experimental protocol involved seeding HEL cells onto cell culture plates, followed by treatment with different concentrations of degraders over a specified time period. After treatment, the cells were harvested, and protein extraction was performed. The extracted proteins were then analyzed and quantified via Western blot.

7.1.2.1. Cell Culture

The experiments were performed by Melisa Halilovic (AG Prof. Krämer, Mainz) with HEL cells, carrying the JAK2V617F mutation, obtained from DSMZ, Braunschweig, Germany. HEL cells were cultured at 37°C with 5% CO2 in RPMI-1640 medium, supplemented with 5% fetal calf serum (FCS) and 1% Penicillin/Streptomycin, under sterile conditions. The cell density was maintained below 400,000 cells/ml by regular splitting at a 1:5 ratio. Culture flasks were replaced every three weeks. Cells were seeded at a density of 200,000 cells/ml by measuring cell concentration using a Neubauer chamber and transferring the appropriate volume into 50 ml Falcon tubes. The cell suspension was centrifuged at 1000 rpm for 5 minutes, after which the medium was discarded and replaced with fresh medium, adjusted to the desired volume for seeding the wells.

7.1.2.2. Western Blot Analysis

Gels prepared using SDS-PAGE were transferred onto nitrocellulose membranes in a Western blot assembly, consisting of Whatman filter paper and the membrane, followed by constant

current application at 350 mA per chamber (each chamber accommodating two blots) for 2 hours. After blotting, membranes were blocked to prevent non-specific antibody binding using a 5% milk-TBS-T solution for 1 hour. Membranes were then incubated with primary antibodies for either 2 hours at room temperature or overnight at 4°C. Following this, secondary antibodies were applied for either 2 hours (for IR-dye detection) or 1 hour (for HRP-based detection). After each antibody incubation, membranes were washed three times with TBS-T solution for 5 minutes each.

Detection was carried out by Melisa Halilovic (AG Prof. Krämer, Mainz) using Odyssey for IR-dyes or iBright for HRP-based antibodies. Data analysis and protein quantification were performed using Image Studio Light 5.2 software.

Selbstständigkeitserklärung/ Declaration of Authorship

Hiermit erkläre ich, dass ich die vorliegende Dissertationsschrift selbständig und ohne fremde Hilfe angefertigt, keine anderen als die angegebenen Quellen und Hilfsmittel benutzt und die aus ihnen wörtlich oder inhaltlich entnommenen Stellen als solche kenntlich gemacht habe. Die Arbeit wurde ausschließlich der Mathematisch-Naturwissenschaftlichen Fakultät der MartinLuther-Universität Halle-Wittenberg vorgelegt und an keiner anderen Universität oder Hochschule weder im In- und Ausland zur Erlangung des Doktorgrades eingereicht.

I hereby declare that I am the sole author of this thesis and that I have not used any sources other than those listed in the bibliography and identified as references. I further declare that I have not submitted this thesis at any other institution in order to obtain a degree.

Halle (Saale), 27.02.2025

RESEARCH EXPERIENCE

- Tarawneh, Amer and Al-Trawneh, Salah and **Yesiloglu, Talha Z**. and Zessin, Matthes and Robaa, Dina and Barinka, Cyril and Schutkowski, Mike and Sippl, Wolfgang and Ross, Samir A., **Efficacy of a New Selective Indole-Based Histone Deacetylase 10 Inhibitor in Targeted Anticancer Therapy**. Available at SSRN: https://ssrn.com/abstract=4900346 (Under Review)

- Sinatra, L., Vogelmann, A., Friedrich, F., **Yesiloglu, T.Z.**, Jung, M., Schiedel, M. **Development of First-in-Class Dual Sirt2/HDAC6 Inhibitors as Molecular Tools for Dual Inhibition of Tubulin Deacetylation.** *Journal of Medicinal Chemistry*, 2023, 66(21), pp. 14787–14814. doi: 10.1021/acs.jmedchem.3c01385

- Herp, D., Ridinger, J., Robaa, D., **Yesiloglu, T.Z.**, Sippl, W., Jung, M. **First Fluorescent Acetylspermidine Deacetylation Assay for HDAC10 Identifies Selective Inhibitors with Cellular Target Engagement.** *Chembiochem*, 2022, 23(14), e202200180. doi:10.1002/cbic.202200180

- Zeyen, P., Zeyn, Y., Herp, D., **Yesiloglu, T.Z.**, Krämer, O.H., Sippl, W. **Identification of Histone Deacetylase 10 (HDAC10) Inhibitors that Modulate Autophagy in Transformed Cells.** *European Journal of Medicinal Chemistry*, 2022, 234, 114272. doi: 10.1016/j.ejmech.2022.114272

- Tallei, T.E., Fatimawali, Yelnetty, A., **Yesiloglu, T.Z.**, Khan, M.A., Celik, I. **An Analysis Based on Molecular Docking and Molecular Dynamics Simulation Study of Bromelain as Anti-SARS-CoV-2 Variants.** *Frontiers in Pharmacology*, 2021, 12, 717757. doi:10.3389/fphar.2021.717757

- Khazneh, E., Saltan, G., Tekin, M., **Yesiloglu, T.Z.**, Özbilgin, S. **The Importance of Achillea Species and Phenolic Compounds in *Achillea schischkinii* Sosn.** *Ankara University Journal of the Faculty of Pharmacy*, 2010, 39(1), pp. 43–50.

- Mahmoudi, F., Mieland, A., Zessin, M., **Yesiloglu, T.Z.**, Hilscher, S., Erdmann, F., Schmidt, M., Robaa, D., Schutkowski, M., Krämer, O.H., Sippl, W. **Structure-Activity Relationships of Piperidine-Based Hydroxamates as Potent and Selective Histone Deacetylase 10 (HDAC10) Inhibitors.** (In preparation).